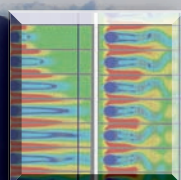
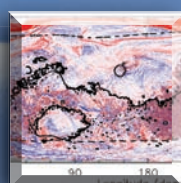
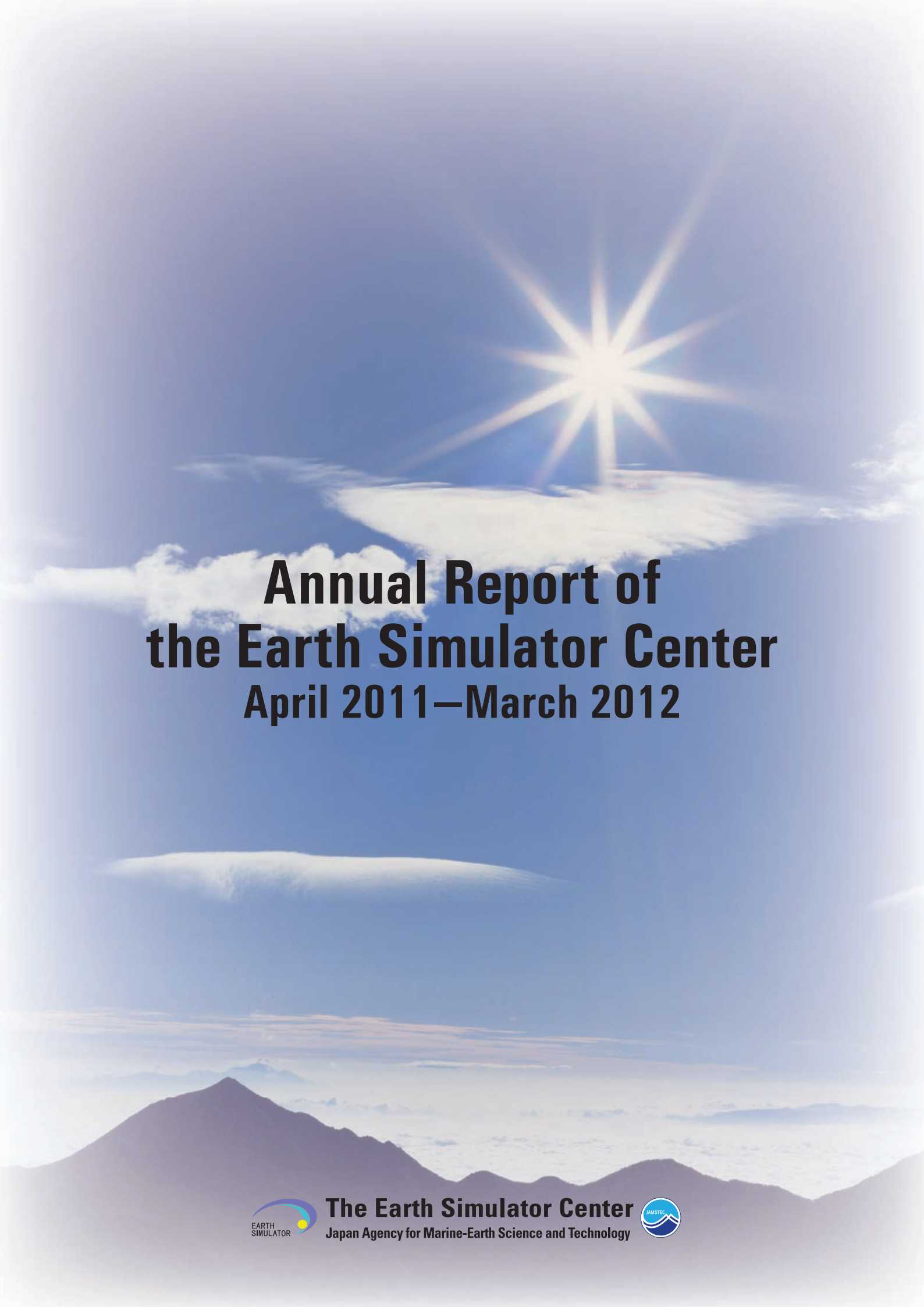


Annual Report of the Earth Simulator Center

April 2011 – March 2012





**Annual Report of
the Earth Simulator Center
April 2011–March 2012**



The Earth Simulator Center
Japan Agency for Marine-Earth Science and Technology



CONTENTS

Outline of the Earth Simulator Project

1. Mission and Basic Principles of the Earth Simulator	1
2. Earth Simulator Research Project	1
3. Collaboration Projects	4
4. System Configuration of the Earth Simulator	4

Earth Simulator Research Projects

Chapter 1 Earth Science

Understanding Roles of Oceanic Fine Structures in Climate and Its Variability III.....	11
Wataru Ohfuchi Earth Simulator Center, Japan Agency for Marine-Earth Science and Technology 海洋微細構造が生み出す気候形成・変動メカニズムの解明 海洋研究開発機構 地球シミュレータセンター 大淵 濟	
Adaptation Oriented Simulations for Climate Variability.....	19
Keiko Takahashi Earth Simulator Center, Japan Agency for Marine-Earth Science and Technology 気候変動に適応可能な環境探索のためのマルチスケールシミュレーション 海洋研究開発機構 地球シミュレータセンター 高橋 桂子	
Development of a High-Resolution Coupled Climate Model for Global Warming Studies	25
Akira Noda Research Institute for Global Change, Japan Agency for Marine-Earth Science and Technology 地球温暖化予測研究のための高精度気候モデルの開発研究 海洋研究開発機構 地球環境変動領域 野田 彰	
Simulations of Atmospheric General Circulations of Earth-like Planets by AFES	33
Yoshi-Yuki Hayashi Department of Earth and Planetary Sciences, Kobe University AFES を用いた地球型惑星の大気大循環シミュレーション 神戸大学大学院 理学研究科 林 祥介	
Study on the Diagnostics and Projection of Ecosystem Change Associated with Global Change	41
Michio J. Kishi Research Institute for Global Change, Japan Agency for Marine-Earth Science and Technology 地球環境変化に伴う生態系変動の診断と予測に関する研究 海洋研究開発機構 地球環境変動領域 岸 道郎	
CFD Simulation of Summertime Air Temperature Distribution of the Ten Kilo-meter Square Area of Center of Tokyo.....	45
Yasunobu Ashie National Institute for Land and Infrastructure Management CFD による東京 10km 四方の夏季気温分布シミュレーション 国土交通省国土技術政策総合研究所 足永 靖信	
Study of Cloud and Precipitation Processes using a Global Cloud Resolving Model.....	51
Masaki Satoh Research Institute for Global Change, Japan Agency for Marine-Earth Science and Technology Atmosphere and Ocean Research Institute, The University of Tokyo 全球雲解像モデルを用いた雲降水プロセス研究 海洋研究開発機構 地球環境変動領域 佐藤 正樹 東京大学 大気海洋研究所	

Process Studies and Seasonal Prediction Experiment using Coupled General Circulation Model	59
Yukio Masumoto Research Institute for Global Change, Japan Agency for Marine-Earth Science and Technology	
大気海洋結合モデルを用いたプロセス研究と季節予測実験	
海洋研究開発機構 地球環境変動領域 升本 順夫	
Simulation and Verification of Tropical Deep Convective Clouds using Eddy-Permitting Regional Atmospheric Models	65
Kozo Nakamura Research Institute for Global Change, Japan Agency for Marine-Earth Science and Technology	
渦解像可能な領域大気モデルを用いた深い対流のシミュレーションとその検証	
海洋研究開発機構 地球環境変動領域 中村 晃三	
A Long-term Ocean State Estimation by using a 4D-VAR Data Assimilation Approach	69
Shuhei Masuda Research Institute for Global Change, Japan Agency for Marine-Earth Science and Technology	
四次元変分法海洋データ同化システムを用いた全球海洋環境の再現	
海洋研究開発機構 地球環境変動領域 増田 周平	
Global Elastic Response Simulation.....	73
Seiji Tsuboi Institute for Research on Earth Evolution / Data Research Center for Marine-Earth Sciences, Japan Agency for Marine-Earth Science and Technology	
全地球弾性応答シミュレーション	
海洋研究開発機構 地球内部ダイナミクス領域 / 地球情報研究センター 坪井 誠司	
Numerical Simulations for Understanding of the Earth's Core Convection	79
Yozo Hamano Institute for Research on Earth Evolution, Japan Agency for Marine-Earth Science and Technology	
地球コア対流の理解のための数値シミュレーション	
海洋研究開発機構 地球内部ダイナミクス領域 浜野 洋三	
FDM Simulation of Broadband Seismic Wave Propagation in 3-D Heterogeneous Structure using the Earth Simulator.....	85
Takashi Furumura Center for Integrated Disaster Information Research, Interfaculty Initiative in Information Studies, The University of Tokyo / Earthquake Research Institute, The University of Tokyo	
地球シミュレータによる3次元不均質媒質中を伝播する広帯域地震動シミュレーション	
東京大学大学院 情報学環総合防災情報研究センター 古村 孝志	
東京大学 地震研究所	
Development of Advanced Simulation Methods for Solid Earth Simulations.....	93
Mikito Furuichi Institute for Research on Earth Evolution, Japan Agency for Marine-Earth Science and Technology	
先端の固体地球科学シミュレーションコードの開発	
海洋研究開発機構 地球内部ダイナミクス領域 古市 幹人	
3-D Numerical Simulations of Eruption Clouds: Effects of Decompression/Compression and Cross-Wind on the Dynamics of Eruption Clouds.....	99
Takehiro Koyaguchi Earthquake Research Institute, The University of Tokyo	
火山噴煙の3次元数値シミュレーション：火口クレーターの形状と風の影響	
東京大学 地震研究所 小屋口 剛博	
Space and Earth System Modeling.....	105
Kanya Kusano Laboratory for Earth Systems Science, Japan Agency for Marine-Earth Science and Technology	
宇宙・地球表層・地球内部の相関モデリング	
海洋研究開発機構 システム地球ラボ 草野 完也	

Numerical Experiments with Multi-Models for Paleo-Environmental Problems	111
Ayako Abe-Ouchi Atmosphere and Ocean Research Institute, The University of Tokyo	
古環境研究のための多階層数値実験	
東京大学 大気海洋研究所 阿部 彩子	
Development of a High-Resolution Climate Model for Model-Observation Integrating Studies from the Earth's Surface to the Lower Thermosphere	119
Shingo Watanabe Research Institute for Global Change, Japan Agency for Marine-Earth Science and Technology	
高解像度気候モデルの開発－地表から下部熱圏大気のモデル・観測統合研究に向けて	
海洋研究開発機構 地球環境変動領域 渡邊 真吾	
 Chapter 2 Epoch-Making Simulation	
Large Scale Simulations for Carbon Nanotubes	127
Syogo Tejima Research Organization for Information Science & Technology	
カーボンナノチューブの特性に関する大規模シミュレーション	
高度情報科学技術研究機構 手島 正吾	
Large-scale Simulation for a Terahertz Resonance Superconductor Device	135
Mikio Iizuka Research Organization for Information Science and Technology	
テラヘルツ発振超伝導素子に関する大規模シミュレーション	
高度情報科学技術研究機構 飯塚 幹夫	
Direct Numerical Simulations of Fundamental Turbulent Flows with the World's Largest Number of Grid-points and Application to Modeling of Engineering Turbulent Flows	141
Yukio Kaneda Graduate School of Engineering, Nagoya University	
乱流の世界最大規模直接数値計算とモデリングによる応用計算	
名古屋大学大学院 工学研究科 金田 行雄	
A Large-Scale Genomics and Proteomics Analyses Conducted by the Earth Simulator	147
Toshimichi Ikemura Nagahama Institute of Bio-Science and Technology	
全ゲノム・全タンパク質配列の自己組織化マップを用いた大規模ポストゲノム解析	
長浜バイオ大学 バイオサイエンス学部 池村 淑道	
First-principles Calculation for the Effect of Hydrogen Atoms on the Mobility of a Screw Dislocation in BCC Iron	155
Hideo Kaburaki Japan Atomic Energy Agency	
第一原理計算による BCC 鉄中らせん転位の移動への水素の影響	
日本原子力研究開発機構 蕪木 英雄	
Development of a Fluid Simulation Approach by Massively Parallel Bit-wise Operations with a New Viscosity Control Method	159
Hiroshi Matsuoka Research Institute of Electrical Communication, Tohoku University	
新粘性制御法による超並列ビット演算流体シミュレーション手法の開発	
東北大学 電気通信研究所 松岡 浩	

Acceleration of the Processing of Linear Equations in Characteristic 2 for RSA Decryption.....	165
Hidehiko Hasegawa Faculty of Library, Information and Media Science, University of Tsukuba	
RSA 暗号の解読処理向け標数 2 の線形計算の高速化	
筑波大学 図書館情報メディア系 長谷川 秀彦	
Development of Sophisticated Simulation Analysis Method of Actual Reinforced Concrete Building by Shaking Table Test-II.....	171
Yoshiyuki Kasai Department of Urban Environment and Information Sciences, Graduate School, Maebashi Institute of Technology	
実大鉄筋コンクリート造建物の振動台実験の精密・詳細シミュレーション解析システムの開発 その2	
前橋工科大学大学院 工学研究科 環境・情報工学専攻 河西 良幸	
Evaluations of Fluid Dynamic Forces and Blood Vessel Stresses of an Artery with a Cerebral Aneurysm	179
Tadashi Tanuma Applied Fluid Dynamics & Energy Machinery Systems, Joint Program Center, Teikyo University	
脳動脈瘤を含む血管系の流体力と応力の評価	
帝京大学 ジョイントプログラムセンター 田沼 唯士	
Large-Scale Electronic-State Calculations of Protein-Ligand Systems for Drug Design with Fragment Molecular Orbital Method.....	185
Shigenori Tanaka Graduate School of System Informatics, Kobe University	
フラグメント分子軌道法による薬剤設計のためのタンパク質-リガンド系に対する大規模電子状態計算	
神戸大学大学院 システム情報学研究所 田中 成典	
Development of the Next-generation Computational Fracture Mechanics Simulator for Constructing Safe and Sustainable Society.....	191
Ryuji Shioya Faculty of Information Sciences and Arts, Toyo University	
安全・安心な持続可能社会のための次世代計算破壊力学シミュレータの開発	
東洋大学 総合情報学部 塩谷 隆二	
 Chapter 3 Visualization	
Studies of Large-Scale Data Visualization: EXTRAWING and Visual Data Mining.....	197
Fumiaki Araki Earth Simulator Center, Japan Agency for Marine-Earth Science and Technology	
大規模データ可視化研究：EXTRAWING とビジュアルデータマイニング	
海洋研究開発機構 地球シミュレータセンター 荒木 文明	

Outline of the Earth Simulator Project

1. Mission and Basic Principles of the Earth Simulator

The Earth Simulator was developed for the following aims. The first aim is to ensure a bright future for human beings by accurately predicting variable global environment. The second is to contribute to the development of science and technology in the 21st century. Based on these aims, the principles listed below are established for the projects of the Earth Simulator.

- 1) Each project should be open to researches in each research field and to the public, rather than it is confined within the limited research society.
- 2) In principle, the research achievements obtained by using the Earth Simulator should be promptly published and returned to the public.
- 3) Each project should be carried out for peaceful purposes only.

2. Earth Simulator Research Project

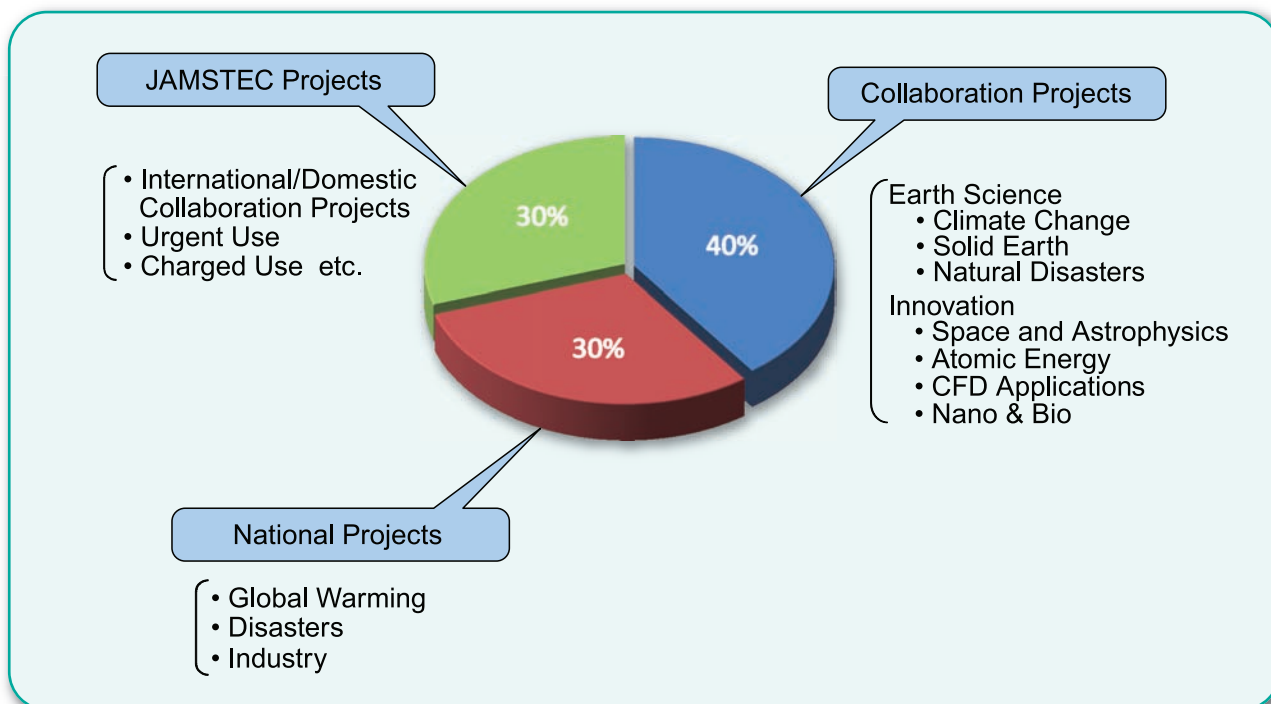
There are two fields of Earth Simulator Research Projects, as follows:

- Earth Science
- Epoch-making Simulation

The allocation of Earth Simulator resources for each research field in FY2011 was decided to be as shown in following graph.

Public project recruitment for Earth Simulator Research Projects in FY2011 was held in February 2011, and 29 research projects were selected by the Selection Committee.

The Allocation of Resources of the Earth Simulator in FY2011



Authorized Projects in FY2011

Earth Science (18 projects)

	Title	Project leader	Affiliation of project leader
1	Understanding Roles of Oceanic Fine Structures in Climate and its Variability	Wataru Ofuchi	ESC, JAMSTEC
2	Simulations of Adaptation-Oriented Strategy for Climate Variability	Keiko Takahashi	ESC, JAMSTEC
3	Development of a High-quality Climate Model for Global Warming Projection Study	Akira Noda	RIGC, JAMSTEC
4	Simulations of Atmospheric General Circulations of Earth-like Planets by AFES	Yoshiyuki Hayashi	Graduate School of Science, Kobe University
5	Study on the Diagnostics and Projection of Ecosystem Change Associated with Global Change	Michio Kishi	RIGC, JAMSTEC
6	Development of a Numerical Model of Urban Heat Island	Yasunobu Ashie	National Institute for Land and Infrastructure Management
7	Study of Cloud and Precipitation Processes using a Global Cloud-system Resolving Model	Masaki Sato	RIGC, JAMSTEC
8	Study on the Predictability of Climate Variations and Their Mechanisms	Yukio Masumoto	RIGC, JAMSTEC
9	Simulation and Verification of Tropical Deep Convective Clouds using Eddy-permitting Regional Atmospheric Models	Kozo Nakamura	RIGC, JAMSTEC
10	Improved Ocean State Estimation and Sensitivity Analysis Experiments for the Optimal Observing System, by using a 4D-VAR Ocean Data Assimilation System	Shuhei Masuda	RIGC, JAMSTEC
11	Global Elastic Response Simulation	Seiji Tsuboi	IFREE/DrC, JAMSTEC
12	Simulation Study on the Dynamics of the Mantle and Core in Earth-like Conditions	Yozo Hamano	IFREE, JAMSTEC
13	Numerical Simulation of Seismic Wave Propagation and Strong Ground Motions in 3-D Heterogeneous Media	Takashi Furumura	Center for Integrated Disaster Information Research, Interfaculty Initiative in Information Studies, The University of Tokyo/Earthquake Research Institute, The University of Tokyo
14	Development of Advanced Simulation Tools for Solid Earth Sciences	Mikito Furuichi	IFREE, JAMSTEC
15	Numerical Simulations of the Dynamics of Volcanic Phenomena	Takehiro Koyaguchi	Earthquake Research Institute, The University of Tokyo
16	Space and Earth System Modeling	Kanya Kusano	IFREE, JAMSTEC
17	Numerical Experiments with Multi-models for Paleo-environmental Problems	Ayako Abe	Atmosphere and Ocean Research Institute, The University of Tokyo
18	Model-observation Integration Study of the Middle-atmosphere Dynamics Using a High-resolution Climate Model and the Antarctic PANSY radar	Shingo Watanabe	RIGC, JAMSTEC

Epoch-making Simulation (11 projects)

	Title	Project leader	Affiliation of project leader
19	Large-scale Simulation on the Properties of Carbon-nanotube	Syogo Tejima	Research Organization for Information Science & Technology
20	Large-scale Simulation for a Terahertz Resonance Superconductors Device	Mikio Iizuka	Research Organization for Information Science & Technology
21	Direct Numerical Simulations of Fundamental Turbulent Flows with the World's Largest Number of Grid-points and Application to Modeling of Engineering Turbulent Flows	Yukio Kaneda	Graduate School of Engineering, Nagoya University
22	A Large-scale Post-genome Analysis using Self-Organizing Map for All Genome and Protein Sequences	Toshimichi Ikemura	Nagahama Institute of Bio-Science and Technology
23	First Principles Calculation on Hydrogen Diffusion Behavior in Iron Containing a Dislocation and Grain Boundary	Hideo Kaburaki	Japan Atomic Energy Agency
24	Development of a Fluid Simulation Approach by Massively Parallel Bits-operations with a New Viscosity Control Method	Hiroshi Matsuoka	Research Institute of Electrical Communication, Tohoku University
25	Development of Adaptive High Accuracy Libraries	Hidehiko Hasegawa	Graduate School of Library, Information and Media Studies, University of Tsukuba
26	Developments of Sophisticated Simulation Analysis Method of Actual Reinforced Concrete Building by Shaking Table Test	Yoshiyuki Kasai	Graduate School Department of Urban Environment and Information Sciences, Maebashi Institute of Technology
27	Theoretical Study of Drug Resistance Mechanism Based on the Fragment Molecular Orbital Method	Shigenori Tanaka	Graduate School of System Informatics, Kobe University
28	Research Project of Biomedical Unsteady Fluid-structure Interaction Analysis for Cerebral Aneurysm and Other Organs	Tadashi Tanuma	Joint Program Center, Teikyo University
29	Development of the Next-generation Computational Fracture Mechanics Simulator for Constructing Safe and Sustainable Society	Ryuji Shioya	Faculty of Information Sciences and Arts, Toyo University

JAMSTEC : Japan Agency for Marine-Earth Science and Technology

IFREE : Institute for Research on Earth Evolution

ESC: Earth Simulator Center

RIGC : Research Institute for Global Change

DrC : Data Research Center for Marine-Earth Sciences

3. Collaboration Projects

Collaboration Projects in FY2011

<ul style="list-style-type: none">• Institut Français de Recherche pour l'Exploitation de la Mer (IFREMER), Département d'Océanographie Physique et Spatiale, France
<ul style="list-style-type: none">• Ernest Orlando Lawrence Berkeley National Laboratory, University of California (LBNL), USA
<ul style="list-style-type: none">• Korean Ocean Research & Development Institute (KORDI), Korea
<ul style="list-style-type: none">• The National Oceanography Centre, Southampton (NOCS), UK
<ul style="list-style-type: none">• The large-scale numerical simulation of the weather/oceanographic phenomena for international maritime transportation : Kobe University
<ul style="list-style-type: none">• Research and development for MSSG calculation performance optimization in the next-generation supercomputer system : RIKEN
<ul style="list-style-type: none">• Collaborative research on the sophistication of the computational simulation software toward constructing the platform for the leading industrial research and development : Institute of Industrial Science, the University of Tokyo

4. System Configuration of the Earth Simulator

The Earth Simulator

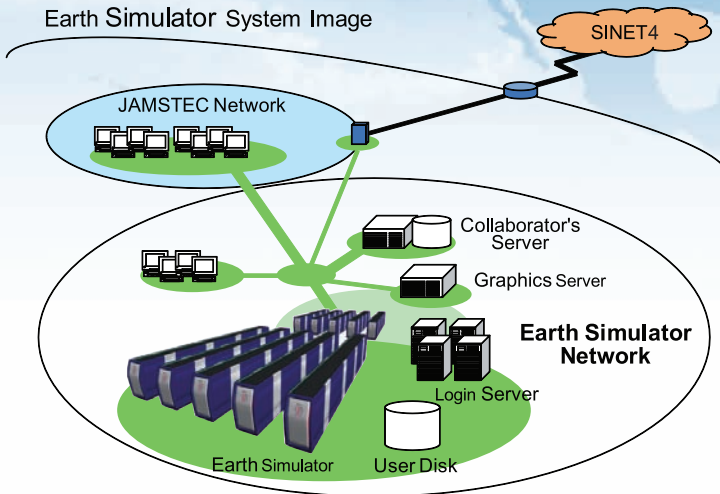
- New Earth Simulator System of Ultra High-speed Vector Parallel Super Computer -

The Earth Simulator is the upgraded system of the previous Earth Simulator, which has significantly contributed to the development of a simulation culture in the area of earth science and related technical fields, and introduces new features to bring accurate and

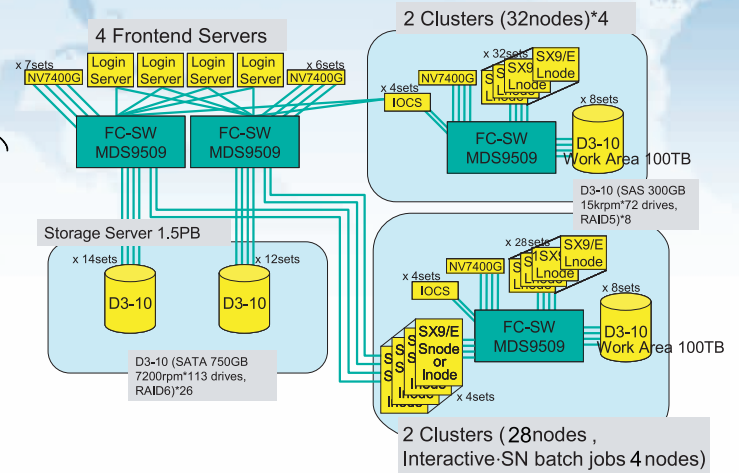
high-speed analysis and projections of global-scale environmental phenomena. The ES is also used to produce numerical simulations for advanced research fields that are beyond the scope of other computing systems.



ES System Outline



Storage System



Features of the Earth Simulator for operation and control

- (1) Clustering of nodes to control the system (transparent for users) .
A cluster consists of 32 nodes,
Most of them are for batch jobs (batch clusters).
- (2) Providing special nodes for TSS and small batch jobs.
- (3) Configuration of the TSS cluster.
 1. TSS nodes [2 nodes],
 2. Nodes for SN (Single Node) batch jobs [2 nodes],
- (4) Configuration of the batch cluster.
 1. Nodes for MN (Multi-Nodes) batch jobs,
 2. System disks for user-file staging,
- (5) Storage of user files for batch jobs on a mass-storage system.
Automated file recall (Stage-In) and migration (Stage-Out).
- (6) Connection of all the clusters to a mass-storage system

Real Applications Benchmark Performance

Application	ES initial (# of CPUs)	ES current (# of CPUs)	Speed up
PHASE	135.3 sec (4096)	62.2 sec (1024)	2.18
NICAM-K	214.7 sec (2560)	109.3 sec (640)	1.97
MSSG	173.9 sec (4096)	86.5 sec (1024)	2.01
SpecFEM3D	96.3 sec (4056)	45.5 sec (1014)	2.12
Seism3D	48.8 sec (4096)	15.6 sec (1024)	3.13

Harmonic Mean of Speed up Ratio : 2.22

 **Earth Simulator Research Projects** 

Chapter 1

■ Earth Science ■

Understanding Roles of Oceanic Fine Structures in Climate and Its Variability III

Project Representative

Wataru Ohfuchi

Earth Simulator Center, Japan Agency for Marine-Earth Science and Technology

Authors

Hideharu Sasaki^{*1}, Bunmei Taguchi^{*1}, Masami Nonaka^{*2}, Mayumi K. Yoshioka^{*3},
Hidenori Aiki^{*2} and Wataru Ohfuchi^{*1}

*1 Earth Simulator Center, Japan Agency for Marine-Earth Science and Technology

*2 Research Institute for Global Change, Japan Agency for Marine-Earth Science and Technology

*3 Hydrospheric Atmospheric Research Center, Nagoya University

We have been investigating air-sea interaction where oceanic structures of small spatial scale play important roles by using high-resolution, primitive equation based, global atmosphere, ocean and coupled models, and a regional non-hydrostatic ocean-atmosphere coupled model. In this report, we present the following four topics: 1) Interannual-to-decadal variability of the sea ice extent in Okhotsk Sea and its associated atmospheric variability, 2) Dynamical feedback in local air-sea interaction along the Hawaiian Lee Countercurrent, 3) Influence of the ocean through sea surface temperature on typhoon intensity, and 4) Predictability of the Kuroshio Extension jet speed.

Keywords: air-sea interaction, oceanic front, air-sea coupled simulation, the Okhotsk Sea, Hawaiian Lee Countercurrent, typhoon, Kuroshio Extension

1. Introduction

We have been studying relatively small spatial scale interaction of the atmosphere and ocean. In this report, we present a role of air-sea and air-sea-ice interactions in the climate and its variations where oceanic structures of small spatial scale play important roles. Section 2 and 3 present studies using CFES, the ocean-atmosphere coupled general circulation model (GCM) for the Earth Simulator (ES). In Section 2, influences of sea ice variability in the Okhotsk Sea on the climate variations are introduced. Local air-sea interactions induced by the sea surface temperature (SST) maximum along the Hawaiian Lee Countercurrent are presented in Section 3. In Section 4, we also report a study using CReSS-NHOES, Cloud Resolving Storm Simulator-Non-Hydrostatic Ocean model for the ES. Influences of SST on the typhoon intensity are revealed. In Section 5, the predictability of Kuroshio Extension jet speed associated with meridionally-confined frontal-scale variability is suggested using OFES, the ocean GCM for the ES.

2. Interannual-to-decadal variability of the sea ice extent in Okhotsk Sea

Sea ice variability has been recognized as an important element of climate system, yet simulating it in climate models is not necessarily successful. Here we focus on the Okhotsk Sea, which is a marginal sea residing just to the north of Japan and is

also the southernmost region of the seasonal sea ice formation regions in the Northern Hemisphere. We investigate the sea ice variability in the Okhotsk Sea and its associated atmospheric variability, using a 120-year CFES simulation integrated at a medium resolutions where the atmospheric component has a horizontal resolution of T119 spectral truncation with 48 vertical σ -levels and the ocean component has 0.5° latitude-longitude grids with 54 z-coordinate vertical levels. The CFES integration exhibits prominent interannual-to-decadal variability in the sea ice extent in the Okhotsk Sea (red curve in Fig. 1a). The analysis of the cause and effect of the simulated sea ice variability confirms that the CFES simulates realistic interactions among the ocean, the sea ice, and the atmosphere. Namely, the larger than normal sea ice extent in the Okhotsk Sea in December tends to be preceded by colder than normal air temperature over the far-east Eurasian region in November (blue curves in Figs. 1a and 1b), and also tends to be followed by the deeper than normal Aleutian low (Fig. 1a gray bar charts, Fig. 1c) leading to the colder air temperature in the northern Japan (not shown) in February. The former atmospheric anomalies in November can be regarded as the forcing for the sea ice variation in the Okhotsk Sea, while the latter atmospheric anomalies in February as an response to the sea ice variation, both of which are consistent with the earlier studies based on observations.

A further analysis reveals that the cold air temperature

anomalies in November is associated with larger than normal sea ice extent in Arctic Sea off East Siberia from September to November (not shown). This link of sea ice variability between the summer-to-fall Arctic Sea and the early winter Okhotsk Sea, which is suggested by the model, is also confirmed with observations, providing an important basis for the seasonal prediction in the areas surrounding the Okhotsk Sea including the Northern Japan.

3. Local dynamical feedback into the Hawaiian Lee Countercurrent

Air-sea interactions not only in the tropics but also in the mid-latitude region are of great interest to researchers. The Hawaiian Lee Countercurrent (HLCC), in which the high SST along the HLCC may generate local air-sea interactions, is one example outside the tropics. The HLCC is a narrow eastward countercurrent extending from Hawaii over the date line, which is driven by an orographic wind wake behind Hawaii. The satellite observations revealed atmospheric response with surface wind convergence and high cloud water over the warm HLCC [1]. However, the local air-sea interactions over the HLCC have not been well understood.

In order to examine the local air sea interaction induced by the high SST along the HLCC, we use a medium resolution

version of CFES (as the one used in Section 2). The CFES control run demonstrates the HLCC with high SST band and the atmospheric response to the high SST (Fig. 2). Comparing with a sensitivity simulation reducing an influence of the high SST on the atmosphere by smoothing the SST around the HLCC, air-sea interaction induced by the high SST is investigated with focus on the local dynamical feedback into the ocean. The HLCC speed is higher in the control simulation than that in the sensitivity simulation (Fig. 3), suggesting that dynamical feedback to the ocean following the atmospheric response to the high SST further drives the HLCC with distinct increase of current speed in the south of the HLCC. Both Ekman suction induced by positive wind curl along the surface wind convergence band and eastward Ekman flow induced by northerly wind south of the HLCC axis play roles in the increase of the HLCC speed. In addition, the HLCC speed increase advects warm water from the west, and causes SST warming locally around the HLCC (not shown). When the HLCC speed is high, the high SST band and atmospheric response are distinct. If following dynamical feedback of the HLCC speed increase is further enhanced, the HLCC variations with both seasonal and interannual time scales become more amplified.

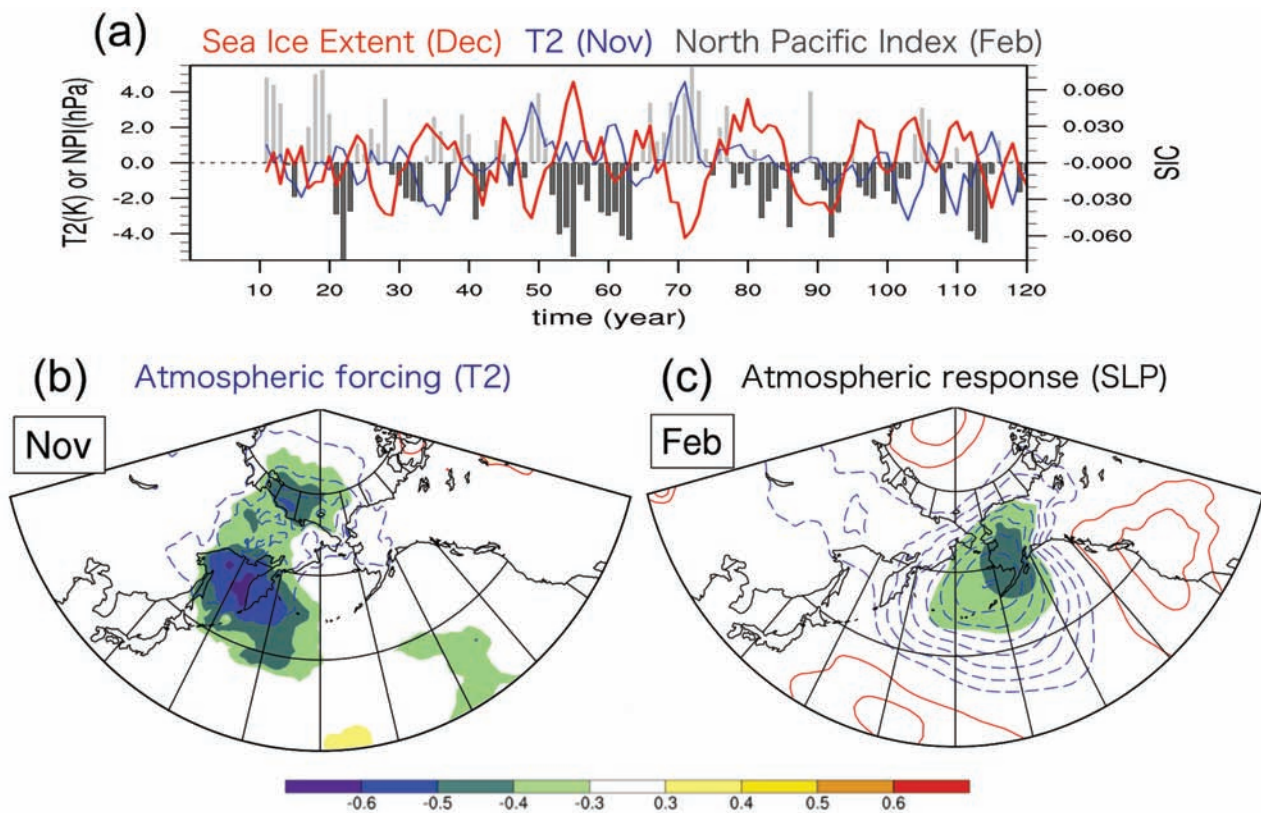


Fig. 1 (a) Time series of sea ice extent averaged over the Okhotsk Sea in December (red), 2-m air temperature averaged over the North East Eurasia (blue), and North Pacific Index (sea level pressure averaged over the central North Pacific; gray bar charts). All the quantities are based on the 120-year CFES integration with 3-year running mean applied after the trend and climatological monthly mean are removed. (b) Lag correlation (color shade) and regression (contours; the interval is 0.2 K) of 2-m air temperature in November onto the area-averaged Okhotsk sea ice variability in December. (c) As in (b) but for sea level pressure in February (contour interval is 2hPa).

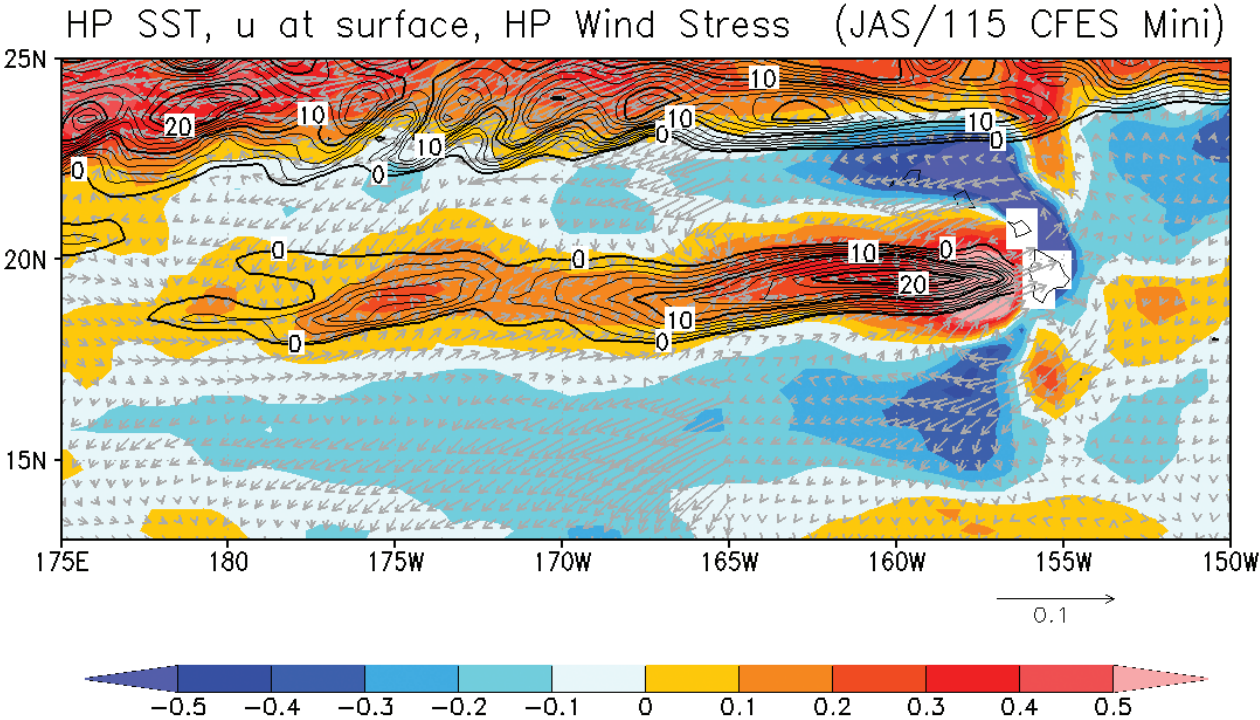


Fig. 2 Geostrophic eastward current speed (contour, cm s⁻¹), SST (color, °C) and wind stress vectors (10⁻¹ N m⁻²) averaged from July to September in the 115th year in the CFES control simulation. Meridional high-pass filter via removing an 8° moving mean is applied to SST and wind stress. Contour intervals are 2 cm s⁻¹. Scale of wind stress vectors east of 165°W is ten times that west of 165°W.

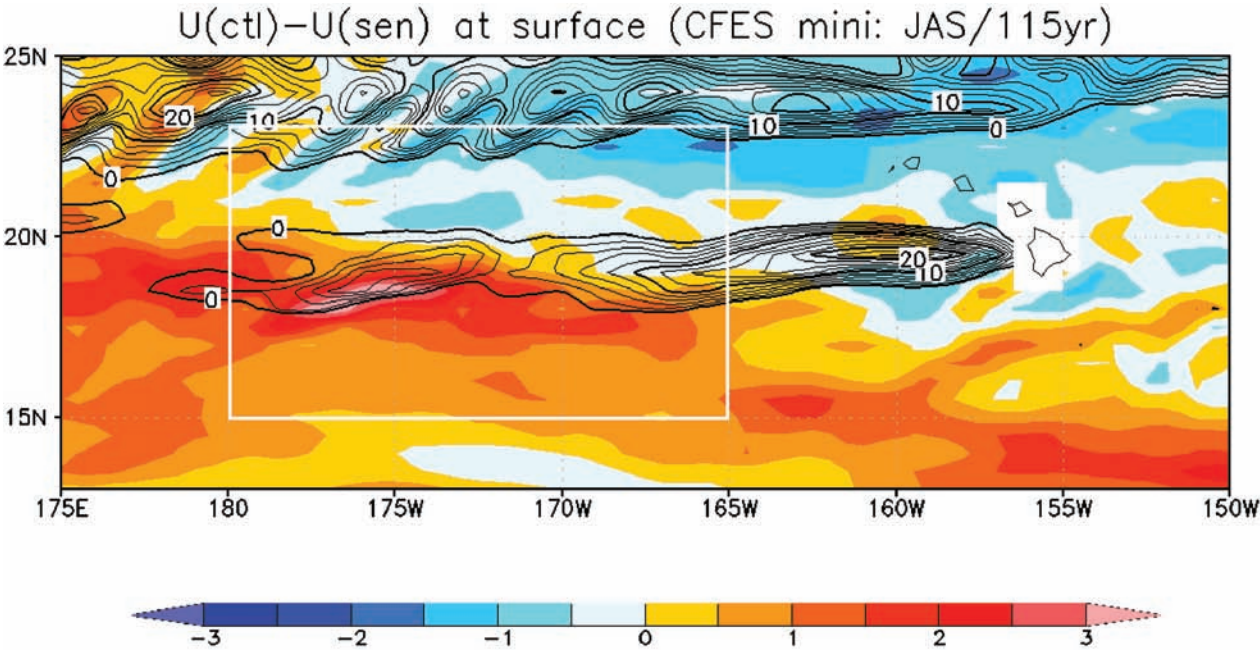


Fig. 3 Eastward surface current speed (cm s⁻¹) in the control simulation minus those in the sensitivity simulation averaged from July to September in the 115th year. Contours indicate eastward current speed in the control simulation. Contour intervals are 2 cm s⁻¹. In the white box, SST is smoothed in the sensitivity simulation.

4. Influence of the ocean through SST on typhoon intensity

Local distribution of the SST decrease is observed around and after a typhoon's passing (e.g. [2]). The SST decreases remarkably when a typhoon moves at slow speed [3]. On the other hand, the cool SST produced by the typhoon's passing affects the intensity of the typhoon itself, through decrease of the sensible/latent heat flux from the ocean surface by air-sea interaction.

Numerical simulations were performed to investigate intensity change through air-sea interaction for the typhoon Roke (T1115) which was generated at September 10 in 2011 and moved almost stationary around eastern off Okinawa Island during September 16-19 after moving very slowly in the north western Pacific. Experiments were designed with utilizing different sea surface conditions, employed 1) non-coupled ocean (fixed SST), 2) coupled one-dimensional ocean which treats upper layers of the ocean of 30m depth (slab-ocean) and 3) coupled three-dimensional ocean, respectively.

CReSS was utilized for the atmospheric model for all experiments. For three-dimensional experiment, CReSS-NHOES was utilized for the coupled experiment. For initial/boundary conditions, JMA/GPV dataset was employed for the atmosphere and JCOPE2 reanalysis dataset was for the ocean. Numerical experiments were performed for 8-days of the horizontal resolution at 4 km in 21°N-41°N, 122°E-142°E latitudinal -longitudinal domain.

In the experiments, Roke was successfully simulated in staying near Okinawa Island during 16-19. Remarkable difference of the intensity of the typhoon appeared in the central pressure after 60 hours of the integration time among the

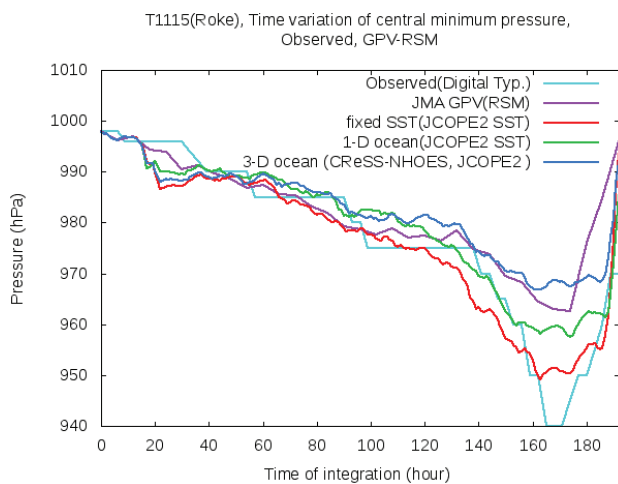
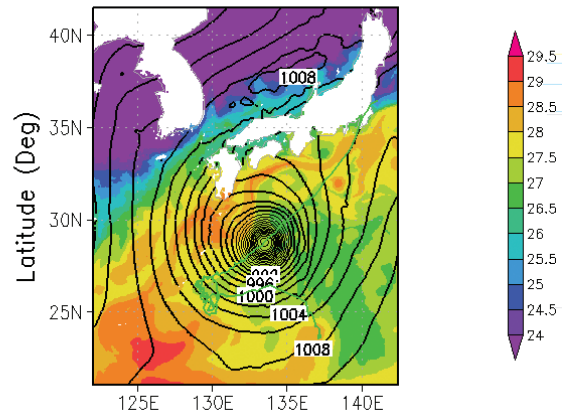


Fig. 4 Time variation of the central pressure simulated for T1115 (Roke). The abscissa is the integration time started from the integration in September 14 00Z. The red line is for the fixed-SST, the green line is for the slab-ocean and the blue is for the CReSS-NHOES coupled experiments, respectively. The values derived from JMA/GPV data and from observation are also plotted with the light blue and purple lines, respectively.

experiments and then was clear after about 80 hours. After about 150 hours, the central pressure in the coupled experiments was higher than that in the fixed SST experiment, of about 10 hPa for slab-ocean experiment and of about 20 hPa for CReSS-NHOES coupled experiment (Fig. 4). The SST distribution of the coupled experiments at September 21 00Z (after 168 hours) are shown in Fig. 5. The cooler SST of 2K appeared in the CReSS-NHOES experiment, which distributed locally in the southwestern part of the Roke's center, where Roke stayed during September 16-19. The warm SST around the Kuroshio currents between Kyushu and Amami islands also decreased in the CReSS-NHOES coupled experiment. At that time, Roke moved to the cooler SST region which generated north-eastern part in Roke's staying. That suggests that three-dimensional response with vertical upwelling and horizontal currents produced by the typhoon Roke induces more SST cooling locally by air-sea interaction than one-dimensional response with vertical mixing only, resulting in more suppression of the central pressure of Roke.

T1115 1Docean Surface Temperature(Deg-C), Day=21,hr=00, P_Min.=959.475(hPa)



T1115 3Docean Surface Temperature(Deg-C), Day=21,hr=00, P_Min.=968.694(hPa)

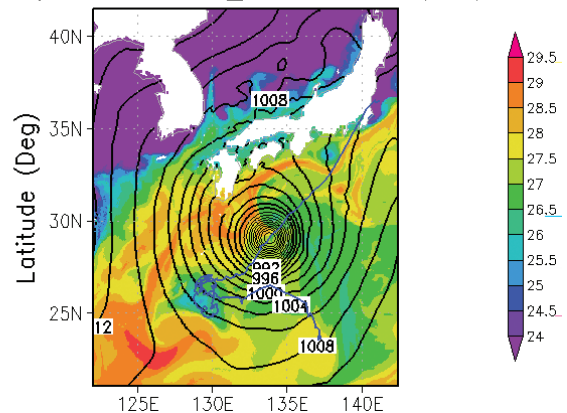


Fig. 5 Snapshot of the SST (colored), the surface pressure (contours), and the tracks of simulated Roke (lines) in the experiments at September 21 00Z : the slab-ocean experiment (upper panel) and the CReSS-NHOES coupled experiment (lower panel), respectively.

Asymmetric SST distribution around the center of the typhoon leads to the regional distribution of the heat flux from the sea surface. Time series of the directional distribution of the heat flux divided the part of north-south/east-west represents the relation between the local SST distribution affected/non-affected by Roke and the location of Roke. Figure 6 shows the time variation of the latent heat flux around the center of Roke averaged within 100 km radius in the experiments. After 120 hours when Roke began to move to north-eastward after staying near Okinawa Island, the flux of the coupled experiments was clearly smaller than that in the non-coupled experiment in the all quadrants, which indicates the suppression of the central pressure shown in Fig. 1. In the northern quadrants after 140 hours of the integration time, the flux of the slab-ocean experiment was greater than that in the CReSS-NHOES coupled experiment. After 150 hours, the flux in of the slab-ocean experiment was as much as that of the fixed-SST experiment and greater than that of the CReSS-NHOES coupled experiment in the north-east quadrant, which indicates that Roke arrived in the region where the ocean was greatly changed in three-dimensionally. In the south-east quadrant, on the other hand, the time varying flux of the slab-ocean experiment is close to

that of the CReSS-NHOES coupled experiment, suggesting less three-dimensional ocean effect in the east off of the Kuroshio currents.

5. Predictability of the Kuroshio Extension jet speed

Potential predictability of interannual variability in the Kuroshio Extension (KE) jet speed attributed to the westward propagation of wind-driven oceanic Rossby waves is investigated through prediction experiments with the OFES under the perfect-model assumption.

Though based on the small number of the experiments due to limited computational resources available, our experimental results suggest some predictability not only in broad-scale sea surface height anomalies (SSHAs) but also in anomalous KE jet speed associated with meridionally-confined frontal-scale variability (Figs. 7a and 7b). Specifically, more than half of the variance in the 13-month running mean KE jet speed can be explained by the ensemble mean of the forecast integrations even in the third year (Fig. 7c). The predictability of the KE jet speed thus revealed has been confirmed in the 61-year long hindcast integration as significantly high correlation ($r =$

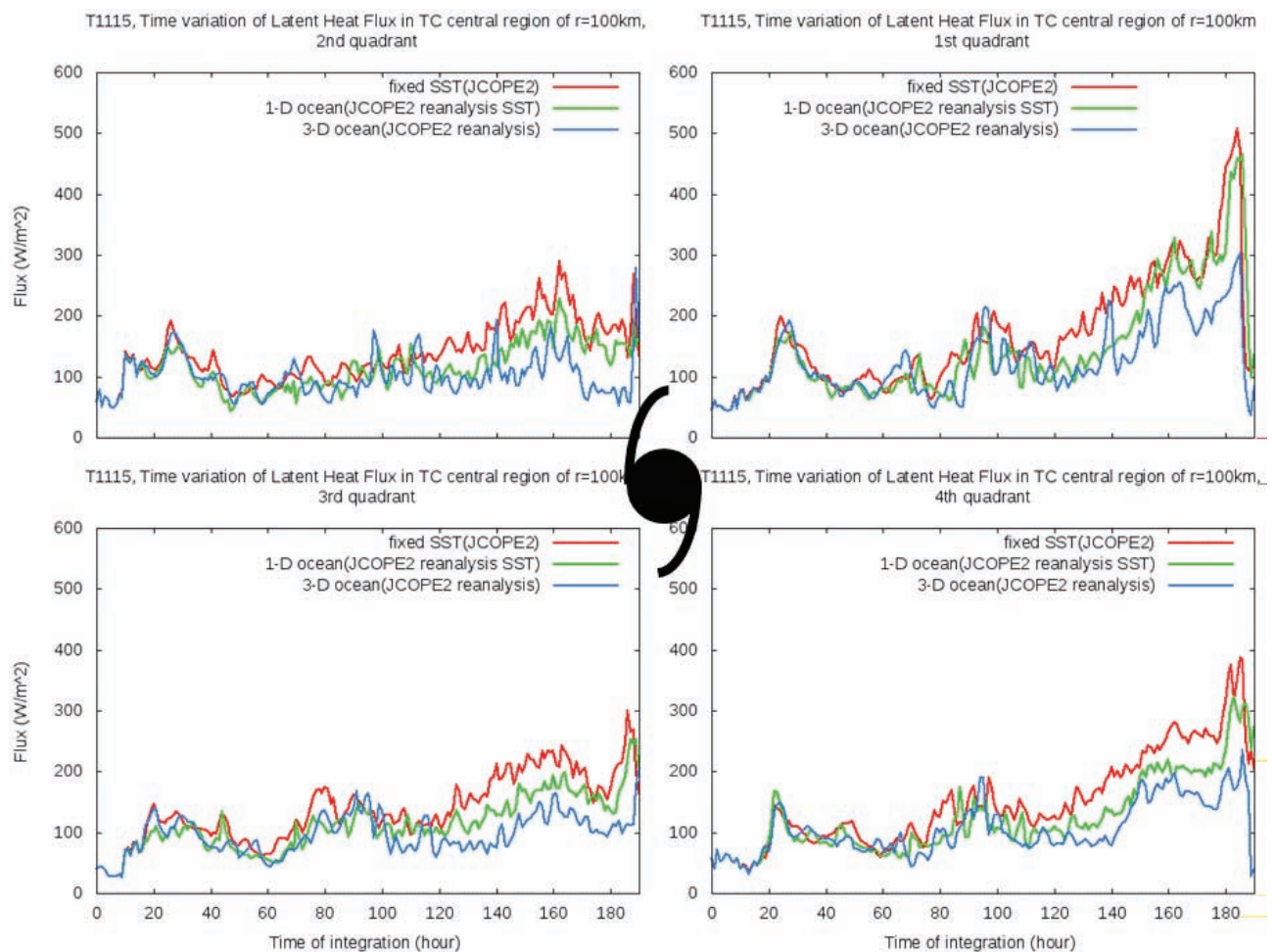


Fig. 6 Time variation of the directional distribution of the latent heat averaged within 100 km around the Roke's center: north-east (upper right), north-west (upper left), south-west (lower left), and south-east (lower right) quadrants, respectively.

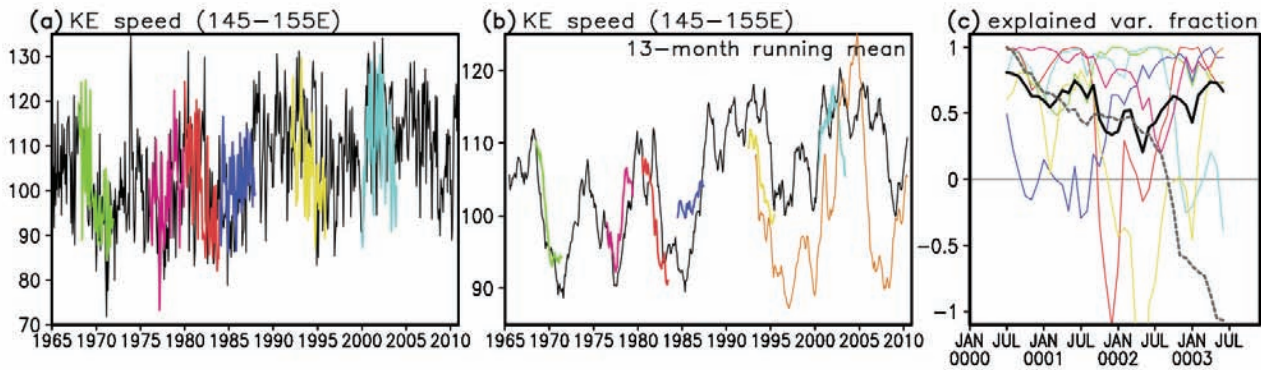


Fig. 7 (a) Time series of the KE jet speed (cm sec^{-1}) averaged over $[145^{\circ}\text{--}155^{\circ}\text{E}]$, based on the OFES hindcast integration (black) and six forecast experiments (colors). (b) Same as (a), but 13-month running mean is applied to reduce influences of eddies. Orange curve is for the observed value. (c) Time series of the corresponding fraction of variance explained by the forecast experiments represented by $1 - (\text{forecast errors})^2 / (\text{signal variance})$ in the KE jet speed in (b). Thick black curve is for the ensemble mean, and grey is for the persistence.

0.68) between the smoothed interannual variability in KE jet speed and SSHAs over the central North Pacific $[30^{\circ}\text{--}34^{\circ}\text{N}, 170^{\circ}\text{E}\text{--}175^{\circ}\text{W}]$ three years earlier (figure not shown). Though limited in their availability, the satellite observed SSHA data and the geostrophically derived KE jet speed are also correlated if the same time lag is assigned.

Recent studies have suggested that decadal changes in the speed of the Kuroshio and an upstream portion of KE can influence natural mortality of infant Japanese sardine, which is known to yield several orders of interdecadal variability in its mass. Prediction of the path and intensity of KE is thus of social and scientific importance.

6. Conclusion

We briefly reported research activities to investigate roles of small-scale oceanic structures in climate and its variability by using simulation results of hydrostatic and non-hydrostatic atmosphere, ocean coupled models. This year, we have concentrated on not only air-sea but also air-sea-ice interactions in the subtropical and subarctic regions. We will study more on interactions between small and large scales and their influence on large-scale climate in the near future.

References

- [1] S.-P. Xie, W. T. Liu, Q. Liu, and M. Nonaka, "Far-reaching effects of the Hawaiian Islands on the Pacific ocean-atmosphere system", *Science*, 292, 2057–2060, 2001.
- [2] J. F. Price, "Upper ocean response to a hurricane", *Journal of Physical Oceanography*, 11, 153–175, 1981.
- [3] M. A. Bender, I. Ginis, and Y. Kurihara, "Numerical simulations of tropical cyclone-ocean interaction with a high-resolution coupled model", *Journal of Geophysical Research*, 98, 23, 245–23, 263, 1993.

海洋微細構造が生み出す気候形成・変動メカニズムの解明

プロジェクト責任者

大淵 濟 海洋研究開発機構 地球シミュレータセンター

著者

佐々木英治^{*1}, 田口 文明^{*1}, 野中 正見^{*2}, 吉岡真由美^{*3}, 相木 秀則^{*2}, 大淵 濟^{*1}

*1 海洋研究開発機構 地球シミュレータセンター

*2 海洋研究開発機構 地球環境変動領域

*3 名古屋大学 地球水循環研究センター

高解像度のプリミティブ方程式と非静力学の全球、または領域の大気、海洋、結合モデルを用いて、海洋の空間的に小さいスケールが重要な役割をはたす大気海洋結合作用を研究している。この報告書では、次の四つの研究成果を取り上げた。全球大気海洋結合モデル CFES を用い、1) 環オホーツク海域における大気海洋海氷相互作用の十年規模変動、2) ハワイ風下反流に伴う大気海洋相互作用の海への力学的フィードバックを明らかにし、3) 非静力学の領域大気海洋結合モデル CReSS-NHOES を用い海面水温の台風強度への影響メカニズムを明らかにした。また、4) 準全球海洋モデル OFES の中で黒潮統流の流速の予測可能性を示した。

キーワード: 大気・海洋相互作用, 海洋前線, 大気海洋結合シミュレーション, オホーツク海, ハワイ風下反流, 台風, 黒潮統流

Adaptation Oriented Simulations for Climate Variability

Project Representative

Keiko Takahashi

Earth Simulator Center, Japan Agency for Marine-Earth Science and Technology

Authors

Keiko Takahashi^{*1}, Ryo Ohnishi^{*1}, Takeshi Sugimura^{*1}, Yuya Baba^{*1}, Shinichiro Kida^{*1},
Koji Goto^{*2} and Hiromitsu Fuchigami^{*3}

*1 Earth Simulator Center, Japan Agency for Marine-Earth Science and Technology

*2 NEC Corporation

*3 NEC Informatec Systems LTD

A coupled atmosphere-ocean-land model MSSG has been developed in the Earth Simulator Center, which is designed to model multi-scale interactions among the atmosphere, the ocean and the coupled system. The MSSG is designed and optimized to be run with high performance computation on the Earth Simulator (ES2). Adding to the computational optimization, advanced cloud micro-physics with turbulence effects, implementation of new computational schemes enables to show preliminary results of multi-scale simulations. Several preliminary results to understand mechanism with several different scales are presented in this report.

Keywords: Coupled atmosphere-ocean model, multi-scale, multi-physics, high performance computing, the Earth Simulator

1. Introduction

Multi-Scale Simulator for the Geoenvironment (MSSG), which is a coupled atmosphere-ocean-land global circulation model, has been developed for seamless simulation based on multi-scale multi-physics modeling strategy in order to predict not only weather but climate variability. MSSG is designed to realize *seamless simulations* with difference scales from global scale to urban city scale, in other words, from climate to weather (Fig. 1). Because the necessary of high performance computation to realize seamless simulation, MSSG is optimized to be run on the Earth Simulator with high computational performance and it is designed to be available with flexibility for different space and time scales [1, 2, 4].

In this fiscal year, we focus on the following issues

- Improvement of accuracy of computational schemes and physical performance of MSSG-A and MSSG-O.
- Computational performance index to show the effect strategy to optimize on the Earth Simulator 2 (ES2), actually the index will be useful on other type of super computers.
- Several simulations have been performed to validate physics in multi-scale multi-physics simulations.

This report summarizes a part of results of this project in FY2011.

2. MSSG Model Improvement

For improving cloud-resolving model using MSSG, developments of both advection scheme were conducted. In the development of advection scheme, WENO scheme is focused

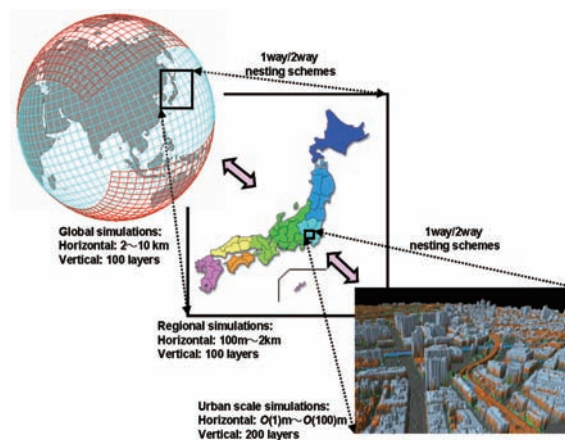


Fig. 1 Scale of MSSG as global/regional models with nesting schemes and resolution.

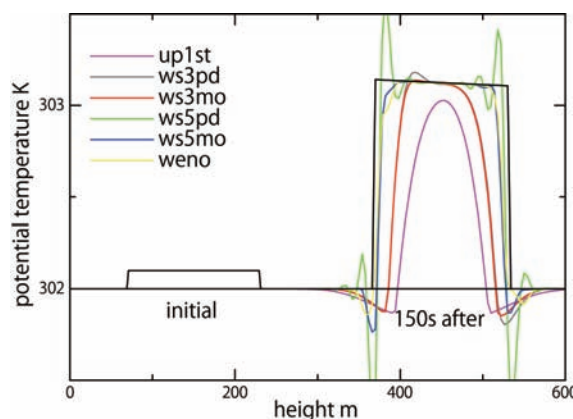


Fig. 2 Solutions of 1-dimensional advection-condensation problem to compare computational accuracy among schemes.

interface between the bin and bulk components. In this fiscal year, the size-dependent interface (SDI) has been developed and implemented in the MSSG-Bin. This enables to keep the size information and computes the interaction between each bin and the ice categories separately. The comparison between the SII and SDI has provided insight into the sensitivity to the hybrid interface (Fig. 5) [3].

MSSG-Ocean model (MSSG-O) is developed to simulate oceanic flow field and tracer fields on various spatial and time scales along with numerical stability and reasonable precision. For this fiscal year, the development of the MSSG-O [5] was focused for its usage as a high-resolution regional model and a basin scale model based on hydrostatic primitive equations. Various process models were also implemented to MSSG-O for complex simulations needed to simulate coastal features and radionuclides.

As a high-resolution regional model, a dispersion model with a focus on radionuclides, a river inflow model, and a tidal forcing model were developed. The dispersion model successfully simulates the C134s along the coasts of Fukushima. The river inflow model also successfully simulates the steady inflow of freshwater input within Tokyo bay. The high-resolution basin scale model was validated using biharmonic mixing or COARE3.0 bulk-flux formula.

3. Trial simulations for adaptation to climate variability

In the evaluation of urban thermal environment, effect of river existence in urban area was focused on (Fig. 6 and Fig. 7).

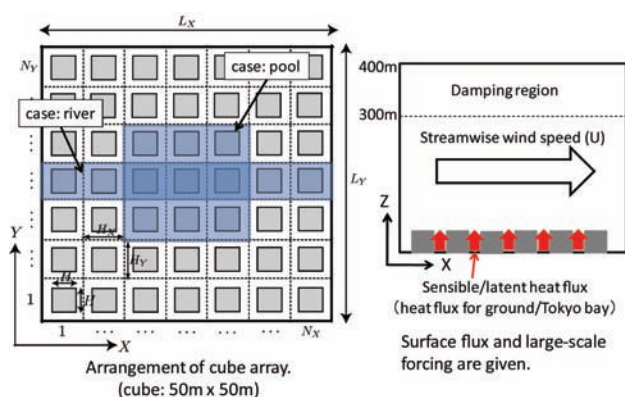


Fig. 6 Simulation conditions to validate heat storage mechanism in urban area.

case	λ_p	$N_x \times N_y$	grid number	river	U m/s
RUN1	0.694	15 × 15	180 × 180 × 80	-	5
RUN2	0.510	16 × 16	224 × 224 × 80	-	5
RUN3	0.390	12 × 12	192 × 192 × 80	-	5
RUN1R	0.694	15 × 15	180 × 180 × 80	line	5
RUN2R	0.510	16 × 16	224 × 224 × 80	line	5
RUN3R	0.390	12 × 12	192 × 192 × 80	line	5
RUNBS	0.694	15 × 15	180 × 180 × 80	box (small)	0.5
RUNBM	0.694	15 × 15	180 × 180 × 80	box (medium)	0.5
RUNBL	0.694	15 × 15	180 × 180 × 80	box (large)	0.5

Fig. 7 Simulation conditions of each case.

The results of idealized experiments showed that net effective temperature in the urban area decreases due to the open space which is created by the existence of the river. The river has two effects on heat flux, i.e., it decreases sensible heat flux whereas increases latent heat flux. Therefore the results indicate that urban design intending to improve the thermal environment should consider the balance between such sensible heat decrease and latent heat increase (Fig. 8).

Interaction between urban area environment and ocean/water front affects temperature distribution over the land and

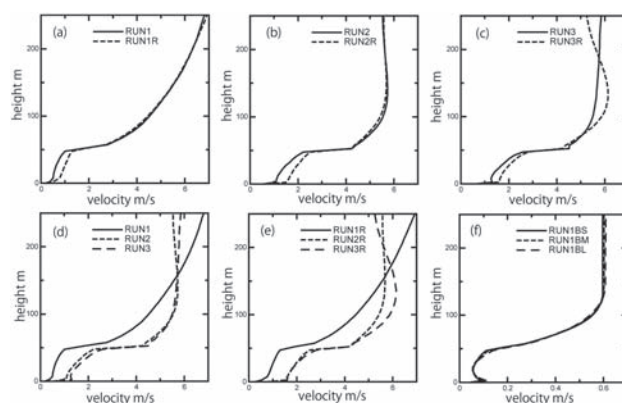


Fig. 8 Differences of temperature distribution in the case of existence of a river or not, which is corresponding to (a), (b) and (c). (d) and (e) show temperature distribution differences due to building-to-land ratio. (f) shows temperature distribution in difference cases of water front area.

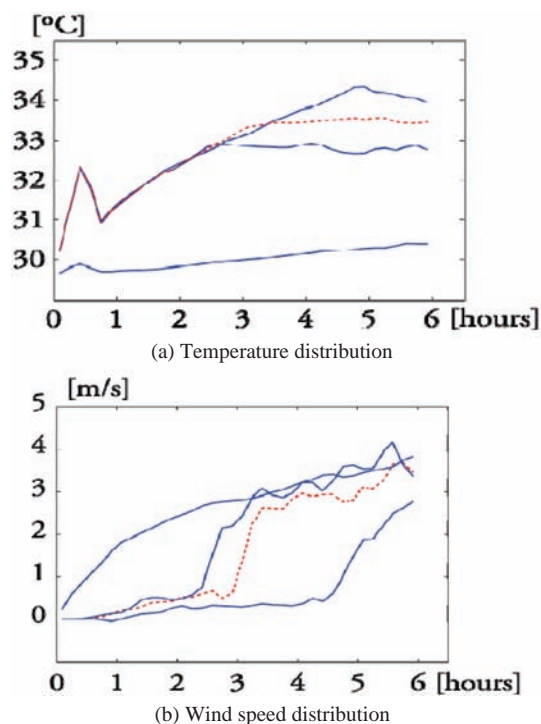


Fig. 9 Temperature (upper) and wind speed (bottom) distributions in the case of warm ocean are showed. Blue lines present the results at 0m (bottom line), 10 m (middle) and 20 m (upper) far from water front. Red dot line shows temperature or wind speed distributions at 10 km far from ocean front in the case of cold ocean simulation.

ocean. Figure 9 shows the results from the differences of heat transfer by land and sea breeze. Those results suggest its impact to environment in the urban area may change due to climate variability.

Several heavy rain simulations over Kanto metropolitan area are performed to test model reproducibility for urban meteorology. Simulated rainfall is in good agreement with observation in terms of timing and location, however, statistical properties for the heavy rain reproducibility is still uncertain if the number of simulation cases is too small. Therefore regional climate model for Kanto metropolitan area is now being constructed.

4. High performance computing of MSSG

Mechanisms of interactions among different scale phenomena play important roles for forecasting of weather and climate. Multi-scale Simulator for the Geoenvironment (MSSG), which deals with multi-scale multi-physics phenomena, is a coupled non-hydrostatic atmosphere-ocean model designed to be run efficiently on the Earth Simulator. We present its simulation results with the world-highest 1.9 km horizontal resolution for the entire globe and a 5 m resolution for an urban area. To gain high performance by exploiting the system capabilities, we propose novel performance evaluation metrics that incorporate the effects of the data caching mechanism between CPU and memory. A potentially attainable computational performance is also introduced by evaluating both computational and memory intensities. The performance indicators introduced in this study are found to be effective in assessing the performance of actual application programs and obtaining a guideline for performance optimization (Fig. 10). By fully utilizing such information, MSSG-A was successfully optimized with a high sustained performance of 42.2 TFLOPS (peak performance ratio of 32.2%) on the 160-node full Earth Simulator system [6].

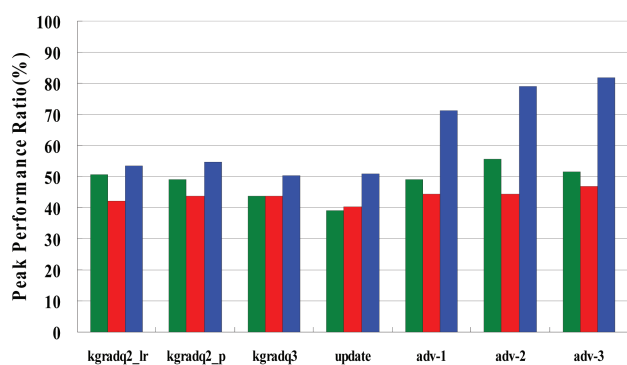


Fig. 10 Peak performance ratios on the ES. Green bar shows measured peak performance ratio; Red bar: Potential Peak Performance ratio (PPP) based on Conventional Byte/Flop (CBF); Blue bar: PPP based on Revised Byte/Flops (RBF).

5. Future work

In this report, we presented advanced schemes introduced in MSSG and improvements of physical performance in MSSG due to state-of-art schemes were introduced. The novel index to optimize computational performance of MSSG. Furthermore, preliminary results were shown in order to perform multi-scale simulations to estimate strategies of adaptation in climate variability. In near future, we are planning to validate the representation such as El Nino and Indian Ocean Dipole by longer integration. The further possibility of multi-scale simulations will be validated by showing whether climate in urban area will be predictable or not under the condition of climate variability.

References

- [1] Keiko Takahashi et al., Non-hydrostatic Atmospheric GCM Development and its computational performance, http://www.ecmwf.int/newsevents/meetings/workshops/2004/high_performance_computing-11th/presentations.html, 2004b.
- [2] Keiko Takahashi et al., Non-hydrostatic atmospheric GCM development and its computational performance, *Use of High Performance computing in meteorology*, Walter Zwiefelhofer and George Mozdzynski Eds., World Scientific, 50-62, 2005.
- [3] Ryo Onishi and Keiko Takahashi, A Warm-Bin / Cold-Bulk Hybrid Cloud Microphysical Model, *Journal of the Atmospheric Sciences*, (accepted).
- [4] Yuya Baba and Keiko Takahashi, Large-eddy simulation of convective boundary layer with density stratification, *Journal of the Meteorological Society of Japan*, Vol.89, pp.105-117, 2011.
- [5] Shinichiro Kida, The impact of Antarctic Slope Front on Antarctic Bottom Water outflows, *J. Phys. Oceanogr.*, 41, 1941-1957, (2011). doi: 10.1175/2011JPO4571.1.
- [6] Keiko Takahashi et al., World-highest Resolution Global Atmospheric Model and Its Performance on the Earth Simulator, *Proceeding of SC '11 State of the Practice Reports*, Doi: 10.1145/2063348.2063376, 2011.

気候変動に適応可能な環境探索のための マルチスケールシミュレーション

プロジェクト責任者

高橋 桂子 海洋研究開発機構 地球シミュレータセンター

著者

高橋 桂子^{*1}, 大西 領^{*1}, 杉村 剛^{*1}, 馬場 雄也^{*1}, 木田新一郎^{*1}, 後藤 浩二^{*2},
 淵上 弘光^{*3}

*1 海洋研究開発機構 地球シミュレータセンター

*2 NEC 株式会社

*3 NEC インフォマティックシステム株式会社

MSSG-A (大気大循環モデルコード)、MSSG-O (海洋大循環モデルコード)、MSSG (大気海洋結合モデルコード) それぞれに対して、短期の事例再現シミュレーションを実行し、特に豪雨については、再現性を飛躍的に向上した。この再現性の向上は、移流スキーム、雲微物理過程スキーム、放射過程スキーム、境界層スキームそれぞれのスキームとモデルの高度化とそれらの検証結果の積み上げが基盤となっている。MSSG-Oにおいて、水平 Biharmonic 粘性・拡散を新たに導入し、高解像度かつ長期シミュレーションが安定して実行できるようにモデルを高度化した。その結果、潮汐・黒潮・親潮等、強い流れの影響を受ける海域でも安定な実験が可能となり、東京湾・日本海・オホーツク海と外洋の相互作用が再現可能であることを示した。さらに、領域モデルからはIOD、ENSO、インドネシア通過流が経年変動を引き起こす季節と領域が限定されていることが明らかになった (図参照)。

世界にも着目されている複数の物理過程の連成モデルの開発に注力し、特に、乱流と降雨過程の関連性は、予測精度に大きな影響を与えることを明らかにした。加えて、雲乱流を扱えるハイブリッドビン法を提案し、高い信頼性と精度で積雲を再現できることを示した。

事例予測シミュレーションとして様々なスケールでダウンスケーリングシミュレーションを実施し、MSSGの有用性を明らかにした。対象は、都市を対象とした微気象現象、メソスケール気象現象、低高気圧の生起から消滅までの総観スケール現象を対象とした系統的実験を実施し、現在、その統計的解析と検証を行っている。また、都市スケールにおける気象現象への海洋の影響について、MSSGを用いて理想実験を実施し、海面温度、海陸風の影響によって、都市域の気象が数時間スケールで影響を受ける可能性を明らかにした。

計算最適化については、計算性能をどのような最適化指針に基づいて実施してゆくべきか、という課題に取り組み、この指針を与えるための新たな計算性能指標を提案した。この新しい指標は、従来から用いられてきたメモリアクセス負荷と計算負荷の混在を許容する指標とは異なり、メモリと計算負荷のいずれに起因する計算コスト負荷であるかを解析した、実機上のハードウェア動作に即した指標である。この指標に基づいて、実アプリケーション (MSSG) の計算性能最適化を行った結果、計算性能を効率的に向上可能であることを示した。

キーワード: Coupled atmosphere-ocean model, multi-scale, multi-physics, high performance computing, the Earth Simulator

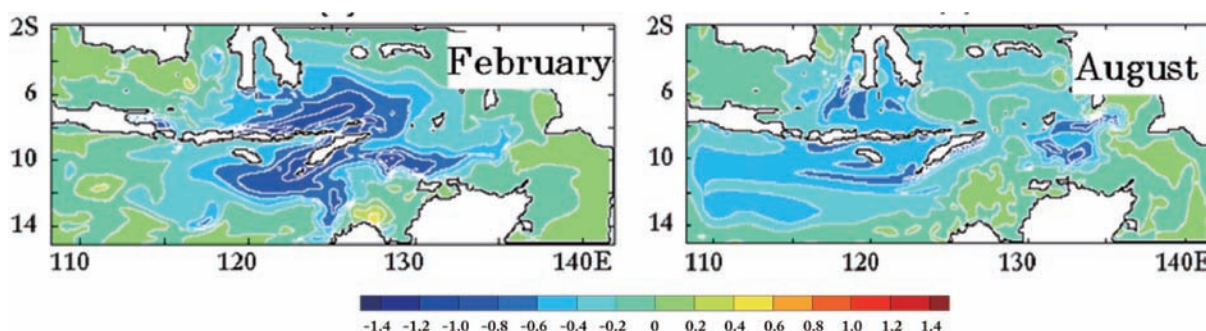


図: インドネシア多島海における潮汐混合の影響と季節変動

Development of a High-Resolution Coupled Climate Model for Global Warming Studies

Project Representative

Akira Noda

Research Institute for Global Change, Japan Agency for Marine-Earth Science and Technology

Authors

Akira Noda^{*1}, Ayako Abe-Ouchi^{*2,1}, Megumi O. Chikamoto^{*1}, Yoshio Kawatani^{*1},
Yoshiki Komuro^{*1}, Masao Kurogi^{*1}, Rumi Ohgaito^{*1}, Fuyuki Saito^{*1}, Kunio Takahashi^{*1},
Kumiko Takata^{*1} and Yukio Tanaka^{*1}

*1 Research Institute for Global Change, Japan Agency for Marine-Earth Science and Technology

*2 Atmosphere and Ocean Research Institute, The University of Tokyo

The purpose of this project is to further develop physical models for global warming simulations, and to investigate mechanisms of changes in global environment as a successor of a previous ES joint project. We have obtained the following results this year.

The effects of sea surface temperature (SST) and CO₂ on future changes in the quasi-biennial oscillation (QBO) are investigated using MIROC-AGCM. The period of the QBO becomes longer by about 1-3 months by increased SST and 1 month by increased CO₂.

A high accuracy tracer advection scheme is implemented into the COCO ocean model, which is an ocean component of MIROC. The newly implemented scheme reduces spurious diffusion and improves the model performance.

Multi-model analysis of PMIP2 and PMIP3 is performed to discuss importance of reduction of the warming bias of the sea surface temperature over Southern Ocean in the modern simulation, in order to reproduce the weaker AMOC at LGM indicated by paleodata. The results are shown to be consistent with a series of sensitivity experiments using MIROC AOGCM.

Diagnostic schemes of snow density and snow thermal conductivity are included as a test, but those are not efficient very much to reduce the biases remained after including the advanced sub-grid snow-cover scheme. Besides, effects of changes in volatile organic carbon (VOC) emitted from vegetation, via changes in aerosols, are examined by conducting the time-slice experiments, focusing on Asian climate. The radiative forcing of secondary organic aerosols (SOA) direct effects induced by VOC increase is only discernible. However, including interactions with the atmospheric circulations and indirect effects of aerosols, precipitation is decreased (increased) where sulfate aerosols are increased (decreased), indicating a negative correlation. The intensity of daily precipitation is also examined to find an increase in heavy rainfall events accompanying the SOA increase.

Parallelization of an ice sheet model Icies is partly implemented for future high-resolution Greenland and Antarctica experiment. Applying a block-cyclic domain decomposition method for effective load-balancing, the solution of the model is confirmed to be equivalent to those obtained by the non-parallel version of the model.

Keywords: Atmosphere-Ocean-Land coupled model, offline biogeochemical model, stratospheric QBO, ice-sheet model

1. Introduction

This project is a successor of one of the previous ES-joint projects named “Development of a High-resolution Coupled Atmosphere-Ocean-Land General Circulation Model for Climate System Studies.” The purpose of this project is to further develop physical models for global warming simulations, and to investigate mechanisms of changes in global environment.

To achieve the purpose, we focus on the development of ice sheet model, permafrost model and sea ice model, improvement of subcomponent models for atmosphere, ocean and land-surface processes in the climate model MIROC, as well as sensitivity studies using climate models relevant to global

warming and paleo-climate.

2. The effects of SST and CO₂ on future changes in the QBO

The effects of sea surface temperature (SST) and CO₂ on future changes in the quasi-biennial oscillation (QBO) have been investigated using a climate model that simulates the QBO without parameterized nonstationary gravity wave forcing. Idealized model experiments using the future SST with the present CO₂ (FS run) and the present SST with the future CO₂ (FC run) were conducted. When compared with the present run, precipitation increases around the equatorial region in the FS run

and decreases in the FC run, resulting in increased and decreased wave momentum fluxes, respectively. In the mid-latitude lower stratosphere, westward (eastward) wave forcing anomalies form in the FS (FC) run. In the middle stratosphere off the equator, westward wave forcing anomalies form in both the FS and FC runs. Corresponding to these wave forcing anomalies, the residual vertical velocity significantly increases in the lower stratosphere in the FS run but decreases to below 70 hPa in the FC run, whereas residual upward circulation anomalies form in both the FS and FC runs in the middle equatorial stratosphere. Figure 1 shows the frequency power spectra of the zonal-mean zonal wind at the equator as a function of height. In the present run, the most dominant period of the QBO is 24 months (not shown). In the FS run, the dominant QBO periods are from 25 to 27 months. In the FC run, the dominant periods are 25 months. The amplitude of the QBO becomes smaller in the lower stratosphere, and the period of the QBO becomes longer by about 1–3 months in the FS run. On the other hand, in the FC run, the QBO extends farther downward into the lowermost

stratosphere, and the period becomes longer by 1 month.

3. Implementation of a high accuracy tracer advection scheme into the ocean model

In the ocean interior amount of diapycnal mixing is much smaller than the along isopycnal mixing and spurious mixing associated with advection scheme may compromise the physical integrity of the simulated results. Therefore, we implemented a high accuracy tracer advection scheme, the second-order moment (SOM) scheme, into the COCO ocean model in addition to the conventional third-order accuracy (TOA) scheme. Figure 2a shows the annual-mean temperature along the equator calculated by using the SOM scheme. The thermocline shoals to the east and its depth defined by the 20°C isotherm is about 180 m (40 m) in the western (eastern) region west of 170E (east of 100W). In the central region (between 170W and 120W), the vertical gradient of temperature (dT/dz) across the thermocline is $0.10^{\circ}\text{C m}^{-1}$. In the observation (Fig. 2c), the depth of the thermocline is about 180 m (40 m) in the western (eastern)

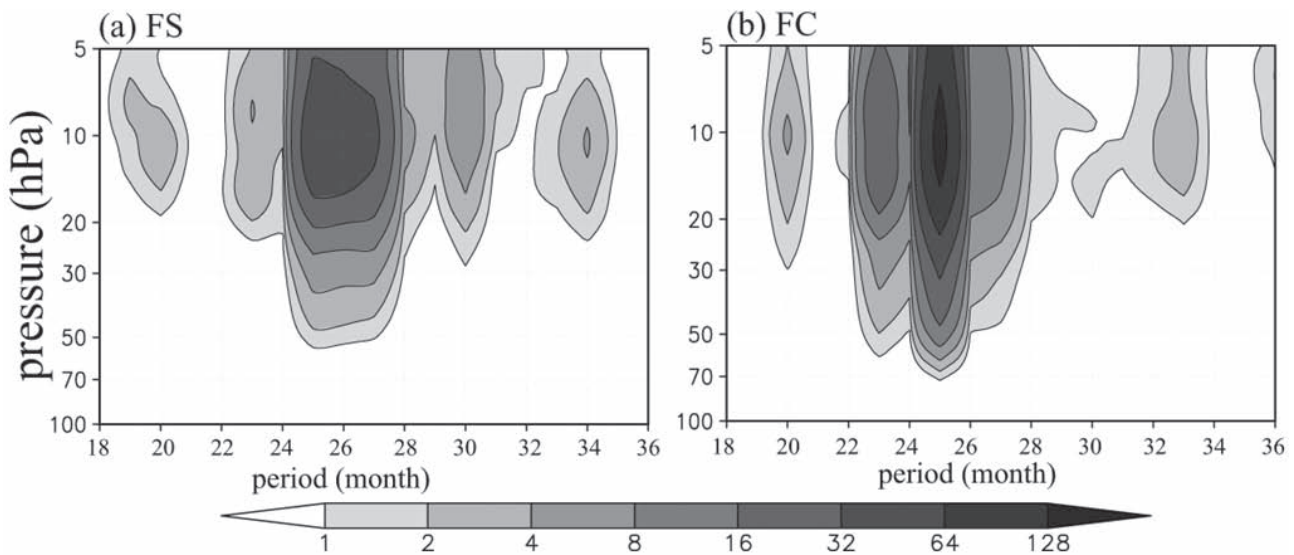


Fig. 1 Frequency power spectra of the zonal-mean zonal wind at the equator as a function of height in the (a) FS, and (b) FC runs. The shaded intervals are 1, 2, 4, 8, 16, 32, 64, and 128 $\text{m}^2 \text{s}^{-2} \text{month}^{-1}$.

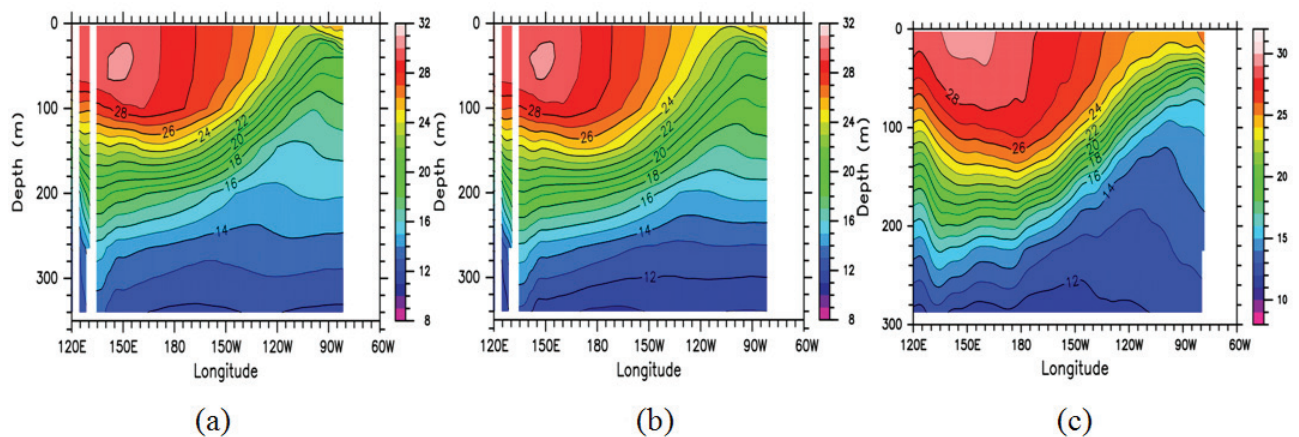


Fig. 2 Annual-mean temperature of the SOM calculation (a), the TOA calculation (b), and observation (c) along the Pacific equator (averaged between 1°S and 1°N). The unit is $^{\circ}\text{C}$.

region and the dT/dz across the thermocline in the central region is $0.12^{\circ}\text{C m}^{-1}$. The depth and sharpness of the equatorial thermocline is in agreement with the observation. On the other hand, the thermocline calculated by using the TOA scheme (Fig. 2b) is clearly more diffuse than the SOM scheme and the observation. The dT/dz across the thermocline in the central region is $0.07^{\circ}\text{C m}^{-1}$, and this is reduced by 30% compared to the SOM scheme. The annual-mean temperature is colder in the SOM scheme calculation than in the TOA scheme one along the lower part of the thermocline over a wide zonal extent (Fig. 2a). Below the thermocline ($<20^{\circ}\text{C}$), the convex shape of isotherms between 130W and 100W seen in the observation is not distinct in the model results. For example, the 14°C isotherm reaches

120 m depth in the observation, but it reaches 220 m depth at most in the SOM scheme calculation. The temperatures below the thermocline are warmer in the model than those in the observation.

4. Paleoclimate simulation by MIROC focusing on AMOC at LGM

We show that the reducing the warming bias of the modern (pre-industrial) sea surface temperature (SST) and sea ice in the Southern ocean are required for reproducing the weaker AMOC (Atlantic Meridional Ocean Circulation) at Last Glacial Maximum (LGM) than modern as in paleodata by both multi-model analysis of PMIP2, PMIP3/CMIP5 and a series of sensitivity experiments using MIROC AOGCM. The sensitivity experiments using MIROC AOGCM show that the AMOC at modern and LGM depend upon the key factors such as the oceanic mixing and the surface heat flux input from the atmosphere to the ocean due to cloud effect. Figure 3 shows two examples for the sensitivity experiments, large SST bias case on the left hand side and little SST bias case on the right hand side. If the warming bias in the modern ocean is reduced, the sea ice at LGM around Antarctica is forming enough to reject brine. This leads to a sufficient strengthening of the AABW and results in a weaker and shoaler AMOC at LGM which simulates realistic pattern of $\delta^{13}\text{C}$ distribution (Figs. 3a to 3f). A series of additional experiments shows that the LGM Northern Hemisphere ice sheets are responsible for strengthening the AMOC in contrary to the effect of lower CO_2 as Green House Gas at LGM for weakening the AMOC (Figs. 3g and 3h). To reproduce the AMOC through this appropriate balance throughout the climate change, it is crucial to reproduce both the oceanic and atmospheric process properly near Antarctica in the Southern ocean region.

5. Land-surface modeling in GCM

Snow cover has large effects on the surface energy/water balances. By introducing the advanced scheme for sub-grid snow-cover ratio (SSNOWD) in the land-surface scheme (MATSIRO) of a global climate model (MIROC), the large-scale distribution of snow cover ratio was improved [4]. However, the positive biases in spring are still remained or even enhanced with SSNOWD. In order to reduce the biases, diagnostic schemes of snow density [5] and snow thermal conductivity [6] were introduced as a test. However, the time evolution of snow was changed only marginally.

In addition, impacts of volatile organic carbon (VOC) change have been investigated, focusing on Asian climate, since the VOC changes lead to changes in the formation of secondary organic aerosols (SOA), which would have direct effects on radiation and indirect effects through cloud and precipitation. Two sets of time-slice experiments were conducted; one (CTL) using the climatological monthly mean BVOC emission (GEIA,

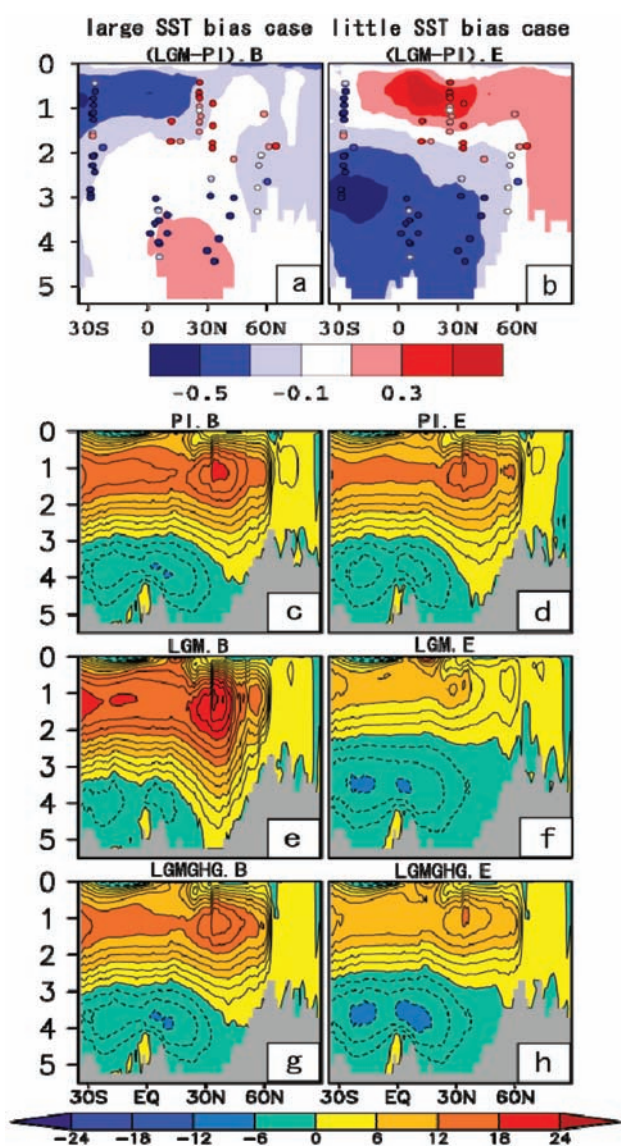


Fig. 3 The left/right column shows the results of the large/small SST bias case. a) and b) $\delta^{13}\text{C}$ distributions in the Atlantic Ocean (per mil.). Shades suggest the results of the MIROC experiments and the colored circles suggest the paleo-data. c)-h) AMOC. c) and d) modern. e) and f) same as in c) and d) but for LGM. g) and h) same as in c) and d) but for the experiments with only greenhouse gas levels changed to the LGM level from the modern experiments.

[1]), and the other (EXP) using the BVOC emission estimated after Ref.[2] considering the land-use changes [3]. Each experiment was integrated for a period of 60 years, and the latter 40 years were used for the analyses.

The BVOC estimation used in EXP simulation results in an overall increase in the SOA flux over most vegetated areas in the South and South East Asian monsoon regions with the changes being regionally as large as the CTL simulation emission flux in the tropical rain forest (Fig. 4). The increased atmospheric aerosol loading of SOA then led to an increased atmospheric optical depth (AOD) of OC across a broader area in the Indian

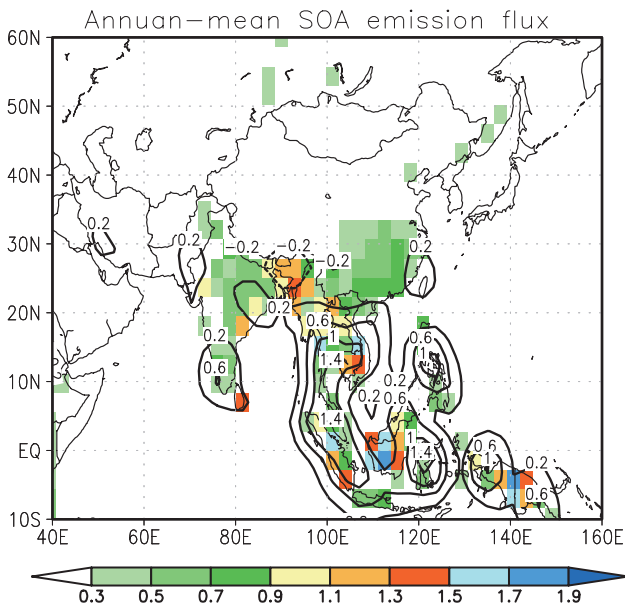


Fig. 4 Annual-mean SOA of CTL (shading) and EXP-CTL (contours). Units are 10^{11} kg/m²/s.

subcontinent (IS), maritime continent (MC), and Southeast Asia (SEA), with a peak appearing in April and May (thick contours in Figs. 5ab). The increased AOD resulted in the negative anomalies of aerosol radiative forcing (shading in Figs. 5ab), but it was not sufficient to significantly alter the broad-scale thermal structures and associated atmospheric circulations and marginally excited the model simulations through the internal variability of the model.

It was, however, able to affect the local water cycle through aerosol indirect effects. Figure 6 presents the differences in rainfall and vertically integrated number concentration of sulfate aerosols between the EXP and CTL simulations. Results showed enhanced rainfall in May at the Bay of Bengal and off the coast of southeastern China where sulfate aerosols were remarkably diminished. In contrast, decreased precipitation was apparent in June over the oceanic regions with abundant sulfate aerosols. Such a negative correlation between sulfate aerosol concentrations and precipitation is consistent with the idea of aerosol nucleation under elevated concentrations of accumulation mode nuclei. We also noted that prominent rainfall variations occurred mostly over the ocean because the emission of DMS is largely of oceanic origin in SPRINTARS. The above diagnostics were repeated for the other aerosol species but no distinctive co-variability was found between rainfall and aerosol number concentration.

At the regional scale, several oceanic areas exhibited rainfall changes, in which aerosol-induced impacts were detectable particularly during May and June. Then the frequency and intensity of daily precipitation was investigated for those months. The histograms of the frequency density of wet-day

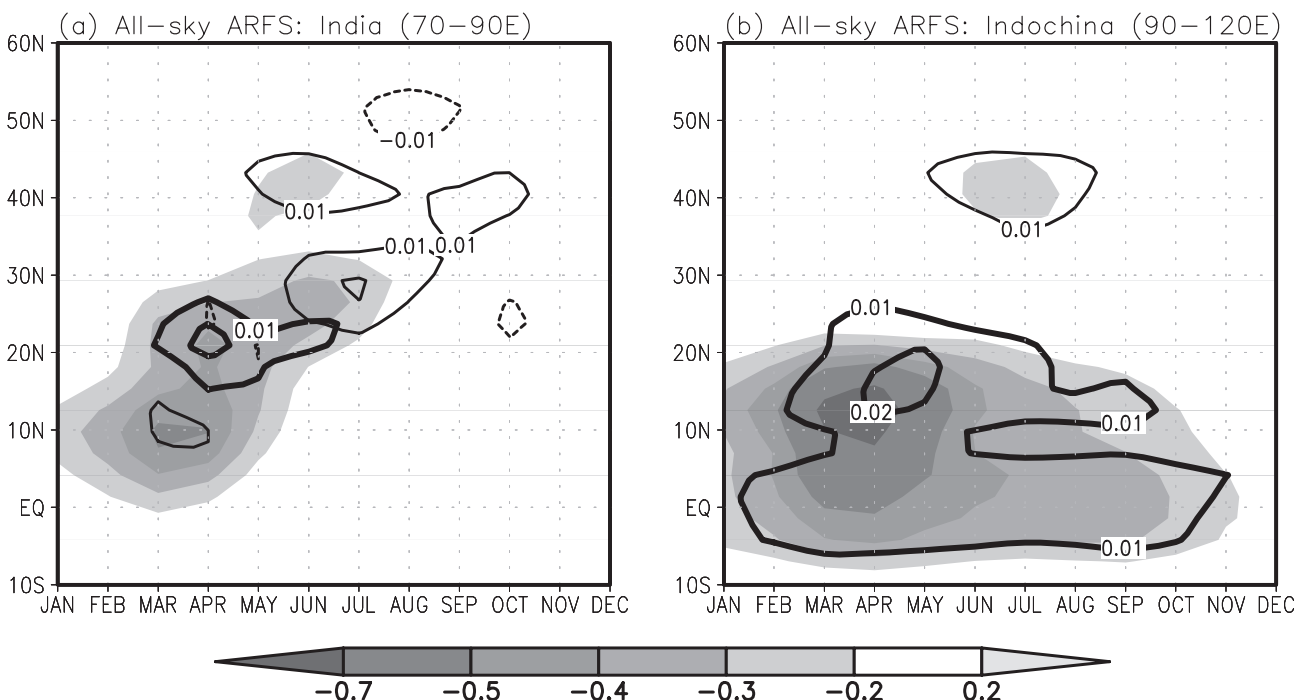


Fig. 5 Time-latitude distributions of the differences (EXP-CTL) in aerosol radiative forcing at the surface (ARFS, W/m²) (shading), AOD for OC (thick contours) and dust aerosol (thin contours) averaged over (a) the Indian subcontinent (70–90°E) and (b) the Indochina Peninsula (90–120°E).

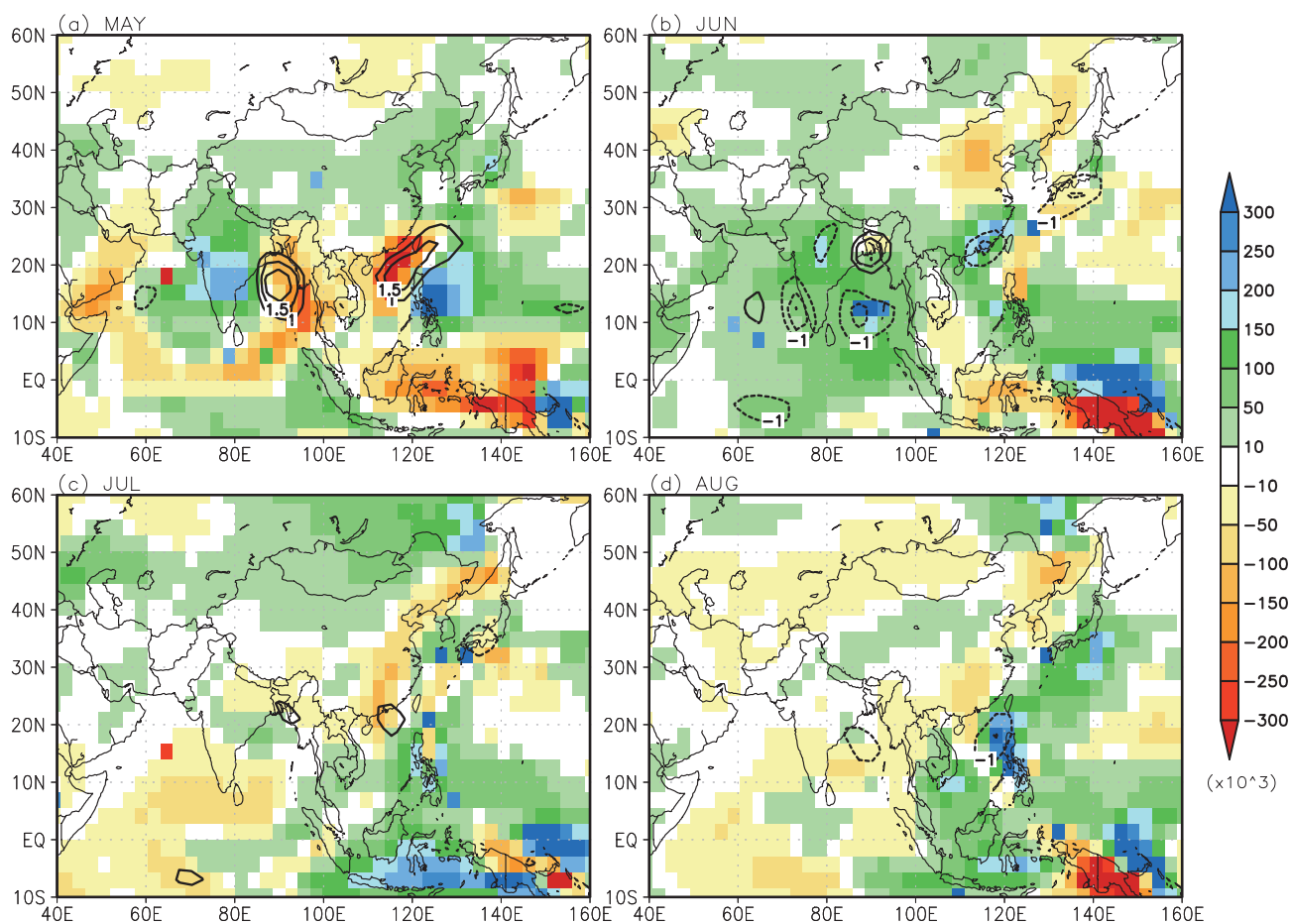


Fig. 6 Differences (EXP-CTL) in rainfall (mm/day, contour) and vertically integrated number concentrations of sulfate aerosol ($\#/cm^2$, shading) from May (upper left) to August (lower right). Rainfall differences greater than ± 1 mm/day are shown with a contour interval of 0.5.

precipitation events May and June agree well with the gamma curves, as pointed out by previous studies. In May for the EXP, the wet-day frequency and intensity increase compared to CTL. As a result, the relative contribution from above-normal and heavy rainfall events increased at the expense of light and near-normal rainfall events. The prominent contribution of the precipitation extremes to the change in total wet-day frequency was also evident in June when the mean precipitation intensity becomes weaker. In June, the changes in frequency of occurrence produced the opposite patterns to those in May, but the changes in extreme rainfall events still explained about 40% of the total wet-day frequency change.

6. Parallelization of an ice-sheet model IcIES

Ice-sheet Model for Integrated Earth-system Studies (IcIES) has been developed for serial-computing environment. This year a parallelization method was implemented on one of the two main equations in the numerical model. The equation integrates the ice thickness spatial distribution to the next time-step, which is computed through a diffusion-type matrix solver. Since it is common to have a highly localized ice sheet distribution in a realistic configuration, a block-cyclic domain decomposition method is adopted in order to reduce the load imbalance among the processors. Tests under an idealistic configuration

are examined by the parallel version of the model for one to eight processors. The results are confirmed to be identical, however, further improvement and optimization are found to be required, e.g., in terms of parallel efficiency. Next year we plan to complete the parallelization of the model (i.e., to parallel remaining one of the two main equations), and develop further to improve the efficiency.

References

- [1] Guenther, A., C. N. Hewitt, D. Erickson, R. Fall, C. Geron, T. Graedel, P. Harley, L. Klinger, M. Lerdau, W. McKay, T. Pierce, B. Scholes, R. Steinbrecher, R. Tallamraju, J. Taylor, and P. Zimmerman, 1995: A global model of natural volatile organic compound emissions, *J. Geophys. Res.*, 100, 8873-8892.
- [2] Guenther, A., T. Karl, P. Harley, C. Wiedinmyer, P. I. Palmer, and C. Geron, 2006: Estimates of global terrestrial isoprene emissions using MEGAN (Model of Emissions of Gases and Aerosols from Nature), *Atmospheric Chemistry and Physics*, 6, 3181–3210, doi:10.5194/acp-6-3181-2006.
- [3] Hurtt, G. C., S. Frolking, M. G. Fearon, B. Moore, E. Shevliakova, S. Malyshev, S. W. Pacala, and R. A. Houghton, 2006: The underpinnings of land-use history: three centuries of global gridded land-use transitions, wood-

harvest activity, and resulting secondary lands. *Global Change Biology*, 12, 1208–1229, doi: 10.1111/j.1365-2486.2006.01150.x .

- [4] Nitta et al., 2012: Representation of subgrid scale snow depth and snow cover variability in global model, 水工学論文集.
- [5] Yang Z.-L., R. E. Dickinson, A. Robock, and K. Ya. Vinnikov, 1997: Validation of the snow submodel of the Biosphere-Atmosphere Transfer Scheme with Russian snow cover and meteorological observational data, *J. Clim.*, 10, 353–373.
- [6] Yen, Y. C. et al., 1981: Review of Thermal Properties of Snow, Ice and Sea Ice. DTIC Document.

地球温暖化予測研究のための高精度気候モデルの開発研究

プロジェクト責任者

野田 彰 海洋研究開発機構 地球環境変動領域

著者

野田 彰^{*1}, 阿部 彩子^{*2,1}, 大垣内るみ^{*1}, 河谷 芳雄^{*1}, 黒木 聖夫^{*1}, 小室 芳樹^{*1},
齋藤 冬樹^{*1}, 高橋 邦生^{*1}, 高田久美子^{*1}, 田中 幸夫^{*1}, 近本めぐみ^{*1}

*1 海洋研究開発機構 地球環境変動領域

*2 東京大学 大気海洋研究所

本研究は、地球温暖化予測のための各種物理モデルの開発を進めながら、地球環境の変動メカニズムの解明を行う。具体的には (1) 氷床モデル・凍土モデル・海水モデルの開発、(2) 大気、海洋、陸面の物理過程の評価と改良、(3) 地球温暖化予測ならびに古気候再現に関わる気候モデルの感度実験、を行う。

本年度は以下の成果を得た。

QBO を再現可能なモデルを用いて、QBO の将来変化に対する二酸化炭素濃度と海面水温の役割を個別に評価した。将来の海面水温変化は QBO の周期を 1 – 3 か月、二酸化炭素濃度変化は 1 か月長くする効果があることが分かった。

海洋モデル開発に関しては、高精度の移流スキームである 2 次モーメント法を MIROC の海洋コンポーネントである COCO に導入した。新しく導入された移流スキームはトレーサー移流に起因する数値拡散を減少させ、モデルのパフォーマンスを向上させた。

古気候モデル実験では、現在気候下での南極周辺の海面水温のモデルバイアスを低減させることが古気候データから示唆される LGM の弱く浅い AMOC を再現することに重要であることを議論するために、PMIP2, PMIP3 のマルチモデル解析を行った。その結果 MIROC AOGCM を用いた様々な感度実験の結果と統合的な傾向があることがわかった。

地表面過程に関しては、積雪のサブグリッド被覆率を高度化 (SSNOWD) しても残るバイアスについて、積雪密度と伝導率の診断方法の改良を試みたが、バイアスの改善効果は小さかった。このほか、植生による揮発性有機炭素 (VOC) 発生量の変化がエアロゾル変化を介してアジア域の気候に及ぼす影響をタイムスライス実験によって調べた。VOC 増大による SOA の直接効果の放射強制力はあまり大きくないものの、4 – 5 月に最大になった。また、気候場との相互作用も含めた間接効果によって、硫酸エアロゾルの増大 (減少) 域で降水が減少 (増大) する負相関が見られた。また日降水量の強度分布を調べたところ、VOC 増大時に強い降水が増大していた。

氷床モデル開発に関しては、モデル内の一部の行列解法に並列化を実装した。領域分割にはブロックサイクリック法を適用し、理想的な実験から結果に問題がないことを確認した。

キーワード: 大気海洋陸面結合モデル, オフライン地球生態化学モデル, 成層圏準二年振動 (QBO), 氷床モデル

Simulations of Atmospheric General Circulations of Earth-like Planets by AFES

Project Representative

Yoshi-Yuki Hayashi

Department of Earth and Planetary Sciences, Kobe University

Authors

Yoshi-Yuki Hayashi^{*1}, Yoshiyuki O. Takahashi^{*1}, Norihiko Sugimoto^{*2}, Masahiro Takagi^{*3}, Masaki Ishiwatari^{*4}, Masatsugu Odaka^{*4}, Shinichi Takehiro^{*5}, Kensuke Nakajima^{*6}, Yuji Kitamura^{*7}, George L. Hashimoto^{*8} and Yoshihisa Matsuda^{*9}

*1 Department of Earth and Planetary Sciences, Kobe University

*2 Research and Education Center for Natural Sciences, Keio University

*3 Department of Earth and Planetary Science, The University of Tokyo

*4 Department of CosmoSciences, Hokkaido University

*5 Research Institute for Mathematical Sciences, Kyoto University

*6 Department of Earth and Planetary Sciences, Kyushu University

*7 Meteorological Research Institute

*8 Department of Earth Sciences, Okayama University

*9 Faculty of Education, Tokyo Gakugei University

High resolution simulations of the Martian atmosphere have been performed by using a General Circulation Model (GCM) based on AFES (Atmospheric GCM for the Earth Simulator). Also performed is a simulation of the Venus atmosphere by using AFES with simplified physical processes and with a resolution higher than previous studies. Our aim is to have insights into the dynamical features of small and medium scale disturbances in the Earth-like atmospheres and their roles in the general circulations. Mars simulations are performed by the use of quite high horizontal resolution which is almost the applicable limit of hydrostatic approximation. The results of the simulations in northern summer show a variety of small scale disturbances, which are qualitatively similar to those observed in a northern fall simulation. However, the resolution dependence of dust mass flux in northern summer shows a trend different from that in northern fall. This difference may be partly attributed to the seasonal difference in distance between the Mars and the sun, but further investigation is needed to understand it. As for the simulation of the Venus atmosphere, baroclinic modes grow at the cloud layer where static stability is low. The structures of unstable modes are similar to those obtained in the linear stability analysis, although they are modified by the time development of the basic state. Analysis of meridional transport of momentum and heat by these unstable modes suggest that those modes significantly contribute the general circulation of the Venus atmosphere. This must be a feature we should consider in the higher resolution numerical experiments.

Keywords: planetary atmospheres, superrotation, dust storm, Earth, Mars, Venus

1. Introduction

The structure of the general circulation differs significantly with each planetary atmosphere. For instance, the atmospheres of the slowly rotating Venus and Titan exemplify the superrotation, while the weak equatorial easterly and the strong mid-latitude westerly jets form in the Earth's troposphere. The global dust storm occurs in some years on Mars, but a similar storm does not exist in the Earth's atmosphere. Understanding physical mechanisms causing such a variety of structures of the general circulations of planetary atmospheres is one of the most interesting and important open questions of the atmospheric

science and fluid dynamics.

The aim of this study is to understand dynamical processes that characterize the structure of each planetary atmosphere by performing simulations of those planetary atmospheres by using GCMs with a common dynamical core of AFES [1]. Appropriate physical processes are adopted for each planetary atmosphere. In our project so far, we have been mainly performing simulations under the condition of Mars. In addition, the accurate radiation model of the Venus atmosphere has been constructed for the simulations under the condition of Venus. In the followings, the particular targets of each simulation, the

physical processes utilized, and the results obtained will be described briefly.

2. Mars simulation

2.1 Targets of simulations

Dust suspended in the Martian atmosphere plays an important role to maintain thermal and circulation structure of the Martian atmosphere through radiative process. However, the physical mechanisms of dust lifting are not understood fully. A previous study by using a Mars GCM [2] suggests that the effects of wind fluctuations caused by small and medium scale disturbances would be important for the dust lifting processes. However, the features of small and medium scale disturbances which may contribute to the dust lifting have not been clarified. Disturbances of these scales are not easy to be observed. In order to examine the disturbances in the Martian atmosphere and its effects on dust lifting, we have been performing medium and high resolution simulations of Martian atmosphere by using a Mars GCM. In this fiscal year, simulations are continued with the condition of northern summer, when a global scale dust storm is not observed on Mars, and examine the seasonal difference by comparing a result with that at northern fall, which was performed last fiscal year.

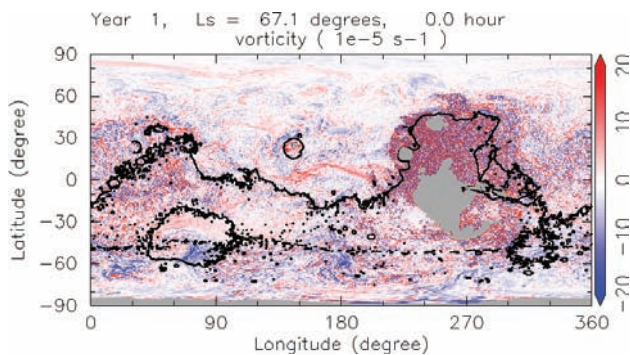


Fig. 1 Global distribution of vorticity at the 4 hPa pressure level at northern summer with the resolution of T639L96. Unit of vorticity is $10^{-5} s^{-1}$. Also shown is the areoid (solid line) and low latitude polar cap edge (dashed line). Gray areas represent mountains at the 4 hPa pressure level.

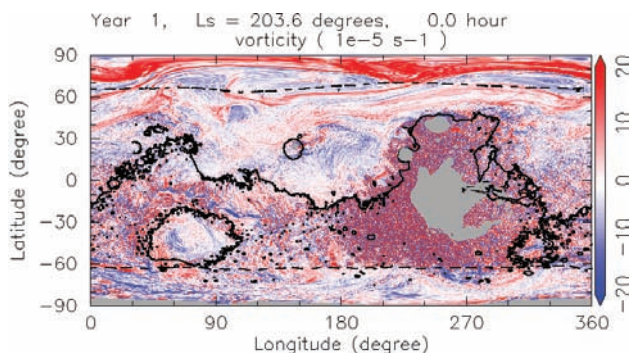


Fig. 2 Same as Fig. 1, but for northern fall.

2.2 Model and experimental settings

Mars simulations are performed with the physical processes introduced from the Mars GCM [3, 4] which has been developed in our group, and the values of physical constants appropriate for the Mars. The implemented physical processes are radiative, turbulent mixing, and surface processes. By the use of this GCM, the simulations in northern summer condition are performed. Resolutions of simulations are T79L96, T159L96, T319L96, and T639L96, which are equivalent to about 89, 44, 22, and 11 km horizontal grid sizes, respectively. The horizontal resolution of T639 is almost the applicable limit of hydrostatic approximation. In the simulation performed in this fiscal year, the atmospheric dust distribution is prescribed, and the dust is uniformly distributed in horizontal direction with an amount corresponding to visible optical depth of 0.2. Nevertheless, the dust lifting parameterization [5] is included in the model to diagnose the possible amount of dust lifting. As for the surface condition, the observed spatial variations of orography, surface albedo, and surface thermal inertia are prescribed. As a sensitivity test, the simulations with flat surface, uniform albedo and thermal inertia, are also performed to examine intrinsic effects of horizontal resolution on disturbance generation and dust lifting without such variations.

2.3 Results

Figure 1 shows a snapshot of global distribution of relative vorticity at the 4 hPa pressure level at northern summer from T639L96 simulation. In the simulation, a variety of atmospheric disturbances can be observed, such as baroclinic waves in the southern middle and high latitudes, medium scale vortices, some of which are associated with mountains, small scale streaks, and small scale vortices in the low latitude. Here, the small scale vortices in low latitude are focused. Comparing the vorticity distribution at northern summer with that at northern fall (Fig. 2),

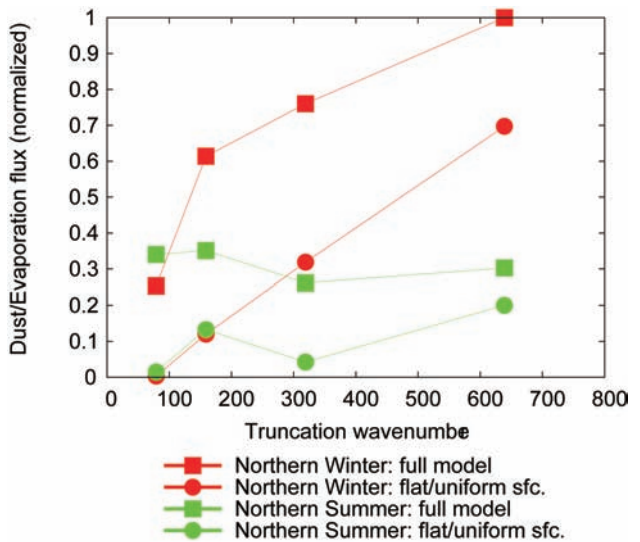


Fig. 3 Resolution dependence of normalized globally integrated dust mass flux. Squares indicate normal simulation, while circles indicate simulations without surface variations.

it is found that the similar small scale vortices are observed in both seasons. As is the case at northern fall, the horizontal size of those small scale vortices at northern summer do not seem to converge up to the highest resolution performed in our study. It is considered that these small scale vortices are representation of vertical convection in the model. The latitude where the vortices are observed is different because of the different seasonal condition. The area where the small scale vortices are observed may be slightly smaller than that at northern summer. This may reflect the facts that the distance between the Mars and the sun is larger at northern summer than that at northern fall, and that the elevation of northern hemisphere is lower than that of southern hemisphere.

In order to assess the effects of small and medium scale disturbances on dust lifting, the resolution dependence of globally integrated dust mass flux diagnosed in the model is examined. Figure 3 shows the resolution dependence of globally integrated dust mass flux. The dust mass fluxes at northern fall and those in the flat/uniform surface experiments are also shown. The globally integrated dust mass fluxes at northern summer do not increase with increasing resolution significantly. This trend is not the same as that at northern fall. This implies that the strength of small scale disturbances represented in our model at northern summer would not be the same as that at northern fall. However, the physical mechanisms of this seasonal difference have not been interpreted yet. Further investigation is needed to understand seasonality of dust lifting.

3. Venus simulation

3.1 Targets of simulations

The mechanism of the super-rotation is one of the most interesting topics in the planetary science. Several mechanisms, such as the Gierasch mechanism [6] through meridional circulation and the thermal tides mechanisms [7] through wave mean flow interaction, have been proposed to explain this special phenomenon. In the results of previous numerical simulations using Venus-like GCMs, both mechanisms can work to generate super-rotation [8, 9]. However, since these models have coarse resolutions and simple physical processes, it is unclear whether the previous results can hold in case of high resolution realistic numerical simulations. In addition, as is usually done in the context of geophysical fluid dynamics on Earth, parameter studies, such as resolution, horizontal and vertical eddy viscosity, topography, heating rate, and radiative process, are also needed to obtain the comprehensive understandings of the atmosphere of Venus.

In the present study, we develop a GCM for Venus by modifying AFES to achieve high resolution numerical simulation for the atmosphere of Venus. Although our final goal is to understand the fundamental mechanism of the super-rotation, we have to check the numerical model before performing long time simulation with high resolution.

Therefore, as a first step, we investigate structure of unstable modes initiated from an initial condition of super-rotating flow and a realistic static stability. In addition, momentum and heat transport achieved by the unstable modes are also addressed in this study.

3.2 Model and experimental settings

Venus simulations are performed with simplified physical processes and physical constants appropriate for the Venus. Experimental settings are basically based on the previous linear stability analysis [10]. Physical processes included in the model are vertical eddy diffusion with a constant diffusion coefficient of $0.015 \text{ m}^2/\text{s}$, a dry convective adjustment, the Newtonian cooling, and the Rayleigh friction at the lowest level to represent the surface friction. Unlike the many previous studies, Rayleigh friction is not imposed in the upper layers. In addition, the model includes 8th order horizontal diffusions (∇^8) with e-folding time for the maximum wavenumber of about 0.8 days. The Newtonian cooling coefficients are based on the observation [11]. The equilibrium temperature distribution toward which the temperature is relaxed by the Newtonian cooling is an initial value written below.

A basic state used in a dynamical core is partly based on an observed static stability distribution [12]. The lower atmosphere close to the ground is weakly stable. In the cloud layer, there is an almost neutral layer (from 55 to 60 km) due to the solar heating. At the bottom of the cloud layer it is stable, and static stability has a maximum at around 45 km. Above the cloud layer (above 70 km), it is strongly stratified. It is expected that unstable modes will appear in the cloud layer.

The resolution used in a simulation is T42L60, which has 128 and 64 grids in the longitudinal and latitudinal direction, respectively. Vertical domain extends from the ground to about 120 km with almost the constant grid spacing of 2 km.

The initial condition is an idealized solid body super-rotating flow. The flow linearly increases with height from ground to 70 km, which is suggested by the observation [13]. Its maximum is 100 m/s at 70 km at the equator, and above there the velocity is constant. Temperature is in balance with the zonally symmetric flow, namely, gradient wind balance. Meridional temperature gradient from equator to pole is about 5 K on a sigma surface at the top of cloud layer. Initiated from this initial condition, the model is integrated for 5 Earth years.

3.3 Results

In the results of numerical simulation, super-rotation gradually decreases in the cloud layer (50 - 70 km). It is the unstable modes of growing vortices that decrease super-rotation in the later stage. Figure 4 shows snapshots of horizontal cross section of vorticity disturbance and zonal mean horizontal flow at 54 km for two different times. Clearly, vortical structure of wavenumber 3 and 4 grow at the mid latitude. They have

significant amplitude at the later time. These growing vortices decrease super-rotating flow where they evolve.

Figure 5 shows height – longitude cross sections of meridional flow disturbance (a) and temperature disturbance

(b) at 40°N where unstable modes grow. The phases of these disturbances are tilted from down-east to up-west. In addition, they are out of phase. That is, while cold air flows downward and southward, warm air flows upward and northward. This

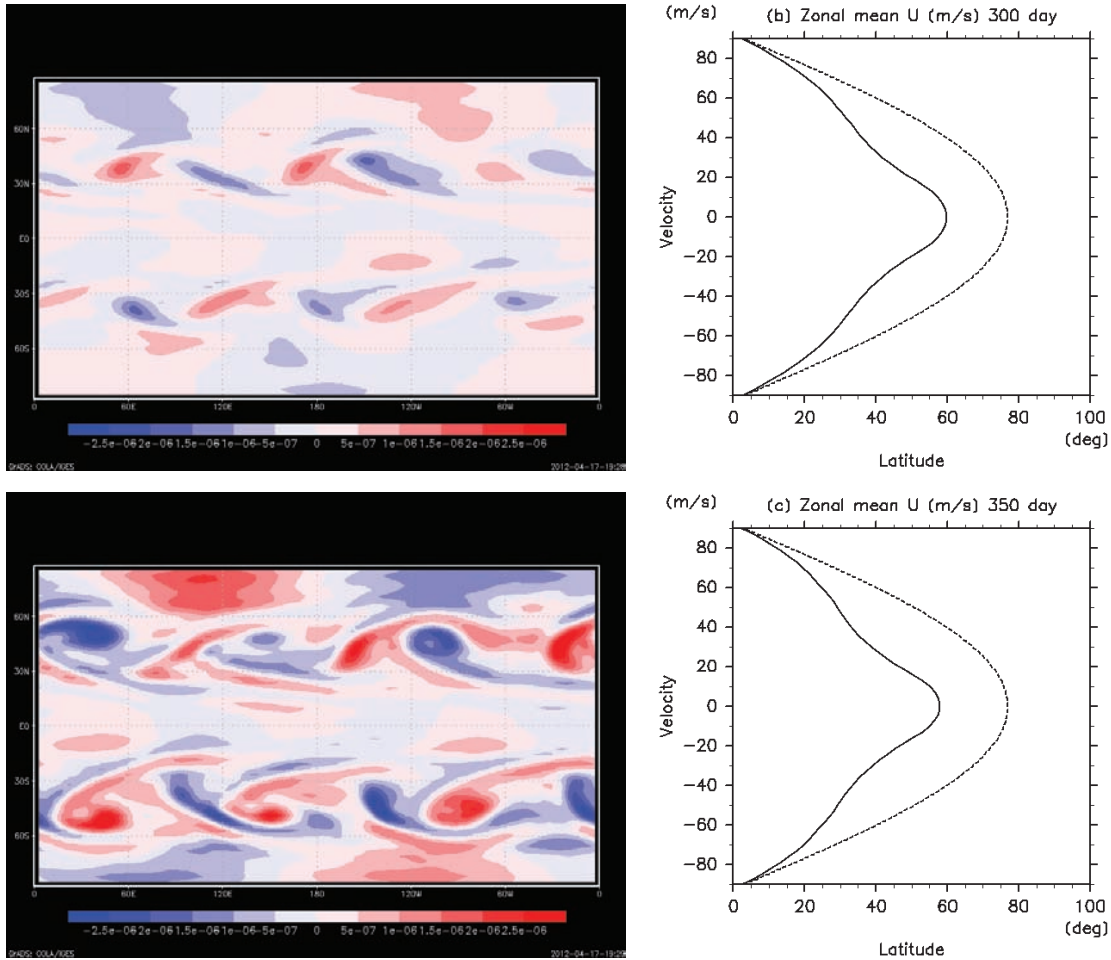


Fig. 4 Snapshots of horizontal cross section of vorticity disturbance (left) and latitudinal profile of zonal mean horizontal flow (right) at 54 km; (top) 300 days and (bottom) 350 days.

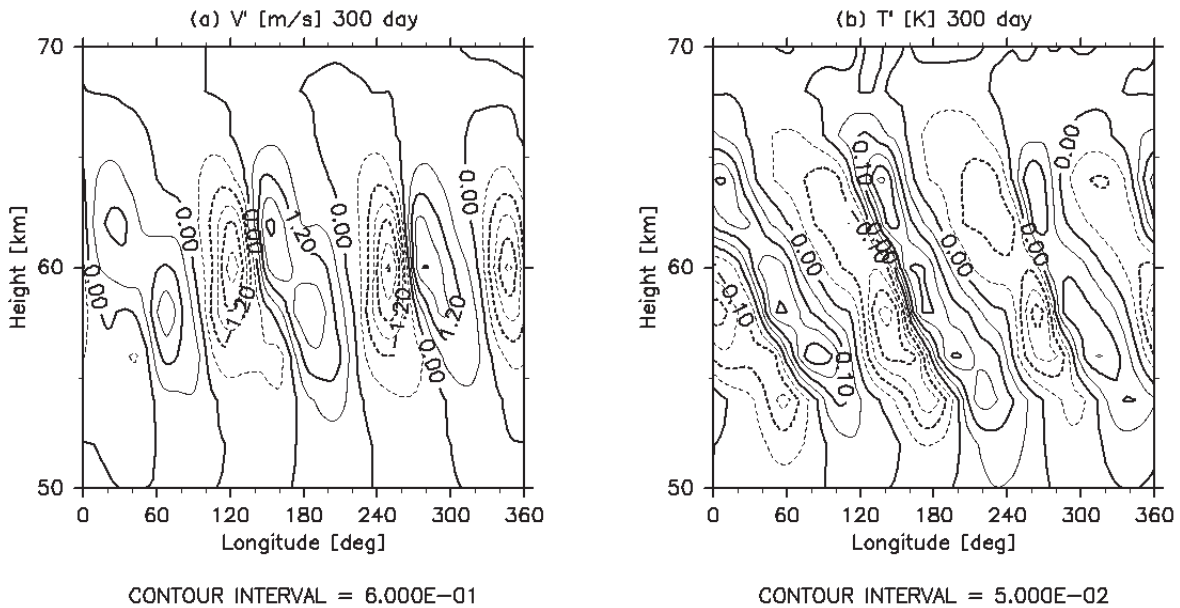


Fig. 5 Height – longitude cross sections at 40 degrees north of meridional flow disturbance (a) and temperature disturbance (b) at 300 days.

is the typical structure of baroclinic instability. It is almost consistent with the results of previous linear stability analysis, although basic zonal flow changed in the time evolution of nonlinear simulation. Since stable layer exists below the cloud layer and density in the lower layer is large, unstable mode does not extend to the lower layer. We investigate momentum and heat transport by growing vortices. It is found that zonal flow is accelerated by unstable modes using available potential energy in the initial stage of baroclinic instability. Thus, momentum flux converges to the position where baroclinic modes develop, and heat flux is poleward in the northern hemisphere.

In order to check the dependence of the results on the resolution we also perform simulation with T21L60 resolution, which has 64 and 32 grids for the longitudinal and latitudinal direction, respectively. Although we used the same condition except for the resolution (and therefore the horizontal diffusion), the flow field is quite different from that of T42L60. Only large scale vortices appear and there is no filament structure of vortex due to lack of the resolution. In addition, it takes more time for unstable mode to develop in T21L60 simulation than in T42L60 simulation. Although further analysis is needed to elucidate the dependence on the resolution, we have to use higher resolution than T21L60, as is done in the present study, in order to investigate these disturbances quantitatively.

So far, there are no observations of baroclinic instability on Venus, though they are considered to be important [14]. This study suggests they could exist in the cloud layer where super-rotating flow is fast and meridional temperature gradient is large, and could be important on maintaining general circulation on Venus through momentum and heat transportation.

Finally, this study treated only an initial growth of baroclinic instability. For future work, we hope to include realistic solar heating in the model to maintain meridional temperature gradient. It is expected that the solar heating will keep strong super-rotation in the cloud layer. As is frequently discussed on Gierasch mechanism, several unstable modes are candidates to transport momentum from pole to equator [15]. Long time numerical simulation initiated from super-rotation would be one of the promising ways to investigate roles of disturbances, including baroclinic modes, on super-rotation. Further study with high resolution simulations and realistic radiative process will reveal generation and maintenance mechanism of super-rotation on Venus.

References

- [1] Ohfuchi, W., Nakamura, H., Yoshioka, M. K., Enomoto, T., Takaya, K., Peng, X., Yamane, S., Nishimura, T., Kurihara, Y., and Ninomiya, K., “10-km Mesh Meso-scale Resolving Simulations of the Global Atmosphere on the Earth Simulator - Preliminary Outcomes of AFES (AGCM for the Earth Simulator)” -, *Journal of the Earth Simulator*, 1, 8, 2004.
- [2] Wilson, R. J. and Hamilton K, “Comprehensive Model Simulation of Thermal Tides in the Martian Atmosphere”, *J. Atmos. Sci.*, 53, 1290-1326, 1996.
- [3] Takahashi, Y. O., Fujiwara, H., Fukunishi, H., Odaka, M., Hayashi, Y.-Y., and Watanabe, S., “Topographically induced north-south asymmetry of the meridional circulation in the Martian atmosphere”, *J. Geophys. Res.*, 108, 5018, doi:10.1029/2001JE001638, 2003.
- [4] Takahashi, Y. O., Fujiwara, H., and Fukunishi, H., “Vertical and latitudinal structure of the migrating diurnal tide in the Martian atmosphere: Numerical investigations”, *J. Geophys. Res.*, 111, E01003, doi:10.1029/2005JE002543, 2006.
- [5] Newman, C. E., Lewis, S. R., and Read, P. L., “Modeling the Martian dust cycle 1. Representation of dust transport processes”, *J. Geophys. Res.*, 107, 5123, doi:10.1029/2002JE001910, 2002.
- [6] Gierasch, P. J., “Meridional circulation and maintenance of the Venus atmospheric rotation”, *J. Atmos. Sci.*, 32, 1038-1044, 1975.
- [7] Fels, S. B. and Lindzen, R. S., “The interaction of thermally excited gravity waves with mean flows”, *Geophys. Fluid Dyn.*, 5, 211-212, 1974.
- [8] Yamamoto, M. and Takahashi, M., “The fully developed superrotation simulated by a general circulation model of a Venus-like atmosphere”, *J. Atmos. Sci.*, 60, 561-574, 2003.
- [9] Takagi, M. and Matsuda, Y., “Effects of thermal tides on the Venus atmospheric superrotation”, *J. Geophys. Res.*, 11, D09112, doi:10.1029/2006JD007901, 2007.
- [10] Takagi, M. and Matsuda, Y., “A study on the stability of a baroclinic flow in cyclostrophic balance on the sphere”, *Geophysical Research letters*, 33, L14807, doi:10.1029/2006GL026200, 2006.
- [11] Crisp, D., “Radiative forcing of the Venus mesosphere: I. solar fluxes and heating rates”, *Icarus*, 67, 484-514, 1986.
- [12] Gierasch, P. J., Goody, R. M., Young, R. E., Crisp, D., Edwards, C., Kahn, R., Rider, D., del Genio, A., Greeley, R., Hou, A., Leovy, C. B., McCleese, D., and Newman M., “The General Circulation of the Venus Atmosphere: an Assessment”, In *Venus II: Geology, Geophysics, Atmosphere, and Solar Wind Environment*. University of Arizona Press, p.459, 1997.
- [13] Shubert, G., “General circulation and dynamical state of Venus atmosphere”, In *Venus (A83-37401 17-91)* edited by D. Hiltner, University of Arizona Press: Tucson, 681-765, 1983.
- [14] Allison, M., Del Genio, A., and Zhou, W., “Zero potential vorticity envelopes for the zonal-mean velocity of the Venus/Titan atmosphere”, *J. Atmos. Sci.*, 51, 694-702, 1994.
- [15] Iga, S. and Matsuda, Y., “Shear instability in a shallow

water model with implications for the Venus atmosphere”,
J. Atmos. Sci., 62, 2514-2527, 2005.

AFES を用いた地球型惑星の大気大循環シミュレーション

プロジェクト責任者

林 祥介 神戸大学 大学院理学研究科

著者

林 祥介^{*1}, 高橋 芳幸^{*1}, 杉本 憲彦^{*2}, 高木 征弘^{*3}, 石渡 正樹^{*4}, 小高 正嗣^{*4},
竹広 真一^{*5}, 中島 健介^{*6}, 北村 祐二^{*7}, はしもとじょーじ^{*8}, 松田 佳久^{*9}

*1 神戸大学 大学院理学研究科

*2 慶應義塾大学 自然科学研究教育センター

*3 東京大学 大学院理学系研究科

*4 北海道大学 大学院理学研究院

*5 京都大学 数理解析研究所

*6 九州大学 大学院理学研究院

*7 気象庁 気象研究所

*8 岡山大学 大学院自然科学研究科

*9 東京学芸大学 教育学部

大気大循環モデル AFES (AGCM (Atmospheric General Circulation Model) for the Earth Simulator) に基づく GCM を用いて、火星大気の高解像度大気大循環シミュレーションを実施した。加えて、これまでに開発してきた高精度の金星大気放射モデルを用いた高解像度シミュレーションの下準備として、簡単な物理過程を用いた中解像度での大気大循環シミュレーションを実施した。我々の研究の目的は、地球型惑星大気における中小規模擾乱の力学的特徴と、その大気大循環への影響を調べることである。火星大気シミュレーションは、おおよそ静水圧近似が成り立つ限界付近の非常に高い解像度で実施した。北半球の夏の時期におけるシミュレーションの結果は、北半球の秋の時期のシミュレーションと定性的に同様な様々な小規模擾乱を示す。しかし、北半球の夏の時期における、ダスト巻き上げフラックスの解像度依存性は、北半球の秋の季節とは異なることが示された。この違いは、部分的には、火星-太陽間距離の季節変化が原因であると考えられるが、その理解のためにはさらに調査が必要である。金星大気シミュレーションに関しては、安定度の小さい雲領域における傾圧不安定モードの成長が示された。これらの傾圧不安定モードの構造は、時間発展していく基本場の影響も受けているようであるが、基本的には線形安定性解析で示されていたものであると考えられる。これらの傾圧不安定モードによる運動量と熱の南北輸送を解析した結果、金星大気大循環において重要な寄与をなしていると評価された。高解像度計算において着目されるべき特徴であると予想される。

キーワード: 惑星大気, スーパーローテーション, ダストストーム, 地球, 火星, 金星

Study on the Diagnostics and Projection of Ecosystem Change Associated with Global Change

Project Representative

Michio J. Kishi

Research Institute for Global Change, Japan Agency for Marine-Earth Science and Technology

Authors

Akio Ishida^{*1,2}, Yoshikazu Sasai^{*1}, Maki Noguchi Aita^{*1}, Eiji Watanabe^{*1}, Taketo Hashioka^{*3}, Takafumi Hirata^{*3} and Yasuhiro Yamanaka^{*1,3}

*1 Research Institute for Global Change, Japan Agency for Marine-Earth Science and Technology

*2 Department of Social Environment, Fuji Tokoha University

*3 Faculty of Environmental Earth Science, Hokkaido University

In this project we will improve the ability to simulate the present status of ocean climate and ecosystems and clarify effects of climate variability on marine biogeochemical cycles and ecosystems by using multiple ocean general circulation models (GCMs) with multiple ecosystem models including marine biogeochemical cycles. We have investigated the impact of climate variability on the marine ecosystem in the northeastern tropical Pacific using our high-resolution model. We also have examined the mechanisms of phytoplankton competition during the spring bloom in the first phase of Marine Ecosystem Model Intercomparison Project (MAREMIP). We also work on the development of Arctic marine ecosystem model to investigate the impact of sea ice and ocean dynamics on the polar ecosystem.

Keywords: Ecosystem, Biogeochemical Cycles, Global Change, Ocean General Circulation Model, Fisheries resources

1. High resolution modeling of biogeochemical cycles and ecosystems

Using an eddy-resolving OGCM (OFES) coupled with a simple ecosystem (NPZD) model, we have investigated the seasonal and interannual variabilities of the chlorophyll in the northeastern tropical Pacific during 2000-2007. The seasonal variability of the surface chlorophyll concentration in the model agrees well with satellite ocean color data, except for the equatorial region [1]. High chlorophyll levels off the Gulf of Tehuantepec, Papagayo, and Panama in winter and in the Costa Rica Dome in summer are well reproduced. Production in these areas is controlled by the supply of nitrate rich-waters through vertical mixing and coastal and open ocean upwelling. The variability of the thermocline depth is strongly connected to the seasonal variability of surface chlorophyll. El Niño Southern Ocean (ENSO) variability has a marked effect on the marine ecosystem in this region. The model reproduces the chlorophyll variability corresponding to the observed ENSO variability.

2. Process modeling in marine ecosystems

In the first phase of Marine Ecosystem Model Intercomparison Project (MAREMIP), we investigated the mechanisms of phytoplankton competition during the spring bloom, one of the most dramatic seasonal events in lower-trophic level ecosystems, in four Plankton Functional Types

(PFTs) models: NEMURO (JAMSTEC, Hokkaido Univ.), PISCES (IPSL, France), PlankTOM5 (UEA, UK) and CCSM-BEC (WHOI, US). As a common feature of all investigated models, the percentage of diatoms with respect to total phytoplankton increases with the magnitude of the spring bloom (Fig. 1). However, the mechanisms governing succession differ among models, despite the fact that current PFT models parameterize the same types of ecophysiological processes. The differences in the mechanisms suggest that the response of marine ecosystems to climate change could significantly differ among models. Through this first model intercomparison of the PFTs models, several key processes for further understanding

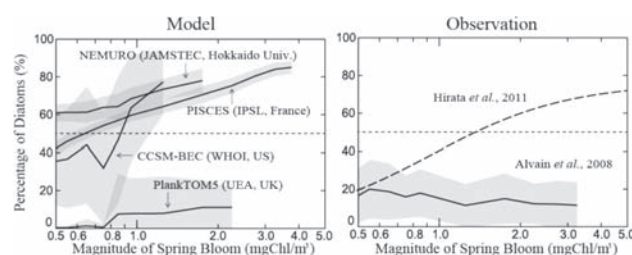


Fig. 1. Percentage of diatoms (large group) with respect to total phytoplankton at the peak timing of the bloom as a function of the bloom magnitude in the North Pacific (right: model results, left: observation). The shades are the spatial standard deviation in the blooming region of each model and satellite estimations.

have been made clear.

In order to assess model performance on spatial distributions of PFTs, spatial patterns of PFTs derived from models were compared to these derived from satellite observation [2, 3]. The model skill score for the advanced version of NEMURO (i.e. Marine Ecosystem Model with Optimal Nutrient Uptake Kinetics, MEM) are shown in Fig. 2 as functions of PFTs pigment biomass (i.e. fractional Chlorophyll-a of PFTs) and spatial scales of their patterns [4]. We found that the model successfully reproduces spatial patterns derived from satellite observation at the spatial scale $> 1800 \text{ km}^2$. Even at smaller spatial scales ($< 200 \text{ km}^2$), spatial patterns in the model tends to agree with those in the satellite, when the pigment biomass is either small or large (but not “intermediate”). This tendency is also found in another model such as the European Regional Sea Ecosystem Model, ERSEM (not shown). Thus, the state-of-the-art models are successful in reproducing spatial patterns when a spatial contrast in pigment biomass is large enough.

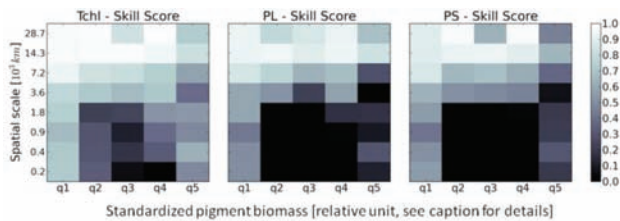


Fig. 2. Model skill score derived from wavelet analysis as functions of the spatial scale (y) and pigment-biomass (x) for Total phytoplankton community (Tchl), Diatoms (PL) and other small-sized phytoplankton (PS). Colour tone shows the skill score (0 to 1), brighter being better and darker being poorer. q1, q2...q5 show quantiles (20%, 40%, ..., 100%) in pigment biomass data distribution.

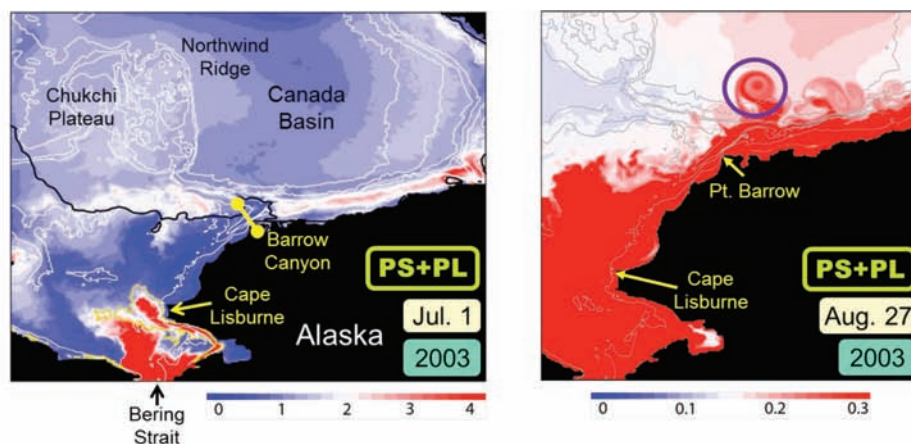


Fig. 3. Surface phytoplankton concentration on (left) July 1 and (right) August 27 in the 2003 case demonstrated by the coupled sea ice-ocean model with a lower-trophic marine ecosystem formulation [mmolN/m^3]. White contours show bottom bathymetry. Black contours in the left figure correspond to the simulated sea ice concentration of 0.5.

3. Process modeling on Arctic marine ecosystem

Response of primary productivity to the Beaufort shelf-break eddies is examined following eddy life stages using an eddy-resolving sea ice-ocean model with a lower-trophic marine ecosystem formulation [5]. During late summer and early autumn, the shelf-break warm eddies initially transport the Chukchi shelf water with high primary productivity toward the southern Canada Basin (Fig. 3). In the eddy-developing period, the anti-cyclonic rotational flow along the outer edge of each eddy occasionally traps the shelf water. In the eddy-maturity period, the primary production inside the warm eddies is maintained by eddy dynamics, partly attributing to turbulent vertical mixing with underlying nutrient-rich water. In the eddy-decay period, light limitation before sea ice freezing shuts down the primary productivity in spite of nutrient recovery. These modeling analyses indicate that the time lag between phytoplankton bloom following summertime sea ice retreat in the Chukchi shelf region and eddy generation north of the Barrow Canyon is an important index to determine biological regimes in the western Arctic basin. Interannual variations in eddy performances would have a significant impact on the bottom-up control of food chains.

References

- [1] Y. Sasai, K. J. Richards, A. Ishida, and H. Sasaki, Spatial and temporal variabilities of the chlorophyll distributions in the northeastern tropical Pacific: The impact of physical processes on seasonal and interannual time scales, *J. Marine Systems*, 96-97, 24-31. DOI:10.1016/j.jmarsys.2012.01.014, 2012.
- [2] T. Hirata, N. J. Hardman-Mountford, R. J. W. Brewin, J. Aiken, R. Barlow, K. Suzuki, T. Isada, E. Howell, T. Hashioka, N. Aita-Noguchi, and Y. Yamanaka, Synoptic relationships between surface Chlorophyll-a and diagnostic pigments specific to phytoplankton functional types, *Biogeosciences*, 8, 311-327, 2011.
- [3] S. Alvain, C. Moulin, Y. Dandonneau, and F. M., Breon, Remote Sensing of phytoplankton groups in case 1 waters from global SeaWiFS imagery, *Deep-Sea Research Part I*, 52, 1989-2004, 2005.
- [4] M. Shigemitsu, T. Okunishi, J. Nishioka, J., H. Sumata, T. Hashioka, M. Aita-Noguchi, S. L. Smith, N. Yoshie, N. Okada, and Y. Yamanaka, Development of one-dimensional ecosystem model including the iron cycle applied to the Oyashio region, western subarctic, *Journal of Geophysical Research – Oceans*, (submitted).
- [5] E. Watanabe, M. J. Kishi, A. Ishida, and M. N. Aita, Western Arctic primary productivity regulated by shelf-break warm eddies, *Journal of Oceanography*, 2012, (in revision).

地球環境変化に伴う生態系変動の診断と予測に関する研究

プロジェクト責任者

岸 道郎 海洋研究開発機構 地球環境変動領域

著者

石田 明生^{*1,2}, 笹井 義一^{*1}, 相田(野口) 真希^{*1}, 渡邊 英嗣^{*1}, 橋岡 豪人^{*3}, 平田 貴文^{*3},
山中 康裕^{*1,3}

*1 海洋研究開発機構 地球環境変動領域

*2 富士常葉大学 社会環境学部

*3 北海道大学 大学院地球環境科学研究院

本プロジェクトでは、空間解像度や複雑さの異なる複数の海洋生態系モデル、海洋大循環モデルを用いて、現在の気候条件における生態系変動再現実験、及び、温暖化気候における将来予測実験を通して、生態系の変動特性の定量化、生態系の将来予測、海域による海洋生態系の違いや卓越種の再現を目指した生態系モデル開発を実施する。今年度は、高解像度海洋大循環・海洋生態系結合モデルを用いて東部赤道太平洋における気候変動が表層のプランクトン分布に与える影響について議論した。また、MAREMIP (MARine Ecosystem Model Intercomparison Project) において、異なる生態系プロセスモデル結果の相互比較、観測データとの比較を通じた植物プランクトンの種間競争メカニズムの解析を行った。さらに、西部北極海を対象とした渦解像海水海洋物理モデルに低次海洋生態系モデル (NEMURO) を結合し、植物プランクトンの主要な時空間変動特性の再現に成功した。その結果、チャクチ陸棚域での植物プランクトンブルームと陸棚海盆境界域での暖水渦生成のタイムラグが渦内部の生物化学的特性および基礎生産性を大きく支配することが明らかになった。

キーワード: 生態系, 物質循環, 気候変動, 高解像度海洋大循環モデル, 水産資源

CFD Simulation of Summertime Air Temperature Distribution of the Ten Kilo-meter Square Area of Center of Tokyo

Project Representative

Yasunobu Ashie

National Institute for Land and Infrastructure Management

Authors

Yasunobu Ashie

National Institute for Land and Infrastructure Management

Koji Kagiya

National Institute for Land and Infrastructure Management

Takaaki Kono

Kanazawa University

We have performed large-scale numerical simulations using the Earth simulator for the estimation of urban heat island phenomena considering detail locations of buildings and roads by means of CFD (Computational Fluid Dynamics). In this fiscal year, a ten kilo-meter square area of center of Tokyo was analyzed by using a horizontal grid spacing of 5 m to examine thermal construction in summer time. For the CFD simulation, building height, land use, anthropogenic heat etc. are databased by a 5 m mesh resolution. In addition, sun shade at each mesh and each time was analyzed considering complex 3D urban forms for the calculation of heat balance of urban surfaces. Numerical results showed air temperature is locally high along main streets at 8 o'clock. This situation may be caused by anthropogenic heat from automobiles of rush hour. In 14 o'clock, simulated air temperatures distributed uniformly except for cooling spots around sea shore and large parks.

Keywords: Heat island, Tokyo, CFD, Air temperature

1. Introduction

Recently, countermeasures against the urban heat island (UHI) effect, such as reduction of anthropogenic heat release and enhancement of urban ventilation, have become increasingly important in Tokyo. The evaluation of urban ventilation requires the construction of a high-resolution computational fluid dynamics (CFD) system, which takes account of complex urban morphology. The morphological complexity arises from multiscale geometry consisting of buildings, forests, and rivers superimposed on varying topography. Considering these backgrounds, we have developed a high-resolution CFD system and have performed simulations of wind and air temperature fields of Tokyo using a horizontal grid spacing of 5 m [1] [2]. It is necessary to accurately handle the heat transfer phenomenon of buildings or the ground prior to fluid analysis of an urban area.

In 2011, we improved the calculation method that grasps the surface temperature of a city in a three-dimensional nonsteady manner. We conducted a radiate calculation considering shadow and angle between sunbeam and building walls, and finally determined the surface temperatures of buildings and the ground. The simulation day is 10 August, 2007.

2. Location of analysis

A ten kilo-meters square area of Tokyo is considered for

analysis (Fig. 1). The computational domain extends vertically to a height of 500 m and is divided into grid cells that vary in height from 1 to 10 m with the smallest grid cells closest to the ground. The domain is horizontally divided into equally-sized 5-m grid cells. In order to obtain the boundary values of the CFD computational domain, the LOCALS-UCSS model [3] is run prior to the CFD analysis. The model is run for two domains with one-way nesting. The length of the sides of the domain and the grid spacing of the coarse grid model are 300 km and 5 km, respectively, and those of the fine grid model are 100 km and 1 km, respectively. The coarse grid model is run using initial and boundary values based on data from the Regional Spectral Model-Grid Point Value (RSM-GPV) provided by the Japan Meteorological Agency. The period of analysis is from 2100 LST on 9 August, 2007 to 2400 LST on 10 August, 2007. Figure 2 shows an example of simulation results by LOCALS-UCSS. Around 23 special wards of Tokyo, urban heat island are clearly formed.

3. Input data

To calculate the effective volume fraction and the open area ratio within each grid cell, the polygon data of each building is extracted from the GIS data of Tokyo. The height of each building is obtained using the aerial laser measurement data of the Geographical Survey Institute of Japan. Figure 3 shows the

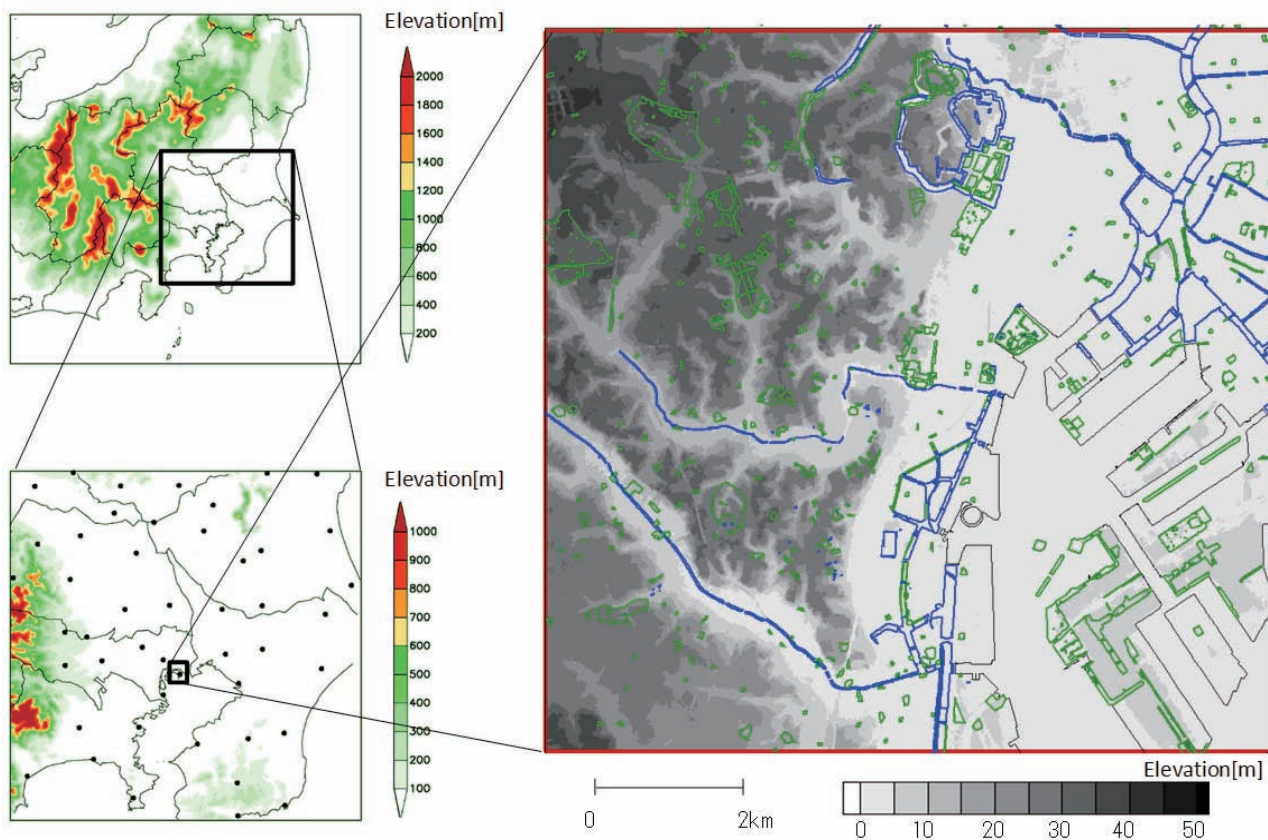


Fig. 1 Simulation domain.

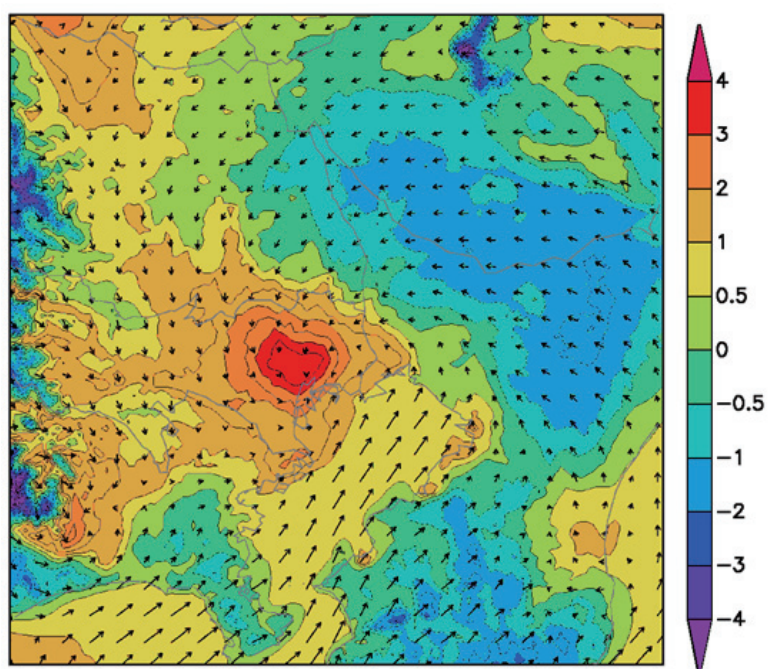


Fig. 2 Simulated air temperature distribution at 2:00 on 10 August, 2007.

distribution of building height in the computational area.

Anthropogenic heat can be classified into sensible heat and latent heat, and they are treated separately in the CFD model. Sensible heat includes heat released from buildings, traffic, and factories. The amount of anthropogenic heat released in individual grid cells for the time of simulation is estimated using the reported values in MLIT/MOE (2004)[4]. The estimation takes into consideration the location of anthropogenic heat releases as well as the total area of rooftops, building walls, and road surfaces in each grid cell. Figure 4 shows the distribution of anthropogenic heat in the computational area.

4. Results

Air temperature and wind distribution at 8 o'clock are shown Fig. 5. Main wind direction is north, and air stream is formed

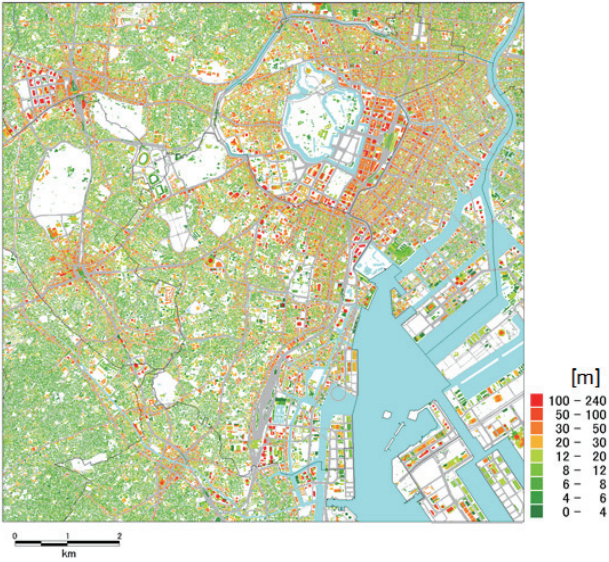


Fig. 3 building height.

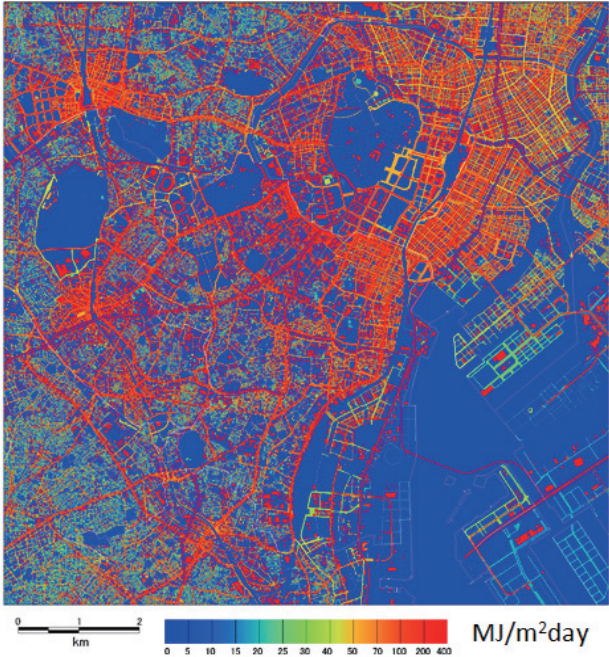


Fig. 4 Anthropogenic heat.

from north region to Tokyo bay along Sumida-river. In addition, it is noticed that high air temperature areas are formed along main traffic roads. This is caused by anthropogenic heat from traffics. In the morning, sun radiation is not so large, and the heat amount by traffic is very large in rush hour.

As time goes by, high air temperature area extends over the land area especially north region. Figure 6 shows air temperatures and wind at 14 o'clock. Cool spots are seen around river, large parks and sea shores. This implies that anthropogenic heat of building and emitted heat from urban materials are important in the formation of air temperatures in the daytime.

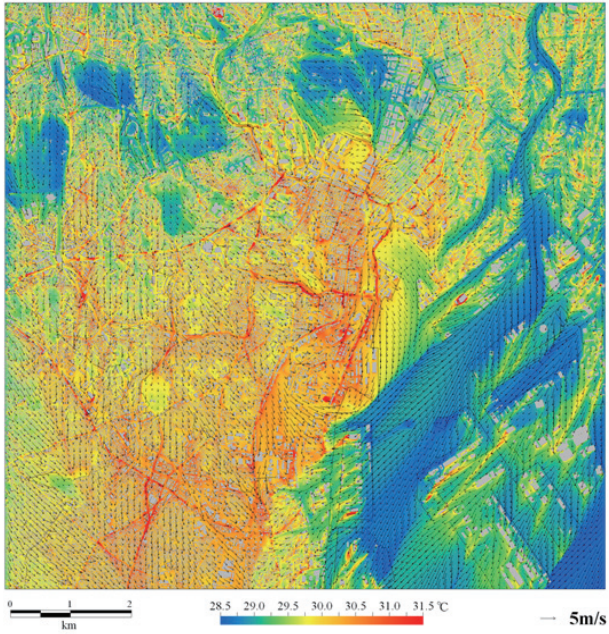


Fig. 5 Simulated air temperature and wind distribution (8:00, August 10, 2007).

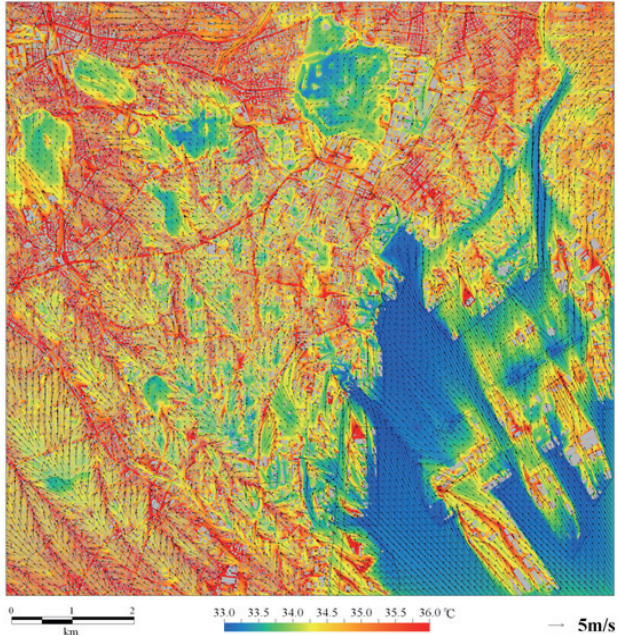


Fig. 6 Simulated air temperature and wind distribution (14:00, August 10, 2007).

References

- [1] Y. Ashie, Urban-scale CFD modeling in Tokyo, Urban climate news, Issue NO.41, International Association for Urban Climate, pp. 5-10, 2011.9.
- [2] Y. Ashie, T. Kono, and K. Takahashi, Computational fluid dynamics simulation of daytime and nighttime summer temperatures in 23 special wards of Tokyo, Annual report of the Earth Simulator Center April 2009 – March 2010, Earth Simulator Center (JAMSTEC), 2010.
- [3] M. Matheson and Y. Ashie, The effect of changes of urban surfaces on rainfall phenomenon as determined by a non-hydrostatic mesoscale model, Journal of the meteorological society of Japan 86-5: 733–751, 2008.
- [4] MLIT/MOE (Ministry of Land Infrastructure, Transport and Tourism, Ministry of the Environment), FY 2003 survey reports on heat-island countermeasures by controlling anthropogenic heat release in urban areas. Available from http://www.mlit.go.jp/sogoseisaku/heat_island/01.pdf, 2004 (in Japanese).

CFD による東京 10km 四方の夏季気温分布シミュレーション

プロジェクト責任者

足永 靖信 国土交通省国土技術政策総合研究所

著者

足永 靖信 国土交通省国土技術政策総合研究所

鍵屋 浩司 国土交通省国土技術政策総合研究所

河野 孝昭 金沢大学

筆者らは CFD（数値流体力学）により街路や建築物を解像可能な詳細なメッシュ分割でヒートアイランド現象を検討してきた。本報では、都心エリア 10km 四方（5m メッシュ）を対象にして夏季の時空間変動のシミュレーションを実施した結果を示す。CFD 解析に当たって、都心 10km 四方の建物高さ、土地利用、人工排熱等を 5m メッシュで整備した。各時刻において都市空間の 3 次元的な日陰形成についてデータベース化し、熱収支計算に反映した。日射ビームの入射角度と建物壁の向きに対応して日射量は変化し、壁や地盤の蓄熱を考慮した熱伝導解析を実施した。その結果、朝 8 時では幹線道路沿いが高温化していることが分かった。日射の影響がそれほど小さくなく、ラッシュアワーであるため交通由来の人工排熱量が顕著である。時間が進むと、このような局所的な高温化傾向は薄れていき、日中 14 時においては都市域は全体的に（面的に）高温化する傾向が見られた。

キーワード: ヒートアイランド, 東京, CFD, 気温

Study of Cloud and Precipitation Processes using a Global Cloud Resolving Model

Project Representative

Masaki Satoh

Research Institute for Global Change, Japan Agency for Marine-Earth Science and Technology
Atmosphere and Ocean Research Institute, The University of Tokyo

Authors

Masaki Satoh^{*1,2}, Hirofumi Tomita^{*1,3}, Tomoe Nasuno^{*1}, Akira T. Noda^{*1}, Shin-ichi Iga^{*1},
Hiroaki Miura^{*1,2}, Kazuyoshi Oouchi^{*1}, Hiroshi Taniguchi^{*1}, Yohei Yamada^{*1},
Wataru Yanase^{*2}, Chihiro Kodama^{*1}, Masayuki Hara^{*1}, Yasutaka Wakazuki^{*1},
Kazuaki Yasunaga^{*1}, Tatsuya Seiki^{*2}, Masanori Yoshizaki^{*1}, Masuo Nakano^{*1} and
Tomoki Miyakawa^{*2}

*1 Research Institute for Global Change, Japan Agency for Marine-Earth Science and Technology

*2 Atmosphere and Ocean Research Institute, The University of Tokyo

*3 Advanced Institute for Computational Science, RIKEN

The objective of this project is to better understand cloud and precipitation processes on the Earth and to improve these processes in climate models by resolving clouds on the whole globe. In the FY2011, three specific themes were pursued as the extension of the FY2010 research: (1) Evaluation of global cloud properties of the 3.5-km mesh Nonhydrostatic Icosahedral Atmospheric Model (NICAM) simulation outputs using a satellite simulator. A sensitivity experiment on cloud microphysical parameters was newly performed for this purpose, (2) Improvement of climatological properties of clouds and precipitation by implementation of a subgrid-scale convection scheme to NICAM. A series of sensitivity experiments showed reduction of the biases in surface precipitation over the Indian Ocean and the South Pacific Convergence Zone (SPCZ), and (3) An idealized experiment with an aquaplanet setup was extended to 160 model days. A slow eastward-propagating mode, resembling the Madden-Julian Oscillation (MJO), was obtained in the experiment. The importance of forcing by Walker circulation to the emergence of this slow mode was found. Preparatory simulations of recently observed prominent MJO events in the field program have also been started.

Keywords: cloud and precipitation processes, global cloud resolving model

1. Introduction

Understanding of cloud and precipitation processes based on latest observational products and numerical simulations are critical to reliable prediction of global climate change. Our research team has been developing a global cloud resolving model, Nonhydrostatic Icosahedral Atmospheric Model (NICAM, Satoh et al. 2008[1]), which is capable of calculating cloud and precipitation processes explicitly on the whole globe. NICAM has been run on the Earth Simulator to produce a number of research products (e.g., Tomita et al. 2005[2]; Iga et al. 2007[3]; Miura et al. 2007[4]; Oouchi et al. 2009[5]; Noda et al. 2010[6]; Yamada et al. 2010[7]). After the renewal of physical packages in the FY2009 (Satoh et al. 2010[8]), evaluations of simulated cloud and precipitation processes in comparison with in-situ observation and satellite data have been promoted in this project (Satoh et al. 2011[9]). In the FY2011, we have extended our research themes on the basis of the FY2010 achievements.

In this article, three major topics are reported in the following sections.

2. Evaluation of cloud properties in the global 3.5-km mesh simulation by J-simulator

Evaluation of the aerosol and clouds simulated with general circulation models (GCMs) and cloud resolving models is an important step toward reducing uncertainty associated with climate and weather prediction. One approach for the evaluation is to simulate the data that satellite would observe based on the atmospheric information simulated with the models. This study uses Joint Simulator for Satellite Sensors (J-simulator) that is being developed under Japan Aerospace Exploration Agency (JAXA) EarthCARE satellite project. The global 3.5-km mesh NICAM simulation data (the FY2010 products, Satoh et al. 2011 [9]) was evaluated against satellite data which was obtained from CloudSat 95 GHz radar and CALIPSO lidar.

In the FY2011, the joint Probability density functions (pdfs) of the signals and temperature (Contoured Frequency by tEmperature Diagram, CFED) were constructed with three different cloud masks that use radar, lidar and both of them, from observed and simulated signals (Fig. 1). The use of temperature as a substitute for altitude gives insights on cloud microphysical processes. NICAM tends to have fewer occurrences of clouds defined with radar mask less than -45°C level, more concentrated reflectivity, and larger reflectivity than observation. On the other hand, the lidar signal indicates more cloud occurrences above -50°C and two modes existing in $T < -40^{\circ}\text{C}$. The portions of the CFEDs are easily related to hydrometeor categories by turning on/off each contribution in J-simulator. Furthermore, the use of radar and lidar signals for a given volume enables us to evaluate the water content and effective radius qualitatively against observation. For example, the water content (effective radius) of snow category was shown less (larger) than the observations.

Based on the assessment of cloud microphysical properties in the NICAM simulation, a global 3.5-km mesh sensitivity experiment was conducted in the FY2011, where the fall speed of cloud ice was decreased to a more realistic value,

and autoconversion rate of cloud ice to snow was accelerated based on the sensitivity study using the 14-km mesh NICAM (Satoh et al. 2011[9]). The sensitivity run was initialized in the same way as the control run and integrated for a three-day period. Figure 2 compares the latitude-height sections of zonally averaged ice condensates in the control and sensitivity runs. As expected, mass of ice condensates of all categories are reduced in the sensitivity run. The CFEDs of the sensitivity run were also evaluated. The slower sedimentation and faster snow growth led to less overlapping areas of radar and lidar signals than the control (not shown). Comparison between observed and simulated IR and evaluation of the lidar CFED suggest excessive amount of cloud ice mass mixing ratio at higher altitude than the control case. This can be related to higher amount of cloud ice above 200 hPa in the sensitivity run than the control case (Fig. 2). In a general sense, no obvious difference in water content and effective radius was indicated in terms of the radar-lidar signal diagnosis.

The direct comparison of cloud microphysical outputs, such as mass mixing ratio and effective radius, between the control and the sensitivity run gives further supporting information. In conclusion, the forward approach with J-simulator is effective to

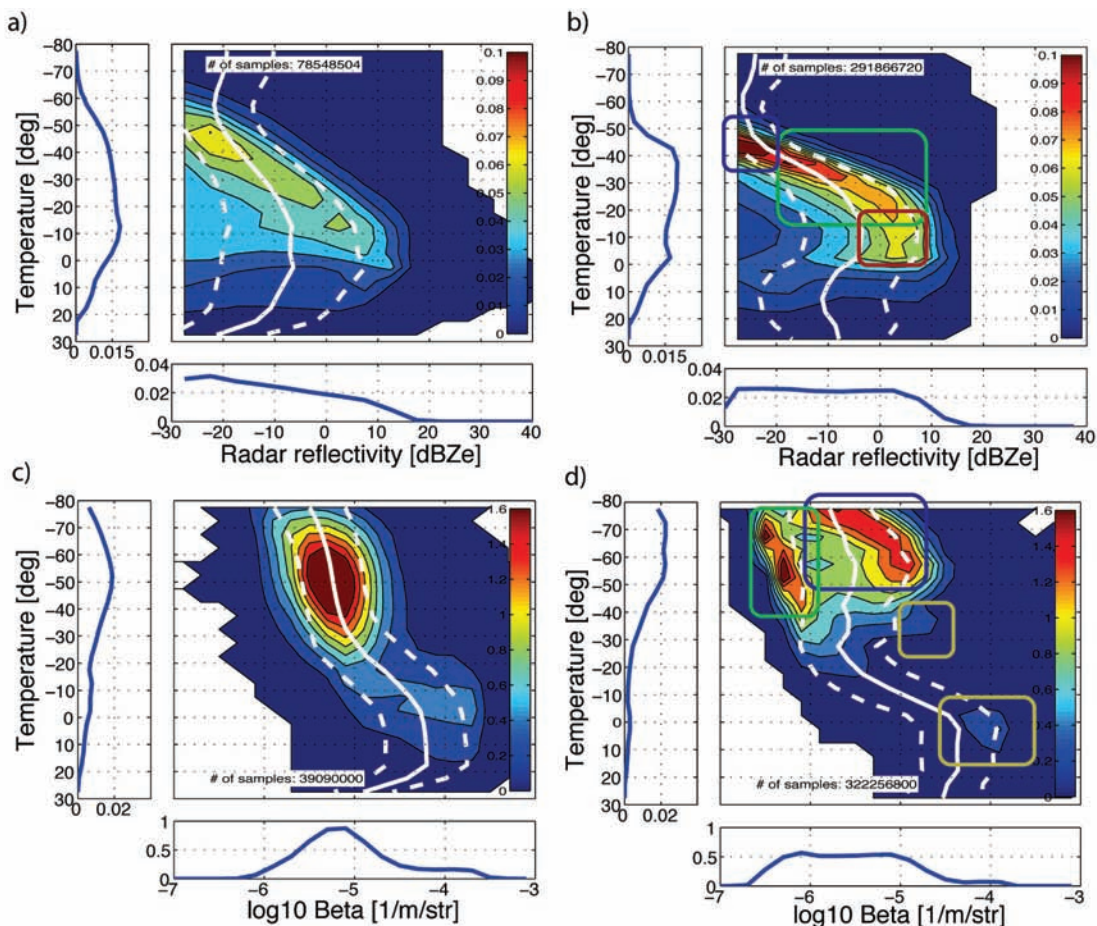


Fig. 1 CFED for 94 GHz radar reflectivity with C1 and 532 nm lidar backscattering with C2. a) and c) are the observation; b) and d) the NICAM simulation. The colorfill shows 100 times of the joint pdf. The white solid curves are the mean, and white broken lines are the mean plus or minus the standard deviation. The marginal pdfs in terms of radar reflectivity and temperature are shown in the bottom and left panel, respectively. The blue, green, red, and yellow round rectangles show the major contributions from cloud ice, snow, graupel, and cloud droplets, respectively. (courtesy of Dr. Tempei Hashino).

evaluate the NICAM simulation.

3. Toward the reduction of precipitation biases in high-resolution simulations

Small-scale convection can hardly be resolved at a horizontal grid size larger than the order of 1 km, although it plays an important role for vertical transport of heat, moisture, and momentum in the tropics. We introduced a cumulus parameterization scheme (Chikira scheme, Chikira

and Sugiyama 2010[10]), aiming at a better representation of the effects of such subgrid-scale convection along with improving model climatology (e.g., the spatial characteristics) of precipitation in a few kilometer mesh NICAM.

In the first place, we conducted a test simulation using the same parameter setting as in the latest version of Model for Interdisciplinary Research on Climate (MIROC) (Fig. 3). The inclusion of the parameterization reduces excessive precipitation over the Indian Ocean. The parameterization acts

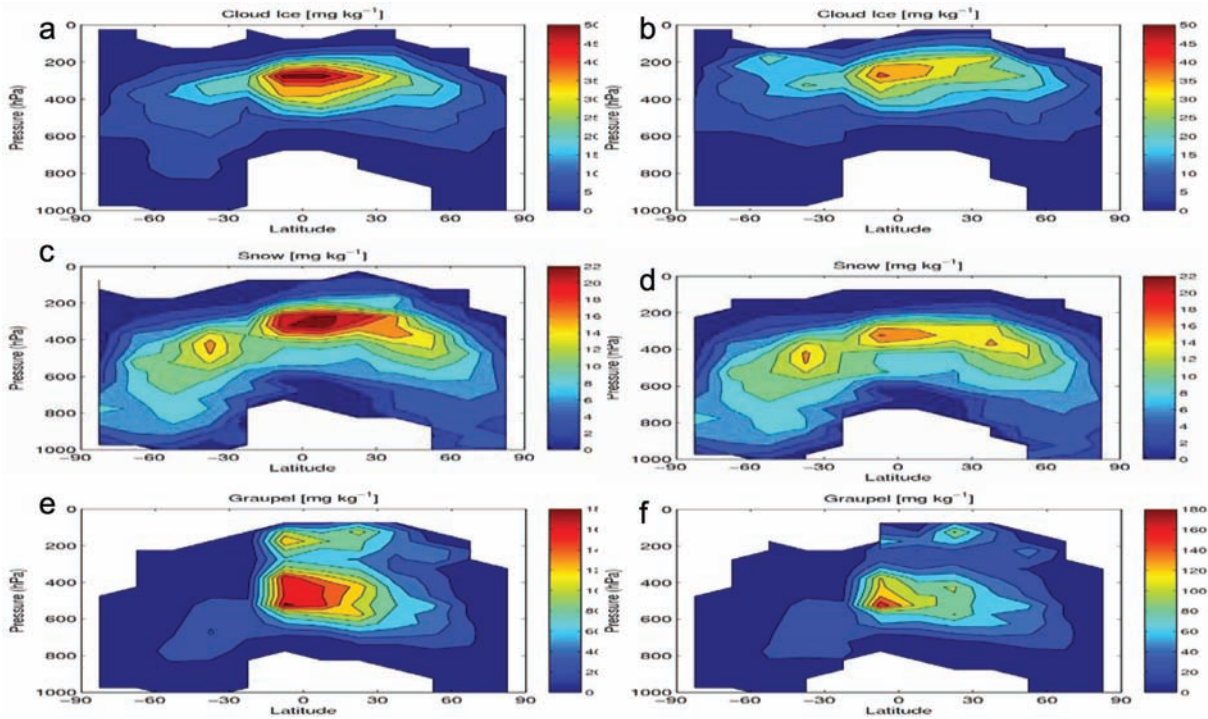


Fig. 2 Latitude-height sections of zonally averaged (a) (b) cloud ice, (c) (d) snow, (e) (f) graupel content (10^6 kg kg^{-1}) for the control run (left panels) and the sensitivity run (right panels) of the global 3.5-km mesh NICAM simulation outputs. The grid points with condensates exceeding $0.2 \times 10^6 \text{ kg kg}^{-1}$ are considered. (courtesy of Dr. Tempei Hashino).

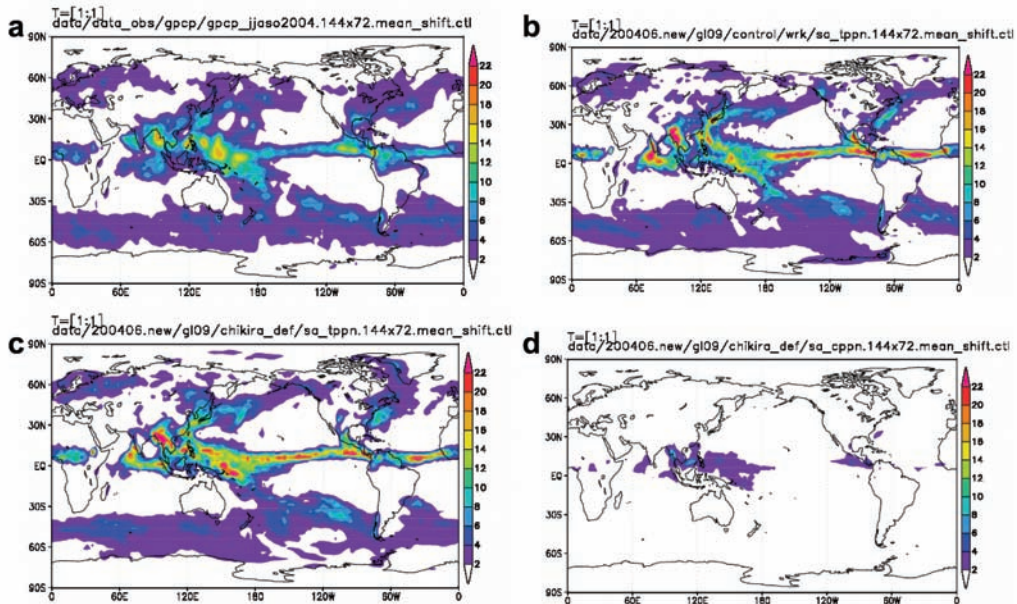


Fig. 3 Comparison of surface precipitation (mm dy^{-1}) of (a) GPCP data and (b)-(d) 14-km mesh NICAM simulations during June 2004. (b) shows the total amount of surface precipitation without the Chikira scheme. (c) and (d) show the total amount of surface precipitation and the contribution by the Chikira scheme, respectively.

to produce surface precipitation especially over the western and eastern parts of the Pacific Ocean in the tropics, although their amplitudes are much smaller than the total surface precipitation.

We also conducted a set of sensitivity experiments regarding unknown parameters of the scheme. The parameters chosen are the ones determining the vertical distribution of subgrid-scale in-cloud vertical velocity (a and C_ϵ of Eq. 4 in Chikira and Sugiyama 2010[10]). The changes of the parameters within a realistic fluctuation range affect the detailed changes of surface precipitation such as its intensity over the SPCZ (Fig. 4). Subsequent sensitivity studies about possible parameters to further reduce the model precipitation biases have been continuing.

4. Aquaplanet experiments

Over the tropics, two types of precipitation systems (PSs), super clusters (SCs) and Madden-Julian Oscillation (MJO), are

frequently observed, having similar symmetric structures about the equator but different eastward-propagating (EP) speeds. In this project, a series of aquaplanet experiments has been conducted to gain insight into these basic regimes of organized clouds and precipitation in the tropics.

Yoshizaki et al. (2012a[11]), focusing on the reasons why these PSs exist, examined the dependence of the longitudinal variations of sea surface temperature (SST) using NICAM with an aquaplanet setups (Fig. 5). Here, a component, A , is written as $\langle A \rangle$ when it is longitudinally averaged, and as A_b when it is temporally averaged. Then, the Hadley circulation (HC) is defined as $\langle A_b \rangle$, and the Walker circulation (WC) as $A_b - \langle A_b \rangle$. In a longitudinally uniform-SST case, only SC-like fast-EP PSs appeared (Fig. 5a). When the longitudinal variation of the SST was increased (Fig. 5c), on the other hand, a stationary WC emerged and MJO-like slowly EP PSs occurred on the western part of a high-SST area. It is expected in the real atmosphere

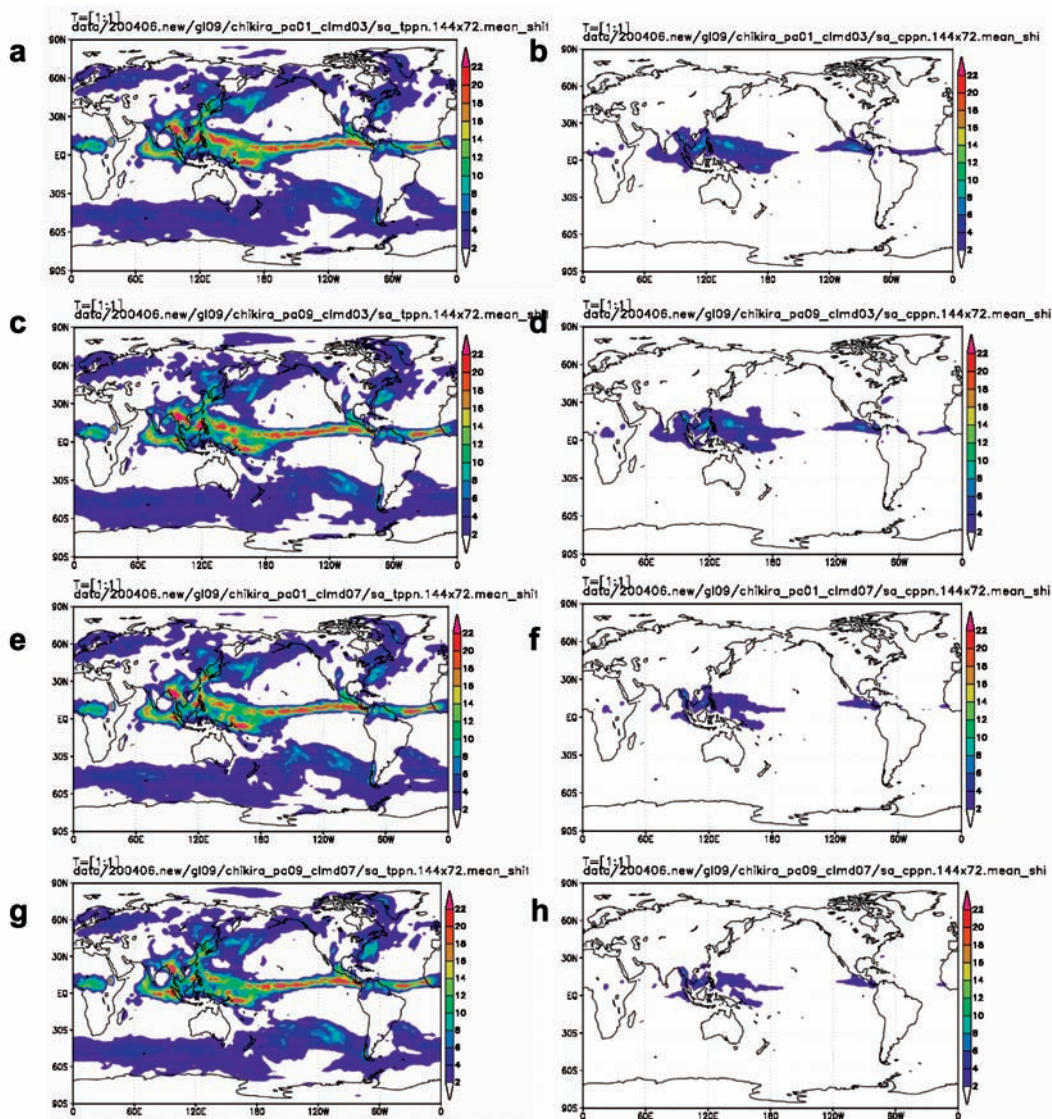


Fig. 4 Sensitivity of parameters (a and C_ϵ) in the Chikira scheme to surface precipitation (mm dy^{-1}) during June 2004 using the 14-km mesh NICAM. (a) and (b) are the total amount of surface precipitation and the contribution by the Chikira scheme, respectively, using $a=0.1$ and $C_\epsilon=0.3$. (c) and (d) are the same as (a) and (b), except using $a=0.9$ and $C_\epsilon=0.3$. (e) and (f) are the same as (a) and (b), except using $a=0.1$ and $C_\epsilon=0.7$. (g) and (h) are the same as (a) and (b), except using $a=0.9$ and $C_\epsilon=0.7$.

that two different types of EP PSs can simultaneously exist due to complex surface conditions: 1) SCs as free PSs and 2) MJOs as forced PSs. Here, free (forced) PSs mean convection, which is uncontrolled (controlled) by the longitudinal variation

of the SST. Owing to the WC (Fig. 6), combined with the HC, the MJO was generated and decayed locally, and westward-propagating PSs were dominantly observed in the subsidence areas of the WC.

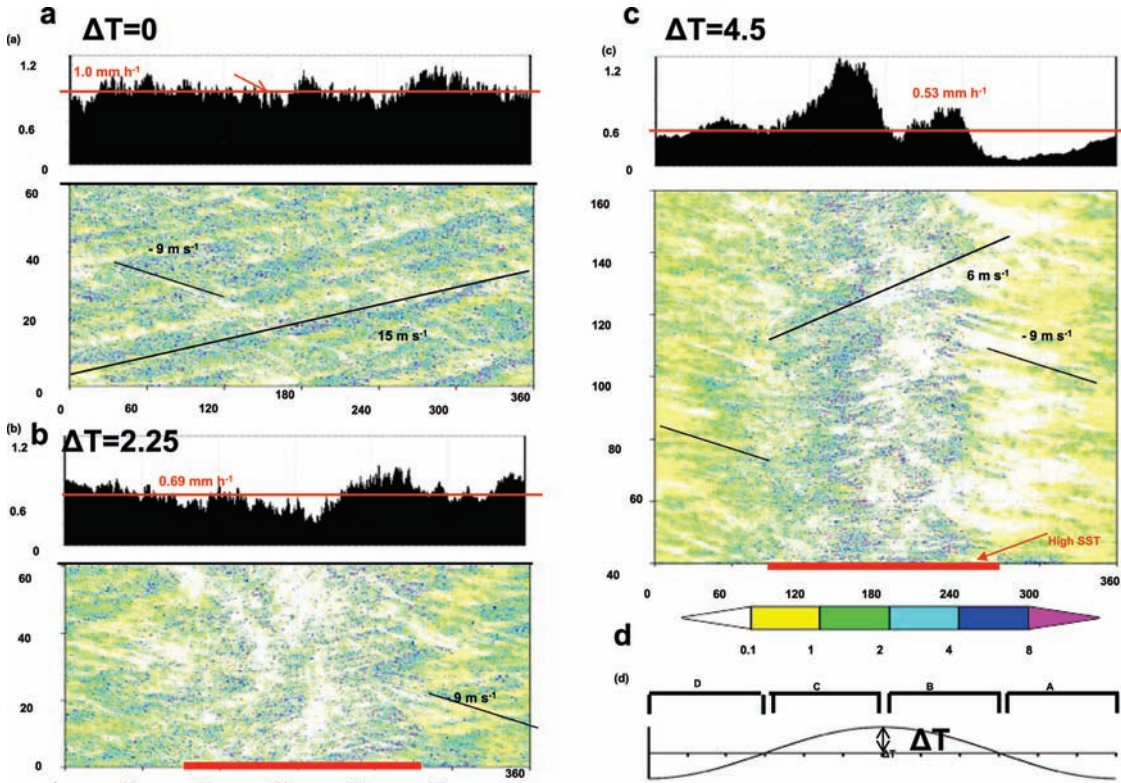


Fig. 5 Time-mean distributions and longitude–time sections of surface precipitation (mm h⁻¹) averaged between 3°S and 3°N for (a) $\Delta T = 0$, (b) $\Delta T = 2.25$, and (c) $\Delta T = 4.5$ cases. (d) Zonal distribution of the SST variation. The figure is adopted from Fig. 2 of Yoshizaki et al. 2012a.

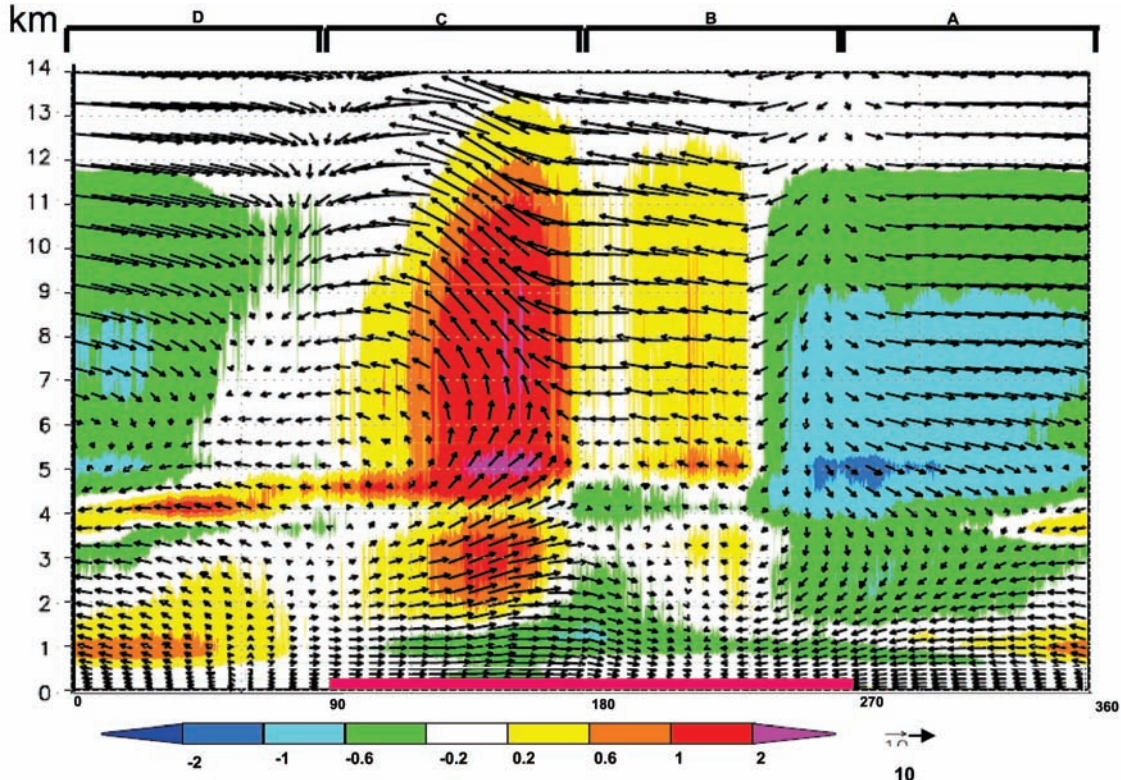


Fig. 6 Longitude – height distribution of the Walker circulation (WC) averaged between 3°S and 3°N for the $\Delta T = 4.5$ case. Wind vectors and a color bar denote $(u, 400w)$ and diabatic heating, respectively. A red line between 90°–270° longitude denotes the high-SST area. The figure is adopted from Fig. 5b of Yoshizaki et al. 2012a.

Yoshizaki et al. (2012b[12]) also studied PSs in coarse resolution simulations. An EP property of the PSs appeared even with the horizontal resolution as coarse as 112 km, so long as the vertical stratification was kept conditionally unstable. The appearance or disappearance of the EP property is explained by comparing mesoscale (100 km) and large-scale (1,000 km) PSs, a non-precipitation system (NPS), and a precipitation system simulated by a dry model (DP) with positive-only wave Conditional Instability of the Second Kind (CISK) heating. By assuming that the height and the updraft intensity of convection are common in these systems, the turnover times of representative convections were estimated. Compared with the time scale of the equatorial beta (T_β), where its effect essentially works and the distinct EP property appears, the turnover times of the large-scale PS and DP were longer than T_β , producing the EP property, whereas those of the NPS and mesoscale PSs were shorter, inducing no EP property. These results are consistent with previous studies based on observations and numerical experiments (Nakazawa 1988[13]; Nasuno et al. 2007[14]).

5. Summary

The goal of this research project is to evaluate cloud and precipitation processes in the global cloud resolving model NICAM and to improve the physical processes in the model. The key issues are: (1) evaluation of the high-resolution simulation results using in-situ and satellite observations, (2) improvement of the model physics in perspective of reliable future climate prediction, and (3) basic understanding of multi-scale mechanisms of organized clouds and precipitation in the tropics. In the FY2011 we investigated these subjects.

The cloud microphysical properties of the global 3.5-km simulation outputs were evaluated in close comparison with satellite data using the J-simulator, which have been developed in the JAXA EarthCARE project (to be launched in 2014). The evaluation by a new analysis method, CFEDs, revealed several conspicuous biases of ice species in NICAM simulation. Sensitivity experiments showed that the total mass of ice condensates can be controlled by properly setting fall speed and autoconversion rate of ice clouds, but cloud microphysical properties (e.g., effective radius) were generally unaltered. The usefulness of this kind of analysis in evaluating the simulation results is confirmed. Improvement of climatological properties of clouds and precipitation is also indispensable to next generation GCMs. The importance of shallow clouds and boundary layer processes, which cannot be resolved by a few kilometer mesh sizes, is increasingly recognized. With this perspective, a subgrid-scale convection scheme (Chikira and Sugiyama 2010[10]) was implemented to NICAM. A series of sensitivity experiments indicated reduction of the biases over the Indian Ocean and SPCZ. Further investigation is in progress. The understanding of basic modes of convective organization in the tropics helps us interpret the simulated clouds and precipitations.

The results from a series of aquaplanet experiments revealed the importance of zonal circulation in the equatorial region (Walker circulation), which is forced by zonal variation of SST (and by land mass distribution in the real atmosphere), to the emergence of slow eastward propagating mode of convection. This mode resembles MJO, and is distinctly different from another typical type of tropical convective disturbance; the fast eastward-propagating 'free' mode.

We have also started a new research subject, namely, understanding of cloud and precipitation in the recently observed MJO events. Preparatory simulations of prominent MJO events which occurred during a field campaign CINDY2011 / DYNAMO (intensive observation period: October 2011 - January 2012) and those during the YOTC period (October 2009 - January 2010 events) have been in progress. This theme will be pursued in the FY2012.

CINDY2011: Cooperative Indian Ocean experiment on interseasonal variability in the year 2011 (http://www.jamstec.go.jp/iorgc/cindy/index_e.html)

DYNAMO: Dynamics of the Madden-Julian Oscillation (<http://www.eol.ucar.edu/projects/dynamo/>)

YOTC: Year of Tropical Convection (<http://www.ucar.edu/yotc/index.html>)

Acknowledgements

Analysis using J-Simulator is conducted by Dr. Tempei Hashino in Atmosphere and Ocean Research Institute / The University of Tokyo as collaborative study with JAXA. ECMWF YOTC operational analysis data is used for the initialization of the global 3.5-km mesh simulation.

References

- [1] Satoh, M. T. Matsuno, H. Tomita, H. Miura, T. Nasuno, and S.-I. Iga, "Nonhydrostatic Icosahedral Atmospheric Model (NICAM) for global cloud resolving simulations," *J. Comput. Phys.*, doi:10.1016/j.jcp. 2007.02.006, the special issue on Predicting Weather, Climate and Extreme events. 2008.
- [2] Tomita, H., H. Miura, S.-I. Iga, T. Nasuno, and M. Satoh, "A global cloud-resolving simulation: Preliminary results from an aqua planet experiment," *Geophys. Res. Lett.*, 32, L08805, doi:10.1029/2005GL022459, 2005.
- [3] Iga, S.-I., H. Tomita, Y. Tsushima, and M. Satoh, "Climatology of a nonhydrostatic global model with explicit cloud processes," *Geophys. Res. Lett.*, 34, L22814, doi:10.1029/2007GL031048, 2007.
- [4] Miura, H., M. Satoh, T. Nasuno, A. T. Noda, and K. Oouchi, "A Madden-Julian Oscillation event realistically simulated by a global cloud-resolving model," *Science*, 318, 1763-1765, 2007.
- [5] Oouchi, K., A. T. Noda, M. Satoh, H. Miura, H. Tomita,

- T. Nasuno, and S.-I. Iga, "A simulated preconditioning of typhoon genesis controlled by a boreal summer Madden-Julian Oscillation event in a global cloud-system-resolving model," *SOLA*, 5, 65-68, doi:10.2151/sola.2009-017, 2009.
- [6] Noda, A. T., K. Oouchi, M. Satoh, H. Tomita, S.-I. Iga, and Y. Tsushima, "Importance of the subgrid-scale turbulent moist process: Cloud distribution in global cloud-resolving simulations," *Atmos. Res.*, 96, 208-217, doi: 10.1016/j.atmosres.2009, 2010.
- [7] Yamada, Y., K. Oouchi, M. Satoh, H. Tomita, and W. Yanase, "Projection of changes in tropical cyclone activity and cloud height due to greenhouse warming: Global cloud-system-resolving approach," *Geophys. Res. Lett.*, 37, doi:10.1029/2010GL042518, 2010.
- [8] Satoh, M., H. Tomita, T. Nasuno, A. T. Noda, S.-I. Iga, H. Miura, K. Oouchi, H. Taniguchi, Y. Yamada, W. Yanase, C. Kodama, M. Hara, Y. Wakazuki, K. Yasunaga, and T. Seiki, "Study of cloud and precipitation processes using a global cloud-system resolving model," *Annual Report of the Earth Simulator Center*, April 2009-March 2010, 49-53, 2010.
- [9] Satoh, M., H. Tomita, T. Nasuno, A. T. Noda, S.-I. Iga, H. Miura, K. Oouchi, H. Taniguchi, Y. Yamada, W. Yanase, C. Kodama, M. Hara, Y. Wakazuki, K. Yasunaga, T. Seiki, and M. Yoshizaki, "Study of cloud and precipitation processes using a global cloud-system resolving model," *Annual Report of the Earth Simulator Center*, April 2010-March 2011, 43-49, 2011.
- [10] Chikira, M. and M. Sugiyama, "A Cumulus Parameterization with State-Dependent Entrainment Rate. Part I: Description and Sensitivity to Temperature and Humidity Profiles," *J. Atmos. Sci.*, 67, 2171-2193, 2010.
- [11] Yoshizaki, M., K. Yasunaga, S.-I. Iga, M. Satoh, T. Nasuno, A. T. Noda, and H. Tomita, "Why do super clusters and Madden Julian Oscillation exist over the equatorial region?" *SOLA*, 8, 33-36, doi:10.2151/sola.2012-009, 2012a.
- [12] Yoshizaki, M., S.-I. Iga, and M. Satoh, "Eastward propagating property of large-scale precipitation systems simulated in the coarse-resolution NICAM and an explanation of its formation," *SOLA*, 8, 21-24, doi:10.2151/sola.2012-006, 2012b.
- [13] Nakazawa, T., "Tropical super clusters within intraseasonal variations over the western Pacific," *J. Meteor. Soc. Japan*, 66, 823-839, 1988.
- [14] Nasuno, T., H. Tomita, S.-I. Iga, H. Miura, and M. Satoh, "Multiscale organization of convection simulated with explicit cloud processes on an aquaplanet," *J. Atmos. Sci.*, 64, 1902-1921, 2007.

全球雲解像モデルを用いた雲降水プロセス研究

プロジェクト責任者

佐藤 正樹 海洋研究開発機構 地球環境変動領域

東京大学 大気海洋研究所

著者

佐藤 正樹^{*1,2}, 富田 浩文^{*1,3}, 那須野智江^{*1}, 野田 暁^{*1}, 伊賀 晋一^{*1}, 三浦 裕亮^{*1,2},
大内 和良^{*1}, 谷口 博^{*1}, 山田 洋平^{*1}, 柳瀬 亘^{*2}, 小玉 知央^{*1}, 原 政之^{*1},
若月 泰孝^{*1}, 安永 数明^{*1}, 清木 達也^{*2}, 吉崎 正憲^{*1}, 中野満寿男^{*1}, 宮川 知己^{*2}

*1 海洋研究開発機構 地球環境変動領域

*2 東京大学 大気海洋研究所

*3 理化学研究所 計算科学研究機構

本プロジェクトは地球上の雲降水プロセスの理解を深め、全球雲システム解像モデルでのこれらのプロセスを改善することを目的とする。今年度は以下の3つの課題を実施した。(1) 全球雲解像モデル NICAM を用いた 3.5 km 格子計算における雲微物理特性について衛星シミュレータを用いた評価を行った。この目的のため、雲微物理パラメタに関する感度実験も新たに行った。(2) 雲降水の気候学的特性を改善するため NICAM にサブグリッド対流スキームを導入し、感度計算を行った。その結果、インド洋や南太平洋取東帯の地表降水において改善が見られた。(3) 水惑星数値実験を160日まで延長し、マッデン・ジュリアン振動 (MJO) に類似する遅い東進速度をもつ対流モードを得た。この遅いモードの発現におけるウォーカー循環の重要性が分かった。近年の観測プロジェクト期間中に発生した MJO 事例を対象とする予備計算も開始した。

キーワード: 雲降水プロセス, 全球雲解像モデル

Process Studies and Seasonal Prediction Experiment using Coupled General Circulation Model

Project Representative

Yukio Masumoto

Research Institute for Global Change, Japan Agency for Marine-Earth Science and Technology

Authors

Swadhin Behera^{*1,2}, Jing-Jia Luo^{*1,2}, Wataru Sasaki^{*2}, Hirofumi Sakuma^{*1,2}, Sebastien Masson^{*4}, Antonio Navarra^{*3}, Silvio Gualdi^{*3}, Simona Masina^{*3}, Alessio Bellucci^{*3}, Annalisa Cherchi^{*3}, Pascal Delecluse^{*5}, Gurvan Madec^{*4}, Claire Levy^{*4}, Marie-Alice Foujols^{*4}, Arnaud Caubel^{*4}, Guy Brasseur^{*6}, Erich Roeckner^{*6}, Marco Giorgetta^{*6}, Luis Kornbluh^{*6}, Monika Esch^{*6}, Toshio Yamagata^{*2} and Yukio Masumoto^{*1}

*1 Research Institute for Global Change, Japan Agency for Marine-Earth Science and Technology

*2 Application Laboratory, Japan Agency for Marine-Earth Science and Technology

*3 Centro Euro-Mediterraneo per i Cambiamenti Climatici, INGV

*4 Laboratoire D'oceanographie et du Climat (LOCEAN)

*5 Meteo France

*6 Max Planck Institute for Meteorology

The SINTEX-Frontier coupled ocean-atmosphere GCM is developed under the EU-Japan collaborative framework to study the variability in global climate and its predictability. The SINTEX-F model is used to produce real-time seasonal climate forecasts in addition to long-term simulations and sensitivity experiments used in climate variation studies. SINTEX-F has successfully predicted recent Indian Ocean Dipole (IOD), El Niño-Southern Oscillation (ENSO) and ENSO Modoki events. The most recent one is the prediction of the return of a La Niña condition in the later half of 2011 after a slight warming in the eastern Pacific in the middle of the year. The model is consistent in its predictions of IOD and ENSO events to maintain its leading position for the seasonal climate predictions in the world. In addition to the tropical Indian and Pacific Ocean conditions, the model has shown excellent skills in the prediction of subtropical Indian and Atlantic Ocean dipoles. Based on the retrospective forecasts, it is demonstrated in a recent study that the subtropical Indian Ocean dipole and the southern subtropical Atlantic Ocean dipole are predictable at least a couple of seasons ahead with good accuracy.

In addition to the real-time predictions, the model is used in sensitivity experiments to understand climate processes. In one such study, using the long simulation results, it is corroborated that the ocean mixed-layer plays an important role in the formation of subtropical dipoles. The high-resolution version of the model known as the SINTEX-F2 is able to simulate the frequency and the genesis bands of tropical cyclones accurately in the global oceans.

Keywords: SINTEX-F, El Niño Modoki, La Niña, Prediction, 2011

1. INTRODUCTION

The SINTEX-F1 coupled general circulation model (CGCM) has emerged as the leading CGCM in the world to provide real-time predictions of seasonal to interannual climate variations. The model has successfully predicted all past El Niño-Southern Oscillation (ENSO) and Indian Ocean Dipole (IOD) events. In a recent study, it is also shown that the model is capable of predicting the ENSO Modoki, which is recently identified as one of the leading modes of variability in the tropical Pacific. In addition to the good predictions at long lead times, the realistic simulation results of SINTEX-F1 are helpful in understanding

the processes associated with climate phenomena. Besides the climate variations in the tropical regions, the model results are useful in understanding the slow processes in higher latitudes. The high-resolution version of the model, the SINTEX-F2, is under development and the model results are expected to help in understanding of finer scale climate processes.

2. CLIMATE PREDICTIONS

The real time climate forecasts for 12-24 lead months are continuously performed and updated every month. Unlike the model predictions from several other climate centers, which

predicted a return of El Niño in 2011, JAMSTEC's SINTEX-F1 model has correctly predicted the return of the La Niña (Fig. 1) after a brief period of La Niña Modoki condition in which the eastern Pacific became warmer than normal around the middle of 2011. The model has been consistent in predicting all of the recent IOD and ENSO events to become the leading prediction model in the world. Because of this, the 2011 La Niña predictions by SINTEX-F were widely reported in various newspapers in Japan, Australia, India and several other Southeast Asian countries. In addition, the forecast results are distributed to many research scientists and operational forecast centers (e.g. IRI, APCC, CLIVAR, IIT) and made available to general public through the JAMSTEC website. Some of the Australian farmers have developed best agricultural practices for their regions based on SINTEX-F1 predictions.

The seasonal to interannual predictability of subtropical dipoles in southern Indian (IOSD) and Atlantic (AOSD) Oceans are found to be very promising in the SINTEX-F1 retrospective forecasts. From a recent study (Yuan et al. 2011[14]), it is found that the subtropical dipoles in those two basins can be predicted at least a couple of seasons ahead with very high reliability. The

overall prediction skills of the IOSD are found to be higher than that of the SASD and a prediction barrier is found in austral autumn for both IOSD and the SASD. Also the predictability of SST anomalies in the northeastern pole of the IOSD is higher than the southwestern pole, whereas no large difference is found in that for the two poles of the SASD. Some of the other studies evaluated the model predictability for ENSO, monsoon, intraseasonal oscillations and interactions among those climate modes (An et al. 2011[1]; Hsu et al. 2011[2]; Jeong et al. 2011[3]; Joseph et al. 2011[4]; Kulkarni et al. 2011[5]; Li et al. 2011[6]; Lin et al. 2011[7]; Luo 2011[8]; Luo et al. 2011[9]; Masson et al. 2011[10]; Terray et al. 2011[13]).

3. PROCESS STUDIES

Interannual variations of subtropical dipole modes are also investigated using SINTEX-F1 results (Morioka et al. 2011[11]). The positive (negative) SST anomaly pole starts to grow in austral spring and reaches its peak in February. From the analysis it is found that the suppressed (enhanced) latent heat flux associated with the variations in the subtropical high causes a thinner (thicker) than normal mixed-layer thickness,

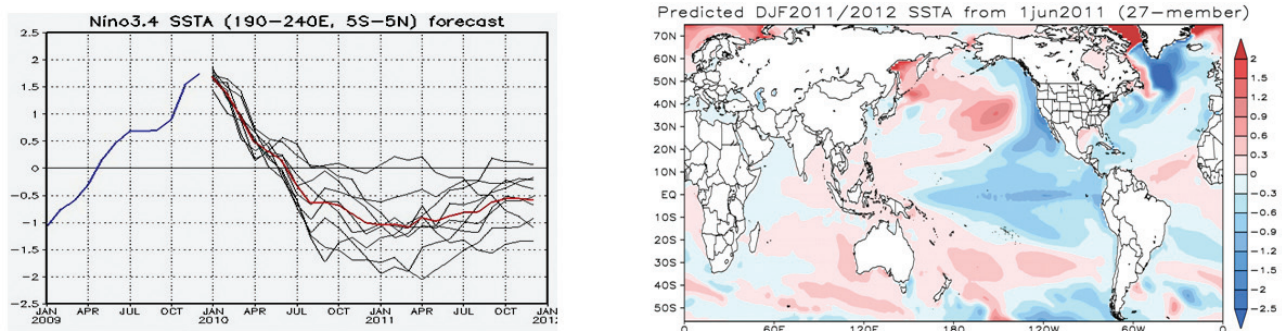


Fig. 1 SINTEX-F real-time prediction of the return of the La Niña state in winter of 2011 from 1 June 2011 initial conditions.

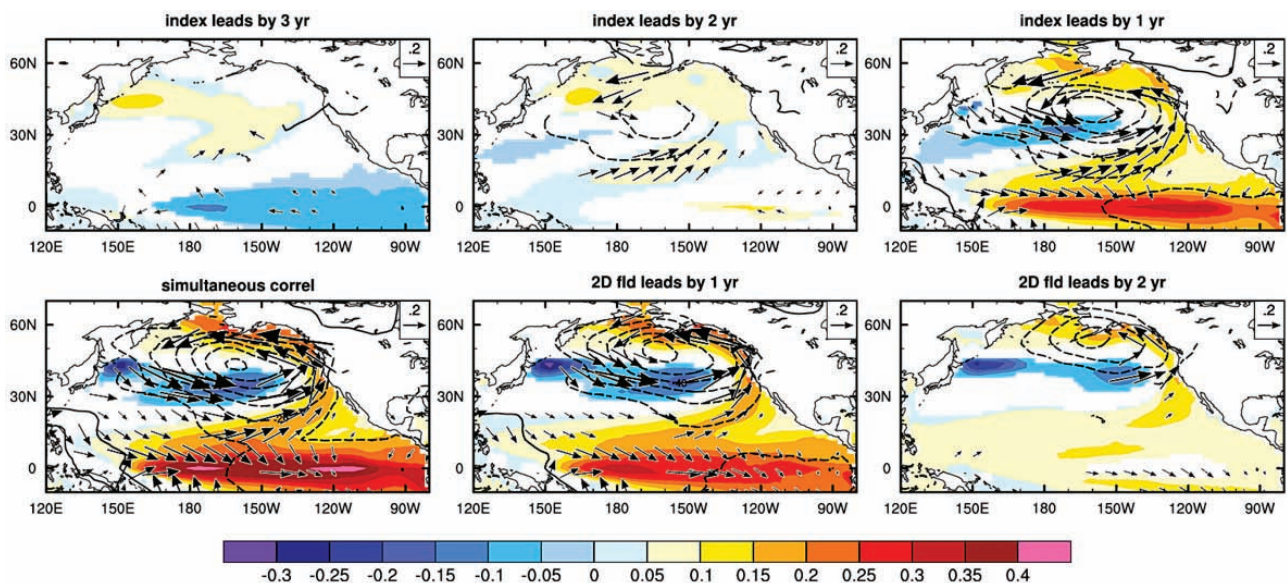


Fig. 2 Regression of SST (shading) and surface wind stress on normalized Nino-3 index at different lead and lag times as indicated in the titles of each plot.

which, in turn, enhances (reduces) the warming of the mixed layer by the seasonal shortwave radiation in austral late spring. The positive (negative) pole gradually decays in austral fall, because the mixed-layer cooling by the entrainment is enhanced (reduced) mostly owing to the larger (smaller) temperature difference between the mixed layer and the entrained water. The increased (decreased) latent heat loss due to the warmer (colder) SST also contributes to the decay of the positive (negative) pole.

In another study, it is found that the low-frequency variations in the Kuroshio Extension region off Japan are modulated by the teleconnection arising from the decadal variations in ENSO (Fig. 2). The two phases of ENSO variability give rise to different patterns of the teleconnection in the midlatitude regions of northern Pacific. This in turn induces decadal variations in the Kuroshio Extension region.

4. SINTEX-F2 DEVELOPMENT

The simulation results from the high-resolution version of the SINTEX-F2 (63×63km atmosphere coupled to 25×25km ocean) are examined in terms of the reproducibility of the northern hemisphere tropical cyclone (TC) activity as well as the associated large-scale environmental conditions (Sasaki et al. 2011[12]). The high-resolution SINTEX-F2 successfully simulates the realistic TC structure, TC-induced ocean response, and TC genesis frequency. Compared to the results of the original medium-resolution model, with atmospheric resolution of 125×125km, the global TC genesis frequency and TC intensities simulated by the SINTEX-F2 are much closer to that of the observed (Fig. 3). It is also found that the high-resolution SINTEX-F2 reasonably reproduces the environmental conditions favorable for the TC genesis; warm sea surface temperature, low-level cyclonic circulation, weak vertical wind shear, and high relative humidity in the mid-troposphere.

Acknowledgement

We appreciate the support extended by the Earth Simulator in achieving our project goals.

References

- [1] An, Z., S. Clemens, J. Shen, X. Qiang, Z. Jin, Y. Sun, W. Prell, J.-J. Luo, S. Wang, H. Xu, Y. Cai, W. Zhou, W. Liu, Z. Shi, L. Yan, X. Xiao, H. Chang, F. Wu, L. Ai, and F. Lu, 2011: Glacial-interglacial Indian summer monsoon dynamics. *Science*, 333, 719-723.
- [2] Hsu, P.-C., T. Li, J.-J. Luo, H. Murakami, A. Kitoh, and M. Zhao, 2011: Increase of global monsoon area and precipitation under global warming: Is it a robust signal? *Nature*, submitted.
- [3] Jeong, H.-I., D. Y. Lee, K. Ashok, J.-B. Ahn, J.-Y. Lee, J.-J. Luo, J.-K. E. Schemm, H. Hendon, K. Braganza, and Y.-G. Ham, 2011: Assessment of the APCC coupled MME suite in predicting the distinctive climate impacts of two flavors of ENSO during boreal winter. *Climate Dynamics*, submitted.
- [4] Joseph, S., A. K. Sahai, B. N. Goswami, P. Terray, S. Masson, and J.-J. Luo, 2011: Possible role of warm SST bias in the simulation of boreal summer monsoon in SINTEX-F2 coupled model. *Climate Dynamics*, revised.
- [5] Kulkarni, M. A., N. Acharya, U. C. Mohanty, A. W. Robertson, J.-J. Luo, and T. Yamagata, 2011: Probabilistic prediction of Indian Summer Monsoon rainfall using global climate models. *Theoretical and Applied Climatology*, accepted.
- [6] Li, S., H. H. Hendon, S. Alves, J.-J. Luo, M. Balmaseda, and D. Anderson, 2011: How predictable is the Indian Ocean Dipole? *Mon. Wea. Rev.*, submitted.
- [7] Lin, A., T. Li, X. Fu, J.-J. Luo, and Y. Masumoto, 2011: Effects of air-sea coupling on the boreal summer intraseasonal oscillations over the tropical Indian Ocean. *Climate Dynamics*, 37, 2303-2322, DOI 10.1007/s00382-010-0943-7.
- [8] Luo, J.-J., 2011: Ocean dynamics not required? *Nature*, 477, 544-546.
- [9] Luo, J.-J., W. Sasaki, and Y. Masumoto, 2011: Indian Ocean warming modulates Pacific climate change. *Nature Climate Change*, under review.
- [10] Masson, S., P. Terray, G. Madec, J.-J. Luo, T. Yamagata, and K. Takahashi, 2011: Impact of intra-daily SST

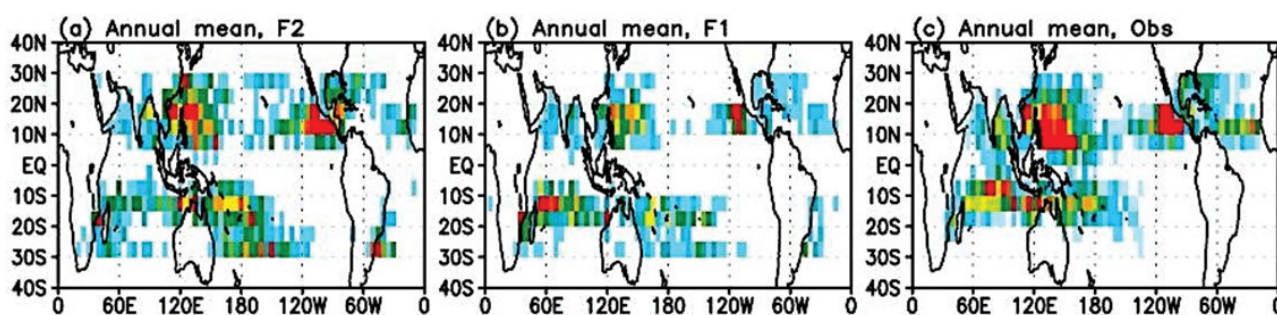


Fig. 3 SINTEX-F simulated tropical cyclone genesis regions in the tropical oceans for a) SINTEX-F2 model simulation, b) SINTEX-F1 simulation and c) observations.

variability on ENSO characteristics in a coupled model. *Climate Dynamics*, submitted.

- [11] Morioka Y., T. Tozuka, S. Masson, P. Terray, J.-J. Luo, and T. Yamagata, 2011: Subtropical dipole modes simulated in a coupled general circulation model. *J. Climate* (in press).
- [12] Sasaki, W., J.-J. Luo, and S. Masson, 2011: Tropical cyclone simulation in a high-resolution atmosphere-ocean coupled general circulation model. *Cyclones: Formation, Triggers and Control*, edited by K. Oouchi, and H. Fudeyasu, (Nova Science Publishers, Inc.).
- [13] Terray, P., K. Kakitha, S. Masson, G. Madec, A. K. Sahai, J.-J. Luo, and Toshio Yamagata, 2011: The role of the intra-daily SST variability in the Indian Monsoon variability and monsoon-ENSO-IOD relationships in a global coupled model. *Climate Dynamics*, (submitted).
- [14] Yuan, C., T. Tozuka., J.-J. Luo, and T. Yamagata, 2011: Predictability of the Subtropical Dipole Modes in a Coupled Ocean-Atmosphere Model. *Climate Dynamics*, (submitted).

Published news articles

- Weekly Times, Australia May 25, 2011
- Weekly Times, Australia August 17, 2011
- Business Line, The Hindu, India April 13, 2011
- N-TV, Germany April 25, 2011 (<http://www.n-tv.de/wissen/Hitzewelle-war-Naturphaenomen-article3175891.html>)
- AFPBB NEWS, Japan October 5 2011 (http://www.afpbb.com/article/disaster-accidents-crime/disaster/2832708/7872333?utm_source=afpbb&utm_medium=topics&utm_campaign=txt_topics)
- National Geographic, Japan November 2011 (<http://nng.nikkeibp.co.jp/nng/article/20111101/289205/index.shtml>)
- NTT Communication, Japan December 2011 (<http://www.nttcom.co.jp/comzine/no103/wise/index.html>)
- NHK World December 2011

大気海洋結合モデルを用いたプロセス研究と季節予測実験

プロジェクト責任者

升本 順夫 海洋研究開発機構 地球環境変動領域

著者

スワディン ベヘラ^{*1,2}, 羅 京佳^{*1,2}, 佐々木 亘^{*2}, 佐久間弘文^{*1,2}, Sebastien Masson^{*4}, Antonio Navarra^{*3}, Silvio Gualdi^{*3}, Simona Masina^{*3}, Alessio Bellucci^{*3}, Annalisa Cherchi^{*3}, Pascal Delecluse^{*5}, Gurvan Madec^{*4}, Claire Levy^{*4}, Marie-Alice Foujols^{*4}, Arnaud Caubel^{*4}, Guy Brasseur^{*6}, Erich Roeckner^{*6}, Marco Giorgetta^{*6}, Luis Kornbluh^{*6}, Monika Esch^{*6}, 山形 俊男^{*2}, 升本 順夫^{*1}

*1 海洋研究開発機構 地球環境変動領域

*2 海洋研究開発機構 アプリケーションラボ

*3 Centro Euro-Mediterraneo per i Cambiamenti Climatici, INGV

*4 Laboratoire D'oceanographie et du Climat (LOCEAN)

*5 Meteo France

*6 Max Planck Institute for Meteorology

気候変動ならびにその予測可能性研究のための日欧研究協力に基づき、SINTEX-Frontier 大気海洋結合大循環モデルの開発および改良を推進し、これを用いた気候変動予測研究を行っている。その第一版である SINTEX-F1 は、リアルタイムの季節・経年変動予測実験に長く用いられており、近年発生したインド洋ダイポールモードやエルニーニョ現象のほとんどを現実的に予測している。2011 年には、年初のラニーニャ現象が夏季に一度弱まった後、再びその勢力を盛り返したことについて、発生の 1 年前から SINTEX-F1 での予測に成功した。さらに、インド洋および大西洋の亜熱帯域に発達する亜熱帯ダイポールモード現象について、それらの予測が半年程度前から可能であることを初めて示した。これらの成果は国内外のメディア等で取り上げられると同時に、世界の気候変動予測研究を先導するモデルとして SINTEX-F の地位を確立する礎となっている。

さらに、SINTEX-F1 モデルは気候変動のメカニズムを解明するための感度実験などにも利用されている。特に今年度は、SINTEX-F1 による長期積分結果の解析から、インド洋および大西洋の亜熱帯ダイポールモード現象の発達に海洋混合層厚の変化が重要な役割を果たしていることを明らかにした。また、SINTEX-F1 を高度化した SINTEX-F2 の精度評価を継続して行い、SINTEX-F2 の結果では、エルニーニョやインド洋ダイポールモード現象などに加えて熱帯低気圧の発生頻度などが向上し、季節内変動も現実的に取り入れた季節予測の精度向上の可能性が示された。

キーワード: SINTEX-F, エルニーニョもどき, 予測, 2011 年ラニーニャ現象

Simulation and Verification of Tropical Deep Convective Clouds using Eddy-Permitting Regional Atmospheric Models

Project Representative

Kozo Nakamura

Research Institute for Global Change, Japan Agency for Marine-Earth Science and Technology

Authors

Kozo Nakamura^{*1}, Masayuki Hara^{*1}, Akira T. Noda^{*1}, Hirofumi Tomita^{*2, 1} and Yasutaka Wakazuki^{*3, 1}

*1 Research Institute for Global Change, Japan Agency for Marine-Earth Science and Technology

*2 Advanced Institute for Computational Science, RIKEN

*3 College of Geoscience, School of Life and Environmental Sciences, University of Tsukuba

The objective of this project is to develop an eddy-permitting regional atmospheric model, which can simulate turbulent motion with deep moist convection. In order to develop the model efficiently, we adopted a model using similar dynamical and physical frameworks to those of a global cloud-resolving model called NICAM (Nonhydrostatic ICosahedral Atmospheric Model). We develop a regional model called a diamond NICAM, whose simulation domain consists of one diamond (two triangles in an icosahedron), although the original NICAM global domain consists of ten diamond-shaped subdomains (twenty triangles). We modified the original NICAM to enable the limited area simulation with minimum modification of source code. The performance of the model is examined. Although the diamond NICAM can be used for a very small region, the model cannot be used for the case of cyclic boundary conditions because the model is based on a spherical-coordinate. Therefore, another model called a plain-coordinate NICAM is also developed which can be used for the case of cyclic boundary conditions. The model is used for the case called the Tropical Warm Pool International Cloud Experiment (TWP-ICE). The results indicate typical characteristics of deep clouds that develop over a boundary layer to a free atmosphere.

Keywords: LES, regional atmospheric model, deep convection, NICAM, cloud resolving model

1. Introduction

The deep convection in tropics is one of the most important heat sources for the planetary-scale atmospheric circulation. Although the convection system occurs in synchronization with a diurnal cycle, the diurnal cycle, intensity and space distribution of deep convection is not well simulated in most of GCMs. Therefore, it is an important task to understand the dynamical aspects of such deep convective systems in relation with the diurnal cycle and local circulation. The purpose of this project is as follows;

- to develop a eddy-permitting regional atmospheric model, which can simulate turbulent motion with deep moist convection, by the use of a grid resolution on the order of a hundred meters, in order to represent explicitly the cloud-scale processes,
- to perform several Large-Eddy Simulation (LES)s for tropical convection using this model, and to improve the model by comparing the results with observation and performing some sensitivity studies,

and

- to investigate the generation and maintenance mechanism of convective systems based on the simulated data, which can be fundamental for improving cumulus parameterization schemes used in larger-scale atmospheric models including GCMs.

For the eddy-permitting regional atmospheric model, we are developing a model based on a global cloud-resolving model called NICAM (Nonhydrostatic ICosahedral Atmospheric Model, Satoh et al., 2008[1]). We develop a regional model called a diamond NICAM, whose simulation domain consists of one diamond (two triangles in an icosahedron), although the original NICAM global domain consists of ten diamonds (twenty triangles). We modified the original NICAM to enable the limited area simulation with minimum modification of source code. The developing process and the results of the test experiments are shown in section 2. Although the diamond NICAM can be used for a very small region, the model cannot be used for the case of cyclic boundary conditions because the

model is based on a spherical-coordinate. Therefore, another model called a plain-coordinate NICAM is also developed which can be used for the case of cyclic boundary conditions. The developing process and the test results are shown in section 3.

2. Diamond NICAM for regional climate simulations

This regional atmospheric model is developed for conducting realistic regional climate simulations, targeted onto a certain limited area. Stretched horizontal grid version of regional model based on global cloud-resolving model, NICAM, had developed and applied by Tomita (2008) [2] and Satoh et al. (2010) [3]. In these simulations, inhomogeneity of horizontal grid sizes causes inconsistency of physical parameterizations such as cumulus convection. Simulation domain of the newly developed regional model (hereafter diamond NICAM) consists of one diamond (two triangles in an icosahedron), although the original NICAM global domain consists of ten diamonds (twenty triangles). Non-hydrostatic equations system version of the diamond NICAM has developed in FY2011. We modified the original NICAM to enable the limited area simulation with minimum modification of source code.

Figure 1 shows the simulation domain of a regional climate simulation targeted on Japan. Lateral boundary of the simulation domain (outer side of the grey line circle of Fig. 1) is forced by reanalysis data. We performed some test simulations using the diamond NICAM and the global NICAM of partly high-resolution with stretched horizontal grid using Schmidt transform to compare the results with each other. Figure 2

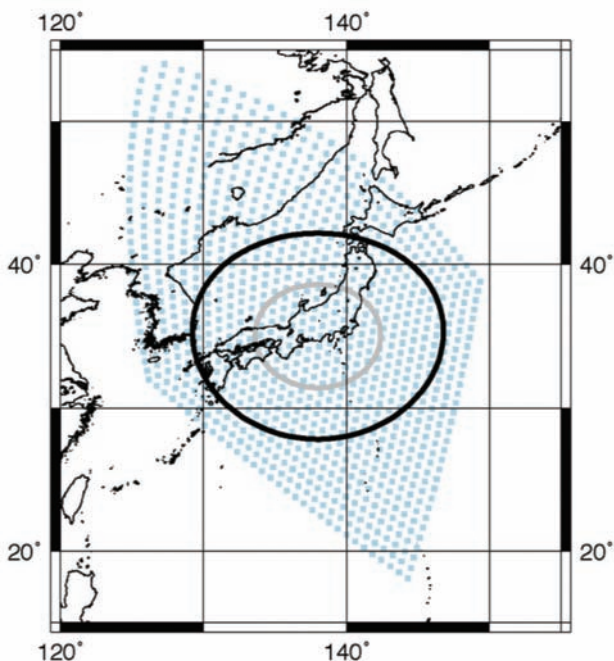


Fig. 1 Simulation domain targeted on Japan. Light blue dots indicates grid points. We applied reanalysis nudging in outer side of grey line circle.

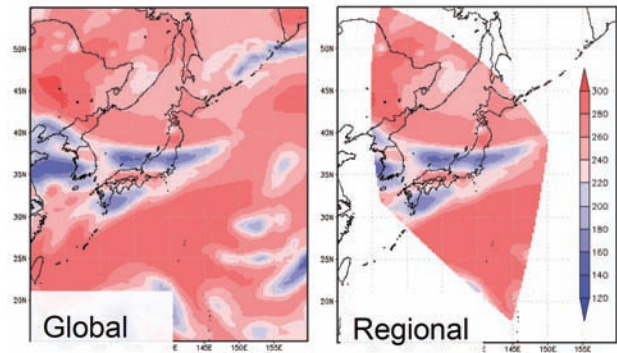


Fig. 2 Outgoing longwave radiation of simulations after two-hour integration. Left panel shows the result by global stretched grid simulation, right panel shows the one by regional simulation.

shows the outgoing long-wave radiation (OLR) of the two models. The result of the diamond NICAM is similar to well-tested stretched grid simulation, and correctly simulates the rain band system over Japan islands.

3. Preliminary experiment of deep convective systems using plain-coordinate NICAM

We developed plain-coordinate NICAM based on former spherical-coordinate NICAM, aiming at conducting much higher resolution simulations with the same physical processes and dynamic core of the spherical model. Herewith, we can directly compare the data using the both models, and improve simulated clouds in the real atmosphere using the spherical model by modifying physical parameterizations including microphysics and turbulent schemes based on high-resolution data in the plain model.

We conducted a high-resolution simulation of deep convective clouds observed during an austral summer season using the plain-coordinate NICAM. The model setting we adopted is the case called the Tropical Warm Pool International Cloud Experiment (TWP-ICE, May et al. 2008[4]), a major field experiment undertaken in the Darwin, Northern Australia, area in January and February 2006. The horizontal and vertical domain sizes are 100 km^2 and 24 km, respectively. The horizontal and vertical grid sizes are 390 m and, in average, 100 m, respectively. We used level 2 of MYNN (Nakanishi and Niino 2004[5]; Noda et al. 2010[6]) for computation of the subgrid-scale turbulence, and NSW6 (Tomita 2008[2]) for process of cloud microphysics, which parameterization schemes are generally being used in cloud-resolving simulations of NICAM.

Figure 3 shows the temporal changes of maxima of vertical velocity and condensates in the computed domain. Intense vertical velocity gradually develops from a 2 km height to higher altitudes after 20 min, and it eventually extends over a 15 km height. The maximum exceeds 60 m/s at around 12 km height by 100 min. The values of condensates become larger

from the lower to the higher troposphere. Different from that of vertical velocity, it shows maximum around the 6 km height, which corresponds to the freezing level. Figure 4 shows the contribution of each category of condensates to the total (shown in Fig. 3b). Quantitatively, the contributions of rain water and graupel are dominant below and above the freezing level, respectively, and next are that of cloud water and cloud ice. The value of snow is the smallest in this case.

We are going to extend the simulation period to 1 day to analyze characteristics of statistical behavior of simulated convective clouds, along with a sensitivity study of horizontal resolution.

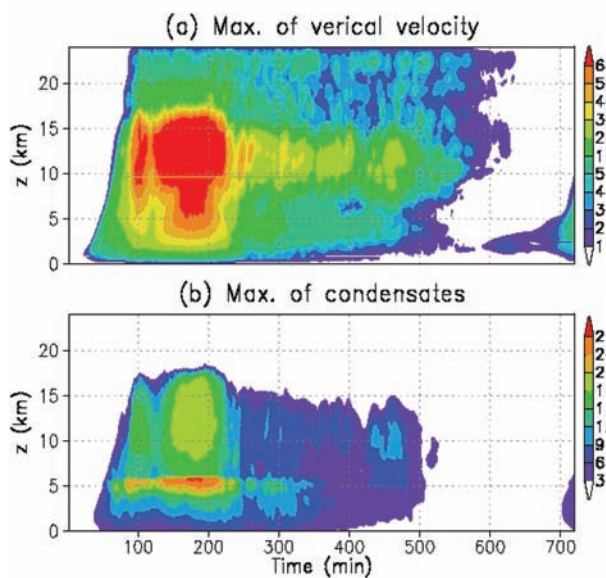


Fig. 3 Temporal changes of simulated deep convective systems. Maxima of (a) vertical velocity (m/s) and (b) condensates (g/kg) in the computed domain are shown.

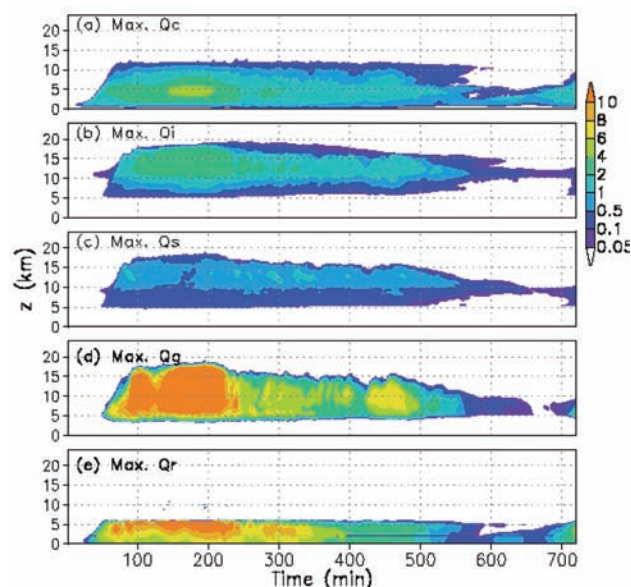


Fig. 4 Vertical distribution of simulated condensates. From left to right, maximum mixing ratios (g/kg) of (a) cloud water, (b) cloud ice, (c) snow, (d) graupel, and (e) rain water.

References

- [1] Satoh, M., T. Matsuno, H. Tomita, H. Miura, T. Nasuno, and S. Iga, "Nonhydrostatic Icosahedral Atmospheric Model (NICAM) for global cloud resolving simulations," *Journal of Computational Physics*, the special issue on Predicting Weather, Climate and Extreme events, 227, 3486-3514, doi:10.1016/j.jcp.2007.02.006, 2008.
- [2] Tomita, H., "A stretched icosahedral grid by a new grid transformation," *J. Meteor. Soc. Japan*, 86A, 107-119, 2008.
- [3] Satoh, M., T. Inoue, and H. Miura, "Evaluations of cloud properties of global and local cloud system resolving models using CALIIPSO/CloudSat simulators," *J. Geophys. Res.*, 115, D00H14, doi:10.1029/2009JD012247, 2010.
- [4] May, P. T., J. H. Mother, G. Vaughan, C. Jakob, G. M. McFarquhar, K. N. Bower, and G. G. Mace, "The tropical warm pool international cloud experiment," *Bulletin of the American Meteorological Society*, 89, 629-645, 2008.
- [5] Nakanishi, M. and H. Niino, "An improved Mellor-Yamada Level-3 model with condensation physics: Its design and verification," *Boundary-Layer Meteor.*, 112, 1-31, 2004.
- [6] Noda, A. T., K. Oouchi, M. Satoh, H. Tomita, S. Iga, and Y. Tsushima, "Importance of the subgrid-scale turbulent moist process: Cloud distribution in global cloud-resolving simulations," *Atmos. Res.*, 96, 208-217, doi, 10.1016/j.atmosres.2009, 2010.

渦解像可能な領域大気モデルを用いた深い対流のシミュレーションとその検証

プロジェクト責任者

中村 晃三 海洋研究開発機構 地球環境変動領域

著者

中村 晃三^{*1}, 原 政之^{*1}, 野田 暁^{*1}, 富田 浩文^{*2,1}, 若月 泰孝^{*3,1}

*1 海洋研究開発機構 地球環境変動領域

*2 理化学研究所 計算科学研究機構

*3 筑波大学 生命環境学群地球学類

本プロジェクトは、十分に細かい格子を用い、深い湿潤対流を解像できるモデルの開発を目的としている。効率的な開発のため、全球雲解像モデル (NICAM, Nonhydrostatic ICosahedral Atmospheric Model) と共通の力学/物理フレームワークを用いた2つのNICAMモデルを開発した。領域版NICAMは全球版NICAMの一部を用いるもので、境界条件やナッジングの方法のチェックを進めた。全球実験とほぼ同じ結果が得られるようになった。領域版NICAMは計算領域が狭くてもあくまでも球面上のモデルであり、周期境界条件を適用することはできない。そこで、周期境界条件を適用することができる平面版NICAMを新たに作成した。予備実験として、通常の積雲対流解像モデルで比較実験が行われているケースのシミュレーション実験を行い、良好な結果を得た。

キーワード: LES, 領域大気モデル, 深い対流, NICAM, 雲解像モデル

A Long-term Ocean State Estimation by using a 4D-VAR Data Assimilation Approach

Project Representative

Shuhei Masuda

Research Institute for Global Change, Japan Agency for Marine-Earth Science and Technology

Authors

Shuhei Masuda^{*1}, Nozomi Sugiura^{*1}, Toshimasa Doi^{*1}, Yoshihisa Hiyoshi^{*2}, Yuji Sasaki^{*2} and Toshiyuki Awaji^{*2}

*1 Research Institute for Global Change, Japan Agency for Marine-Earth Science and Technology

*2 Data Research Center for Marine-Earth Sciences, Japan Agency for Marine-Earth Science and Technology

We have conducted a global ocean synthesis on the basis of in-situ temperature and salinity observations, satellite altimetry and a global ocean general circulation model through a 4D-VAR data assimilation to obtain a comprehensive 4-dimensional integrated dataset from the sea surface to the ocean bottom for all the major ocean basins for the period of 1967-2009. The assimilated elements are historical hydrographic data of temperature and salinity from the ENSEMBLES (EN3) data set, NOAA Optimum Interpolation SST values and sea level anomaly data derived from the high-precision multi-satellite altimetry products were distributed by Aviso. The obtained dynamically self-consistent 4-dimensional dataset can offer greater information content on ocean climate changes than can be derived from models or data alone.

Keywords: Ocean, Data assimilation, Climate change, 4D-VAR

1. Introduction

The spatio-temporal coverage of hydrographic data is still sparse. Data assimilation approaches have recently focused on the derivation of an optimal synthesis of observational data and model results for better descriptions of the ocean state (*e.g.*, Stammer *et al.*, 2002)[1].

Within this background, (Rienecker *et al.* 2010)[2] mentioned an advantage of “Integrated Earth System Analyses” at OceanObs’09. A physical-biogeochemical ocean model, coupling with the atmosphere, sea-ice, and also with the land surface is a promising in climate research in the future.

In this study, we have conducted a global ocean synthesis on the basis of in-situ temperature and salinity observations, satellite altimetry and a global ocean general circulation model through a 4D-VAR data assimilation to obtain a comprehensive 4-dimensional integrated dataset. The dataset include an estimate of the global biogeochemical variables with a new lower-trophic ecosystem model toward an Integrated Earth System Analyses.

2. Model

The used OGCM is based on version 3 of the GFDL Modular Ocean Model (MOM) (Pacanowski and Griffies, 1999)[3] with major physical parameter values determined through a variational optimization procedure (Menemenlis *et al.*, 2005)[4]. The horizontal resolution is 1° in both latitude and longitude, and there are 46 vertical levels for the global ocean

basin. The adjoint code of the OGCM was obtained using the Transformation of Algorithms in Fortran (TAF).

Our ocean data assimilation system has been executed on the Earth Simulator 2 to obtain a comprehensive 4-dimensional dataset (*e.g.*, Masuda *et al.*, 2010)[5]. The assimilated elements are historical hydrographic data of temperature and salinity from the ENSEMBLES (EN3) dataset which was quality-controlled using a comprehensive set of objective checks developed at the Hadley Centre of the UK Meteorological Office (Ingleby and Huddleston, 2007)[6]. In addition of EN3 dataset, recent data obtained/compiled in JAMSTEC (independent MIRAI RV profiles) are simultaneously incorporated. NOAA Optimum Interpolation SST (NOAA_OI_SST_V2) values, and sea-surface dynamic-height anomaly data derived from the high-precision multi-satellite altimetry products produced by Ssalto/Duacs are also assimilated.

A new bio-geochemical model NPDZC-model was introduced based on the obtained dynamical ocean state. It consists of 6 state variables representing the biomass of phytoplankton (P), zooplankton (Z), nitrogen (N), carbon (C), and detritus (D).

3. Ocean State Estimate

The assimilation is based on a 4D-VAR adjoint approach which can precisely determine the time-trajectory of the ocean states, and thus can provide analysis fields in super

quality through 4-dimensional dynamical interpolation of in-situ observations for water temperature, salinity and sea surface height anomaly, as obtained from various instrumental sources. Figure 1 shows estimated sea surface and deep water temperature distributions in December 1980, 2005, and 2008. Gradual warming trend at each depth is apparently visible (e.g., Fukasawa *et al.*, 2004)[7]. The analysis fields successfully

capture the realistic time trajectory of ocean properties from 1957 to 2009.

4. Applications to Bio-geochemical Model

We estimated the global biogeochemical variables with a new lower-trophic ecosystem model (Fig. 2). The 53-year synthesized ocean dataset provides a dynamically self-consistent

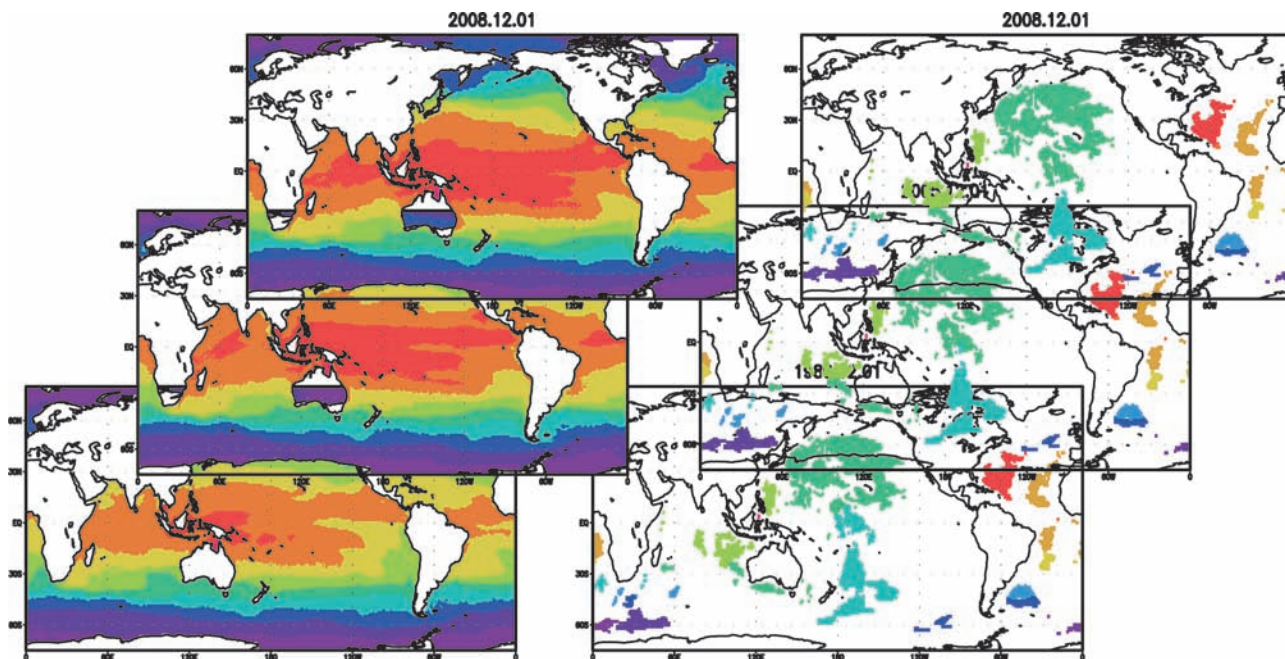


Fig. 1 Sea Surface Temperature and 5000-m depth water temperature estimated from 4D synthesis dataset.

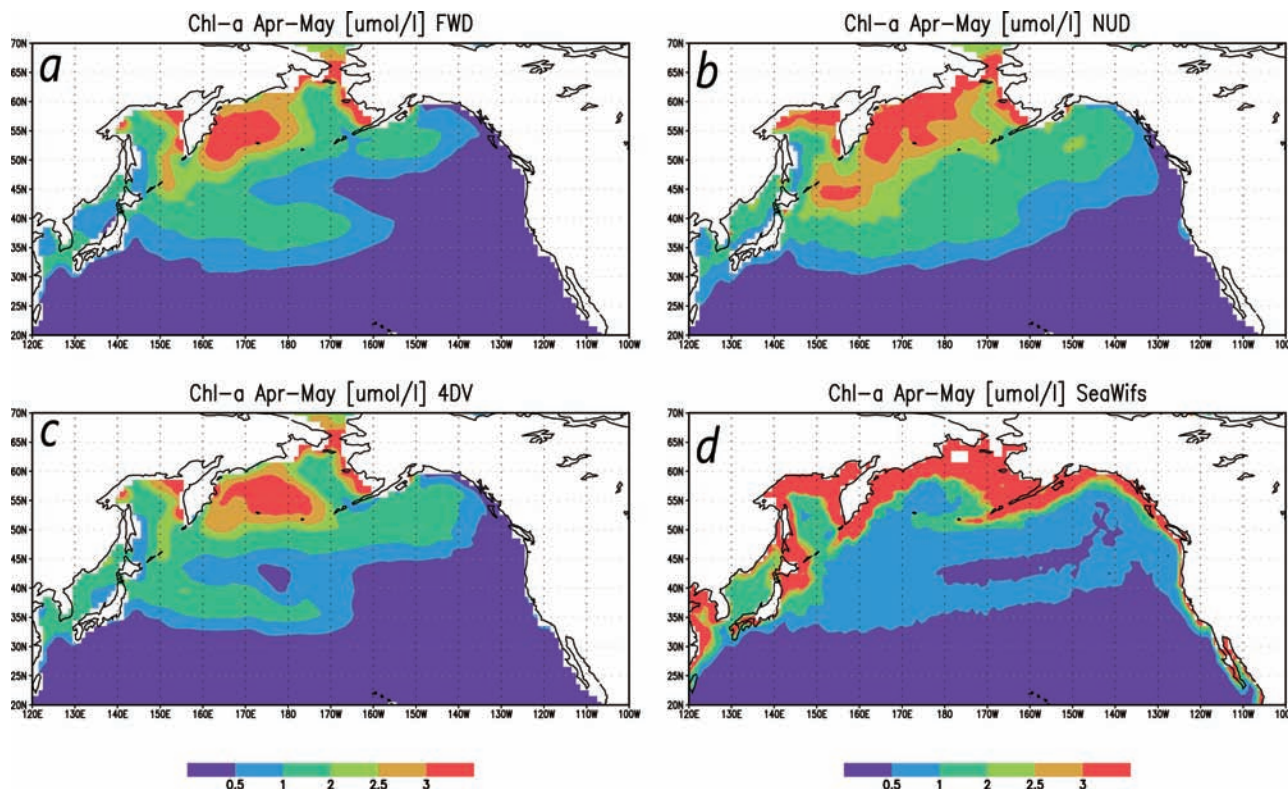


Fig. 2 Distribution of estimated Chlorophyll-a; (a) simulation, (b) simulation with ocean property nudging, (c) 4D-VAR product, and (d) SeaWiFS satellite product.

ocean current field for the ecosystem model. Bio-geochemical model parameter values will be optimized in the global ocean through the Green's function approach. The optimized parameter set enables us to estimate a realistic time-varying bio-geochemical fields consistent with observations, which should offers a better description of oceanic material transport inclusive of carbon.

5. Concluding Remarks

Advanced ocean data assimilation techniques have led to better understanding of ocean climate change and will possibly contribute to the construction of an optimal ocean observing system (*e.g.*, Oke *et al*, 2009)[8]. Our data assimilation system can provide a model sensitivity, which facilitates the identification of the mechanism, origins and pathways of specific climate changes, thus would lead to an effective strategic planning for the spatial and temporal deployment of measurement instruments and hydrographic surveys. It is a promising perspective of our research.

Acknowledgement

We thanks J. P. Matthews, Y. Ishikawa, and M. Kamachi for helpful discussion.

References

- [1] Stammer, D., C. Wunsch, I. Fukumori, and J. Marshall, "State Estimation in Modern Oceanographic Research", *EOS, Transactions*, American Geophysical Union, Volume 83, Nr. 27, p. 289, 294-295, 2002.
- [2] Rienecker, M., T. Awaji, M. Balmaseda, B. Barnier, D. Behringer; M. Bell, M. Bourassa, P. Brasseur; L.-A. Brevik, and J. Carton, "Synthesis and Assimilation Systems - Essential Adjuncts to the Global Ocean Observing System" in *Proceedings of OceanObs'09: Sustained Ocean Observations and Information for Society (Vol. 1)*, Venice, Italy, 21-25, 2010.
- [3] Pacanowski, R. C., and S. M. Griffies, *The MOM 3 manual*, report, 680 pp., Geophys. Fluid Dyn. Lab., Princeton, N. J, 1999.
- [4] Menemenlis, D., I. Fukumori, and T. Lee, Using Green's functions to calibrate an ocean general circulation model, *Mon. Wea. Rev.*, 133, 1224-1240, 2005.
- [5] Masuda, S., T. Awaji, N. Sugiura, J. P. Matthews, T. Toyoda, Y. Kawai, T. Doi, S. Kouketsu, H. Igarashi, K. Katsumata, H. Uchida, T. Kawano, and M. Fukasawa, Simulated Rapid Warming of Abyssal North Pacific Waters, *Science*, 329, 319-322, DOI: 10.1126/science.1188703, 2010.
- [6] Ingleby, B. and M. Huddleston, Quality control of ocean temperature and salinity profiles - historical and real-time data, *Journal of Marine Systems*, 65, 158-175, DOI: 10.1016/j.jmarsys.2005.11.019, 2007.
- [7] Fukasawa, M., H. Freeland, R. Perkin, T. Watanabe, H. Uchida, and A. Nishina, Bottom water warming in the North Pacific Ocean, *Nature*, 427, 825-827, 2004.
- [8] Oke, P. R., M. A. Balmaseda, M. Benkiran, J. A. Cummings, E. Dombrowsky, Y. Fujii, S. Guinehut, G. Larnicol, P.-Y. Le Traon, and M. J. Martin, Observing system evaluations using GODAE systems. *Oceanogr.*, 22, 144-153, 2009.

四次元変分法海洋データ同化システムを用いた全球海洋環境の再現

プロジェクト責任者

増田 周平 海洋研究開発機構 地球環境変動領域

著者

増田 周平^{*1}, 杉浦 望実^{*1}, 土居 知将^{*1}, 日吉 善久^{*2}, 佐々木祐二^{*2}, 淡路 敏之^{*2}

*1 海洋研究開発機構 地球環境変動領域

*2 海洋研究開発機構 地球情報研究センター

船舶、衛星観測などから得られる海洋観測データの時空間な分布密度は比較的観測の多い水温データでも地球規模の気候変動研究を進めるうえで十分に密であるとは言えない。気候変動現象をより精緻に解析するためにはデータ同化技術を用いた力学補完が有効である。本研究では四次元変分法海洋同化システムを用いて、高精度な海洋環境再現データを作成した。また、このデータセットを用い、生物化学変量の推定も行った。

キーワード: 海洋, データ同化, 気候変動, 4D-VAR

Global Elastic Response Simulation

Project Representative

Seiji Tsuboi

Institute for Research on Earth Evolution / Data Research Center for Marine-Earth Sciences,
Japan Agency for Marine-Earth Science and Technology

Authors

Seiji Tsuboi

Institute for Research on Earth Evolution / Data Research Center for Marine-Earth Sciences,
Japan Agency for Marine-Earth Science and Technology

Nozomu Takeuchi

Earthquake Research Institute, The University of Tokyo

In this project, we conduct waveform inversion to obtain detailed whole mantle seismic velocity model using the direct solution method. Here we compare our new model with previous model and discuss which features are newly identified in our new model. We also pursue accurate numerical techniques to obtain theoretical seismic waves for realistic three dimensional (3-D) Earth models using Spectral-Element Method. We calculate synthetic seismic waveform for 2011 Tohoku earthquake ($M_w 9.0$) using fully 3-D Earth model. Our results indicate that the earthquake rupture model we have used for this simulation is fairly accurate to grasp the rupture propagation along the earthquake fault.

Keywords: Synthetic seismograms, 3-D velocity structure of the Earth, Spectral Element Method

1. Comparison of SH18CEX and SH18CE

We previously obtained the whole mantle SH velocity models, SH18CE (Takeuchi, 2007 [1]; Tsuboi and Takeuchi, 2007 [2]) and SH18CEX (Tsuboi and Takeuchi, 2011 [3]). In this paper, we compare these two models and discuss which features are newly identified in SH18CEX. We also discuss which part of the dataset contributed to the improvements.

The data set used in obtaining SH18CEX is a combination of the data set of SH18CE (hereafter, referred to as “Data Set 1”) and the new data set (hereafter, referred to as “Data Set

2”). Data Set 1 includes only data for large events ($M_w \geq 6.5$), whereas Data Set 2 includes data for smaller events (the smallest M_w is 6.0). The entire data set used for SH18CEX consists of 54,790 traces (271,798 time windows), which is approximately 3.5 times the number of traces used for SH18CE. With the exception of the data set used, the methods and parameters employed are exactly the same.

First, we compare the lowermost mantle models of SH18CEX and SH18CE via visual inspection (Fig. 1). We see that the overall patterns, i.e., the long-wavelength features,

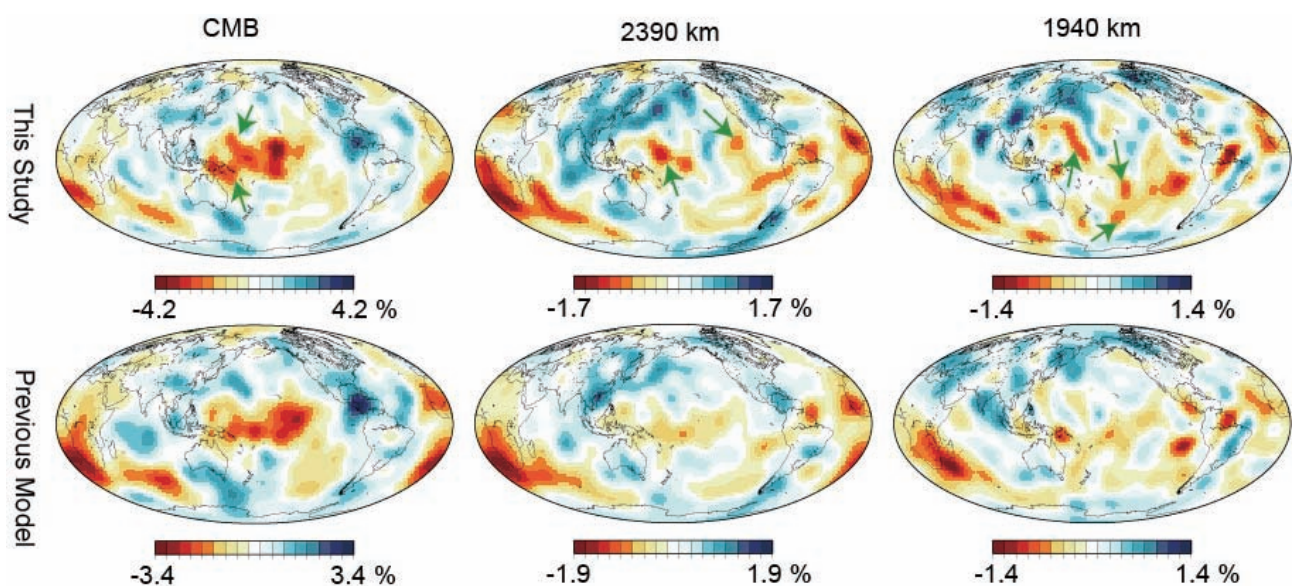


Fig. 1 Comparison between SH18CEX (upper figures) and SH18CE (lower figures) in the lowermost mantle. The green arrows indicate examples of the prominent features observed only in SH18CEX.

Table 1 Comparison of variance improvements.

	Data Set 1		Data Set 2	
	SH18CE	SH18CEX	SH18CE	SH18CEX
200-400 s	42 %	44 %	30 %	32 %
100-200 s	41 %	42 %	33 %	37 %
50-100 s	34 %	31 %	23 %	31 %

of the two models are nearly invariant, but the significant differences between the models are the relatively small-scale anomalies observed only in SH18CEX (such as the features indicated by the green arrows in Fig. 1). This can probably be attributed to the resolution improvement in the new model.

The newly identified small-scale features appear to be constrained primarily by the body waveforms in Data Set 2. Table 1 summarizes the variance improvements due to SH18CE and SH18CEX. SH18CEX exhibits improvements comparable with those of SH18CE for the periodic ranges of 200-400 s and 100-200 s (Table 1, top). For the periodic range of 50-100 s, SH18CEX also exhibits comparable improvements for the existing data (34% for SH18CE and 31% for SH18CEX); on the other hand, it exhibits greater improvements for the incremental data (23% for SH18CE and 31% for SH18CEX) (Table 1, top). Improvements for the incremental data themselves are not surprising because they are included only in the inversion for SH18CEX, but note the larger improvements for the periodic range of 50-100 s compared with the other ranges. Considering that the data set of 50-100 s primarily consists of body waveforms, the results suggest that the incremental constraints on the Earth's structures are primarily attributable to the body waveforms in the incremental data set.

For the periodic range of 200-400 s, the improvements for Data set 1 are greater than those for Data set 2 (e.g., 44% and 32%, respectively, for SH18CEX) (Table 1, top). This is probably due to the fact that the signal-to-noise ratios of Data Set 2 are not adequate for longer periods because Data Set 2 includes data for smaller events. Indeed, for the periodic range of 200-400 s, variance improvements for larger events ($M_w \geq 6.5$) are significantly larger than those for the data for smaller events ($M_w < 6.5$) (38 % and 21 %, respectively, for SH18CEX) (Table 1, bottom). However, note that this does not hold for the periodic range of 50-100 s (30% and 32%, respectively, for SH18CEX) (Table 1, bottom), which suggests that such problems are not encountered in this periodic range. Therefore, we can conclude that the small-scale features in the lower mantle would be better constrained by the incremental data set.

2. 2011 Tohoku earthquake

2.1 Earthquake rupture mechanism

We apply the waveform inversion to obtain slip distribution in the source fault at the 2011 Tohoku earthquake in the same manner as our previous work (Nakamura et al., 2010 [4]). We use 22 broadband seismograms of IRIS GSN seismic stations

	Data Set 2 ($M_w \geq 6.5$)		Data Set 2 ($M_w < 6.5$)	
	SH18CE	SH18CEX	SH18CE	SH18CEX
200-400 s	36 %	38 %	20 %	21 %
100-200 s	34 %	38 %	32 %	36 %
50-100 s	21 %	30 %	24 %	32 %

with epicentral distance between 30 and 100 degrees. The broadband original data are integrated into ground displacement and band-pass filtered in the frequency band 0.002-1 Hz. We use the velocity structure model IASP91 (Kennet and Engdahl, 1991 [5]) to calculate the wavefield near source and stations. We assume that the strike of the fault plane is 201 degree and the dip angle is 9 degree, based on Global Centroid Moment Tensor solution. The length of subfault used for our inversion is 30 km in the strike direction and 20 km in the dip direction. The assumed fault length is totally 460 km consistent with the aftershock distribution. We assume that rupture velocity along the fault is about 2.0 km/s. The results of the inversion show the bilateral rupture to the northeast and southwest with two main asperities along the fault; the maximum slip of 49 m with the reverse fault mechanism at approximately 100 km northeast of the epicenter and another large slip with reverse fault mechanism at 100 km southwest of the epicenter. The total amount of the released seismic moment corresponds to moment magnitude $M_w=9.1$. The duration of source time function is 150 sec. The fault length of 450 km and the source duration time of 150 sec are typical for $M_w 9.1$ earthquake. However, the maximum slip of 49 m is unusually large. Also the rupture velocity of 2.0 km/s may characterize this earthquake as slow tsunami generating earthquake. We should note that the fault rupture model, we have obtained, is not unique in the sense that the variance reduction is not significant. There are possibilities of other models, which show much slower rupture velocity or larger slip. Thus, we examine the validity of these fault rupture parameters by comparing the theoretical seismograms computed for this fault model with the observed seismograms.

2.2 Broadband synthetic seismograms

We calculate broadband synthetic seismograms with this source propagation model for a realistic 3D Earth model using the spectral-element method (Komatitsch and Tromp, 2002 [6]). The simulations are performed using 726 processors, which require 91 nodes of the Earth Simulator 2. We use a mesh with 200 million spectral-elements, for a total of 13 billion global integration grid points. This translates into an approximate grid spacing of 2.0 km along the Earth's surface. On this number of nodes, a simulation of 30 minutes of wave propagation accurate at periods of 3.5 seconds and longer requires about 7 hours of CPU time. An example of waveform matches are shown in Fig. 2, where three component broadband seismograms are compared with the observations at teleseismic stations, AFI

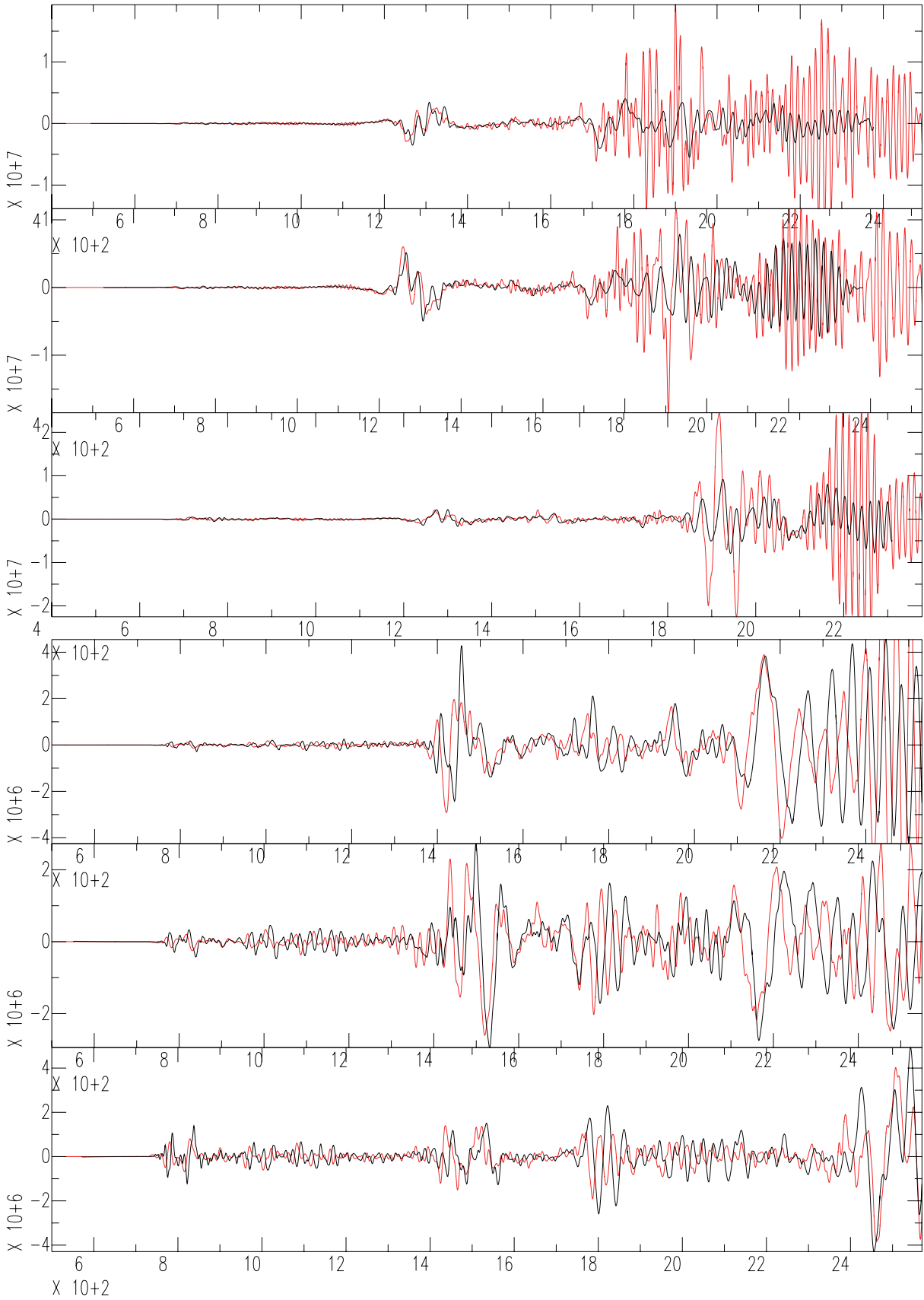


Fig. 2 Comparisons of synthetic seismograms and observation for IRIS GSN station AFI (top), ESK (bottom), where the epicentral distances are 67 degree, 81 degree, respectively. The synthetics and the observations are in red and black, respectively. Instrument responses are convolved to synthetics to convert them to ground velocity. Traces are EW, NS, and UD components from top to bottom, respectively. The origin of the time axis is origin time of the event and the vertical axis shows digital count. All of the traces are bandpass filtered between 500 sec and 10 sec.

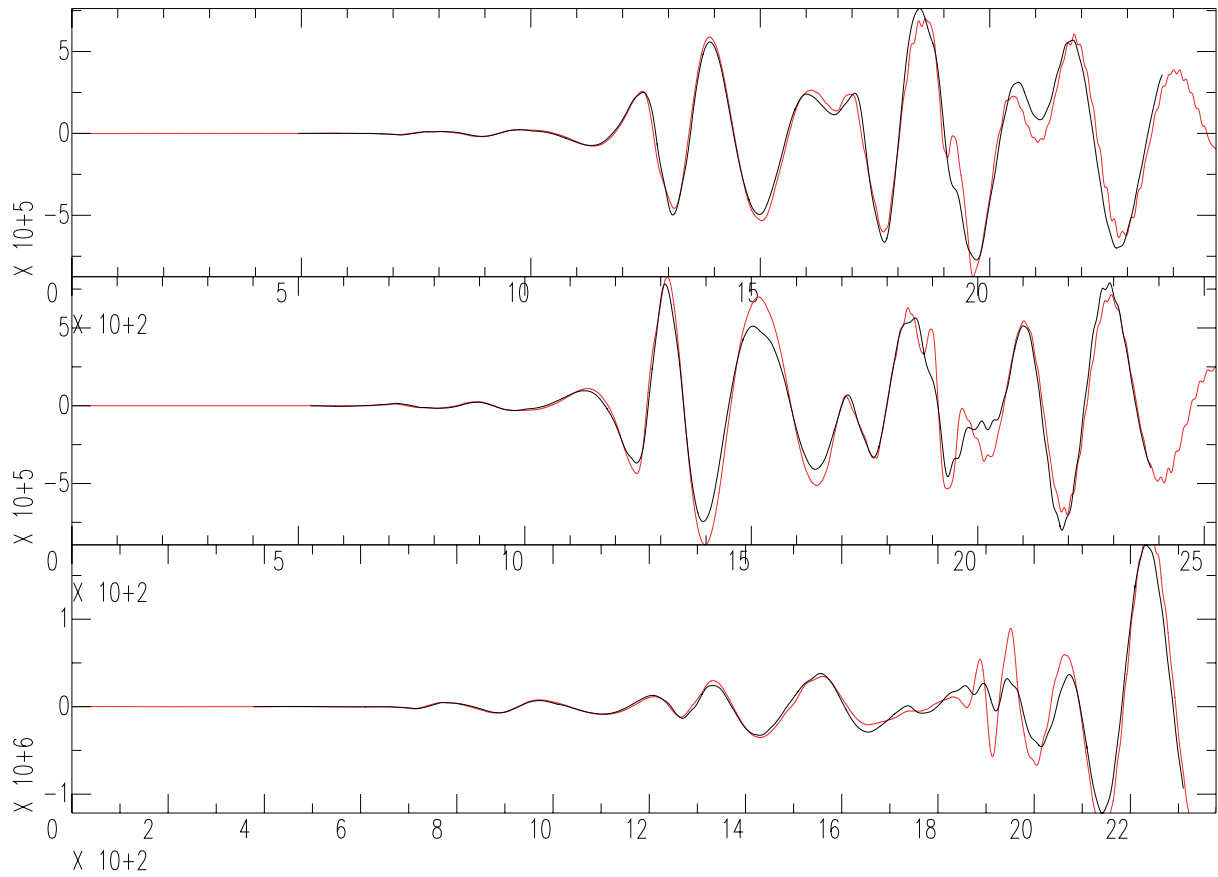


Fig. 3 Comparisons of synthetic seismograms for station AFI. Bandpass filtered at 500 sec and 200 sec.

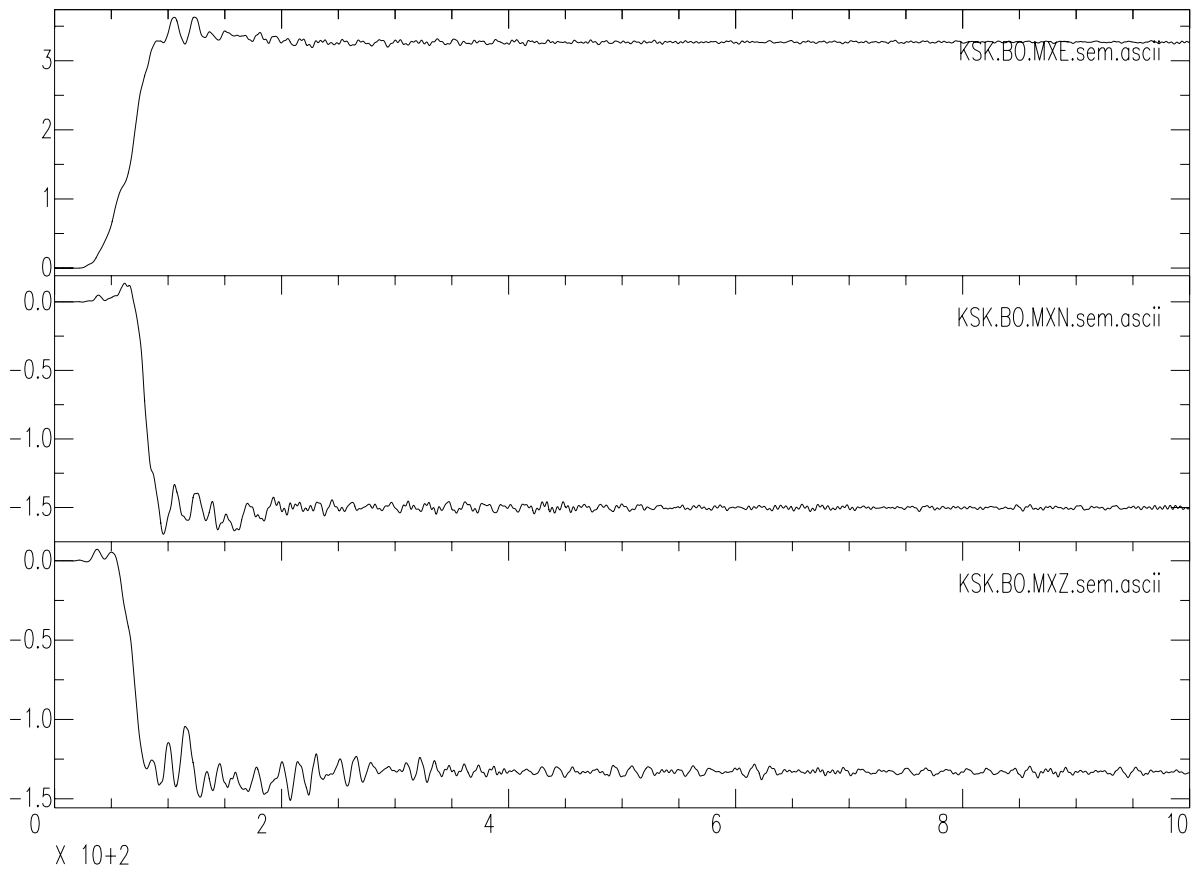


Fig. 4 Synthetic seismograms of Fnet network stations, KSK. Three component theoretical displacement seismograms are shown. 1000 sec records of EW, NS, UD are shown from top to bottom. Vertical unit is in m. Estimated static displacements are east 3.2m, south 1.5m, and down 1.3m for KSK.

(Afiamaluu, Samoa Islands, epicentral distance 67 degrees), ESK (Edinburgh, U.K., 81 degrees). Each trace is bandpass filtered between 0.002 Hz and 0.1 Hz. We may say that the synthetic seismograms reproduces observed seismograms generally well for body waves. Although surface waves are not modeled well, but it is because the surface waves with this period range depend on shallow crustal structure, which may not be modeled well in the 3D mantle model. Figure 3 demonstrates example of comparison in lower frequency range for station AFI and shows that the agreement is excellent in lower frequency range. Figure 4 shows synthetics for near field station KSK (3.1 degree), of F-net broadband network in the coast of Tohoku region. Because of proximity of the station location to the epicenter, the displacement shows static displacement, whose pattern is consistent to the observed crustal deformation.

These results indicate that the synthetic seismograms computed for this finite source model reproduce observed seismograms for both near field and teleseismic stations, which suggest that this source model captures rupture properties of this earthquake.

References:

- [1] Takeuchi, N., 2007. Whole mantle SH velocity model constrained by waveform inversion based on three-dimensional Born kernels, *Geophys. J. Int.*, 169, 1153-1163.
- [2] Tsuboi, S. and Takeuchi, N., 2007. Global Elastic Response Simulation, Annual Report of the Earth Simulator Center, April 2006-March 2007, 69-73.
- [3] Tsuboi, S. and Takeuchi, N., 2011. Global Elastic Response Simulation, Annual Report of the Earth Simulator Center, April 2010-March 2011, 75-80.
- [4] Nakamura, T., Tsuboi, S., Kaneda, Y., and Yamanaka, Y., 2010. Rupture process of the 2008 Wenchuan, China earthquake inferred from teleseismic waveform inversion and forward modeling of broadband seismic waves, *Tectonophysics*, 491, 72-84.
- [5] Kennet, B. L. N. and Engdahl, E. R., 1991. Traveltimes for global earthquake location and phase identification. *Geophys. J. Int.*, 105, 429.
- [6] Komatitsch, D. and Tromp, J., 2002. Spectral-element simulations of global seismic wave propagation-I. Validation, *Geophys. J. Int.*, 149, 390-412.

全地球弾性応答シミュレーション

プロジェクト責任者

坪井 誠司 海洋研究開発機構 地球内部ダイナミクス領域 / 地球情報研究センター

著者

坪井 誠司 海洋研究開発機構 地球内部ダイナミクス領域 / 地球情報研究センター

竹内 希 東京大学 地震研究所

Direct Solution 法を用いた波形インバージョンにより、地球内部マントル 3 次元地震波速度構造モデルを改善した。今回得られた新しいモデルと、これまでに得られたモデルとを比較することにより、新しいモデルでは下部マントルでの分解能が向上したことを確認した。

スペクトル要素法により現実的な 3 次元地球モデルに対する理論地震波形記録を 2011 年東北地方太平洋沖地震 (Mw9.0) に対して計算した。計算は地球シミュレータの 91 ノードを用いて、周期約 5 秒の精度で行った。計算した理論地震波形は観測波形をよく説明しており、用いた地震断層モデルがよく断層における破壊過程をモデル化していることを示している。計算した地震波形は遠地観測点のみならず、近地における地殻変動のパターンも良く再現していることが分かった。

キーワード:理論地震波形記録, 3次元地球内部構造, スペクトル要素法

Numerical Simulations for Understanding of the Earth's Core Convection

Project Representative

Yozo Hamano

Institute for Research on Earth Evolution, Japan Agency for Marine-Earth Science and Technology

Authors

Ataru Sakuraba

Department of Earth and Planetary Science, School of Science, The University of Tokyo

Futoshi Takahashi

Department of Earth and Planetary Sciences, School of Science and Engineering, Tokyo Institute of Technology

Hisayoshi Shimizu

Earthquake Research Institute, The University of Tokyo

Takatoshi Yanagisawa

Institute for Research on Earth Evolution, Japan Agency for Marine-Earth Science and Technology

Yozo Hamano

Institute for Research on Earth Evolution, Japan Agency for Marine-Earth Science and Technology

Some results of numerical experiments are reported for better understanding of the Earth's core convection and the geomagnetic field generation. We find a dynamo solution that produces a high ratio of magnetic to kinetic energy densities in a relatively low Ekman-number condition. The solution exhibits a very large-scale convection pattern, which we surmise is a general tendency in a convective regime of Earth-like high magnetic energy ratio. The processes of the magnetic field generation are analyzed in detail and the importance of the field stretching due to the large-scale azimuthal flow is pointed out. Numerical experiments of a spherical-shell dynamo with a thermally stable layer at the top are performed for a rough understanding of compositional convection. The results indicate that the existence of the stable layer suppresses the large-scale flow structure and decreases the energy ratio, and this tendency becomes more prominent when the Prandtl number is greater than unity. A comparison study is made between laboratory experiments and numerical simulations of liquid-metal Bénard convection in the presence of a magnetic field and rotation. Numerical simulations for the magnetoconvection problem well reproduce four characteristic convective regimes including a regime of random reversals of roll-type circulations that have found in the laboratory experiments.

Keywords: Geodynamo, Geomagnetic field, Core convection, Rayleigh-Bénard convection, Magneto hydrodynamics

1. Introduction

The primordial internal energy of the Earth is the primary origin of a variety of dynamic natural phenomena on our planet. The mantle convection, driven by both cooling of the Earth and internal radiogenic heating, takes the form of rigid-plate motions at the surface, and sometimes leads to disastrous earthquakes. As the mantle cools, the underlying liquid metallic core becomes thermally unstable and the resulting convective motion causes generation of the geomagnetic field and its time variations. As a result of cooling of the liquid core containing some lighter elements, a solid denser inner core grows from below, causing compositional instability in the liquid outer core too.

Our group has made step-by-step efforts to understand the dynamic state of the Earth's deep interior by means of

realistic numerical modeling of the core and mantle convection. Each subsystem of this global heat engine can be treated independently because of vast disparity of convective time scales. We have mainly studied physically essential processes in each convective subsystem, and here report some progress of the research on the core convection, but our ultimate goal is to assess possible interactions between the core and the mantle and to illuminate behaviors of the overall solid-Earth system in geological time scales.

2. Emergence of a large-scale flow structure with a strong magnetic field

The generation of magnetic fields by convective motions of an electrically conducting fluid in a rotating spherical shell is a fundamental problem of geophysical and astrophysical

fluid dynamics. Owing to recent advances in three-dimensional numerical magnetohydrodynamic (MHD) dynamo simulations, we have obtained many insights into how convection and magnetic field generation generally occur in rotating spherical shells [1].

The Earth's core convection is considered to be in a peculiar dynamical state known as the magnetostrophic state, where viscous and inertial forces are of little importance and Coriolis and Lorentz forces dominate instead. The ratio of viscous to Coriolis forces can be represented by the Ekman number, $E = \nu/2\Omega D^2$, where Ω is the angular velocity of the spherical shell, D is the shell thickness and ν is the kinematic viscosity. A realistic value of E in the Earth's core is $O(10^{-15})$, whereas most numerical dynamo simulations are performed at $E > 10^{-6}$. Similarly, the ratio of Lorentz to inertial forces can be represented by the ratio, ε , of magnetic to kinetic energy densities. The energy ratio in the outer core is believed to be $O(10^2)$ to $O(10^3)$, but most of previous numerical models could reach a state where ε was only around 10 or less. The Ekman number is an input parameter in simulating MHD dynamos and should be set as small as possible, but the energy ratio is an output parameter that depends on other dimensionless parameters and boundary conditions even when E is same.

Keeping the remoteness from the real Earth in mind, we here focus on understanding of fundamental physical processes of an MHD dynamo in a rapidly rotating spherical shell rather than attempt to predict the magnetic fields of planets and stars quantitatively. Although a similar approach has been taken in many papers [2-4], they are restricted to relatively large values of the Ekman number, $E > 10^{-4}$, except for a few numerical experiments [5, 6]. In this study, we extend our investigation to $E = 10^{-5}$ using our new code [7, 8].

At $E = 10^{-5}$, we obtain a strong dipolar solution that produces $\varepsilon = 55$ on average, which is fairly higher than in other previous models. The convection structure consists of a few large-scale

retrograde flows in the azimuthal direction and some localized thin sheet-like plumes (Fig. 1). Considering our small E and large ε , we surmise that the flow structure and the dynamo processes simulated in this study well represent those in a magnetostrophic regime of a spherical-shell dynamo. A detailed term-by-term analysis of the magnetic field amplification processes shows that the magnetic field is amplified through stretching of magnetic lines, which occurs typically through four types of flow: the retrograde azimuthal flow near the outer boundary, the downwelling flow of the sheet plume, the prograde azimuthal flow near the rim of the tangent cylinder, and the cylindrical radially alternating flows of the plume cluster (Fig. 2). The current loop structure emerges as a result of stretching the magnetic lines along the magnetic field by the flow acceleration. The most remarkable effects of the generated

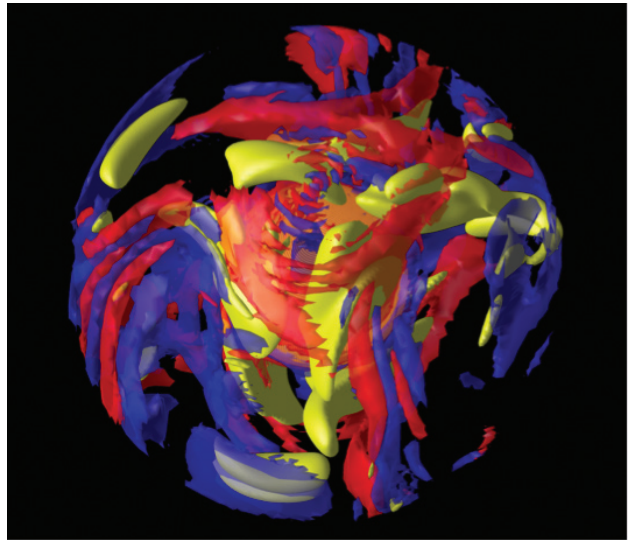


Fig. 2 Bird's-eye view of a snapshot of magnetic field and convection. The magnetic field is represented by yellow isosurfaces of $|B| = 2.5$. The axial vorticity ω_z is also shown by isosurfaces. Positive (negative) values are denoted in red (blue).

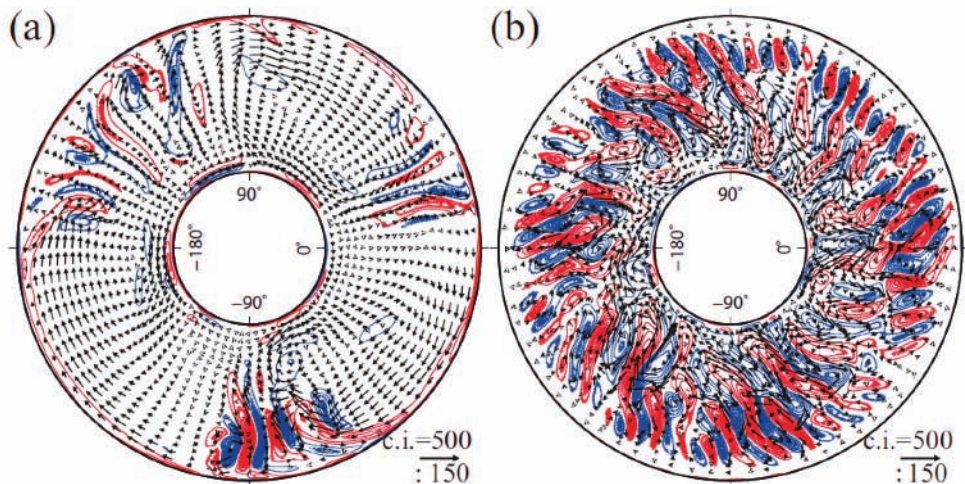


Fig. 1 Snapshot of convection structure on the plane at $z = 0.2$ viewed from the north, where z is the distance from the equatorial plane. Cases for dynamo (a) and purely thermal convection (b) are shown. The axial component of the vorticity (ω_z) is drawn by contour lines. Red (blue) lines represent positive (negative) values. The horizontal component of convection (u_h) is drawn by arrows.

magnetic field on the flow come from the strong azimuthal (toroidal) magnetic field. Similarities of the present model in the convection and magnetic field structures to previous studies at larger and even smaller Ekman numbers suggest universality of the dynamo mechanism in rotating spherical dynamos.

3. Conditions for a large-scale flow structure

The large-scale flow with a strong dipolar magnetic field as shown in the previous section is definitely a preferred convective state in low- E dynamos and we believe that the Earth's core convection is in such a state. However, this is not always the case of low- E dynamos. Sakuraba and Roberts [5] performed two low- E dynamo simulations with different boundary conditions for the core surface temperature and found that the uniform surface-temperature (UST) model did not produce a large-scale flow pattern contrary to the case of the uniform heat-flux (UHF) boundary condition. Here we show that a similar phenomenon can occur when there is a thermally stable layer at

the top of the core. In the present model, the heat flux is uniform at the core surface like the UHF model but zero everywhere. We assume that the outer core is heated from below but a uniform volumetric heat sink in the fluid layer compensates the basal heating. A similar model has been considered to mimic compositional convection (CC) caused by release of lighter elements from the inner core surface [9].

Using dimensionless parameters comparable to the previous study [5], we find that the “CC” (zero-flux) model produces a relatively weaker magnetic field compared to the thermal-convection (TC) model that uses the UHF condition (Fig. 3). The large-scale structure, as seen in the TC model, does not develop very much. The characteristics of the CC model are rather similar to those of the previous UST models [5, 6], in which the energy state tends to be equipartition ($\varepsilon = 1$). If our zero-flux model represents Earth-type compositional convection, the Prandtl number (Pr) should be greater than unity because the diffusion coefficient of the light element is much smaller than

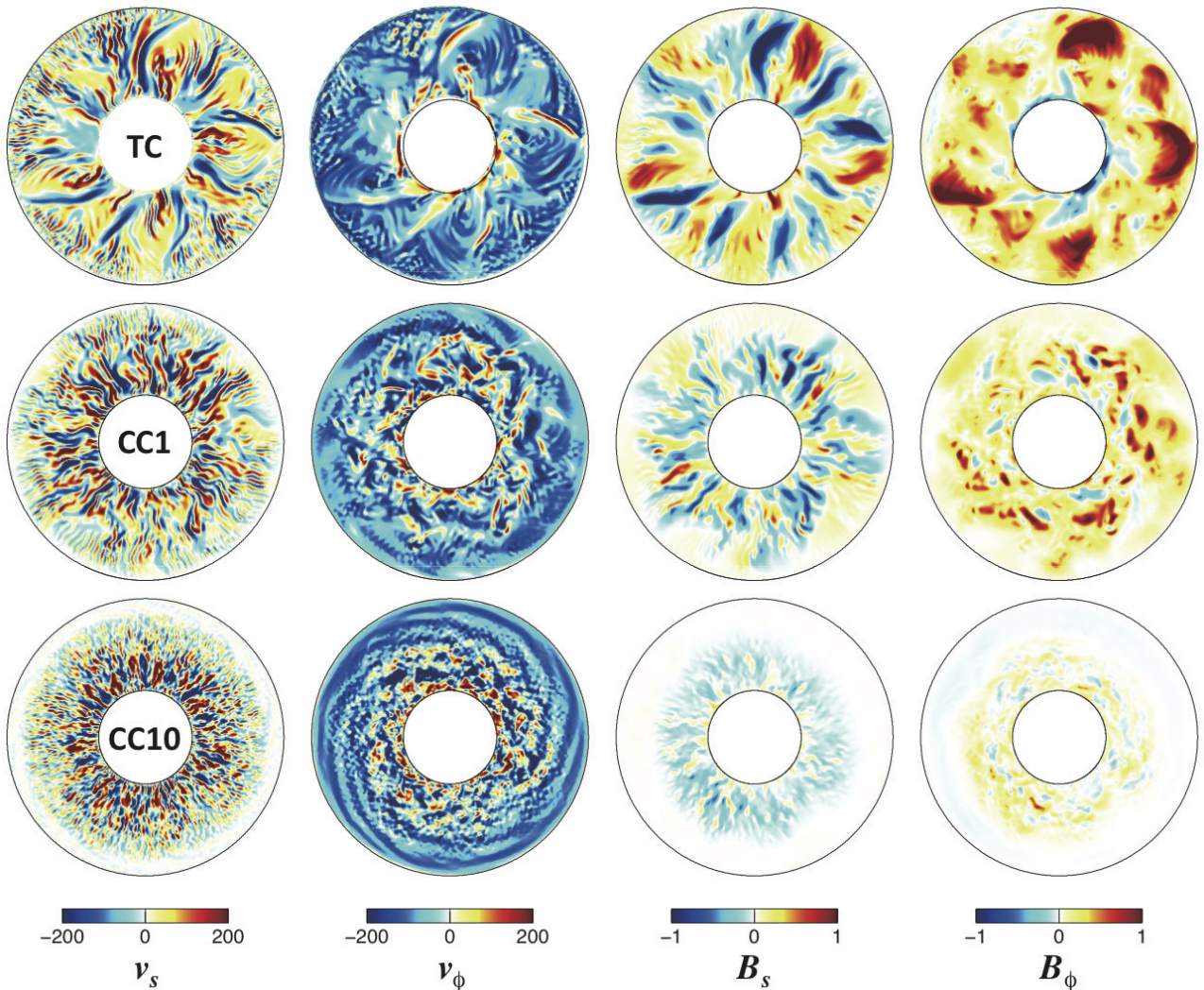


Fig. 3 The convective structures of our TC model of $Pr = 1$ (top), CC model of $Pr = 1$ (middle), and CC model of $Pr = 10$ (bottom). From left to right, the cylindrically radial and the azimuthal velocities, the radial and the azimuthal magnetic fields are shown at $z = 0.1$. The TC model is identical to our previous UHF model [5]. In the CC model, the reference temperature gradient is assumed to be proportional to $r - 1/r^2$, where r is the radius normalized by the core radius.

the thermal diffusivity. Our numerical experiment of $Pr = 10$ indicates that the suppression of the large-scale structure and the decrease of the magnetic energy are more evident than the case of $Pr = 1$.

4. Liquid-metal thermal convection in the presence of a magnetic field and rotation

The study on the nature of thermal convection of liquid metals is essential to understand the dynamics of the Earth's outer core, where Lorentz and Coriolis forces dominate, and experiments on turbulent flows in the presence of a magnetic field (Case I) and rotation (Case II) are of great importance. We performed both laboratory experiments and numerical simulations of Rayleigh-Bénard convection of highly conductive and low- Pr fluids. In many dynamo simulations, Pr is set to be around unity, but the actual value of Pr for liquid metals is $O(10^{-2})$. Here we provide fundamental dataset for realistic liquid metal convection.

Theoretical studies [10, 11] have shown that for highly conductive fluids like liquid metals the axis of the roll structure is forced to align in the direction of the applied magnetic field in Case I, and the Rayleigh number, Ra , at which transition to time-dependent flows occurs is increased. Even at such higher Ra that turbulence develops when the magnetic field is absent,

suppression of turbulence and formation of anisotropic flow structure are expected under a strong magnetic field.

In the laboratory experiments of Case I at higher Ra , we observed four flow regimes depending on Ra and the Chandrasekhar number, Q , which measures the square of the imposed field intensity; that is, a steady two-dimensional roll regime, an oscillatory roll regime, a regime of random reversals of roll-type flow circulations, and a turbulent regime with large-scale structures [12]. In the regime of random reversals, a roll-type structure is dominant in most of the time and the flow keeps its two-dimensionality. However, a new circulation suddenly emerges near the sidewall, triggering a global reorganization that causes reversal of the overall flow direction. The process of the reversal is over in a relatively short time, which is comparable to the circulation time of a convection roll. The reversals of the flow direction occur randomly with a typical time interval between reversals much longer than the circulation time. We performed numerical simulations of magnetoconvection using parameters and boundary conditions comparable to the laboratory experiments and successfully reproduced these four flow regimes (Fig. 4). We analyzed details of the three-dimensional structure in each regime, and clarified the cause of these variations.

In Case II, linear studies on the onset of thermal instability

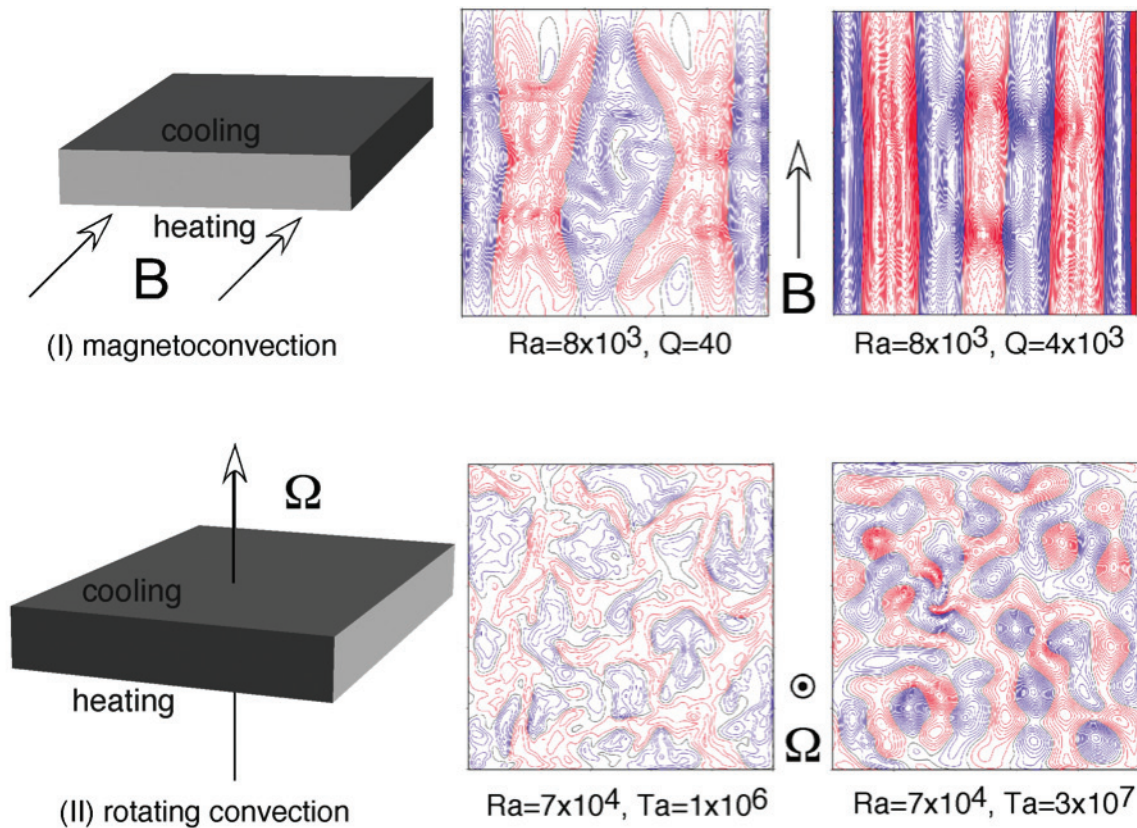


Fig. 4 Setting and result of numerical simulations. (I) Convection under uniform horizontal magnetic field. (II) Convection on a rotating system. Pr of the fluid is 0.025. The contours are flow velocity in vertical direction; red indicates the upward flow, and blue indicates downward flow. In (I), the flow pattern is restricted to be rolls in the direction of magnetic field for larger Q . In (II), the pattern is composed of vortices and gets shorter for larger Ta .

[10] indicate that the critical Rayleigh number is proportional to $Ta^{2/3}$ in an asymptotic form, where $Ta = 4E^{-2}$ is the Taylor number, and overstability occurs for $Pr < 0.6$. The horizontal scale of convection pattern becomes smaller with the increase of Ta . Our numerical results well reproduced the relation of the critical Ra on Ta , depending on Pr (Fig. 4). Convection patterns above the critical Ra are consistent with that observed in the laboratory experiments and theoretical studies.

References

- [1] M. Kono and P. H. Roberts, “Recent geodynamo simulations and observations of the geomagnetic field”, *Rev. Geophys.* 40, 1013. doi:10.1029/2000RG000102, 2002.
- [2] A. Kageyama and T. Sato, “Generation mechanism of a dipole field by a magnetohydrodynamic dynamo”, *Phys. Rev. E* 55, 4617-4626, 1997.
- [3] F. Takahashi and M. Matsushima, “Dynamo action in a rotating spherical shell at high Rayleigh numbers”, *Phys. Fluids*. 17, 076601, 2005.
- [4] J. Aubert, J. Aurnou, and J. Wicht, “The magnetic structure of convection-driven numerical dynamos”, *Geophys. J. Int.* 172, 945-956, 2008.
- [5] A. Sakuraba and P. H. Roberts, “Generation of a strong magnetic field using uniform heat flux at the surface of the core”, *Nature Geosci.* 2, 802-805, 2009.
- [6] T. Miyagoshi, A. Kageyama, and T. Sato, “Formation of sheet plumes, current coils, and helical magnetic fields in a spherical magnetohydrodynamic dynamo”, *Phys. Plasmas*. 18, 072901, 2011.
- [7] F. Takahashi, “Implementation of a high-order combined compact difference scheme in problems of thermally driven convection and dynamo in rotating spherical shells”, *Geophys. Astrophys. Fluid Dyn.* 106, 231-249, 2012.
- [8] F. Takahashi and H. Shimizu, “A detailed analysis of a dynamo mechanism in a rapidly rotating spherical shell”, *J. Fluid. Mech.*, doi:10.1017/jfm.2012.154, in press, 2012.
- [9] C. Kutzner and U. Christensen, “Effects of driving mechanisms in geodynamo models”, *Geophys. Res. Lett.* 27, 29-32, 2000.
- [10] S. Chandrasekhar, *Hydrodynamic and hydromagnetic stability*, Oxford Univ. Press, London, 1961.
- [11] P. A. Davidson, *An Introduction to Magnetohydrodynamics*, Cambridge Univ. Press, Cambridge, 2001.
- [12] T. Yanagisawa, Y. Yamagishi, Y. Hamano, Y. Tasaka, and Y. Takeda, “Spontaneous flow reversals in Rayleigh-Bénard convection of a liquid metal”, *Phys. Rev. E* 83, 036307, 2011.

地球コア対流の理解のための数値シミュレーション

プロジェクト責任者

浜野 洋三 海洋研究開発機構 地球内部ダイナミクス領域

著者

櫻庭 中 東京大学 大学院理学系研究科 地球惑星科学専攻

高橋 太 東京工業大学 大学院理工学研究科 地球惑星科学専攻

清水 久芳 東京大学 地震研究所

柳澤 孝寿 海洋研究開発機構 地球内部ダイナミクス領域

浜野 洋三 海洋研究開発機構 地球内部ダイナミクス領域

地球の冷却に起因するマントル対流とコア対流は、固体地球上に生起するさまざまな自然現象の原因をつかさどる、根本的な物理プロセスであると考えられる。われわれはこれまで、マントルとコアという2つの対流系を、より実際の地球に近い条件のもとで、数値的にモデリングする研究をおこなってきた。本年度は、そのうちとくにコアの対流に焦点をあてて研究をおこなったので、その成果を報告する。

地球のコア対流は、運動方程式における粘性項と慣性項とが無視できる、いわゆる磁気地衡流状態にあると考えられる。コリオリ力に対する粘性力の比はエクマン数という無次元数であらわされ、これが小さいことがまず重要である。さらに慣性力に対するローレンツ力の比は、端的には対流の運動エネルギー密度に対する磁気エネルギー密度の比としてあらわすことができ、この比が大きいことも磁気地衡流の条件である。われわれは、比較的小さいエクマン数のもとでダイナモの数値シミュレーションをおこない、これまでの同様の研究に比べて、著しく大きい磁気エネルギー密度比をもつ解を見いだした。そこでは、東西方向の波数が小さい、大規模対流構造が顕著であり、これが磁気地衡流の一般的性質であると推察する。磁場の生成機構を詳細に調べたところ、とくに西向きの大規模流による磁力線の引き延ばし効果が重要であることがわかった。

地球のコアでは、内核成長にともない軽元素が液相に濃集する結果、組成対流もおこっていると考えられる。これをモデル化するために、コア表層に熱的に安定な層がある場合のダイナモシミュレーションをおこなった。その結果、通常の熱対流モデルでみられる大規模対流構造が顕著でなくなり、磁場も弱まることがわかった。これは、コア表面の温度を水平方向に一樣とする境界条件のもとでの熱対流が駆動するダイナモの解と、特徴がよく似ており、磁気エネルギーと運動エネルギーとが等分配的になる傾向を示唆している。さらにこの傾向は、プラントル数を大きくするとより顕著になる。

コアの乱流的なふるまいをよりよく理解するために、液体金属のベナール対流の室内実験をおこない、それをさらに数値的にモデリングし、解析した。一樣磁場を印加した磁気対流の場合について、レイリー数と印加磁場強度を系統的に変えてシミュレーションをおこなったところ、室内実験でみられた4つの特徴的な対流状態がよく再現された。そのうちあるパラメータ領域では、印加磁場方向にそろったロール状対流セルが、比較的短時間のうちに、循環する方向が逆転するという興味深い現象が再現された。

キーワード:地球ダイナモ, 地磁気, コア対流, レイリー・ベナール対流, 磁気流体力学

FDM Simulation of Broadband Seismic Wave Propagation in 3-D Heterogeneous Structure using the Earth Simulator

Project Representative

Takashi Furumura

Center for Integrated Disaster Information Research, Interfaculty Initiative in Information Studies / Earthquake Research Institute, The University of Tokyo

Authors

Shunsuke Takemura^{*1}, Takashi Furumura^{*1,2} and Takuto Maeda^{*1,2}

*1 Earthquake Research Institute, The University of Tokyo

*2 Center for Integrated Disaster Information Research, Interfaculty Initiative in Information Studies, The University of Tokyo

We conduct finite-difference method (FDM) simulation of broadband ($f = 0.125\text{--}4$ Hz) seismic wave propagation in southwestern Japan using the heterogeneous structure model including surface topography and small-scale velocity fluctuation in the crust and mantle. By the comparison of dense seismic observations and FDM simulations, we examine the effect of small-scale heterogeneities in the seismic wavefield. The observed seismogram envelope shape and longer duration coda waves are well reproduced by introducing surface topography to ordinary layered structure model, although the simulated spatial amplitude pattern and amplitude decay are not good agreement with observation. Heterogeneous structure model including both topography and velocity fluctuation in the crust and mantle can reproduce the observed seismic wave envelope shape, amplitude decay and maximum amplitude pattern.

Keywords: High-frequency seismic wave, heterogeneity, topography, scattering

1. Introduction

Broadband seismic wavefield including low-frequency to high-frequency ($f > 1$ Hz) seismic wavefields is very complicated, because the scattering of seismic waves due to small-scale heterogeneities in the crust and upper-mantle structure along the propagation path gradually dominates in the high-frequency seismic wavefield with frequencies over $f > 1$ Hz. Observed characteristics of the low-frequency ($f < 0.5$ Hz) wavefields can be reproduced by using the layered-structure model in which the large-scale structure is described by a number of layers with different velocity, density and attenuation parameters (e.g., Furumura et al., 2003)[1]. On the other hand, propagation features of the high-frequency ($f > 1$ Hz) seismic waves are completely different compared with those of low-frequency seismic waves due to the dominance of small-scale heterogeneities with shorter characteristic scale than wavelength of high-frequency seismic waves.

A few studies have demonstrated that the finite-difference-method (FDM) simulation of seismic wave propagation using a composite model including small-scale velocity fluctuation embedded over averaged layered-structure model can reproduce the observed characteristics of the high-frequency seismic waves very effectively (e.g., Nielsen et al., 2003 [2]; Furumura

and Kennett, 2005 [3], 2008 [4]; Kennett and Furumura, 2008 [5]). However, in these studies, the effect of the scattering of high-frequency waves due to surface topography was not examined. Kumagai et al. (2011)[6] may be an exception who recently conducted a numerical simulation for seismic wave propagation at Mt. Cotopaxi using a complex, realistic surface topography model with fluctuation of velocities in the structure. Through their simulations, Kumagai et al. demonstrated that the simulated high-frequency ($f > 5$ Hz) seismic wavefield is strongly influenced by both surface topography and velocity fluctuation in the subsurface structure.

In this report, we simulate broadband seismic wavefield including low- to high-frequency components using the heterogeneous layered-structure model including crust-mantle (Moho), mid-crust (Conrad) interfaces etc., and with surface topography and stochastic random velocity fluctuation in each layer. By the direct comparison of simulated and observed waveforms, we examine the effects of heterogeneities on the broadband seismic wavefields.

2. FDM simulation of broadband seismic wave propagation in 3-D heterogeneous structure

We conduct FDM simulation of seismic wave propagation in the Chugoku–Shikoku area of southwestern Japan to examine the effects of heterogeneous structures on the seismic wavefield by comparison of the simulated waveforms and the observations at seismic stations. Figure 1 shows the region of the FDM simulation and distribution of the broadband F-net, and strong motion K-NET and KiK-net stations. The model of FDM simulation is covering the zone 204.8 km by 204.8 km by 64 km, which is discretized by 0.1 km in horizontal direction and 0.05 km in vertical direction. To take the complex topography into account in the model, we employ a finer grid model in the vertical direction. The seismic wave propagation at each grid point in the elastic model is calculated by solving the equation of motion in 3-D based on the 4th order staggered-grid FDM in space and 2nd-order scheme in time (e.g., Graves, 1996) [7]. To conduct large-scale 3-D FDM simulations of seismic

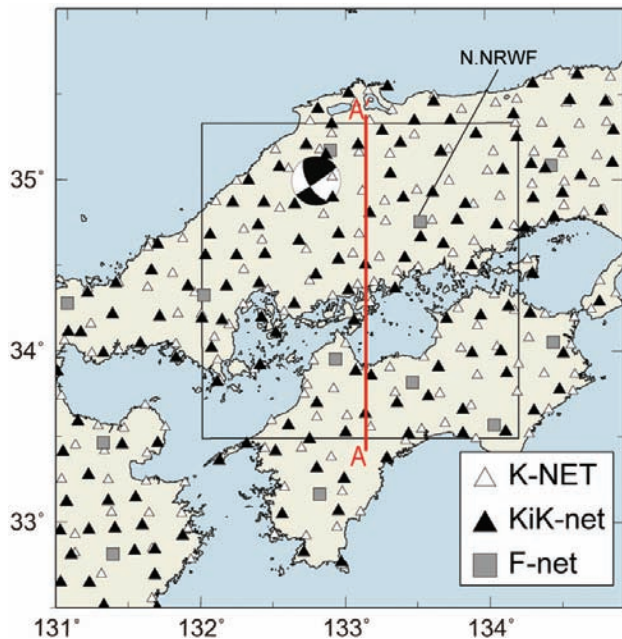


Fig.1 Model region and station distribution. Black triangle, white triangle, and gray square denote K-NET, Hi-net/KiK-net, and F-net stations, respectively. The squared region inside the map is the area of the FDM simulation of seismic wave propagation.

wave propagation, we employ a technique involving domain partitioning for parallel FDM using a large number of processors using a Message Passing Interface (MPI) for inter-processor communication (e.g., Furumura and Chen, 2004 [8], 2005 [9]).

The 3-D seismic velocity model used in this simulation is constructed according to the heterogeneous crust and upper-mantle structural models derived based on the receiver function studies (e.g., Shiomi et al., 2004 [10], 2007[11]) with the upper plane of the Philippine Sea plate and the Moho and Conrad discontinuities. The average P - and S -wave velocities, density, and attenuation (Q_p and Q_s) parameters of each layer are shown in Table 1. The minimum average S -wave velocity is $V_s = 3.1$ km/s. It is expected that the scattering and amplification of seismic wave due to variation in the very shallow layer, which has a depth of less than several ten meters beneath each station and S -wave velocity below $V_s < 3.1$ km/s, may be difficult to handle in the present FDM simulations. However, it is confirmed in the Chugoku-Shikoku area that the variation of the site amplification factors estimated by the coda-normalization method is not so strong to cause strong variation at each station as is often observed in compared northern Japan (Takemoto et al., 2011 [12]).

A complex topography model with a 50-m resolution provided by the Geospatial Information Authority of Japan is used in the present simulation. In order to achieve the precise simulation of high-frequency seismic scattering due to topography, we apply suitable boundary conditions for the irregular solid/air boundary for FDM simulation. Though the simulation of seismic wave propagation is conducted based on 4th-order staggered grid FDM, we use 2nd-order FDM across the solid/air boundary to realize accurate free-surface boundary condition (e.g. Maeda and Furumura, 2011)[13].

Small-scale velocity heterogeneities in the model are constructed by stochastic random velocity fluctuations in 3-D space $\zeta(x,y,z)$ embedded over a uniform background velocity V_0 , which is described as $V(x,y,z) = V_0[1+\zeta(x,y,z)]$. The velocity fluctuation models for the crust and upper-mantle structure are stochastically characterized by an exponential-type PSDF with parameters of the correlation distance $a = 5$ km and rms strength $\varepsilon = 0.05$ in the crust, and $a = 20$ km and $\varepsilon = 0.02$ in the mantle

Table 1 Average background velocities, density, and attenuation coefficients in each layer.

Medium Column	V_p [km/s]	V_s [km/s]	ρ [kg/m ³]	Q_p	Q_s
Air	0.0	0.0	1.0	0	0
Upper crust	5.50	3.10	2600	300	300
	6.00	3.53	2700	680	400
Lower crust	6.70	3.94	2800	680	400
Mantle	7.80	4.60	3200	850	500
Philippine Sea plate	5.50	3.10	2600	300	300
	6.80	4.00	2900	510	300
	8.00	4.70	3200	850	500

(e.g. Saito et al., 2005 [14]; Takemura et al., 2009 [15]).

Figure 2 shows an example of the S -wave velocity structure along the cross-section from south to north of the simulation model, including homogeneous and heterogeneous crust and mantle structures, the shallowly dipping Philippine Sea plate, and irregular surface topography. Most present simulations of seismic wave propagation use layered structure model (Fig. 2a). Based on this, we introduced the surface topography (Fig. 2b) and velocity fluctuation (Fig. 2c) into the layered structure model. Such layered structure and surface topography are determined directly from geophysical and geological experiments, although the velocity fluctuations are not estimated directly from the experiments and so we assumed here stochastically.

The seismic source at the Shimane–Hiroshima boundary which occurred in May 13, 2007 at depth of 8 km is used in this study. Focal mechanism with strike/dip/rake = 56/86/152 and moment magnitude of $M_w = 4.3$ for this event is derived by a CMT solution provided by the F-net. To model the source

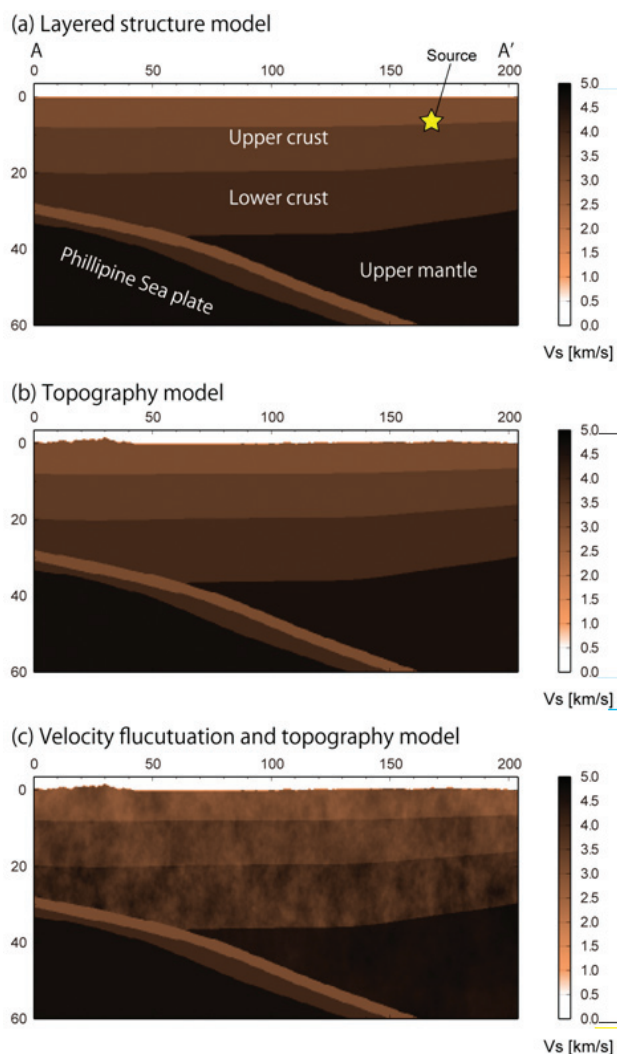


Fig.2 2-D vertical profiles of the S -wave velocity structure cross-section of the 3-D heterogeneous models along the path A-A' (Fig. 1). (a) Layered-structure model, (b) topography model, and (c) both velocity fluctuation and topography model.

rupture process of a small earthquake, we assume a normalized moment rate function that is represented by the asymmetric cosine function (Ji et al., 2003) [16] with dominant period 0.5 sec.

Through a set of experiments, we compare simulated waveforms with observed waveforms in the frequency range of 0.01–5 Hz, because it is found that the high-frequency components of the observed source spectrum drop below noise level over this frequency band.

3. Comparison of simulation results and dense seismic observations

The FDM simulation results for seismic wave propagation using various heterogeneous models are shown in Fig. 3 as paste ups of the radial-component velocity waveforms derived by the simulation using different structural models (Figs. 3b–d), and that of the observed Hi-net record (Fig. 3a) for frequency range from 0.125–4 Hz. Each trace of the seismogram paste up is multiplied by its hypocentral distance to compensate geometrical spreading factor of the body waves.

The observed waveforms shown in Fig. 3a show very much complicated properties with multiple reflected signals and long-duration P - and S -coda waves. On the other hand, the simulated waveform from the layered-structure model shown in Fig. 3b consists of a number of spiky signals for both P and S waves, with no clear coda waves generated following the body P and S waves. These spiky signals are developed by coherent multiple reflections of the direct P and S waves from each layer in the model. Such anomalous spiky signals developed by the layered model are weakened significantly by introducing the irregular topography at the top of the model as the incoherent multiple reflections disrupt the coherent pattern of multiple reflections, and also by enhancing the scattering of high-frequency seismic waves (Fig. 3c). The long-duration coda waves due to the scattering of seismic waves in the irregular topography also appear following direct wave arrivals. It is confirmed that the variation of the waveform amplitude at each station is very strong due to localized amplification of seismic wave caused by the surface topography in nearby stations. By adding the velocity fluctuation in each layer, the properties of the decay rate of wave amplitude with increasing epicentral distance match to the observations due to the loss of seismic energy by strong seismic wave scattering of high-frequency signals in the heterogeneous structure (Fig. 3d).

In order to compare the observed and simulated broadband waveforms derived by the FDM simulation using different structural models, including surface topography and velocity fluctuations, we compare the EW-component broadband (0.125–4 Hz) velocity waveforms recorded at the F-net station of N.NRWF at hypocentral distance of 73 km between simulations and observation. Figure 4 shows the observed and simulated seismograms of EW component recorded at N.NRWF. For the

observed F-net waveform (Fig. 4a), the amplitude of *P* wave is slightly less than later *S*-wave amplitude. However, the simulated waveforms derived from the layered structure model (Fig. 4b) and topography model (Fig. 4c) show much larger and impulsive *P*-wave signal in the EW component compared

with observation. By introducing velocity fluctuation in the simulation model (Fig. 4d), the *P*-wave amplitude clearly decrease compared with other two models. It is indicating that the cause of amplitude decay of *P* wave may be the seismic wave scattering due to velocity fluctuation along propagation

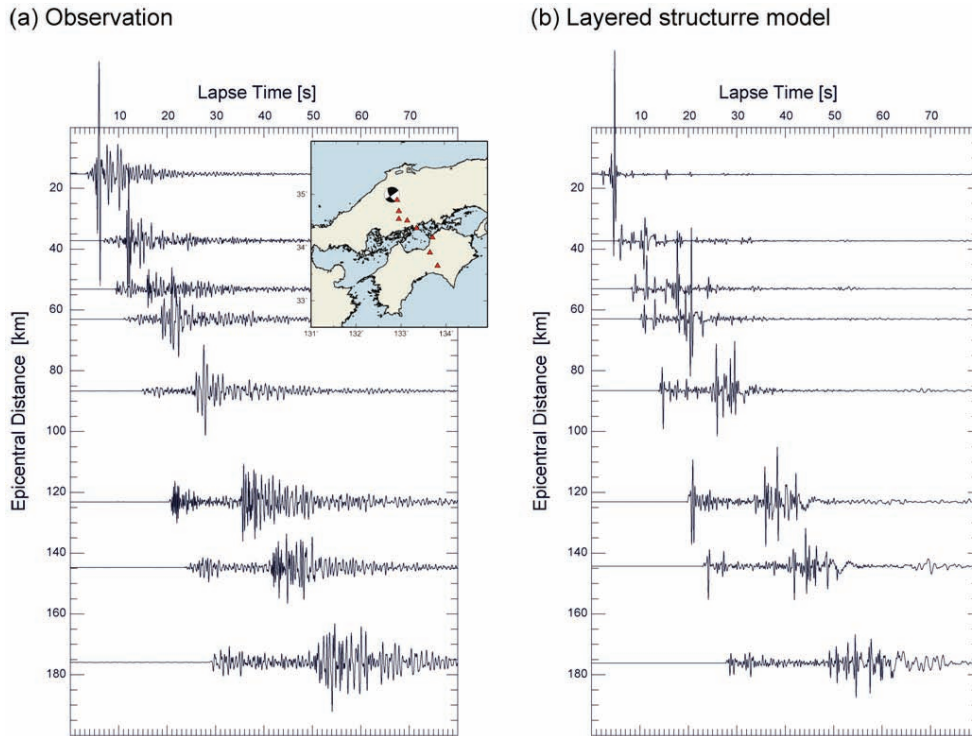


Fig. 3 Comparison of the observed and simulated waveforms of radial component velocity motion for broadband (0.125-4 Hz) waveforms. (a) Observed waveforms at Hi-net stations and (b) simulated waveforms using the layered-structure model. Each trace is multiplied by hypocentral distance to compensate geometrical spreading.

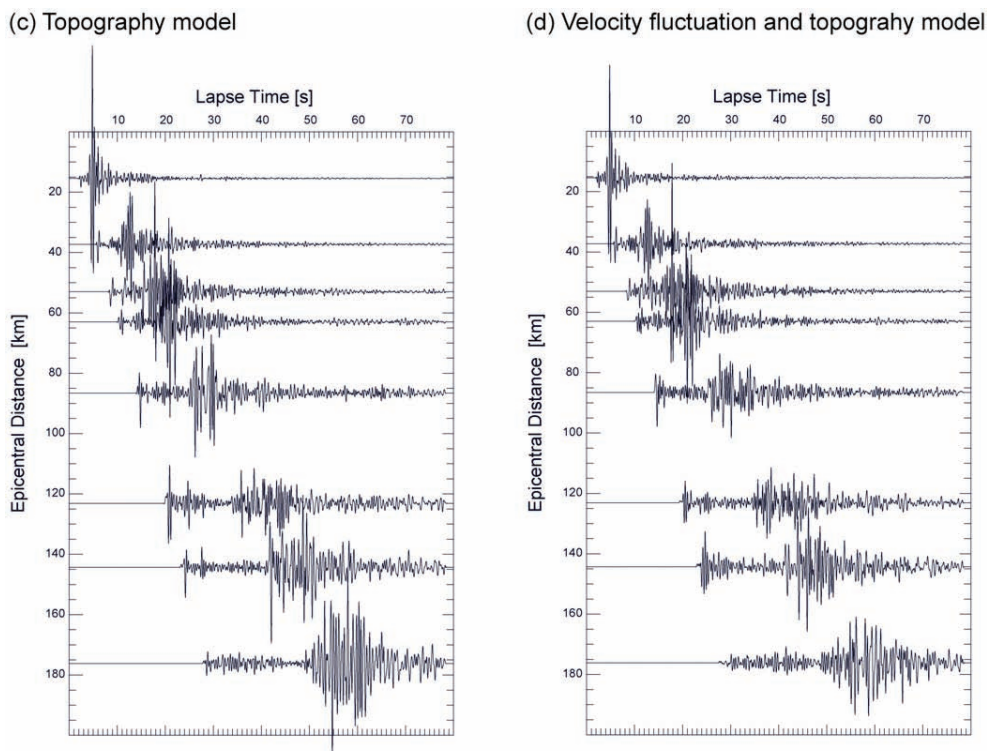


Fig. 3 (continued) (c) simulated waveforms using the topography model and (d) both velocity fluctuation and topography model.

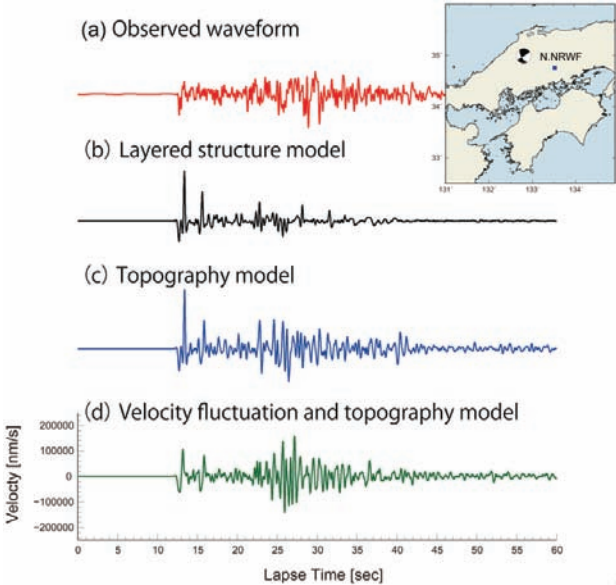


Fig. 4 Comparison of simulated and observed broadband ($f = 0.125\text{--}4$ Hz) seismic waves of EW component recorded at N.NRWF station (Fig. 1).

path. FDM simulation in the layered structure model with topography and suitable velocity fluctuation can reproduce the observed waveform shape, direct-wave duration, later coda excitation and amplitude ratio.

In the case of homogeneous medium, it is theoretically predicting that the spatial amplitude pattern of S wave is showing four-lobe pattern. However, some studies demonstrated that in high frequency ($f > 1$ Hz), the spatial pattern of maximum S -wave amplitude shows almost isotropic pattern (e.g. Takemura et al., 2009)[15]. Here, we examine the spatial pattern of the peak ground velocity for the high-frequency band derived by the simulation using different structural model and observation. Figure 5 shows the spatial distribution of maximum S -wave amplitude of the ground velocity examined at the K-NET and the KiK-net strong motion stations. The resultant pattern of ground motions derived from the simulation of the layered-structure and topography models maintain the four-lobe portion of the S -wave radiation pattern for the strike-slip fault source (Figs. 5a, b). However, in the simulation result, including both velocity fluctuation and topography model (Fig. 5c), the

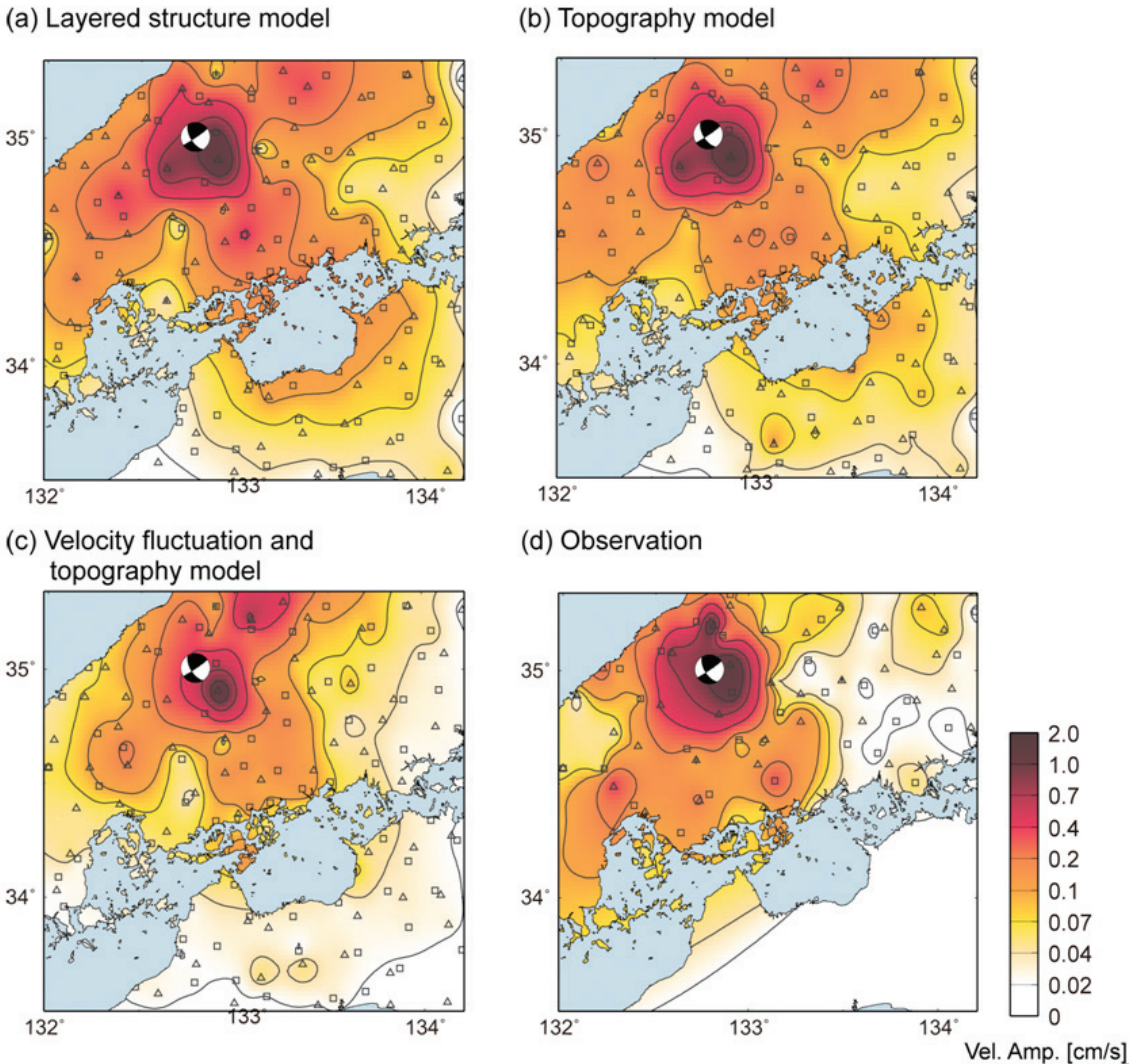


Fig.5 Comparison the maximum S -wave amplitude distribution in the high-frequency ($f > 1$ Hz) band derived from (a-c) simulation using different heterogeneous model and (d) observation at K-NET and KiK-net station at free surface.

pattern is considerably distorted, showing almost isotropic pattern at longer distances, which is almost comparable with observations (Fig. 5d). However, the observed amplitude pattern shows a more complicated pattern that may be caused by other heterogeneities, such as site amplification, mesoscale heterogeneities, and source rupture processes.

4. Conclusion

We conducted FDM simulations of broadband seismic wave propagation using ordinal layered structure model with realistic surface topography and small-scale velocity fluctuation in order to construct the heterogeneous structure model which can explain characteristics of complex observed seismic wavefield.

The ordinal layered structure model can not reproduce complex fetures of the observed broadband seismic wavefield. By introducing surface topography and suitable small-scale velocity fluctuation models in the model, complex body waves and longer duration coda waves appear in simulated seismograms. However, the observed maximum amplitude pattern and amplitude decay derived from the simulation in the model with topography alone don't have good agreements with observations. One of the causes of this discrepancy between observation and simulation in the model with topography alone is the scattering properties of seismic waves on the surface topography, which seismic wave scattering due to topography occurs on the free surface only. Simulation results derived from both velocity fluctuation and topography model match to the observed maximum amplitude pattern and amplitude decay because of strong seismic scattering due to small-scale velocity fluctuation along propagation path.

For estimating strong ground motion disaster associated with larger earthquakes, the contribution of the site amplification effect due to shallow low-velocity layers is also very important. Therefore, in the future, we should consider such site effect on the high-frequency seismic wave to achieve more practical strong motion prediction for feature large earthquakes.

Acknowledgements

We acknowledge the National Research Institute for Earth Science and Disaster Prevention, Japan (NIED) for providing the K-NET, KiK-net, Hi-net and F-net waveform data and CMT solution. The computations were conducted on the Earth Simulator at the Japan Agency for Marine-Earth Science and Technology (JAMSTEC) under the support of a joint research project "Seismic wave propagation and strong ground motion in 3-D heterogeneous structure" between the Earthquake Research Institute, The University of Tokyo and the Earth Simulator Center. Shunsuke Takemura is grateful for support from Grant-in-Aid for JSPS (the Japan Society for Promotion of Science: grant No. 21.3509) fellows. Some figures in the present study were drawn using the Generic Mapping Tools (GMT) software package developed by Wessel and Smith (1998).

References

- [1] T. Furumura, K. Koketsu, and B. L. N. Kennett, "Visualization of 3D wave propagation from the 2000 Tottori-ken Seibu, Japan, earthquake: observation and numerical simulation" *Bull. Seismol. Soc. Am.*, 93, pp.870-881, 2003.
- [2] L. Nielsen, H. Thybo, A. Leavander, and L. N. Solodilov, "Origin of upper-mantle seismic scattering-evidence from Russian peaceful nuclear explosion data" *Geophys. J. Int.*, 154, pp.196-204, 2003.
- [3] T. Furumura and B. L. N. Kennett, "Subduction zone guided waves and the heterogeneity structure of the subducted plate: intensity anomalies in northern Japan" *J. Geophys. Res.*, 110, pp.B10302, 2005.
- [4] T. Furumura and B. L. N. Kennett, "A scattering waveguide in the heterogeneous subducting plate" *Advances in Geophysics, Scattering of Short-Period Seismic Waves in Earth Heterogeneity*, Eds. H Sato and M. Fehler, Elsevier, 50, Chap.7, pp.195-217, 2008.
- [5] B. L. N. Kennett and T. Furumura, "Stochastic waveguide in the lithosphere: Indonesian subduction zone to Australian craton" *Geophys. J. Int.*, 172, pp.363-382, 2008.
- [6] H. Kumagai, T. Saito, G. O'Brien, and T. Yamashita, "Characterization of scattered seismic wavefields simulated in heterogeneous media with topography" *J. Geophys. Res.*, 116, pp.B03308, 2011.
- [7] R. W. Graves, "Simulating seismic wave propagation in 3D elastic media using staggered-grid finite differences" *Bull. Seismol. Soc. Am.*, 86, pp.1091-1106, 1996.
- [8] T. Furumura and L. Chen, "Large scale parallel simulation and visualization of 3D seismic wavefield using Earth Simulator" *CMES*, 6, pp.153-168, 2004.
- [9] T. Furumura and L. Chen, "Parallel simulation of strong ground motions during recent and historical damaging earthquakes in Tokyo, Japan" *Parallel Computing*, 31, pp.149-165, 2005.
- [10] K. Shiomi, H. Sato, K. Obara, and M. Ohtake, "Configuration of subducting Philippine Sea plate beneath southwest Japan revealed from receiver function analysis based on the multivariate autoregressive model" *J. Geophys. Res.*, 109, pp.B04308, 2004.
- [11] K. Shiomi, M. Matsubara, Y. Ito, and K. Obara, "Simple relation between seismic activity along Philippine Sea slab and geometry of oceanic Moho beneath southwest Japan" *Geophys. J. Int.*, 173, pp.1018-1029, 2008.
- [12] T. Takemoto, T. Furumura, T. Saito, T. Maeda, and S. Noguchi, "Spatial- and Frequency-dependent properties of site amplification factors in Japan derived from coda normalized method" *Bull. Seismol. Soc. Am.*, in press, 2012.
- [13] T. Maeda and T. Furumura, "FDM simulation of seismic

waves, ocean acoustic waves, and tsunami based on tsunami-coupled equation of motion” *Pure Appl. Geophys.*, published online, doi:10. 1007/s00024-011-0430-z, 2011.

- [14] T. Saito, H. Sato, M. Ohtake, and K. Obara, “Unified explanation of envelope broadening and maximum amplitude decay of high-frequency seismograms based on the envelope simulation using Markov approximation: Forearc side of the volcanic front in northeastern Honshu, Japan” *J. Geophys. Res.*, 110, pp.B01304, 2005.
- [15] S. Takemura, T. Furumura, and T. Saito, “Distortion of the apparent S-wave radiation pattern in the high-frequency wavefield: Tottori-Ken, Seibu, Japan, earthquake of 2000” *Geophys. J. Int.*, 178, pp.950-961, 2009.
- [16] C. Ji, D.V. Helmberger, D.J. Wald, and K.F. Ma, “Slip history and dynamic implication of the 1999 Chi-Chi, Taiwan, earthquake” *J. Geophys. Res.*, 108, pp.2412, 2003.

地球シミュレータによる3次元不均質媒質中を伝播する広帯域地震動シミュレーション

プロジェクト責任者

古村 孝志 東京大学 大学院情報学環総合防災情報研究センター
東京大学 地震研究所

著者

武村 俊介^{*1}, 古村 孝志^{*1,2}, 前田 拓人^{*1,2}

*1 東京大学 地震研究所

*2 東京大学 大学院情報学環総合防災情報研究センター

西南日本を対象として、小さなスケールの速度不均質構造と実際の地表面形状を含んだ構造モデルを用いて差分法による広帯域地震動シミュレーションを行った。高密度な地震観測網で得られた観測記録とシミュレーション波形を比較することで、それぞれの不均質構造が地震波動場におよぼす影響を検討した。その結果、地形や速度ゆらぎなどの短波長不均質構造による地震波散乱によって、観測波形に見られる複雑な実体波やCoda波が励起していることが明らかとなった。但し、地形のみを考慮したモデルでは最大振幅の空間分布や距離減衰の様子を再現することができず、速度ゆらぎと表層地形の双方を仮定することによって、観測される地震動の包絡線形状、最大振幅の空間変化を再現することができた。

キーワード:地震, 高周波数地震動, 不均質構造, 地形, 地震波散乱

Development of Advanced Simulation Methods for Solid Earth Simulations

Project Representative

Mikito Furuichi

Institute for Research on Earth Evolution, Japan Agency for Marine-Earth Science and Technology

Authors

Mikito Furuichi^{*1}, Akira Kageyama^{*2}, Takehiro Miyagoshi^{*1}, Masanori Kameyama^{*3}, Nobuaki Ohno^{*4}, Mamoru Hyodo^{*1}, Takashi Nakagawa^{*1} and Kensuke Yokoi^{*5}

*1 Institute for Research on Earth Evolution, Japan Agency for Marine-Earth Science and Technology

*2 Graduate School of System Informatics, Kobe University

*3 Geodynamics Research Center, Ehime University

*4 Graduate School of Simulation Studies, University of Hyogo

*5 Cardiff University

Numerical planet: We have developed the simulation code for the core formation process by solving the 3-D Stokes flow motion with the free surface under the self-gravitating field. Our simulation schemes are designed for the massively parallel/vector supercomputer system Earth Simulator 2(ES2). In this FY, in order to investigate the core formation with the impact of planetesimal, we implement the impact-differentiation melting model which is parameterized on the basis of a theoretical model. The simulation result suggests that the PP material could have survived impact events in the deep interior because of the thick mantle that formed before giant impacts. **Geodynamo:** We have done product runs by using newly developed magnetohydrodynamic dynamo code which can deal with length-of-day variation. We found there is a phase gap between length-of-day variation and geomagnetic field variation. In the long period case (20,000 years), amplitude of geomagnetic field variation is several ten percent, while short period case (200 years) it is about one percent. These trends match the observational geomagnetic field variation. **Mantle convection:** We are also developing a simulation code of mantle convection which includes the effect of two-phase flow, i.e., molten and solid phases. By properly adapting the solution techniques for advection by non-solenoidal and multi-dimensional flows, we successfully solved a coupled system with thermal convection and two-phase motion by permeable flow.

Keywords: Geodynamo simulation, Length-of-Day variation, Yin-Yang grid, Mantle convection, Core formation, Stokes flow, mixed precision arithmetic, Two-phase flow, Permeable flow

1. Development of numerical planet simulation code (Furuichi)

Development of the Stokes flow simulation code which can deal realistic mechanical boundary (surface) conditions is an interesting challenge for the field of computational geoscience, because such Stokes system is relevant to the long-time scale evolution of the planetary interior. Our new solution code named “Nplat”, can solve the Stokes flow motion with free surface under a self-gravitation by using the sophisticated algorithms designed for ES2 [1-4]. Expressing the free surface motion, a stick air layer, which is the low viscosity layer surrounding the planetary surface, is assumed. An ill conditioned Stokes problem of the finite difference discretization on a staggered grid, is solved by iterative Stokes flow solver which is robust to large viscosity jumps by using a strong Schur complement

preconditioner and mixed precision arithmetic utilizing the double-double method [3].

In this FY, with the simulation code developed in this project, we investigate the growing planet with the core formation by the impact of planetesimal. The formation of a metallic core is widely accepted as the major differentiation event during the planetary formation process. The early Earth hypothesis also suggested that the core formation process would be an important for understanding the initial condition (both thermal and chemical) of mantle convection.

Our simulation starts from the proto-planet (PP) with Martian size under the self-gravitating field. The core formation occurs when the planet experiences the large impact assumed with adding the mixture of silicate and metal rich materials to the planetary surface. This setup simplifies the differentiated

melt fraction of the magma pond. The sinking metal layer in planetary interior and the post-impact rebound of planetary surface are captured with the deformable free surface with updating the gravity potential field.

Figures 1 (a)–(c) show temporal variations in the simulated core formation process caused by a number of impacts. The time interval of impacts is set as a constant $\delta t = 0.01\text{Ma}$, the size of impactor is set as 10% of the volume of the growing planet. Figure 1 (a) is a snapshot at the first impact. Figure 1 (b) shows that the metal-blob at the first impact sinking into the center when second impact occurs. After several impacts, the accumulated silicate mantle covers a planetary surface and the metal-rich material form the core at the center. At the end of the simulation, we find the presence of PP fractions above the metallic core in Fig. 1 (c). It implies that the dynamical change of the internal structure during core formation could lead to the remaining dense PP material on the CMB. This result indicates the new hypothetical scenario of the formation process of the primordial material layer suggested by geochemical and seismological studies.

2. Geodynamo simulation (Miyagoshi)

The length-of-day variation of the Earth probably affects outer core convection and geomagnetic field. For example, Hamano (1992) pointed out relation between geomagnetic field variation and length-of-day variation associated with Milankovitch cycle [5]. However, there are no geodynamo models which can deal with length-of-day variation effect. We developed magnetohydrodynamic geodynamo code which deals with the length-of-day variation in the last fiscal year and have done product runs by the code in this fiscal year. The Yin-Yang dynamo model [6, 7] was developed for this purpose.

From geomagnetic field observation, during last eighty thousand years, geomagnetic field intensity varies in the period of tens of thousands years. The amplitude of its variation is several tens of percent [8]. On the other hand, in shorter time scale (recent one hundred years), geomagnetic field intensity

variation is also seen. The period of variation is several decades, and the amplitude is about one percent [9]. Between long and short time scales, the amplitude of variation is very different. So we have investigated geomagnetic field variation in both long and short period case.

We have done numerical simulations in both long and short period cases. The model parameters are as follows. The Ekman number, Rayleigh number, Prandtl and magnetic Prandtl numbers are $1.9\text{E-}5$ and $1.5\text{E}8$, unity and unity respectively. The rotational speed variation is given as a sine function depending on time with amplitude of two percent.

In the long period case, the period is the same as the magnetic diffusion time. It corresponds to twenty thousand years in the Earth. This also corresponds to one of the Milankovitch cycle. Numerical simulation results show the length-of-day variation causes variation of magnetic energy in the outer core, kinetic energy of convection, and magnetic dipole moment. The amplitude of magnetic energy and dipole moment variation is about thirty percent, which is much larger than the amplitude of the rotational speed variation (two percent). We found the phase of magnetic energy variation is not the same as the phase of the rotational speed variation. The phase difference between magnetic energy and rotational speed is π over two. In addition, the phase difference between magnetic energy and time difference of rotational speed is π . The phase of magnetic dipole moment is the same as that of magnetic energy. On the other hand, the phase difference between magnetic energy and convection kinetic energy variation is π .

In the shorter period case, the period is given by 1 percent of the magnetic diffusion time. It corresponds to two hundred years in the Earth. In this case, magnetic dipole moment and convection kinetic energy varies although magnetic energy does not vary. The amplitude of magnetic dipole moment variation is about one percent, which is much smaller than the long period case. This tendency matches the observational geomagnetic field variation.

The variation depends on the Ekman number. We calculated

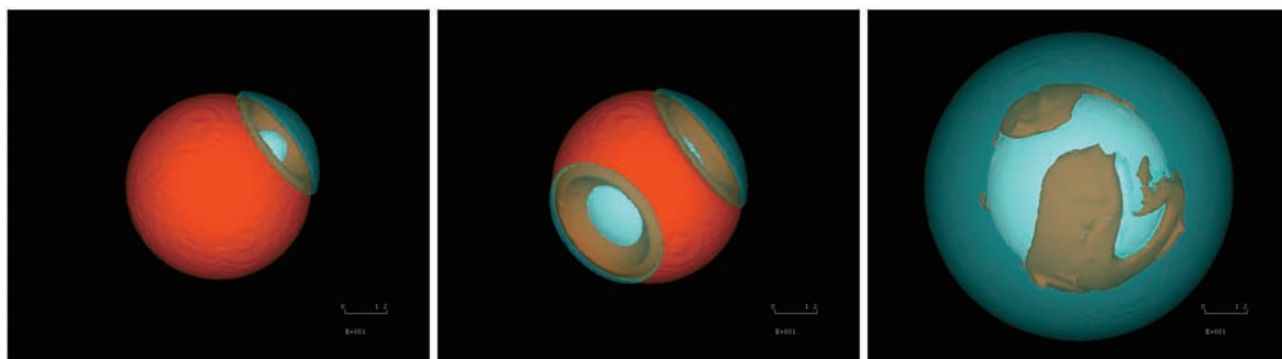


Fig. 1 Snapshot of the simulated evolution of the planet with core formation by the impact (a) initial state with first impact; (b) intermediate state with second impact; (c) final state with a radius $r = 0.8 R_e$. The white and orange isosurface represent metal-rich and PP materials respectively. The semi-transparent green iso-surface indicates the silicate rich material. In this simulation viscosity of metal-rich, PP and silicate-rich materials are 10^{20} [Pa.s], 10^{22} [Pa.s] and 10^{19} [Pa.s] respectively.

the case with high Ekman number ($O(10E-4)$) and rotational speed variation amplitude 6.7%. In this case, magnetic energy as well as convection kinetic energy does not vary although the amplitude is larger than the previous low Ekman number ($O(10E-5)$) case. The Ekman number represents the intensity of rotational effect. So it can be intuitively understood that larger amplitude is needed in high Ekman number cases. In the Earth's outer core, the Ekman number ($O(10E-15)$) is much smaller than that of our model (and today's all geodynamo models). So the geomagnetic variation by length-of-day variation is expected to easily occur because necessary amplitude becomes small.

3. Development of mantle convection simulation code (Kameyama)

In this project, we are developing a new simulation code of mantle convection, based on our code named "ACuTEMan" [10-12], which includes the effect of two-phase flow, i.e., the presence and/or migration of molten materials in a solid mantle. Through the temporal evolution of the terrestrial planets, two-phase flow is considered to play crucial roles in the development of thermal and chemical structures of the interior by, for example, an intrusion of molten liquid iron into an unmolten (silicate) protocore in the earliest stage of the planets. Therefore, it is one of the most important directions of solid Earth sciences to establish numerical techniques of large-scale simulations of mantle convection incorporating the effects of two-phase flow.

In this FY, we concentrated our effort to (i) an adaptation to ES2 of the routine for solving the creeping flow of solid phase,

and (ii) an improvement of the numerical techniques of material transport in two-phase system. The former task includes an enhancement of vectorization of loops which calculate the flow fields of (truncated) anelastic fluid, and that of conformance with Fortran 90 standards. The latter task, on the other hand, includes developments of solution routines for (a) an advection equation based on FCT (Flux-Corrected Transport) method, (b) a relative motion between the solid and liquid phases based on Darcy's law of permeable flow, and (c) a coupled flow between the thermal convection and two-phase motion. By conducting several preliminary calculations with moderate problem sizes, we confirmed that our technique successfully calculates the coupled system with thermal convection and two-phase motion by permeable flow (Fig. 2). Our experiences suggest that an appropriate choice of solution techniques is quite important in solving the advection in multi-dimensions when the flow fields are not solenoidal (i.e., associated with source and/or sink terms). In particular, by the help of "flux limiter", one can avoid spurious concentration or rarefaction of advected quantities.

References

- [1] M. Furuichi, M. Kameyama, and A. Kageyama, *J. Comput. Phys.*, 227, 4977-4997, 2008.
- [2] M. Furuichi, M. Kameyama, and A. Kageyama, *Phys. Earth Planet. Inter.*, 176, 44-53, 2009.
- [3] M. Furuichi, D. A. May, and P. J. Tackley, *J. Comput. Phys.*, 230, 8835-8851, 2011.
- [4] M. Furuichi, Proceedings of International Conference on

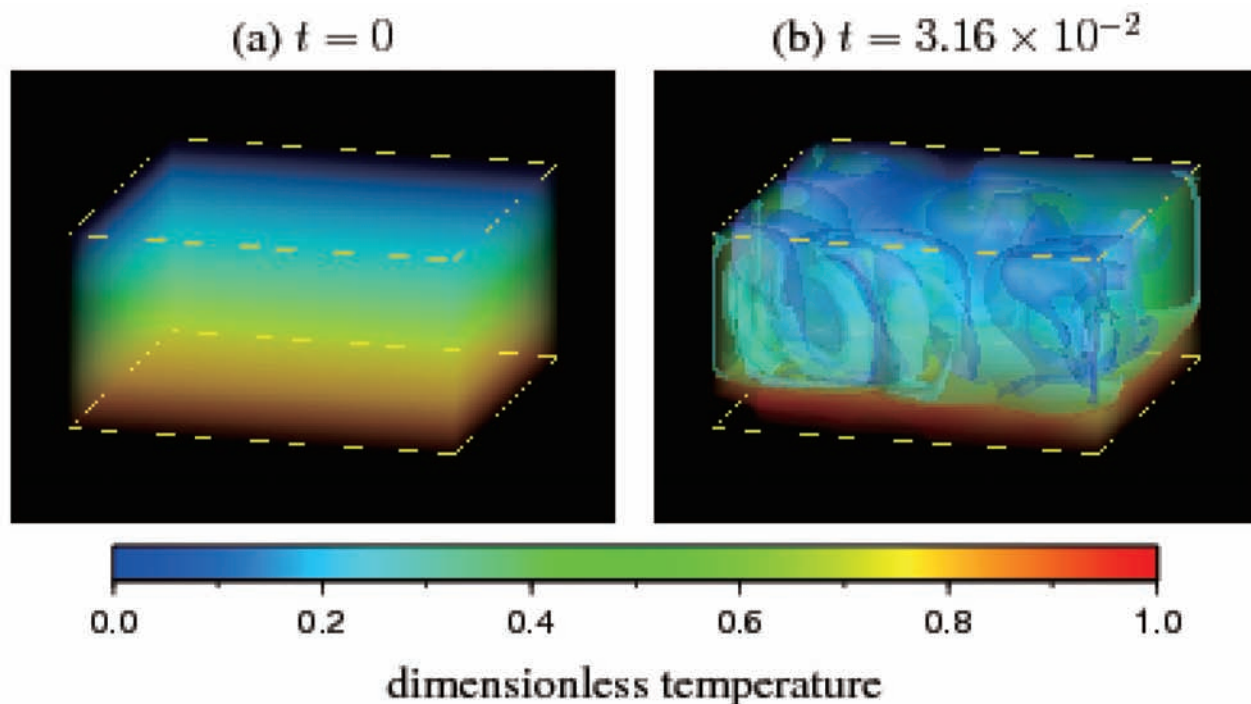


Fig. 2 Snapshots of distributions of temperature and liquid phase obtained by the thermal convection of two-phase motion by permeable flow at the elapsed times indicated in the figure. Shown in colors are the distributions of dimensionless temperature, while indicated by isosurfaces are those of volume fraction of liquid. In this calculations, the liquid phase, whose density is assumed to be larger than that of solid, is not only migrated downward by the permeable flow but also driven upward by the overall thermal convection.

Computational Science, ICCS 2011, 2011.

- [5] Yoza Hamano, (In Japanese) *Kagaku*, vol.62, No.1, pp.14-18, 1992.
- [6] Akira Kageyama, Takehiro Miyagoshi, and Tetsuya Sato, *Nature*, vol. 454, pp. 1106-1109, 2008.
- [7] Takehiro Miyagoshi, Akira Kageyama, and Tetsuya Sato, *Nature*, vol. 463, pp. 793-796, 2010.
- [8] Toshitsugu Yamazaki, (In Japanese) *Journal of Geography*, vol. 114, pp.151-160, 2005.
- [9] M. Korte and C. G. Constable, *Earth and Planetary Science Letters*, vol. 236, pp.348-358, 2005.
- [10] M. Kameyama, A. Kageyama, and T. Sato, *J. Comput. Phys.*, 206, 162-181, 2005.
- [11] M. Kameyama, *J. Earth Simulator*, 4, 2-10, 2005.
- [12] S. King, C. Lee, P. van Keken, W. Leng, S. Zhong, E. Tan, N. Tosi, and M. Kameyama, *Geophys. J. Int.*, 180, 73-87, 2010.

先端的固体地球科学シミュレーションコードの開発

プロジェクト責任者

古市 幹人 海洋研究開発機構 地球内部ダイナミクス領域

著者

古市 幹人^{*1}, 陰山 聡^{*2}, 宮腰 剛広^{*1}, 亀山 真典^{*3}, 大野 暢亮^{*4}, 兵藤 守^{*1},
中川 貴司^{*1}, 横井 研介^{*5}

*1 海洋研究開発機構 地球内部ダイナミクス領域

*2 神戸大学 大学院システム情報学研究科

*3 愛媛大学 地球深部ダイナミクス研究センター

*4 兵庫県立大学大学院 シミュレーション学研究科

*5 カーディフ大学

我々は、惑星の形成過程から地球ダイナモの生成並びにマントル対流の駆動といった固体地球科学ダイナミクスの諸問題に包括的に取り組むために、地球シミュレータ2の特徴を生かした先端的なシミュレーションコードを開発し、その応用を行っている。

数値惑星：前年度までに開発した、自己重力下での自由境界表面を伴う3次元地球中心核形成シミュレーションコードに、新たに惑星衝突のモデルを実装すること成功した。そして、幅広い衝突パラメータ空間におけるシミュレーションによって、惑星衝突によるコア形成時に地球内部に不均質な層が構築されることを見出した。このような結果は、地球深部にその存在が示唆されている始原物質層の形成過程の新しい仮説を導くものである。

ダイナモ：昨年度開発した地球自転速度変動の効果を考慮した地球ダイナモシミュレーションコードを用いてプロダクトランを行った。変動周期が磁場散逸時間（地球では2万年に相当）の場合、磁場のダイポール成分が約30%変動したが、その1/100の周期（同200年）では約1%の変動であった。これらは観測されているそれぞれの時間スケールでの磁場変動の振幅と傾向が合っている事が分かった。

マントル：固液2相系のマントル対流シミュレーションにあたり、(i) 固体の流動を計算する機能のES2向け改良、及び(ii) 物質の移動を計算する機能の構築、の2つを集中的に行った。中規模モデルによるテスト計算により、浸透流による2相の相対運動と熱対流運動のカップリングの取り扱いができることを確認した。

キーワード: 地球ダイナモ, インヤン格子, 地球回転変動, マントル対流, コア形成, ストークス流れ, 2相流, 浸透流

3-D Numerical Simulations of Eruption Clouds: Effects of Decompression/Compression and Cross-Wind on the Dynamics of Eruption Clouds

Project Representative

Takehiro Koyaguchi Earthquake Research Institute, The University of Tokyo

Authors

Yujiro Suzuki Earthquake Research Institute, The University of Tokyo

Takehiro Koyaguchi Earthquake Research Institute, The University of Tokyo

During explosive eruptions, a mixture of volcanic ash and gas forms a buoyant eruption column or a pyroclastic flow after the decompression and/or compression in/above the crater. When the mixture forms a buoyant eruption column in the atmosphere, the buoyant column is distorted by a cross-wind and shows a bent-over trajectory. In this project, we aim to understand these dynamics of eruption clouds. In this report, we investigate two effects on the dynamics of eruption cloud by performing three-dimensional (3-D) numerical simulations: the effect of decompression and/or compression on the critical condition for the generation of pyroclastic flow, and the effect of cross-wind on the column height. In the first problem, we found a new mechanism that enhances the generation of stable buoyant plume for the flow freely decompressed in the atmosphere just above the vent. Our results indicate that the free decompression flow is vertically separated into two flows above the Mach disk: the central subsonic flow and the annular supersonic flow. The annular supersonic flow becomes highly turbulent, and mixes with ambient atmosphere. This mixing between the annular supersonic up-flow and ambient air stabilizes the eruption column. In the second problem we develop a numerical model of eruption cloud which can employ the arbitrary cross-wind profiles. The numerical model successfully reproduced the bent-over eruption column. The bent-over eruption column is characterized by the spiral structures of vortices at the edge of the flow, which enhances entrainment of ambient air. The enhancement of entrainment causes the decrease in the maximum height of eruption columns under the cross-wind condition compared with the eruption column in a still atmosphere.

Keywords: volcanic eruption, eruption column, pyroclastic flow, turbulent mixing, volcanic hazard

1. Introduction

During explosive volcanic eruptions, a mixture of hot pyroclasts (volcanic ash) and volcanic gas is released from the vent into the atmosphere. The mixture generally has an initial density several times larger than atmospheric density at the volcanic vent. As the ejected material entrains ambient air, the density of the mixture decreases because the entrained air expands by heating from the pyroclasts. If the density of the mixture becomes less than the atmospheric density before the eruption cloud loses its upward momentum, a buoyant plume rises to form a plinian eruption column. On the other hand, if the mixture loses its upward momentum before it becomes buoyant, the eruption column collapses to generate a pyroclastic flow. Because the impact and type of volcanic hazards are largely different between the two eruption styles, it has been a central subject of volcanology to quantitatively predict the condition where an eruption column collapses to generate a pyroclastic flow; we refer to this condition as “the column collapse condition”.

When the buoyant plume develops in the atmosphere, the

plume interacts with the wind. If the plume has much greater vertical velocity than the cross-wind speed, its trajectory is not significantly controlled by the wind and rises vertically (referred to as “strong plume” [1]). On the other hand, if the vertical velocity is much smaller than the cross-wind speed, the plume is largely distorted by the cross-wind and shows a bent-over trajectory (“weak plume”); this effect can modify the maximum eruption column height. Because the height of eruption column is one of the few available data for estimating the eruption conditions, it is of critical importance to clarify the relationship between the eruption condition and column height under the cross-wind conditions.

In this report, we aim to investigate the effect of decompression and/or compression in/above the crater on the column collapse condition (Section 2), and the effect of the cross-wind on the column height (Section 3).

2. Effects of Decompression and/or Compression on the Column Collapse Condition

When magma properties (e.g., water content and temperature) are fixed, the column collapse condition has been considered to depend primarily on magma discharge rate [e.g., 2]. Here, we show that the column collapse condition also strongly depends on the crater shape.

According to Koyaguchi et al. [3], the flow in/above the crater is divided into 4 regimes in the parameter space of mass flow rate at the crater base (q_b/q^* in Fig. 1) and the ratio of sectional area between the top and base of the crater (A_t/A_b in Fig. 1). Here q_b is the mass flow rate at the crater base, q^* is the mass flow rate for the reference flow (sonic flow at 1 atm), and A_t and A_b are the sectional areas at the crater top and base, respectively. When q_b is small, the magma ascends as a subsonic flow through both the conduit and the crater. As q_b increases, the flow reaches the choking condition at the base or top of the crater. When A_t/A_b is around unity, the flow is choked at the crater top. It has an exit pressure (p_t) greater than the atmospheric pressure (p_a) and is freely decompressed into the atmosphere. We refer to this type of flow as “free decomposition flow”. When A_t/A_b exceeds a certain value, the flow reaches the choking condition and changes from a subsonic to a supersonic flow at the crater base. Flow that is choked at the crater base is subdivided into four types. When A_t/A_b is relatively small or q_b is large, the gas-pyroclast mixture issues from the crater top as a supersonic flow with $p_t > p_a$. The flow

is decompressed and generates rarefaction waves just above the crater. We refer to this type as “underexpanded flow”. As A_t/A_b increases or q_b decreases, the exit pressure (p_t) decreases. When $p_t = p_a$, the expansion of the gas-pyroclast mixture in the crater is most efficiently transferred to upward momentum. This flow type is referred to as “correctly expanded flow”. For greater A_t/A_b or smaller q_b , the gas-pyroclast mixture erupts as a supersonic flow with $p_t < p_a$, and is then compressed and decelerated by oblique shocks just above the crater. This flow type is referred to as “overexpanded flow”. As A_t/A_b further increases or q_b decreases, a shock forms inside the crater. In this instance, the gas-pyroclast mixture is compressed and decelerated by the shock and issues from the crater top as a subsonic flow.

Koyaguchi et al. [3] proposed that the column collapse condition for these flow regimes can be roughly estimated from the 1-D steady decomposition model above the crater [4, 5] and the 1-D steady eruption column dynamics model [e.g., 6]; however, the two 1-D steady decomposition models provide different results of column collapse condition for the free decomposition flow. Woods and Bower [4] proposed that the free decomposition flow is efficiently accelerated because of expansion above the vent so that it tends to generate stable buoyant column. On the other hand, Ogden et al. [5] proposed that the vertical acceleration is reduced because of the effect of radial expansion in the free decomposition flow so that the generation of pyroclastic flow is more likely to occur than the prediction by Woods and Bower [4]. In this study we test this point on the basis of a series of 3-D simulations.

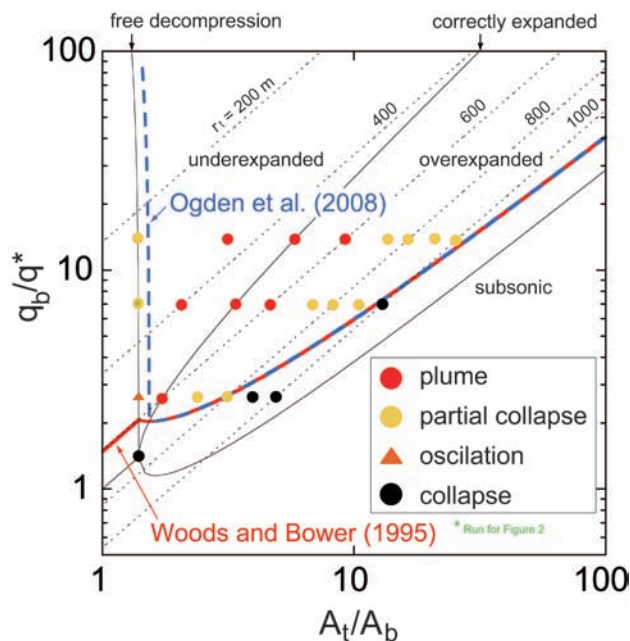


Fig. 1 Regime map for flows inside craters and eruption column dynamics in the q_b/q^* - A_t/A_b space. The boundary of different flow regimes inside craters are based on Koyaguchi et al. [3]. Flow regimes for eruption column dynamics are based on the 3-D simulations in this study. Column collapse conditions based on Woods and Bower [4] and Ogden et al. [5] are also shown in this diagram.

2.1 Model Description

The numerical model is designed to describe the injection of a gas-pyroclasts mixture from a circular vent above a flat surface with a temperature gradient typical of the tropical atmosphere. The vent is located in the center of the ground surface. The physical domain involves a vertical and horizontal extent of several tens of kilometers. At the ground boundary, the free-slip condition is assumed for the velocities of the ejected material and air. At the upper and other boundaries of computational domain, the fluxes of mass, momentum, and energy are assumed to be continuous. We assume steady conditions; for each run, vent radius and exit velocity are fixed. The initial temperature and water content are set to be $T_0=1053$ K and $n_{g0}=0.06$, respectively.

We apply a pseudo-gas model; we ignore the separation of solid pyroclasts from the eruption cloud and treat an eruption cloud as a single gas whose density is calculated from mixing ratio of the ejected material and entrained air. The fluid dynamics model solves a set of partial differential equations describing the conservation of mass, momentum, and energy, and constitutive equations describing the thermodynamics state of the mixture of pyroclasts, volcanic gas, and air. These equations are solved numerically by a general scheme for

compressible flow. Details of the numerical procedures are described in Suzuki et al. [7].

2.2 Numerical Simulations

Fig. 2 shows a representative result of our 3-D simulations of free decompression flow. The free decompression flow accelerates because of expansion and becomes a supersonic flow with high Mach number. Along the jet axis, the pressure continuously decreases to values below the ambient pressure, which discontinuously increases by passing through the shock wave, so-called Mach disk; the flow along the jet axis decelerates by this shock and becomes subsonic above it. The free decompression flow is also expanded radially at the exit, and the flow boundary forms an expanded shape. Expansion waves originating at the exit corner are reflected at the jet boundary as compression waves; these compression waves coalesce to form the so-called barrel shock. The flow passing through the barrel shock is compressed by the reflected shock. Because the barrel shock and the reflected shock are oblique to the flow, the deceleration by these shocks is limited; the flow passing through these shocks is still supersonic. The annular supersonic flow is separated from the inner subsonic flow by the slip line.

Our results are consistent with the conclusion by Ogden et al. [5] in the sense that the effects of the radial expansion and the deceleration by Mach disk play an important role in the column dynamics. However, as far as the column collapse condition is concerned, our results support the prediction by Woods and Bower [4]. In our simulations the high speed annular flow is highly turbulent, and mixes with ambient atmosphere. It is suggested that the instability in the annular supersonic up-flow enhances mixing between ejected material and ambient air, and

hence, stabilizes the eruption column.

3. Effects of Cross-Wind on Column Height

Because the plume height is principally determined by the balance between the thermal energy ejected from the vent and the work done in transporting the ejected material plus entrained air through the atmospheric stratification, it is controlled by the efficiency of turbulent mixing; as the amount of entrained air increases, the plume height decreases. Bursik [8] presented a theoretical model of steady eruption column in a cross-wind and demonstrated that cross-wind causes enhanced entrainment of ambient air and the plume height decreases as the wind speed increases. In his model, the entrainment velocity is given as a simple function of the relative velocity between the eruption column and cross-wind. However, the laboratory experiments of turbulent jet/plumes indicated that in the bent-over jet/plumes the cross-wind generates complex 3-D vortical structures which control the turbulent mixing [e.g., 9].

In this study, we aim to develop a numerical model which can reproduce the 3-D vortical structures in the bent-over plumes of eruption clouds, and investigate the effects of cross-wind on the column height.

3.1 Model Description

The numerical model is based on the one described in Section 2.1. We assume that the cross-wind speed increases linearly with height, z [km], as $U_w=0.8z$ [m/s]. The mid-latitude atmosphere is applied to the atmospheric condition. The computational domain of the numerical model extends 12 km vertically, 1 km upstream and 20 km downstream from the volcanic vent. It also extends 7 km from the vent in the horizontal direction perpendicular to the wind. In this study, the calculations are performed on a

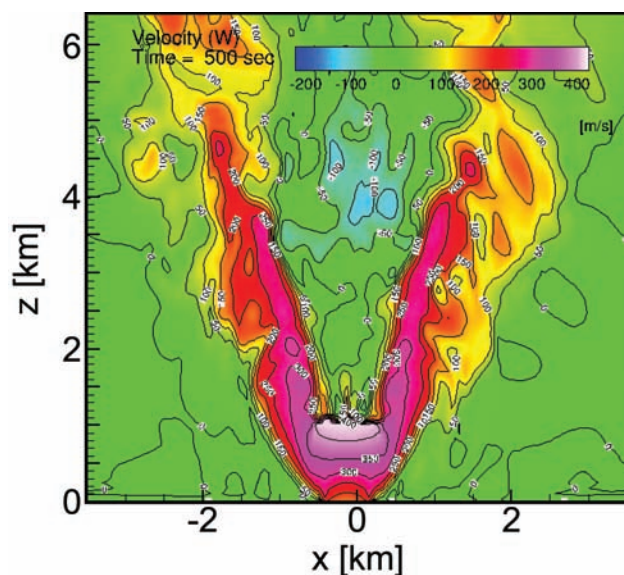


Fig. 2 Representative result of the free decompression flow near the vent. The distribution of vertical velocity at 500 s is presented. See text for explanation.

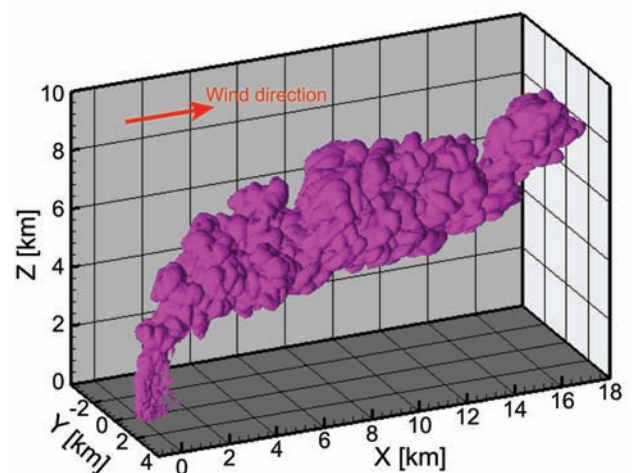


Fig. 3 Simulation result of the eruption cloud ejected in the cross-wind. Bird's-eye view of the iso-surface of the mass fraction of the ejected material (0.01) at 406 s after the beginning of eruption. Red arrow represents the wind direction.

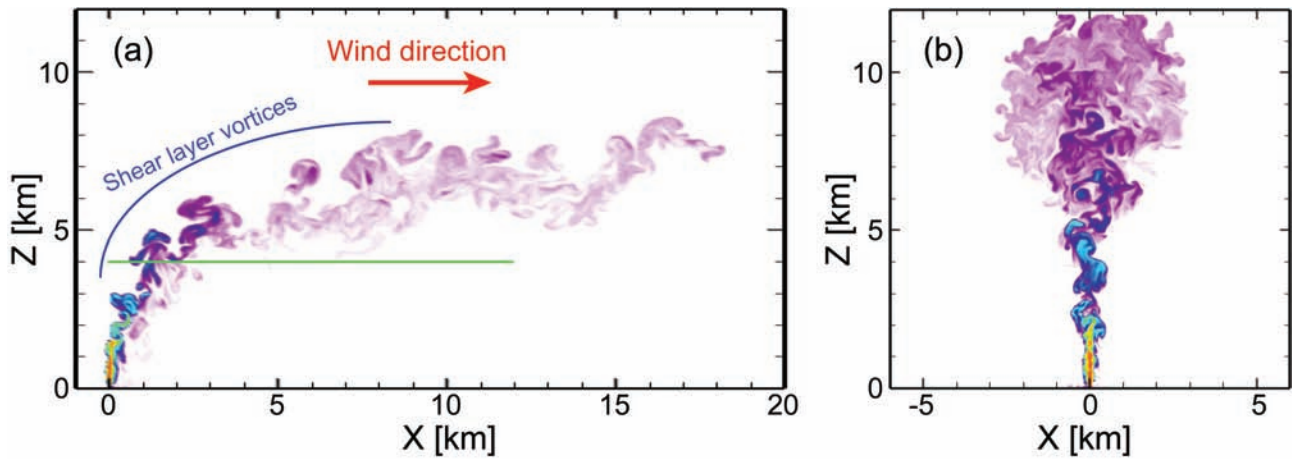


Fig. 4 Simulation results of (a) the bent-over plume in the cross-wind and (b) the vertical plume in the still atmosphere at 406 s. Cross-sectional distributions of the mass fraction of the ejected material in x - z space ($y=0$ km). Red arrow in (a) represents the wind direction. Green line indicates the position of the slice in Fig. 6.

3-D domain with a non-uniform grid with $1014 \times 512 \times 512$ grid points. The grid size is set to be sufficiently smaller than $L_0/8$ near the vent, and to increase at a constant rate (by a factor of 1.02) with the distance from the vent up to L_0 , where L_0 is the vent radius.

Our primary concern is how the maximum height of bent-over plume deviates from those in a still atmosphere. For this purpose, it is important to set vent radii sufficiently smaller than the length scale at which the initial upward momentum is lost in the simulations. When the vent radius is greater than a few hundred meters, the eruption cloud loses its momentum before turbulent mixing fully develops from the edge to the core of the flow; as a result, the heavy unmixed core forms a radially

suspended flow and another type of vortical structure develops [7]. In order to avoid additional effects caused by this vortical structure, we set vent radii to be narrow (26.7 m). An initial temperature of $T_0=1000$ K and water content of $n_{g0}=0.0284$ are assumed. The exit velocity is set to be the sound velocity of the gas-pyroclasts mixture. We assume that the pressure at the vent is same as the atmospheric pressure for simplicity.

3.2 Numerical Simulations

Our simulation has successfully reproduced the bent-over plume of eruption cloud (Figs. 3 and 4a). Near the vent, the eruption cloud rises vertically. As it rises, the plume is highly unstable and undergoes a meandering instability that induces efficient mixing so that its radial scale gradually increases with height. Above 3 km, the cloud is largely distorted by the cross-

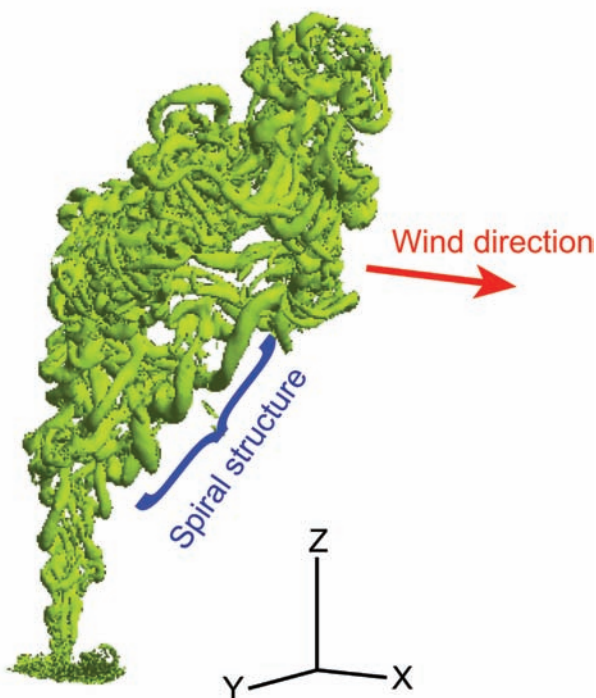


Fig. 5 Vortical structures in the bent-over plume. Iso-surface of Q -value (0.002) at 232 s. Red arrow represents the wind direction.

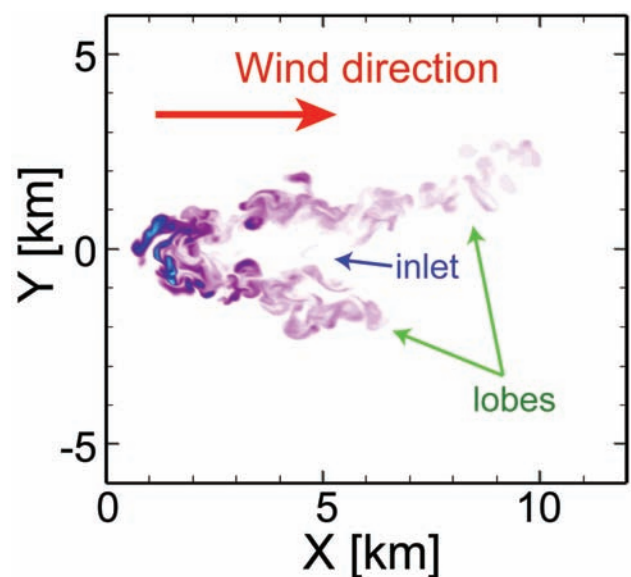


Fig. 6 Simulation result of the bent-over plume. Cross-sectional distribution of the mass fraction of the ejected material in x - y space ($z=4$ km as indicated in Fig. 4a) at 406 s. Red arrow represents the wind direction.

wind. Then, the eruption cloud stops to rise and eventually spreads horizontally along the wind direction around the height of 5-8 km.

Some characteristic structures are observed in the bent-over plume. First, a spatially periodic structure forms in the upper part of the bent-over plume (Fig. 4a). This coherent structure is generated just after the flow is distorted by the cross-wind ($z > 3$ km) and is similar to “the shear layer vortices” observed in the laboratory experiments of bent-over jet/plumes, which result from the Kelvin-Helmholtz instability in the shear layer when the two streams meet [9]. Secondly, the spiral structure develops at the edge of the plume (Fig. 5). This structure is also generated after the flow shows a bent-over trajectory and is similar to “the counter-rotating vortex” observed in the laboratory experiments [9], which occurs as a result of process of roll-up, tilting and folding of the shear layer vortices. Finally, the plume develops an inlet at the front and splits into two distinct lobes (Fig. 6). These structures were also reported by the experimental studies [9]. Ernst et al. [10] suggested that the pressure distribution around the counter-rotating vortex initially triggers such bifurcation.

For comparison, we also carried out a simulation of eruption column in a still atmosphere in which eruption conditions at the vent are same as those for the above simulation with cross-wind. In the simulation in the still atmosphere, the eruption plume reaches up to 12 km (Fig. 4b), which is substantially greater than the maximum height of the bent-over plume (8 km; see Fig. 4a). This difference in the maximum column height between the cases with and without the cross-wind can be accounted for by the fact that the efficiency of entrainment is enhanced by the cross-wind. It is suggested that the shear layer vortices and counter-rotating vortices cause more efficient turbulent mixing.

References

- [1] C. Bonadonna, J. C. Phillips, and B. F. Houghton, “Modeling tephra sedimentation from a Ruapehu weak plume eruption”, *J. Geophys. Res.*, vol.110, B08209, 2005.
- [2] G. Carazzo, E. Kaminski, and S. Tait, “On the dynamics of volcanic columns: A comparison of field data with a new model of negatively buoyant jets”, *J. Volcanol. Geotherm. Res.*, vol.178, 94-103, 2008.
- [3] T. Koyaguchi, Y. J. Suzuki, and T. Kozono, “Effects of the crater on eruption column dynamics”, *J. Geophys. Res.*, vol.115, B07205, 2010.
- [4] A. W. Woods and S. M. Bower, “The decompression of volcanic jets in a crater during explosive volcanic eruptions”, *Earth Planet. Sci. Lett.*, vol.131, pp.189-205, 1995.
- [5] D. E. Ogden, K. H. Wohletz, G. A. Glatzmaier, and E. E. Brodsky, “Numerical simulations of volcanic jets: Importance of vent overpressure”, *J. Geophys. Res.*, vol.113, B02204, 2008.
- [6] M. I. Bursik and A. W. Woods, “Buoyant, superbuoyant and collapsing eruption columns”, *J. Volcanol. Geotherm. Res.*, vol.45, pp.347-350, 1991.
- [7] Y. J. Suzuki, T. Koyaguchi, M. Ogawa, and I. Hachisu, “A numerical study of turbulent mixing in eruption clouds using a three-dimensional fluid dynamics model”, *J. Geophys. Res.*, vol.110, B08201, 2005.
- [8] M. Bursik, “Effect of wind on the rise height of volcanic plumes”, *Geophys. Res. Lett.*, vol.28(18), pp.3621-3624, 2001.
- [9] T. F. Fric and A. Roshko, “Vortical structure in the wake of a transverse jet”, *J. Fluid Mech.*, vol.279, pp.1-47, 1994.
- [10] G. G. J. Ernst, J. P. Davis, and R. S. J. Sparks, “Bifurcation of volcanic plumes in a crosswind”, *Bull. Volcanol.*, vol.56, pp.159-169, 1994.

火山噴煙の3次元数値シミュレーション： 火口クレーターの形状と風の影響

プロジェクト責任者

小屋口剛博 東京大学 地震研究所

著者

鈴木雄治郎 東京大学 地震研究所

小屋口剛博 東京大学 地震研究所

本プロジェクトでは、固体地球と地球表層・大気にまたがる火山現象について、大規模数値シミュレーションを用いた物理過程の理解と計算結果の防災への応用を目指している。平成23年度は、特に、火山噴煙において(1)火口クレーターでの加圧・減圧過程が火砕流発生条件に与える影響、(2)大気の流れが噴煙高度に与える影響について研究を進めた。

(1) 火口クレーターでの加圧・減圧過程が火砕流発生条件に与える影響

爆発的火山噴火では一般に、噴煙柱と火砕流という二つの特徴的な噴火レジームが見られる。これら二つのレジームの境界を火砕流発生条件と呼ぶ。マグマの性質(例えば含水量・温度)が与えられた場合、火砕流発生条件は、主に噴出率によって決定されると考えられている(例えば、Carazzo et al., 2008)。但し、火口の形状(例えば火口上端の径)が変化した場合、一定の噴出率の下で噴出圧力、噴出速度が変化し、それが火砕流発生条件に影響を与える。Koyaguchi et al. (2010)は、火口直上での減圧過程について定常1次元モデル(Woods and Bower, 1995)と非定常2次元モデル(Ogden et al., 2008)に基づいて火砕流発生条件を求め、自由膨張流として噴出する場合に、両モデルに基づく火砕流発生条件が大きく食い違うことを指摘した。そこで、本研究では、非定常3次元噴煙モデル(Suzuki et al., 2005)によるシミュレーションを行い、同条件下における火砕流発生条件を求めた。

シミュレーションの結果、3次元計算による火砕流発生条件はWoods and Bower (1995)の予測と半定量的に一致した。自由膨張領域の計算条件下でシミュレーションを行なったところ、広い計算条件で安定な噴煙柱を形成する結果が得られた。この結果は、Ogden et al. (2008)のモデルよりもWoods and Bower (1995)のモデルに基づく火砕流発生条件を支持する。このような自由膨張流では、バレルショックとマッハディスクが形成され、マッハディスク直上で中心部亜音速流と外縁部超音速流に分離する。外縁部超音速流では、圧力変動を伴う不安定な流れが発生し、それが大気と噴煙の効率的な混合を促すことによって、安定な噴煙柱を形成しやすいことが新たに分かった。

(2) 大気の流れが噴煙高度に与える影響

噴煙高度は単位時間にマグマから大気に供給される熱エネルギーの直接的指標であり、爆発的噴火過程や噴火強度を推定する上で貴重な情報源となる。これまでに、定常1次元噴煙モデル(Woods, 1988)によって、噴煙高度は主に火口での噴出率で決定されると予想されていた。Bursik (2001)は、大気中に風が存在する場合、噴煙と大気の混合が促進され、その結果、噴煙高度が低下する可能性を示した。しかし、Bursik (2001)のモデルでは風と大気の混合効率について単純な関数が仮定されており、横風を受けるジェットやプルームで見られるような複雑な3次元的渦構造(Fric and Roshko, 1994)が混合効率に与える影響について系統的な評価がされていない。そこで、本研究では、3次元シミュレーションで渦構造を含めた噴煙構造を直接的に再現することを試みた。

シミュレーションの結果、風によってその軌跡が大きく曲がる噴煙を、3次元的に初めて再現することに成功した。噴出率が 4×10^6 kg/sの場合、横風を受けた噴煙の到達高度は、風がない場合に比べ4km低下した。噴煙内部の渦構造を可視化したところ、風で曲がり始める領域で噴煙側部から中心に向かって巻き込むような渦構造(counter-rotating vortices)が観察された。この現象は、風によって形成される渦構造が噴煙と大気の混合を促進し、その結果として噴煙高度を低下させることを合理的に説明する。

キーワード: 火山噴煙, 火砕流, 擬似ガスモデル, 乱流混合, 火山災害

Space and Earth System Modeling

Project Representative

Kanya Kusano

Laboratory for Earth Systems Science, Japan Agency for Marine-Earth Science and Technology

Authors

Kanya Kusano^{*1, 5}, Wataru Ohfuchi^{*2, 1}, Shin-ichiro Shima^{*3}, Yusuke Chikaraishi^{*4, 1} and Ryohei Suzuki^{*4, 1}

*1 Laboratory for Earth Systems Science, Japan Agency for Marine-Earth Science and Technology

*2 Earth Simulator Center, Japan Agency for Marine-Earth Science and Technology,

*3 Graduate School of Simulation Studies, University of Hyogo

*4 Tokyo Institute of Technology

*5 Solar-Terrestrial Environment Laboratory, Nagoya University

The Earth is not isolated from space and astronomical dynamics, which play a crucial role for the variability of terrestrial environment in different time-scale. However, it is not well understood yet how the evolution of terrestrial environment is related to the outside of the Earth. The objective of the Earth Simulator Project “Space and Earth System Modeling” is to advance our understanding for the variability of terrestrial environment caused by the dynamics in space. In FY 2011, we have continued the development of the several simulation models for sun-earth connection systems for cloud and global circulation in earth’s atmosphere as well as solar flares, respectively.

Keywords: space weather, space climate, multi-scale, multi-physics, plasma, cloud, aerosols, solar flares, Earth Simulator

1. Introduction

Earth’s environment is not isolated from the outside of the atmosphere as well as from the interior of the solid earth. In fact, the several evidences indicate that there is clear correlation between the climate variation and sunspot activity. Also it is widely believed that giant volcanic eruption may impact the worldwide climate. However, the mechanism whereby the solar activity may affect the climate is not well understood yet.

Earth Simulator Project “Space and Earth System Modeling” was established in order to understand the mutual relationship between the surface environment and the activity in space. In FY 2011, we have continued the development of the several numerical models which will compose a space climate system simulation. They are the cloud simulation in terms of super-droplet method, the global circulation model for the study on the galactic cosmic ray and climate relation, and the magnetohydrodynamics simulation for solar flares. In the following sections, we will explain about the detail of the each particular model.

2. Simulation study on the bistability of the cloud-rain system

Although clouds play a crucial role in atmospheric phenomena, the numerical modeling of clouds remains somewhat primitive. We have developed a novel, particle-

based, probabilistic simulation scheme of cloud microphysics, named the Super-Droplet Method (SDM), which enables accurate numerical simulation of cloud microphysics with less demanding cost in computation [1]. The SDM is implemented on the Cloud Resolving Storm Simulator (CRess), which is a well-established cloud-resolving model developed by Tsuboki et al., and we call this new model the CRess-SDM.

In 2011 FY, we started to challenge the bistability hypothesis of clouds, originally proposed by Baker and Charlson [2]. They suggested that clean/precipitating and dirty/non-precipitating atmosphere could be both stable under a certain atmospheric condition. This phenomenon is considered to occur as a result of the interaction between cloud/rain particles and aerosols, hence the CRess-SDM is a suitable tool for addressing this open problem.

For the first step, we added three more microphysical processes into the CRess-SDM: the Brownian coagulation of aerosols, the Brownian scavenging of aerosols by rain droplets, and the nucleation of aerosols. All of these processes play important roles in the bistability scenario.

Next, we performed a series of simulations to see how the aerosol nucleation rate affects the equilibrium state of precipitating trade-wind cumuli system. The simulations are carried out using a set-up based on the RICO composite case defined in Ref. [3] and corresponding to atmospheric state

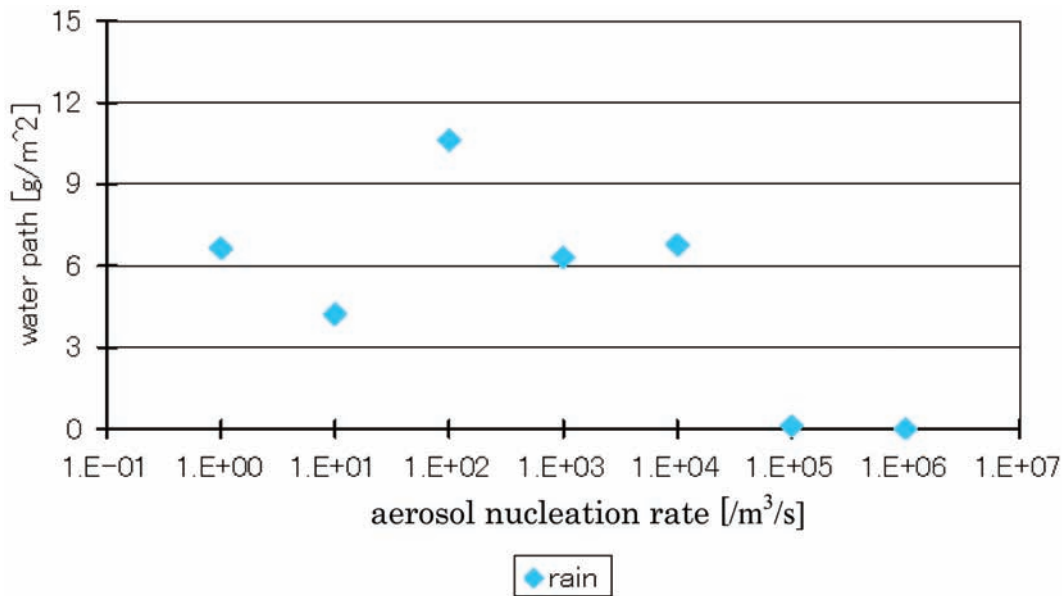


Fig. 1 Average rain water path for various aerosol nucleation rates. Rain droplets suddenly disappear when the nucleation rate is larger than 10^5 /m³/s. This could be a glimpse of the bistability of the cloud-rain system.

measured and modeled in context of the Rain in Cumulus over Ocean (RICO) field project [4]. We compared the equilibrium states of the system for various aerosol nucleation rates. In Fig. 1 we can see rain water path suddenly goes to zero when the nucleation rate is larger than 10^5 /m³/s. Although further careful investigations are necessary, this result may suggest the bistability of cloud-rain system.

3. Influence of cloud droplet size to climate

The purpose of this study is to investigate the influence of changes in size of cloud droplets may give to the earth surface air temperature, using a coupled atmosphere-ocean general circulation model (GCM), called CFES (Coupled model For the Earth Simulator). The last year, we conducted a set of 10-year simulations with different cloud droplet sizes. This year,

we continued the simulations for 10 more years in order to get more reliable statistics. First, CFES was spun up for 100 years with a default size of cloud droplets. The control run afterward was run for 20 years further without changing the diameter of cloud droplets (control run). Two sensitivity experiments were performed for 20 years by suddenly making the diameter of cloud droplets half (half run) and double (double run). The global mean surface air temperature decreased 3.7 K in the half run and increased 3.7 K in the double run within 20 simulation years. The cross section of a cloud droplet increases with r^2 , where r is the droplet radius, while the number density of cloud droplets decreases with r^{-3} . This explains the colder (warmer) climate for the half (double) run.

There are some feedback processes in the climate system. Figure 2 shows the time series of global and monthly mean low cloud amount. The low cloud amount increases in the half run while it decreases in the double run. The low clouds are known to cool the earth's surface temperatures [5]. While the mechanism is not clear, yet, the changes in low cloud amount is a positive feedback and enhances cooling and warming induced by the droplet size change.

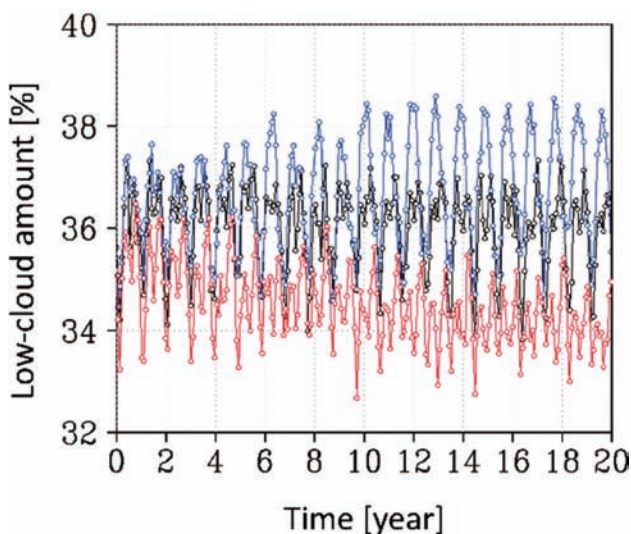


Fig. 2 Time series of monthly-global mean surface air temperatures. Black curve is for the control run, blue the half run, and red the double run.

4. Predicting the onset of solar flares

Solar flares and coronal mass ejections are the most catastrophic events in our solar system, and they sometimes impact the terrestrial environment and our infrastructure. Although these solar eruptions are widely believed to be driven by magnetic energy stored in the solar corona, what triggers their onset remains poorly understood. Hypotheses for the trigger mechanism include the emerging flux model, which proposed that the small magnetic flux emerging onto the solar surface may lead to the solar eruptions. However, what kind of the emerging flux is capable to trigger the eruptions is unclear. This severely

limits our capacity to predict the occurrence of solar eruptions and forecast space weather. In this study, we systematically survey the nonlinear dynamics caused by emerging fluxes in terms of three-dimensional (3D) magnetohydrodynamics (MHD) simulations, and find that there are two different types of small magnetic structures triggering the solar eruptions.

The first type of magnetic structure causing flares is called the opposite polarity type, in which the small magnetic bipole opposite to the major magnetic polarity in an active region drives the solar eruption as shown in Fig. 3 A-C. The second type is called the reversed shear type, in which the cancellation of magnetic shear on the polarity inversion line may cause

the onset of eruption (see Fig. 3 D-F). We have compared the simulation results and the data of Hinode solar observation satellite, and found that major flare events can be classified into these two types. These results suggest that solar flares are predictable if we can measure the detail structure of small magnetic field triggering solar eruption [6].

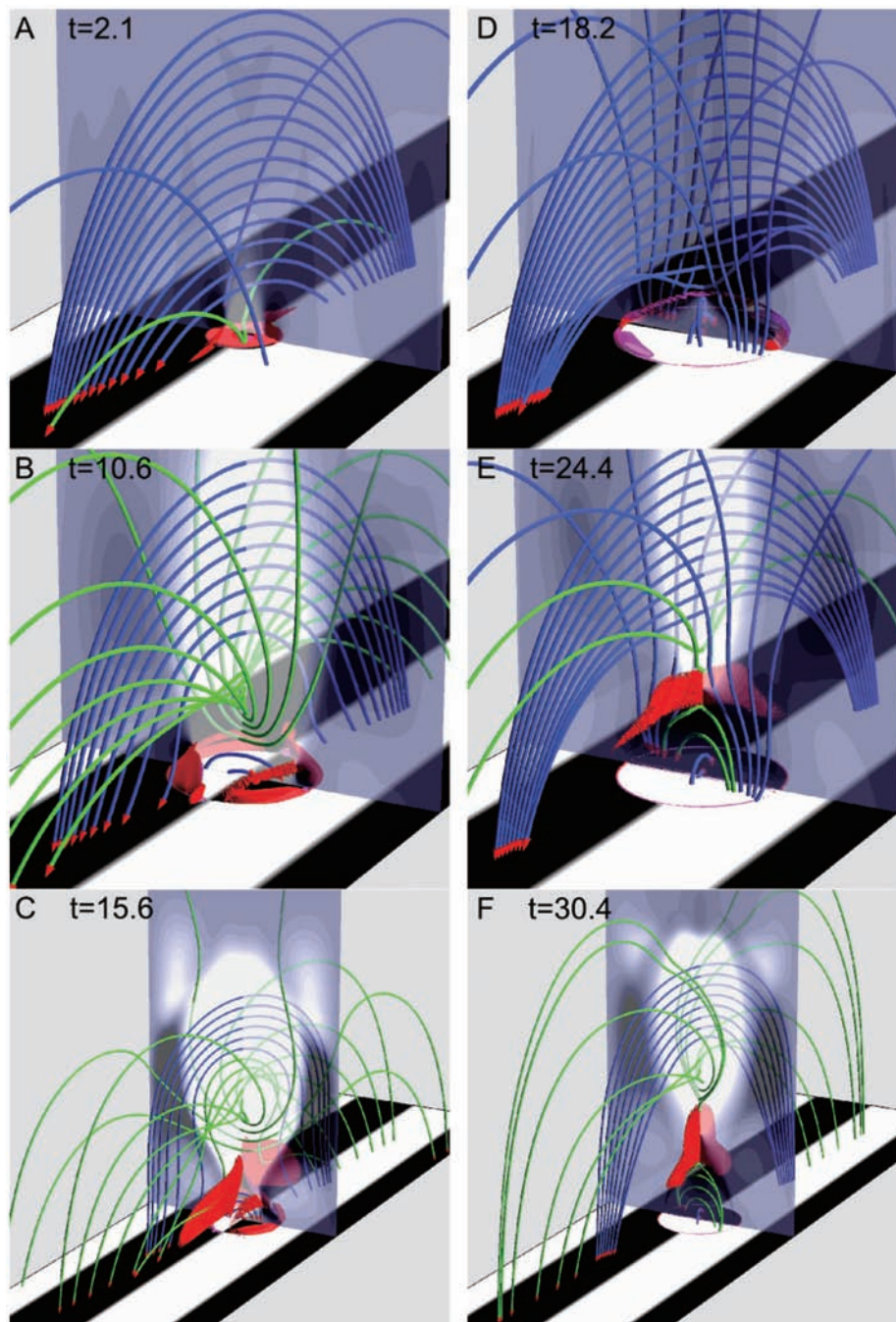


Fig. 3 Typical results of solar flare simulations for the two different scenarios: The left column [panels A-C] and the right column [panels D-F] are for the opposite polarity type and the reversed shear type scenarios, respectively.

References

- [1] S. Shima, K. Kusano, A. Kawano, T. Sugiyama, and S. Kawahara, The super-droplet method for the numerical simulation of clouds and precipitation: a particle-based and probabilistic microphysics model coupled with a non-hydrostatic model, *Quarterly Journal of the Royal Meteorological Society*, Vol. 135, 642, pp.1307–1320, 2009.
- [2] M. B. Baker and R. J. Charlson, Bistability of CCN concentrations and thermodynamics in the cloud-topped boundary layer, *Nature*, Vol. 345, 142-145, 1990.
- [3] M. van Zanten et al., Controls on precipitation and cloudiness in simulations of trade-wind cumulus as observed during RICO, *J. Adv. Model. Earth Sys.*, <http://cavern.atmos.colostate.edu/~rames/ojs224/index.php/JAMES/article/view/56/118>, 2010.
- [4] R. Rauber et al., Rain in Shallow Cumulus Over the Ocean - The RICO Campaign, *Bull. Amer. Meteor. Soc.*, Vol. 88, pp. 1912-1928, 2007.
- [5] S. Manabe and F. R. Strickler, Thermal equilibrium of the atmosphere with a convection adjustment, *J. Atmos. Sci.*, Vol. 21, pp. 361-385, 1964.
- [6] K. Kusano, Y. Bamba, et al., Magnetic field structures triggering solar flares and coronal mass ejections, submitted to *The Astrophys. J.*, 2012.

宇宙・地球表層・地球内部の相関モデリング

プロジェクト責任者

草野 完也 海洋研究開発機構 システム地球ラボ

著者

草野 完也^{*1,5}, 大淵 済^{*2,1}, 島 伸一郎^{*3}, 力石 祐介^{*4,1}, 鈴木 遼平^{*4,1}

*1 海洋研究開発機構 システム地球ラボ

*2 海洋研究開発機構 地球シミュレータセンター

*3 兵庫大学 大学院シミュレーション学研究科

*4 東京工業大学 大学院理工学研究科

*5 名古屋大学 太陽地球環境研究所

地球環境システムは内部（地殻、マントル、コア）、表層（大気海洋）および外部（宇宙）が互いに影響を及ぼしながら変動進化する相関システムである。本プロジェクトは地球環境の大規模変動と太陽及び宇宙空間ダイナミクスの関係を探るために、先進的な相関モデルを開発する目的で2009年度より開始された。本プロジェクトでは、特に宇宙線と雲の関係及び太陽活動と地球環境の関係に注目し、それらの理解と予測を目指したシミュレーション研究を実施している。2011年度はその結果、以下の3つの成果を得た。①超水滴法を利用した積雲成長シミュレーションにより雲降水システムが雲核生成率に対して双安定状態を持つことを示唆する結果を得た。②大気海洋結合全球循環モデルを用いて銀河宇宙線の影響によって生成されると考えられている雲凝結核の変化による気候変動に関するシミュレーションを実施し、雲核数の変化による平均粒径の変化が地球表面温度に大きな影響を与えることを見出した。③地球環境に大きな影響を与える巨大太陽フレアの発生が2つのタイプに分類できることを見出すと共に、フレア発生の予測可能性を示した。

キーワード:宇宙天気, 宇宙気候, マルチスケール, マルチフィジックス, プラズマ, 雲, エアロゾル, 太陽フレア, 地球シミュレータ

Numerical Experiments with Multi-Models for Paleoenvironmental Problems

Project Representative

Ayako Abe-Ouchi Atmosphere and Ocean Research Institute, The University of Tokyo

Authors

Ayako Abe-Ouchi^{*1}, Masakazu Yoshimori^{*1}, Wing-Le Chan^{*1}, Ryouta O'ishi^{*1} and Kazue Suzuki^{*2}

*1 Atmosphere and Ocean Research Institute, The University of Tokyo

*2 Research and Development Center for Data Assimilation, The Institute of Statistical Mathematics, Research Organization of Information and Systems

Climate simulations for two different time periods were conducted using MIROC3.2 and MIROC4m AOGCMs. The first period focuses on the climate of the mid-Pliocene which was a warm period 3.0-3.3 million years ago. Results show that the global average surface air temperature increases by about 3.5°C. Polar amplification, resulting mostly from diminished ice sheets, leads to a reduction in the meridional temperature gradient. Warming in the northern North Atlantic and the Nordic Seas is not as high as that suggested by SST reconstructed from proxy data. The second period focuses on the climate of the last millennium (850-2000 A.D.). Three experiments using the three different boundary conditions were carried out, which differ in solar and volcanic forcings. One of the two volcanic forcing used tends to show too strong a response in the Northern Hemisphere temperature, but overall simulations agree reasonable well with a range of reconstructions. More simulations are needed to isolate causes of the simulated variations and distinguish them from internal variability. The weather regime analysis in the North Atlantic region suggests similar characteristics between the warm Medieval Climate Anomaly and cold Little Ice Age periods, in contrast to the recently proposed interpretation of reconstructions.

Keywords: atmosphere-ocean GCM MIROC, paleoclimate modeling, mid-Pliocene, last millennium

1. Introduction

The mid-Pliocene warm period (mPWP), defined as the period between 3.0 and 3.3 million years ago, was the most recent in the earth's history during which global mean temperatures were comparable to those predicted for the late 21st century by many climate models [1]. Land-sea configuration and global ocean circulation were similar to those of present day and a variety of proxy data have recently become available. The mPWP has thus become a period of particular interest for the development of models used for future climate predictions. Climate variations over the last millennium have also received much attention recently. In the latest report of the Intergovernmental Panel on Climate Change (IPCC-AR4), for example, 18 pages were allocated to the climate of the last 2000 years. While reconstructions provide information on past climate events/excursions (date, magnitude, frequency, spatial and temporal extents) and place the recent warming trend in the long-term perspective, they are limited in addressing mechanisms behind observed changes. Climate modeling, if used in tandem, may provide the following: 1) a quantification of the unforced, internal variability and detection of externally-

forced changes in observed records; 2) a means to attribute observed changes (climate, glaciers, sea level) to a specific origin (e.g., solar, volcanic, or anthropogenic); 3) an insight into multi-decadal to centennial variability for which only limited length of instrumental observations are available.

2. Modeling of the mid-Pliocene

A coupled atmosphere-ocean general circulation model (AOGCM), MIROC4m, has been used to simulate mid-Pliocene climate [2] with boundary conditions created from recent datasets released by the US Geological Survey PRISM project as part of the recent Pliocene Model Intercomparison Project (PlioMIP) [3, 4]. These datasets include sea surface temperatures (SST), topography, vegetation distribution and ice sheet extent. Vegetation types are converted into the biomes as specified in the model (Fig. 1). The land-sea mask is modified to include changes in northern Canada, the Hudson Bay, the southern half of which is changed to land, and west Antarctica, where much of the ice shelf has been removed. Atmospheric CO₂ concentration is set to 405 ppm, whereas levels of other trace gases and orbital parameters are left unchanged.

MIROC4m is a mid-resolution model – the atmospheric component has resolution T42 resolution (2.8° grid size) and 20 vertical levels and is coupled to the MATSIRO land surface model. The ocean model has a 192×256 horizontal grid with realistic bathymetry. Refer to K-1 model developers [5] for a full description of the model. In the mid-Pliocene experiment, a 1400-year integration is performed with the AOGCM. Model results are then compared with pre-industrial experimental data. A shorter experiment consisting of a 50-year integration is also carried out with an atmosphere general circulation model (AGCM).

Results show that surface air temperature in the AOGCM increases over most regions, with a global increase of 3.5°C. Increases are largest over the polar regions (Fig. 2), especially during their winter seasons. Large increases are also found over northern Africa, the Arabian peninsula and central Asia where the deserts have reduced in area. The zonally averaged temperature increases by about 10°C at high latitudes, accompanied by a decrease in the meridional temperature gradient. In the AGCM run with fixed mid-Pliocene SST, the

globally averaged surface air temperature increases by 2.8°C. Increases over the polar regions are slightly higher than those of the AOGCM, whereas there is minimal change at low latitudes which means that the meridional temperature gradient is greater in the AGCM. There are areas where the reconstructed mid-Pliocene elevation is higher than that of present day, for example, parts of the Rocky Mountains, eastern Peru and central Asia. In these areas, temperatures decrease in the mid-Pliocene case, although this is more evident in the AGCM. Separate sensitivity experiments confirm that the reduction in ice sheets is responsible for much of the warming at high latitudes leading to polar amplification (Fig. 3). Increasing CO₂ levels has a more uniform effect on the zonal mean temperature, accounting for a 2-4°C increase. Globally averaged total precipitation increases, more so in the AOGCM, despite a decrease in snowfall. Increased precipitation is found over much of the tropics and high latitudes (Fig. 2). Decreased precipitation over the tropical Atlantic suggests a meridional shift in the Hadley circulation.

The SST as simulated by the AOGCM shows discrepancies in certain regions when compared to PRISM SST data which

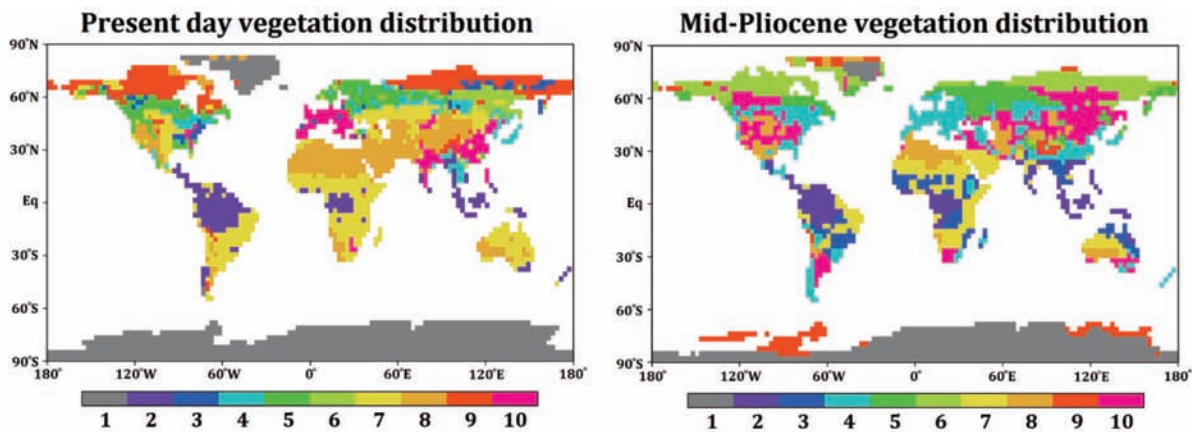


Fig. 1 Present day and mid-Pliocene vegetation distribution. Key: (1) continental ice, (2) broadleaf evergreen forest, (3) broadleaf deciduous forest and woodland, (4) mixed coniferous, broadleaf deciduous forest and woodland, (5) coniferous forest and woodland, (6) high latitude deciduous forest and woodland, (7) wooded C4 grassland, (8) shrubs and bare ground, (9) tundra, (10) C3 grassland.

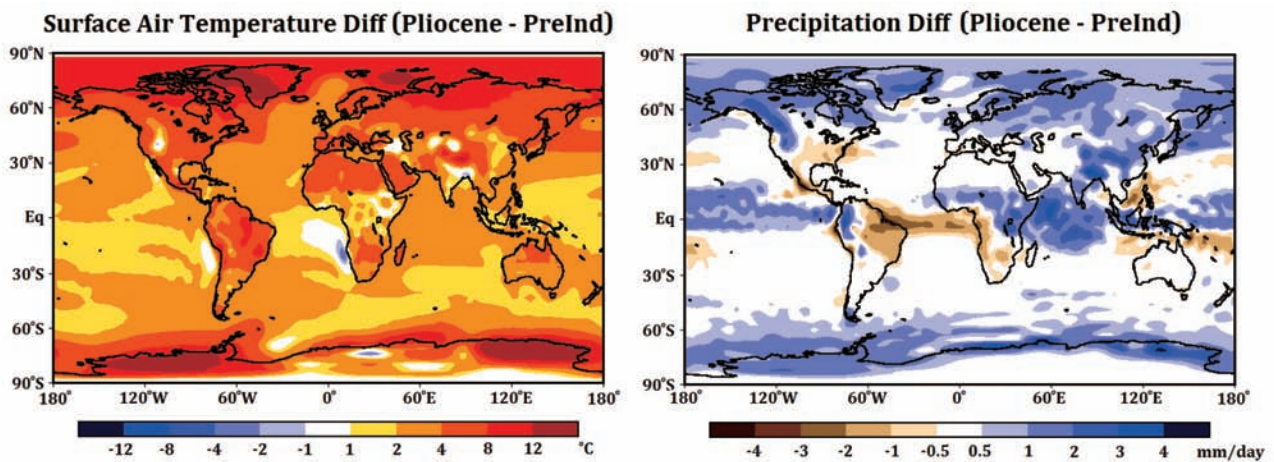


Fig. 2 Annual mean surface air temperature difference and precipitation difference (mid-Pliocene minus pre-industrial) as simulated by the MIROC4m AOGCM.

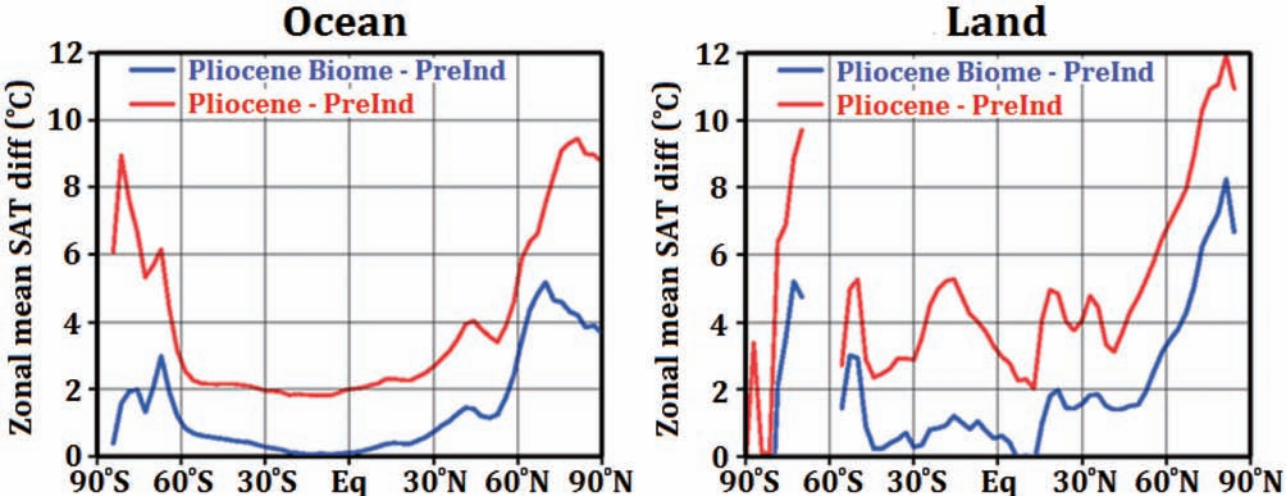


Fig. 3 Zonal mean surface air temperature difference over the ocean (left) and land (right). Red lines refer to the mid-Pliocene experiment and blue lines to an experiment in which only the biomes are changed to mid-Pliocene values.

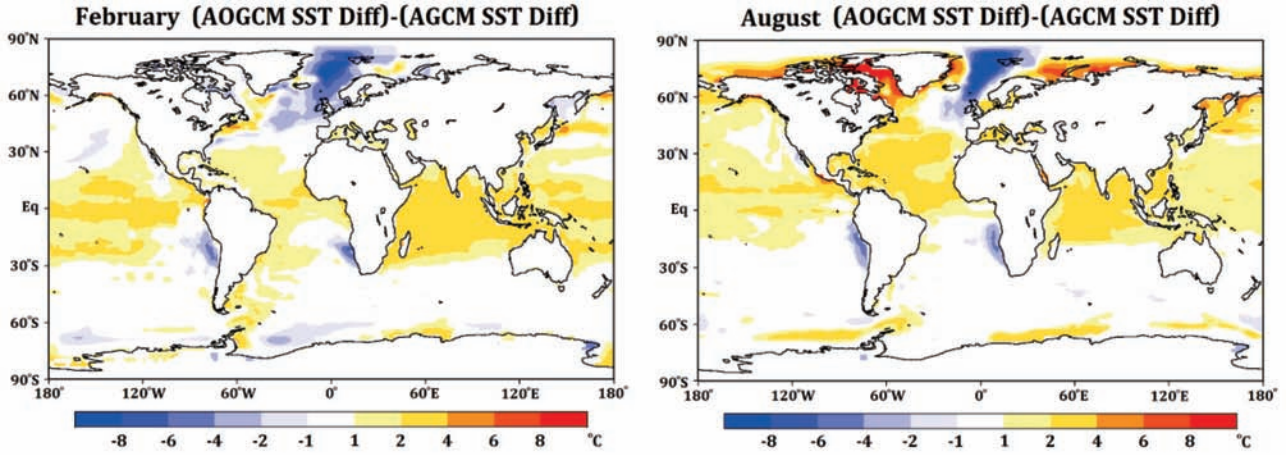


Fig. 4 Difference between AOGCM and AGCM sea surface temperature anomalies for February and August.

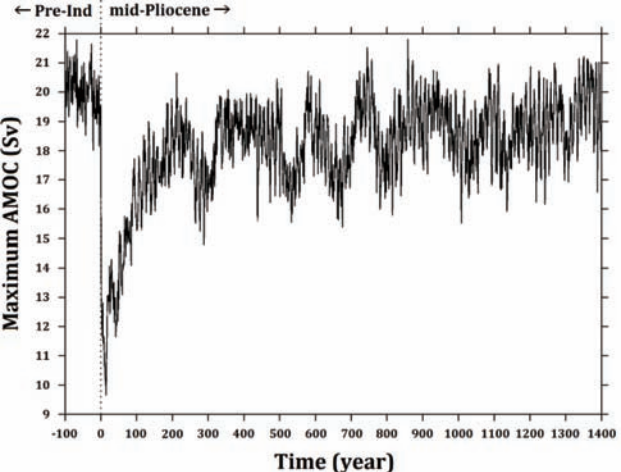


Fig. 5 Time series of the maximum value of the Atlantic meridional overturning circulation (AMOC).

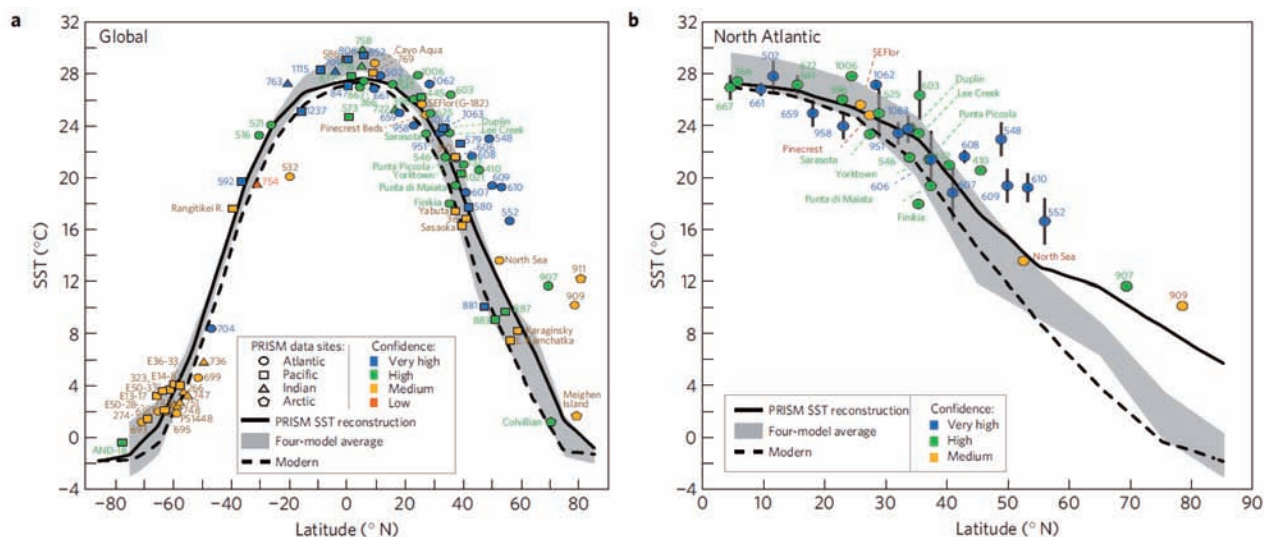


Fig. 6 Comparison of sea surface temperatures reconstructed from PRISM proxy data with multi-model means, zonally averaged over the whole globe (a) and over the North Atlantic(b). Multi-model means were produced from four climate models, including MIROC4m. Gray band has width equal to $\pm 2\sigma$. Figure taken from [8].

are used in the AGCM. Figure 4 compares the change in the AOGCM SST (mid-Pliocene minus pre-industrial) with that in the AGCM SST. In the northern North Atlantic and Nordic Seas, the AOGCM simulates a much smaller increase in SST than suggested by proxy data. As the PRISM SST datasets show the largest increase in these regions, it is important to further investigate why the discrepancy is large. The region is thought to be sensitive to the bathymetry – other model experiments have shown that a deepened Greenland-Scotland ridge can affect Pliocene climate by allowing more heat to be transported to the Nordic Seas [6]. The Atlantic meridional overturning circulation (AMOC) in the mid-Pliocene experiment only weakens by about 1 Svedrup (Fig. 5). In the present experiments, the bathymetry remains unchanged. However, a deeper Greenland-Scotland ridge may lead to an increase in the AMOC, as has been suggested by carbon isotope data [7], thereby enhancing the warming in the Nordic Seas and reducing the disparity between model and proxy data.

Comparisons with some other climate models [8] run under similar boundary conditions as part of PlioMIP show good qualitative agreement in the zonally averaged SST in the southern hemisphere (Fig. 6a). Although there is less agreement in the North Atlantic (Fig. 6b), neither the individual models

tested nor the multi-model mean show warming as high as that suggested by proxy data.

3. Modeling of the last millennium

The last millennium simulation (850 – 2000 A.D.), designed under the Paleoclimate Modelling Intercomparison Project phase 3 (PMIP3, [9]) and included in a suite of tier 2 experiments in the Coupled Model Intercomparison Project phase 5, is now being carried out by multiple climate modeling centers over the world and archived. In this project, we aim to conduct not only a basic millennium simulation but also several sensitivity experiments in order to evaluate a model, investigate the uncertainty in the simulations, and pin down the cause of the simulated changes.

Three millennial simulations were performed with the Model for Interdisciplinary Research on Climate, medium-resolution version, MIROC3.2 and MIROC4m. The 20th century simulations, future projections, and other experiments with MIROC3.2, are archived as the World Climate Research Programme (WCRP) Coupled Model Intercomparison Project phase 3 (CMIP3) multi-model dataset. MIROC4m is essentially the same as MIROC3.2 but is renamed after a bug fix related to the calculation of surface fluxes over ice sheets.

Table 1 A list of experiments.

Run	Model	Solar	Volcano	GHG	Orbital variations	Land use	Vegetation
1	MIROC3.2	BCL	G08	PMIP3+CMIP3	Included	PI	PI
2	MIROC4m	DB09	G08	PMIP3+CMIP5	Included	PI	PI
3	MIROC4m	DB09	C08	PMIP3+CMIP5	Included	PI	PI

BCL: Spliced data sets of Bard[11], Crowley[12] and Lean et al.[13].

DB09: Delaygue and Bard[14] spliced into Wang et al.[15] after 1610 A.D.

G08: Gao et al.[16] and Sato et al.[17] (updated) after 1850 A.D.

C08: Crowley et al.[12] and Sato et al.[17] (updated) after 1850 A.D.

DB09 is one of four recommended solar forcings by PMIP3, and G08 and C08 are two recommended volcanic forcings by PMIP3.

Run 1 was conducted with MIROC3.2, and Runs 2 and 3 were conducted with MIROC4m (Table 1). The millennial simulations were carried out after spinning up the model to the stable conditions under the perpetual 850 A.D. boundary conditions. Solar forcing is represented by altering the total solar irradiance, and volcanic forcing is represented by specifying the aerosol optical depth. Orbital variations were included following Berger [10], and greenhouse gas (GHG) concentrations based on ice core records were taken from the PMIP3. Preindustrial (PI) conditions were specified for land use and vegetation in all experiments. No carbon cycle feedback was included.

Figure 7 shows the Northern Hemisphere (N. Hem.) mean temperature time series from the last millennial simulations starting from stable 850 A.D. conditions. Relatively large amplitude of solar variations is applied to run1, while much flatter solar forcing is applied to run2 and run3. Stronger volcanic forcing is applied to run1 and run2 while moderate strength is applied to run3. Although volcanic response in run3 appears to be more consistent with reconstructions, a recent study claims that reconstructions based heavily on tree rings may underestimate the volcanic response [18], and thus more careful examination is necessary.

Figure 8 shows N. Hem. mean temperature time series of the last 150 years from the millennial simulations compared with IPCC-AR4 MIROC3.2 10 ensemble members starting from stable 1850 A.D. conditions (as well as an instrumental record). The overall features originating from the two different initial conditions in Fig. 8a are not significantly different. In Fig. 8b, weaker solar forcing resulted in apparent weaker warming in the first part of the 20th century compared to observations although large internal variability requires more ensemble members.

Next, simulated regional response near North Atlantic is investigated. Figure 9 shows weather regime frequencies between the relatively warm Medieval period (MP) and the relatively cold Little Ice Age (LIA) for three different models. In all models we find a marginal (but insignificant) increase of Blocking frequency when moving from MP to LIA. The North Atlantic Oscillation phases do not yield such systematic shifts (even small) between those two periods. Overall, the frequencies of the weather regimes are remarkably stable, in spite of the strong temperature difference between the periods of high vs. low solar activity. This led to the conclusion that the recent interpretation of proxy records in terms of atmospheric variability by Trouet et al. [19] should be revised in order to take into account the structure of daily meteorological patterns, and/or climate models are too constrained to infer large changes of atmospheric variability. More details are being published in You et al. [20].

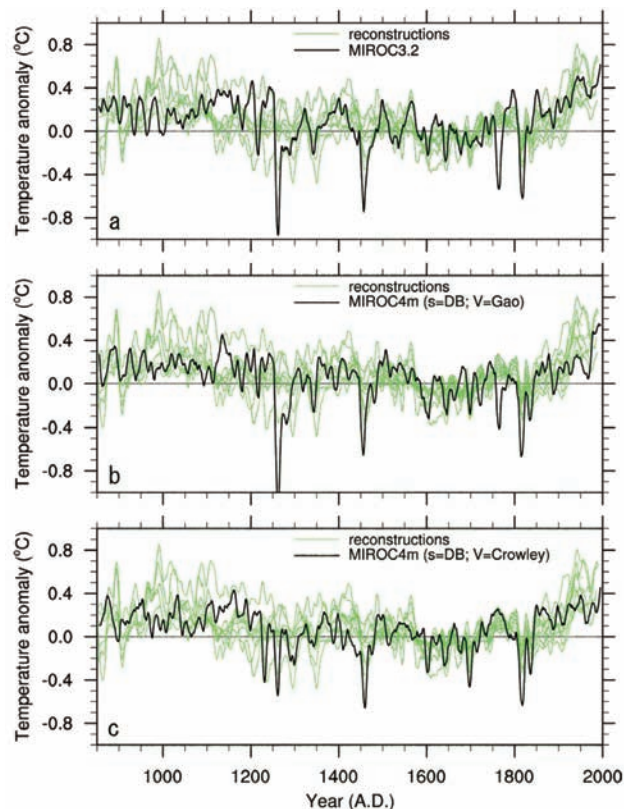


Fig. 7 Last millennial simulations with MIROC: a) run1; b) run2; and c) run3 in Table 1. Anomaly is taken from the average over 1500–1799. 11-yr Gaussian filter is applied.

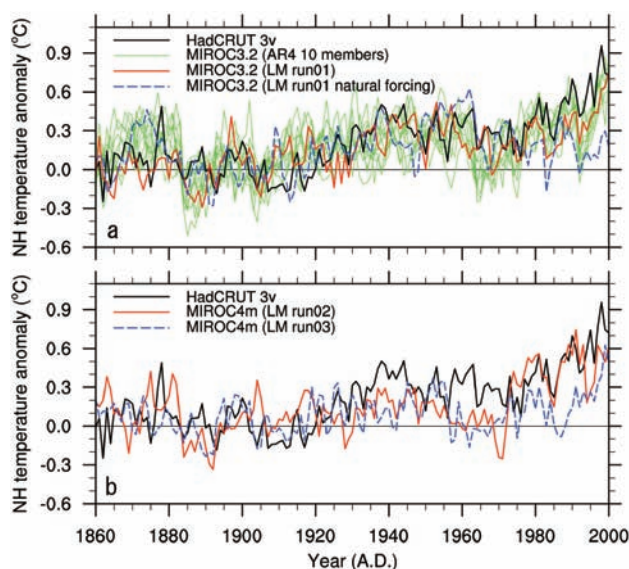


Fig. 8 20th century simulations: a) run1 and b) run2 and run3. Anomaly is taken from the average over 1881–1910. No filter is applied. See text for details.

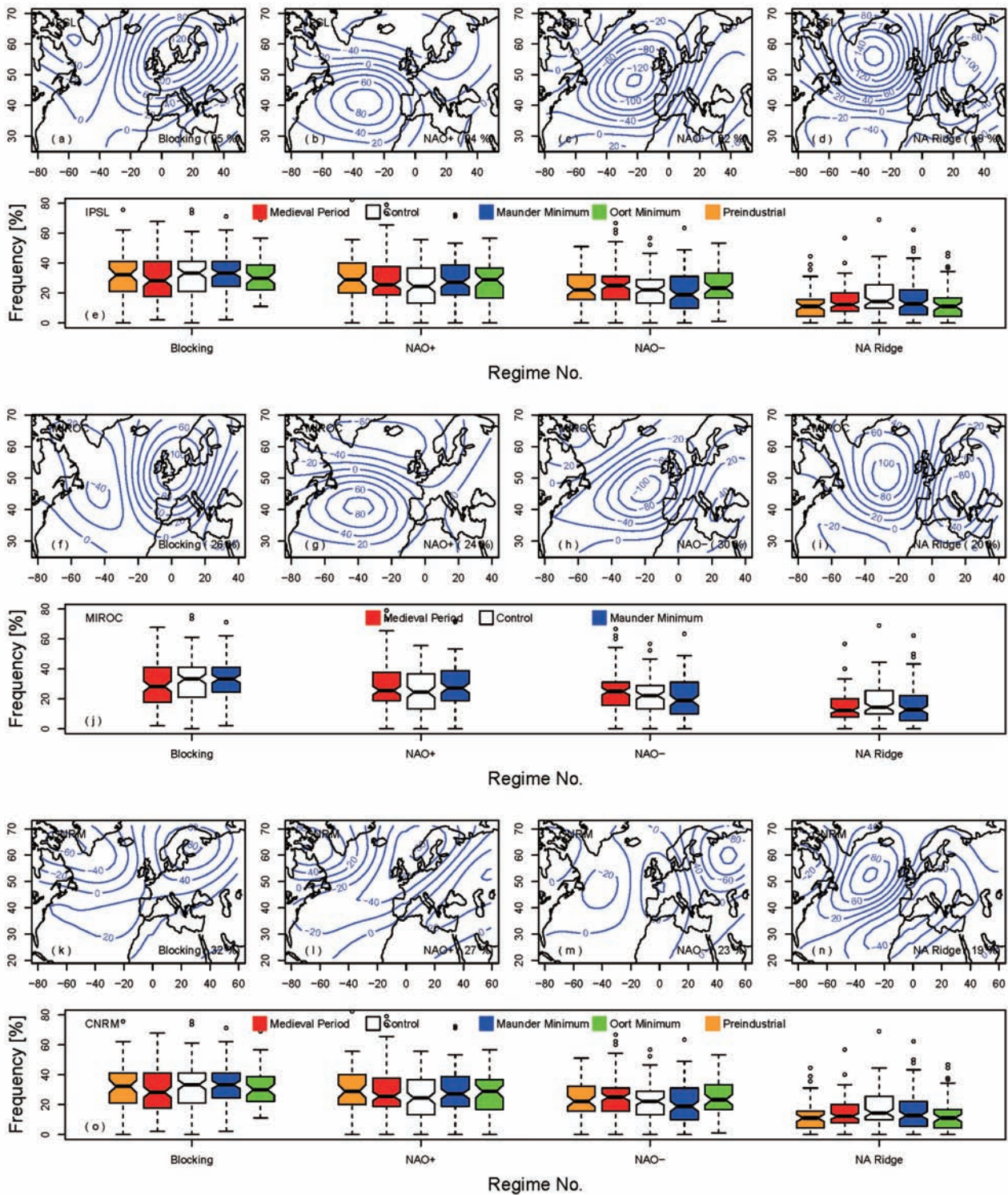


Fig. 9 Winter weather regimes in the IPSL (a-d), MIROC (f-i) and CNRM (k-n) control simulation. Percentages indicate the respective weather regime frequencies. Boxplots of the winter frequencies of each weather regimes for the Medieval Period (red), Control (white) and Maunder Minimum (blue) for IPSL (e), MIROC (j) and CNRM (o) models. Reproduced from Yiou et al. [20].

References

- [1] E. Jansen, J. Overpeck, K. R. Briffa, J.-C. Duplessy, F. Joos, V. Masson-Delmotte, D. Olago, B. Otto-Bliesner, W. R. Peltier, S. Rahmstorf, R. Ramesh, D. Raynaud, D. Rind, O. Solomina, R. Villalba, and Zhang, *Palaeoclimate*, in: *Climate Change 2007: The Physical Science Basis. Contribution of Working Group I to the Fourth Assessment Report of the Intergovernmental Panel on Climate Change*, S. Solomon, D. Qin, M. Manning, Z. Chen, M. Marquis, K. B. Averyt, M. Tignor, and H. L. Miller, ed., Cambridge University Press, Cambridge and New York, 2007.
- [2] W.-L. Chan, A. Abe-Ouchi, and R. Ohgaito, “Simulating the mid-Pliocene climate with the MIROC general circulation model: experimental design and initial results,” *Geoscientific Model Development*, vol. 4, pp. 1035-1049, 2011.
- [3] A. M. Haywood, H. J. Dowsett, B. Otto-Bliesner, M. A. Chandler, A. M. Dolan, D. J. Hill, D. J. Lunt, M. M. Robinson, N. A. Rosenbloom, U. Salzmann, and L. E. Sohl, “Pliocene Model Intercomparison Project (PlioMIP): experimental design and boundary conditions (Experiment 1)”, *Geoscientific Model Development*, vol.3, pp. 227-242, 2010.
- [4] A. M. Haywood, H. J. Dowsett, M. M. Robinson, D. K. Stoll, A. M. Dolan, D. J. Lunt, B. Otto-Bliesner, and M. A. Chandler, “Pliocene Model Intercomparison Project (PlioMIP): experimental design and boundary conditions (Experiment 2)”, *Geoscientific Model Development*, vol. 4, pp. 571-577, 2011.
- [5] K-1 model Developers, *K-1 coupled GCM (MIROC) description*, Center for Climate System Research, Hasumi, H. and S. Emori, ed., The University of Tokyo, Japan, 2004.
- [6] M. M. Robinson, P. J. Valdes, A. M. Haywood, H. J. Dowsett, D. J. Hill, and S. M. Jones, “Bathymetric controls on Pliocene North Atlantic and Arctic sea surface temperature and deepwater production”, *Palaeogeogr., Palaeoclimatol., Palaeoecol.*, vol. 309, pp. 92-97, 2011.
- [7] M. E. Raymo, B. Grant, M. Horowitz, and G. H. Rau, “Mid-Pliocene warmth: stronger greenhouse and stronger conveyor”, *Mar. Micropaleontol.*, vol. 27, pp. 313–326, 1996.
- [8] H. J. Dowsett, M. M. Robinson, A. M. Haywood, D. J. Hill, A. M. Dolan, D. K. Stoll, W.-L. Chan, A. Abe-Ouchi, M. A. Chandler, N. A. Rosenbloom, B. L. Otto-Bliesner, F. J. Bragg, D. J. Lunt, K. M. Foley, and C. R. Riesselman, “Assessing confidence in Pliocene sea surface temperatures to evaluate predictive models,” *Nature Clim. Change*, vol. advance online publication, 2012.
- [9] G. A. Schmidt, J. H. Jungclauss, C. M. Ammann, E. Bard, P. Braconnot, T. J. Crowley, G. Delaygue, F. Joos, N. A. Krivova, R. Muscheler, B. L. Otto-Bliesner, J. Pongratz, D. T. Shindell, S. K. Solanki, F. Steinhilber, and L. E. A. Vieira, “Climate forcing reconstructions for use in PMIP simulations of the last millennium (v1.0)”, *Geosci. Model Dev.*, vol. 4, pp. 33-45, doi:10.5194/gmd-4-33-2011.
- [10] A. L. Berger, “Long-term variations of daily insolation and Quaternary climatic changes”, *Journal of Atmospheric Sciences*, vol. 35, pp. 2362-2367, 1978.
- [11] E. Bard, G. Raisbeck, F. Yiou, and J. Jouzel, “Solar irradiance during the last 1200 years based on cosmogenic nuclides,” *Tellus B*, vol. 52, pp. 985-992, 2000.
- [12] T. J. Crowley, “Causes of climate change over the past 1000 years,” *Science*, vol. 289, pp. 270-277, 2000.
- [13] J. Lean, J. Beer, and R. Bradley, “Reconstruction of solar irradiance since 1610: Implications for climate change,” *Geophysical Research Letters*, vol. 22, pp. 3195-3198, 1995.
- [14] G. Delaygue and E. Bard, “Solar forcing based on Be-10 in Antarctica ice over the past millennium and beyond,” in *EGU 2009 General Assembly*, 2009, pp. EGU2009-6943.
- [15] Y. M. Wang, J. Lean, and N. Sheeley Jr, “Modeling the sun’s magnetic field and irradiance since 1713,” *The Astrophysical Journal*, vol. 625, p. 522, 2005.
- [16] C. Gao, A. Robock, and C. Ammann, “Volcanic forcing of climate over the past 1500 years: An improved ice core-based index for climate models,” *Journal of Geophysical Research, Atmospheres*, vol. 113, p. D23111, 2008.
- [17] M. Sato, J. E. Hansen, M. P. McCormick, and J. B. Pollack, “Stratospheric aerosol optical depths, 1850–1990,” *Journal of Geophysical Research*, vol. 98, pp. 22987-22994, 1993.
- [18] M. E. Mann, J. D. Fuentes, and S. Rutherford, “Underestimation of volcanic cooling in tree-ring-based reconstructions of hemispheric temperatures,” *Nature Geoscience*, vol. 5, pp. 202-205, Mar 2012.
- [19] V. Trouet, J. Esper, N. E. Graham, A. Baker, J. D. Scourse, and D. C. Frank, “Persistent Positive North Atlantic Oscillation Mode Dominated the Medieval Climate Anomaly,” *Science*, vol. 324, pp. 78-80, Apr 3 2009.
- [20] P. Yiou, J. Servonnat, M. Yoshimori, D. Swingedouw, M. Khodri, and A. Abe-Ouchi, “Stability of weather regimes during the last millennium from climate simulations”, *Geophys. Res. Lett.*, in press (accepted on 27 March), doi:10.1029/2012GL051310, 2012.

古環境研究のための多階層数値実験

プロジェクト責任者

阿部 彩子 東京大学 大気海洋研究所

著者

阿部 彩子^{*1}, 吉森 正和^{*1}, Wing-Le Chan^{*1}, 大石 龍太^{*1}, 鈴木香寿恵^{*2}

^{*1} 東京大学 大気海洋研究所

^{*2} 情報・システム研究機構 統計数理研究所 データ同化開発研究センター

大気海洋結合モデル MIROC3.2 および MIROC4m を用いて二つの時代についての気候シミュレーションを行った。一つ目の時代は温暖な約 3.0 ~ 3.3 百万年前の更新世中期である。計算された全球平均気温は産業革命前に比べて約 3.5°C 高かった。主にこの時代の縮小した氷床によって極域の温暖化増幅がもたらされ、結果として南北温度勾配は現在に比べて小さくなったことがわかった。二つ目の時代は西暦 850 年から 2000 年までの過去約千年である。3つの異なる境界条件を用いた実験を行った。それぞれは太陽と火山フォーシングが異なるが、強い火山フォーシングを使用した実験では、復元された短期の北半球気温変動を過大評価していることが示唆された。長期的変動についてはどの実験も全体的に復元データと整合的であった。変動の原因を特定し、内部変動と区別するためには、感度実験などさらに多くの実験が必要である。北大西洋域の天候レジームの解析では、温暖な中世温暖期と寒冷な小氷期において天候レジームの出現頻度がほとんど変わらないことが示された。これは最近提案された復元データの解釈と矛盾しており、復元データの再解釈かモデルの再評価の必要性が指摘された。

キーワード: 大気海洋大循環モデル MIROC, 古気候モデリング, 鮮新世中期, 過去千年

Development of a High-Resolution Climate Model for Model-Observation Integrating Studies from the Earth's Surface to the Lower Thermosphere

Project Representative

Shingo Watanabe

Research Institute for Global Change, Japan Agency for Marine-Earth Science and Technology

Author

Shingo Watanabe

Research Institute for Global Change, Japan Agency for Marine-Earth Science and Technology

The purpose of this project is to further develop a climate model for high-resolution simulations of the Earth's atmosphere from the surface to the lower thermosphere (we particularly focus on 0-100 km), and to investigate dynamics of the middle atmosphere by comparing the model's results to upcoming high-resolution observations which would be obtained by newly developed observation systems with balloons, radars, lidars, airglow imagers, and satellites. The main focus of this high-resolution study is on atmospheric gravity waves which have finer scales, i.e., horizontal wave length of O (10-100 km), than usual climate models resolve, and their characteristics and roles in the middle atmosphere have yet sufficiently understood. We are developing a gravity-wave-resolving high-resolution climate model which has horizontal resolutions of T213 and T639, corresponding to the minimal resolved horizontal wave lengths of 188 km and 62 km, respectively. The vertical resolution of the model is about 500 m. The model's spatial resolution is comparable to that of aforementioned observations, and T639 is enough to resolve large portion of gravity wave spectra which are observed in the middle atmosphere. This year we performed a single year pilot run of the T213 model to evaluate model's basic performance, and obtained simulation results which generally agree with observations. Results of an initial test run of the T639 model are briefly presented, too.

Keywords: High-resolution climate model, atmospheric internal gravity waves

1. Introduction

Long-term future climate change projections obtained by climate model simulations include large uncertainties arising from small-scale atmospheric gravity waves, i.e., horizontal wave length of O (10-100 km), which are not explicitly resolved by the climate models and instead approximately represented by using gravity wave parameterizations (Alexander et al. [1]). We have developed a high-resolution climate model, which explicitly resolves gravity waves, and investigated their characteristics and roles in the atmosphere (e.g., Watanabe et al. [2]). Those outcomes have been used to constrain gravity wave parameterizations to reduce their uncertainty (e.g., Watanabe [3]).

On the other hand, high-resolution observation systems, e.g., utilizing balloons, radars, lidars, airglow imagers, and satellites, have been newly developed. Some of those have global coverage, and others are focused into particular places. The Antarctic Syowa station is one of the latter, where newly developed systems of a MST radar (PANSY: Program of the Antarctic Syowa MST (Mesosphere/Stratosphere/Troposphere) / IS (Incoherent Scatter) Radar) and lidar start their operations. The radar has vertical resolution of O (100 m) and temporal resolution of O (1 min) and observes three dimensional

wind fields, which will be compared to our model results in this project. The lidar observes temperatures with a little bit less vertical and temporal resolutions. By combination and integration of those high-resolution observations with model results, our understanding of atmospheric small-scale processes, e.g., gravity waves, will be greatly improved.

2. The high-resolution climate model

The high-resolution climate model is based on JAGUAR (Japanese Atmospheric General circulation model for Upper Atmosphere Research; Watanabe and Miyahara, [4]), which has been developed as a hybrid of the MIROC (Model for Interdisciplinary Research On Climate) -AGCM (K-1 model developers [5]) and Kyushu-GCM (Yoshikawa and Miyahara [6]). The model has a top boundary at about 150 km, whereas conventional climate models have their tops near 30-50 km (IPCC, 2007). Gravity waves are generally generated in the troposphere and propagate upward, and some of them propagate up to the mesosphere and lower thermosphere (MLT) region ($z = 50-120$ km) and dissipate there to affect background fields. In order to study such processes, we construct the high-top and high-resolution climate model. In addition to physical parameterizations used in conventional climate models, e.g.,

cumulus convection, boundary layer, large-scale precipitation, our model includes some more parameterizations required in the MLT region, e.g., radiation schemes based on non-local thermal equilibrium (important above 70 km), molecular viscosity, molecular thermal conductance, chemical heating, and ion drag (important above 100 km). A height dependent horizontal diffusion is introduced into the model's MLT to represent effects of background small-scale turbulences, whose strength is presumed to increase with increasing height from 60 km to 140 km.

The model has horizontal resolutions of T213 and T639, corresponding to the minimal resolved horizontal wave lengths of 188 km and 62 km, respectively. The vertical resolution of the model is about 500 m. These model's spatial resolutions are comparable to the aforementioned observations, and T639 is enough to resolve large portion of gravity wave spectra which are observed in the middle atmosphere (e.g., Alexander et al. [1]).

The T213 model is fully optimized for the Earth Simulator by the MIROC group with supports from the Earth Simulator Center. Although the T639 model could have a room of optimizations, scalability from T213 to T639 is relatively good, which is estimated based on theoretical expectations: an expected computational time becomes 27 times as long as the original one when we triple the horizontal resolution, and our model have achieved c.a. 32.

3. T213 pilot simulation

In order to investigate basic performance of T213 model to reproduce observed climatological wind and temperature fields, we performed a single year pilot simulation which starts from June of a certain model year and ends in next May. This is a free-running simulation that does not incorporate any observed fields into the model's atmosphere. Sea surface temperatures and sea-ice distribution are prescribed using observed climatology. Figure 1 compares the zonal mean temperature and the zonal mean zonal wind obtained with this simulation to the Met Office assimilation data (below 50 km) (Swinbank and O'Neill, [7]) and the 1986 Committee on Space Research (COSPAR) International Reference Atmosphere (CIRA) data (above 50 km) (Fleming et al. [8]). The model well reproduces observed wind and temperature distributions, especially below a 50 km level. It is challenging to reproduce winds and temperatures in the MLT region (50-100 km). The model qualitatively succeeds to reproduce them, but several biases are obvious. The model underestimates a temperature minimum near the Arctic summer mesopause (around 90 km) by 10-20 K. In the winter (southern) hemisphere, the model overestimates a temperature maximum above the Antarctic wintertime stratopause (around 60 km) by 10-20 K, and underestimates a temperature minimum around the mesopause (~100 km). These temperature biases are likely caused by biased distributions of vertical wind motions, which cause biases in dynamical heating. The first observation of

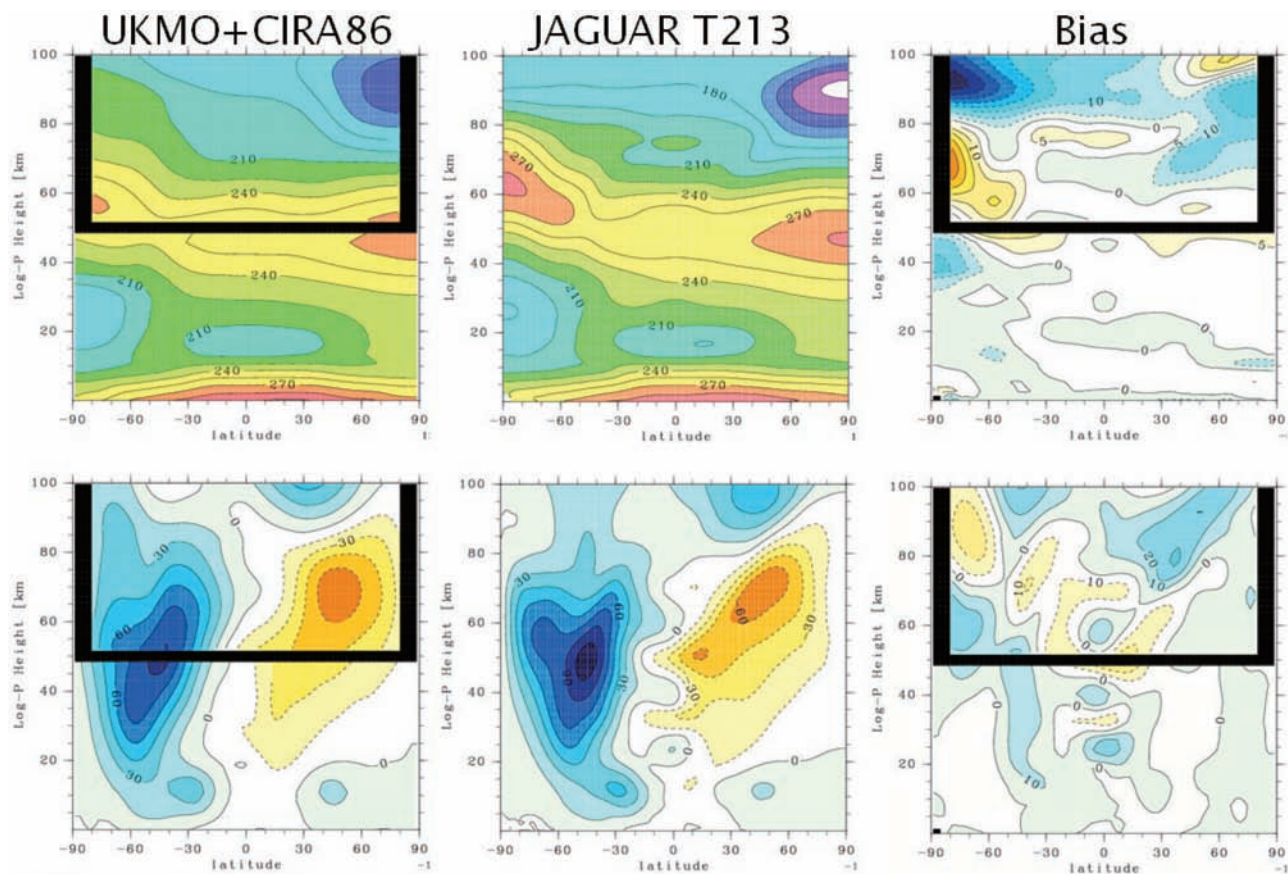


Fig.1 The zonal mean zonal wind and the zonal mean temperature in July.

vertical winds over the Antarctic MLT region will be done by the PANSY radar, and it would be very useful to further evaluate the model's result. It would be also important to investigate sensitivity of model's performance to changing the horizontal resolution, which would also be tackled in this project.

Figure 2 shows seasonal evolution of zonal and meridional winds over the Syowa station simulated with the T213 model. Strong westerly winds are predominant in wintertime lower mesosphere (60-70 km), above which the westerly winds rapidly decrease with increasing altitude (70-75 km) and weak westerly winds exist in the upper mesosphere and lower thermosphere (75-100 km). The meridional winds are generally weaker than the zonal winds, and poleward flows are dominant around 75 km, where the strong reduction of westerly winds occurs. This reduction of westerly winds with altitude is caused by dissipation of gravity waves in the model (e.g., Watanabe et al. [2]), and will be further investigated in this project. In summer, easterly winds exist in an altitude range of 60-90 km, above which they reverse to westerly winds. Strong equatorward flows exist between the easterly and westerly winds. This vertical inversion of zonal winds must also be explained by effects of gravity waves, which will be elucidated in this project using model's three dimensional data. Overall, the seasonal evolution of horizontal winds is qualitatively similar to that obtained by MF radar observations at the Syowa station (e.g., Tsutsumi et al. [9]), which is encouraging for us to develop the finer T639 model and further investigate dynamics in the MLT region by combining the model's result with observations.

4. T639 initial run

Since we ran the T639 model for the first time, we had to obtain an initial condition by interpolating the T213 model's data. This section describes rather a technical issue to prepare initial conditions used in the finer T639 resolution. A simple linear interpolation was used to convert T213 grid data into the T639 grid. On the other hand, the surface topography in the T639 model is (independently) generated from surface elevation dataset and is generally finer and steeper than that for T213. Hence, an imbalance occurs between the interpolated surface pressure and wind fields and the finer surface elevation in the T639 model. This imbalance causes an initial shock in the model fields; rapid adjustment processes occur and spurious dispersive gravity waves are emitted from near the surface, which three-dimensionally propagate far away from their source regions, continuously reaching the MLT region. These spurious gravity waves generally have huge amplitudes, small horizontal wavelengths and large vertical group velocities, and easily reach the MLT region and violate temperature and wind structures there. Therefore we have to reduce their amplitude by introducing unusually strong scale-selecting damping of wave motions until the initial shocks calm down. This damping, of course, damps gravity waves originally existing in the T213 model's fields, too, which means that T639 model's wind and temperature fields just after the damping retain only very small information of the T213 wave fields. After several initial trials, we have found that about 3 days are needed with the enhanced damping to obtain a proper initial condition that does not contain suspicious large amplitude small-scale waves. Figure 3 demonstrates such spin-up processes in terms of time evolution

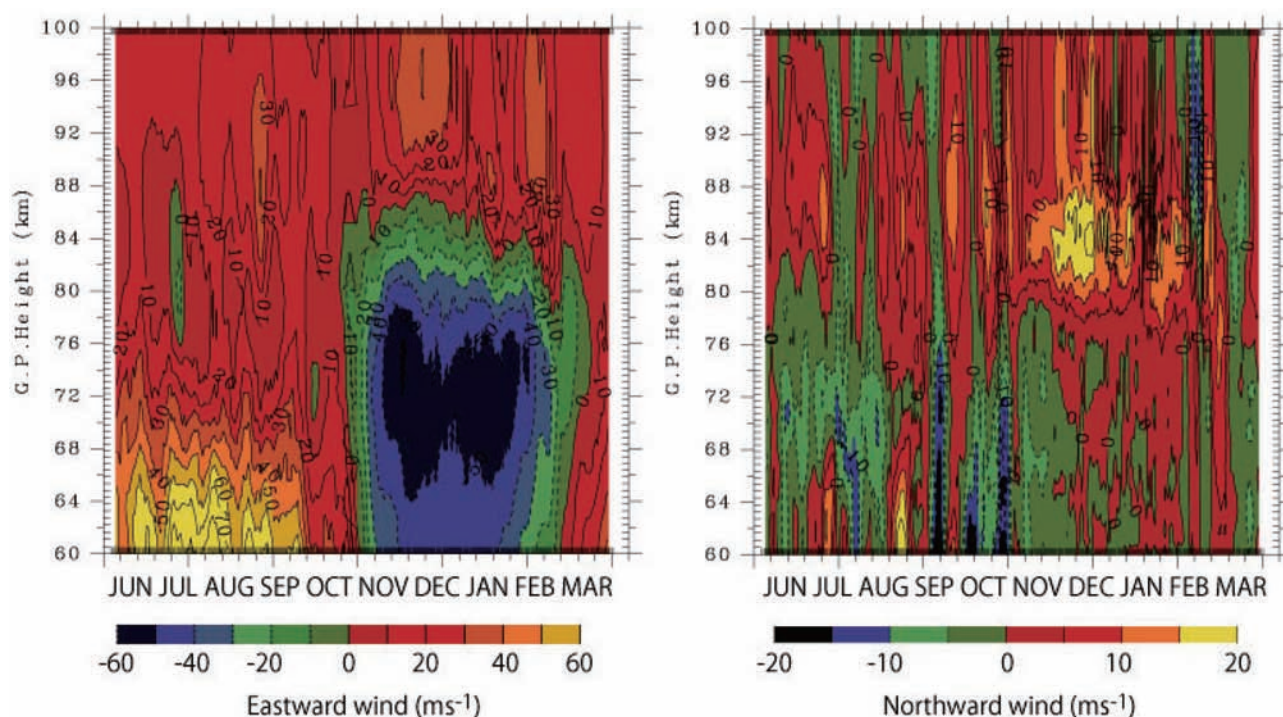


Fig. 2 Time evolution of horizontal wind profiles over the Syowa station simulated with the T213 model.

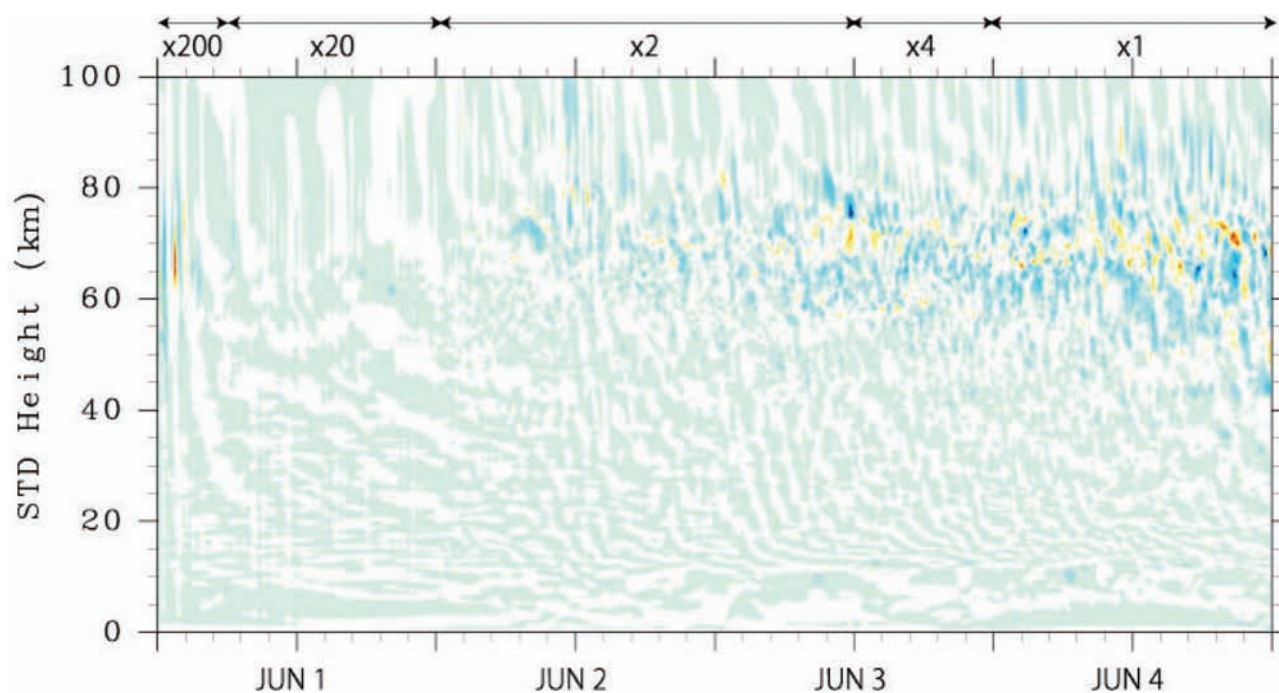


Fig. 3 Time evolution of horizontal divergence profile over the Antarctic Syowa station simulated with the T639 model. The numbers with arrows on the top of the figure show the strength of the scale-selective damping relative to its standard value. After appearance of the initial shocks in the first 6 hours, the damping is reduced so that wave motions relevant to the T639 horizontal resolution gradually spin-up. Around 12:00 universal time on the third day, a rapid amplification of suspicious gravity waves arising from the initial adjustment processes terminated the model's integration, which occurred in different grid points. Therefore the strength of damping was doubled for 12 hours, and then the model started running successfully.

of horizontal wind divergence profiles, which approximately show gravity wave phase patterns, over the Antarctic Syowa station.

5. Summary

The motivation and goal of the present project are described, that is, to improve our understanding of atmospheric small-scale processes, e.g., gravity waves, the state-of-art high-resolution climate model and high-resolution observation (including the PANSY radar at the Antarctic Syowa station) are going to be combined and integrated. The model we are going to develop and use in this project resolves wave motions with 62 km in horizontal and 1 km in vertical at the minimum scale, which can be closely compare to the upcoming high-resolution observations.

The single year pilot simulation using the lower (~188 km) horizontal resolution model shows generally encouraging results, which qualitatively agree with observations in terms of the monthly averaged zonal mean zonal winds and temperatures and the temporal evolution of horizontal wind profiles at the Antarctic Syowa station. To further improve model's results, the usefulness of upcoming observation data set is undoubtful.

The spin-up processes of the higher-horizontal resolution model are also briefly presented, which may be informative for initialization of any forecast / assimilation experiments which we are planning to perform later in this project. Overall, the

initial goals we expected in the first year of this project have successfully been achieved.

References

- [1] ALEXANDER, M. J., M. GELLER, C. MCLANDRESS, S. POLAVARAPU, P. PREUSSE, F. SASSI, K. SATO, S. ECKERMANN, M. ERN, A. HERTZOG, Y. KAWATANI, M. PULIDO, T. SHAW, M. SIGMOND, R. VINCENT, AND S. WATANABE, 2010: Recent developments in gravity wave effects in climate models, and the global distribution of gravity wave momentum flux from observations and models. *Q. J. Roy. Met. Soc.*, 136, 1103–1124, doi:10.1002/qj.637.
- [2] WATANABE, S., Y. KAWATANI, Y. TOMIKAWA, K. MIYAZAKI, M. TAKAHASHI, AND K. SATO, 2008: General aspects of a T213L256 middle atmosphere general circulation model. *J. Geophys. Res.*, 113, doi:10.1029/2008JD010026.
- [3] WATANABE, S., 2008: Constraints on a non-orographic gravity wave drag parameterization using a gravity wave resolving general circulation model. *SOLA*, 4, 061-064, doi:10.2151/sola.2008-016.
- [4] WATANABE, S. AND S. MIYAHARA, 2009: Quantification of the gravity wave forcing of the migrating diurnal tide in a gravity wave-resolving general circulation model. *J. Geophys. Res.*, 114, D07110,

doi:10.1029/2008JD011218.

- [5] K-1 MODEL DEVELOPERS, 2004: K-1 coupled GCM (MIROC) description, *K-1 Tech. Rep.*, 1, pp. 1–34, Univ. of Tokyo, Tokyo, Japan.
- [6] YOSHIKAWA, M. AND S. MIYAHARA, 2005: Excitations of nonmigrating diurnal tides in the mesosphere and lower thermosphere simulated by the Kyushu-GCM. *Adv. Space Res.*, 35, 1918–1924, doi:10.1016/j.asr.2005.03.023.
- [7] SWINBANK, R. AND A. O'NEILL, 1994: A stratosphere-troposphere data assimilation system. *Mon. Weather Rev.*, 122, 686–702, doi:10.1175/1520-0493(1994)122<0686:AS TDAS>2.0.CO;2.
- [8] FLEMING, E. L., S. CHANDRA, J. J. BARNETT, AND M. CORNEY, 1990: Zonal mean temperature, pressure, zonal wind, and geopotential height as functions of latitude, COSPAR International Reference Atmosphere: 1986, Part II: Middle atmosphere models. *Adv. Space Res.*, 10, 11 – 59, doi:10.1016/0273-1177(90)90386-E.
- [9] TSUTSUMI, M., T. ASO, AND M. EJIRI, 2001: Initial results of Syowa MF radar observations in Antarctica. *Adv. Polar Upper Atmos. Res.*, 15, 103-116.

高解像度気候モデルの開発 - 地表から下部熱圏大気のモデル・観測統合研究に向けて

プロジェクト責任者

渡邊 真吾 海洋研究開発機構 地球環境変動領域

著者

渡邊 真吾 海洋研究開発機構 地球環境変動領域

本研究の目的は、地球大気地表から下部熱圏（0-100km）までの高解像度シミュレーションを行うことができる気候モデルを開発・発展させるとともに、そのモデルのシミュレーション結果と、最新の高解像度の観測を比較することによって中層大気の力学過程を詳細に調べることである。（観測データは気球、大気レーダー、ライダー、大気光イメージャおよび衛星測器のものを用いる。）

我々の高解像度研究の主要な対象は、通常の気候モデルでは解像することができず、いまだ中層大気中におけるそれらの性質や役割の理解が十分でない小規模の大気内部重力波である。このため、我々は重力波を直接解像できるような高解像度気候モデルを開発している。モデルの水平解像度は T213 と T639 の 2 バージョンがあり、それぞれの解像できる最小水平波長はおよそ 188km と 62km に相当する。モデルの鉛直解像度は 500m であり、水平解像度とともに、上述の観測データと 1 対 1 比較できるほどの解像度を持っている。

本年はモデルの基本的な性能を評価するために、T213 モデルで 1 年間の試行実験を行い、観測データとの比較を行った。モデルの結果は観測された温度や風の場を概ね良く再現することが確認できた。また、T639 モデルを用いたスピンアップ実験の結果も簡単に報告する。

キーワード: 高解像度気候モデル, 大気内部重力波

Chapter 2

■ **Epoch-Making Simulation** ■

Large Scale Simulations for Carbon Nanotubes

Project Representative

Syogo Tejima

Research Organization for Information Science & Technology

Authors

Syogo Tejima^{*1}, Satoshi Nakamura^{*1}, Yoshiyuki Miyamoto^{*2} and Hisashi Nakamura^{*1}

*1 Research Organization for Information Science & Technology (RIST)

*2 National Institute of Advanced Industrial Science and Technology (AIST)

Nanosystem Research Institute (NRI)

CARBON NANOTUBE RESEARCH GROUP

Morinobu Endo, Eiji Osawa, Atushi Oshiyama, Yasumasa Kanada, Susumu Saito, Riichiro Saito, Hisanori Shinohara, David Tomanek, Tsuneo Hirano, Shigeo Maruyama, Kazuyuki Watanabe, Takahisa Ohno, Yutaka Maniwa, Yoshikazu Fujisawa, Yoshiyuki Miyamoto, Hisashi Nakamura

Our study consists of two parts: development of a model and application of different models that had been optimized by our group for the Earth Simulator. The first one is extending a linear combination of atomic orbitals model to finite temperature case. For the second one, we present the simulation results of the following four studies: (1) controllable gap of Mackey crystal for a solar cell material, (2) ability of adsorption of cesium on carbon-nanotube, (3) electron transport properties of grapheme for electric device, and (4) collective motion of molecular dimer of acetylene molecules inside carbon-nanotube.

Keywords: Large scale simulation, TB theory, ab initio theory, Time-dependent DFT, Carbon Nanotube, Fullerenes, Graphene, Mackay crystal, solar cell, Green energy, quantum electronic transport, photoelectric material

1. Introduction

Nano-carbon materials such as nanotube, fullerene and graphene have potential for applications to the advanced industries. For nano-carbon materials, it has been recognized that large-scale simulation is a powerful and efficient tool to find and create novel functional nano-carbon materials.

Our aim is to investigate fundamental properties of nano-scale phenomena and to design nanostructure materials, using Earth Simulator. To this end, so far we have developed different large-scale simulation models, including tight-binding molecular dynamics model, *ab-initio* density functional theory (DFT) model, and time-dependent DFT model.

Our subjects in the current year are classified into two categories: development of a model and application of different models that had been optimized by our group for the Earth Simulator. The first one is extending a linear combination of atomic orbitals model to finite temperature case. The second one contains the following four physical studies: (1) controllable band gap of Mackey crystal for a solar cell material, (2) ability of adsorption of radioactive cesium and strontium on carbon-nanotube, (3) electron transport properties of grapheme for electric device, and (4) collective motion of molecular dimer of acetylene molecules inside carbon-nanotube (CNT).

2. Development of a model

2.1 Finite-temperature LCAO method using Slater-type basis functions

Linear combination of atomic orbitals (LCAO) methods have made a great success in the study of electronic structures of atoms, molecules, and solids. The conventional LCAO methods, however, are formulated for ground-state systems. This makes it difficult to extract finite-temperature properties from those calculations.

The aim of our study is to propose an approach for extending the conventional LCAO methods to finite-temperature case. As an application of our approach, we have developed a code named MORIS, which calculates finite-temperature electronic structure within the unrestricted Hartree-Fock approximation.

In the implementation of most LCAO methods, the true atomic orbitals are not used, but approximate atomic orbitals are used instead. They are called basis functions. Among the basis functions, Gaussian-type orbitals (GTOs) and Slater-type orbitals (STOs) are extensively used in literature. We adopt STOs, since they resemble the true atomic orbitals more closely than GTOs.

Figure 1 shows the Helmholtz free energy for a hydrogen fluoride (HF) molecule at $T=300$ [K] within the unrestricted

Hartree-Fock approximation with STOs. The orbital exponents without optimization are set to the values of isolated H and F atoms.

As seen from Fig. 1, when the optimization of the orbital exponents is not performed, the calculated values of the bond length and dissociation energy are 0.99[Å] and 2.28[eV], respectively. On the other hand, when the optimization of the orbital exponents is performed, the calculated values of the bond length and dissociation energy are 0.93[Å] and 3.25[eV], respectively. Since the experimental values of the bond length and dissociation energy for a HF molecule are 0.92[Å] and 5.84[eV], respectively, we find that the optimization of the orbital exponents makes a significant modification of the bond length and dissociation energy. Figure 2 shows the optimized values of the orbital exponents as a function of the bond length. We can see that the values of the orbital exponents for a HF molecule are considerably different from those for separated hydrogen and fluorine atoms. This indicates that using the orbital exponents for isolated atoms is not appropriate in the case of molecules. In the conventional LCAO methods, the orbital exponents are determined to be the best for the electronic structure not of the entire molecule but of each atom; therefore the feature of our LCAO method consists in being able to

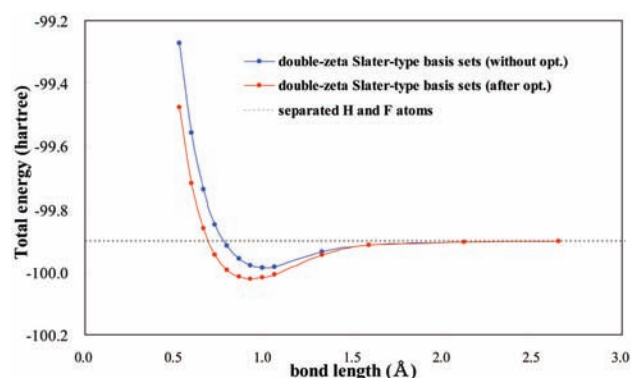


Fig. 1 The Helmholtz free energy for a HF molecule at $T=300$ [K]. The blue and red lines represent the simulation results without and after optimization of orbital exponents, respectively. The orbital exponents without optimization are set to the values of isolated H and F atoms.

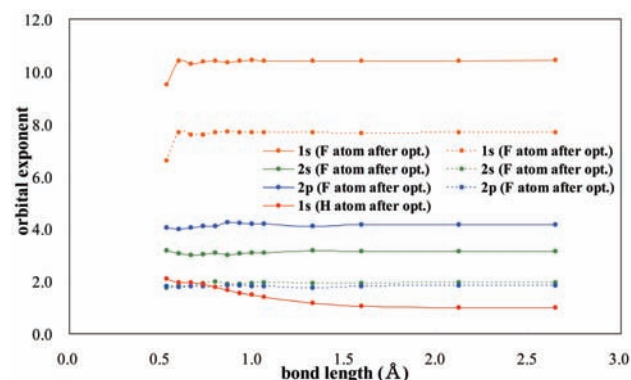


Fig. 2 The optimized values of the orbital exponents for a HF molecule at $T=300$ [K].

optimize the orbital exponents as well as in being able to calculate the electronic structure at finite temperature.

3. Physical studies on nano carbon-based materials

3.1 Controllable band gap of Mackay crystal for a solar cell material

We have been carrying out the whole simulations on the Mackay crystals using GSW method to find synthesis process and DFT approximation to obtain mechanical and electrical properties. These simulations showed the band gap for Mackay crystals are ranged from 0.05 eV to 0.94 eV in the different sizes, P48, P144 and P192, respectively. On the basis of this prediction, we proposed a tandem-type solar cell designed by stacking Mackay crystal films with the different band gap. Such a solar cell would be able to absorb the sun light with spread spectrum.

In this year, the possibility whether the band gap can be controlled by putting pressure and distorting the lattice, besides by using the different sizes, is investigated. Figures 3 and 4 show the effect of crystal strain on band gap. Where Fig. 3 is for zigzag type, Fig. 4 armchair and the top figure represents total energy vs. lattice constant, bottom figure band gap vs. lattice constant. The lattice constant of a steady Mackay crystal with the minimum value in terms of total energy is shown by the arrow in the figure.

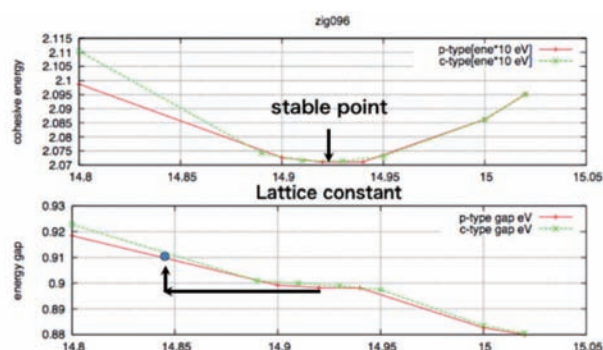


Fig. 3 For zigzag type, top figure represents total energy vs. lattice constant, bottom figure band gap vs. lattice constant. The band gap increases with decreasing the lattice constant.

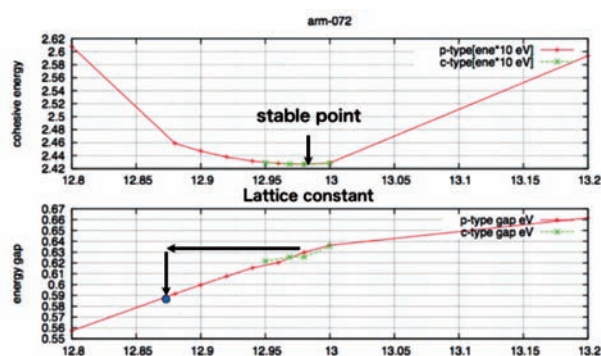


Fig. 4 For armchair type, top figure represents total energy vs. lattice constant, bottom figure band gap vs. lattice constant. The band gap decreases with decreasing the lattice constant.

In general, if the lattice constant decreases, then the wave function of atomic orbitals may overlap each other. Thus the crystal becomes metallic and the band gap decreases or disappears. This scenario agrees with the result of armchair type. Conversely, in the case of zigzag type, the band gap extends if lattice constant decrease. Such a interested band mechanism is unknown yet.

By compression of crystal (lattice constant becomes to decrease), one type of crystal extends band gap and the other type of crystal narrow. The band gap is controllable by compressing the lattice constant. We expect the high efficient tandem-type solar cell consisting of different band gap of Mackay crystal.

3.2 The ability of adsorption of cesium on CNT^[1]

The remediation of environment contaminated by the falling radioactive species as cesium and strontium, is one of the urgent technical targets of our society. It is required to develop the new materials having features as effective absorbent, low cost, abundant supplies and incineration or so for the practical cleaning operation and deployment. In this context, we have studied the ability of carbon nanotubes to adsorb the radioactive cesium atoms.

From the view point of atomic binding energy, we have investigated the adsorption process of cesium atoms on CNT through simulation. As first stage we modeled that both cesium and carbon of nanotube exist only in the atmosphere.

Simulations showed that when the isolated three cesium atoms form a cluster, the total energy decrease by the formation energy, about 0.7 eV per atom. The cluster state is then stable than the isolated. Furthermore, when a cesium cluster is

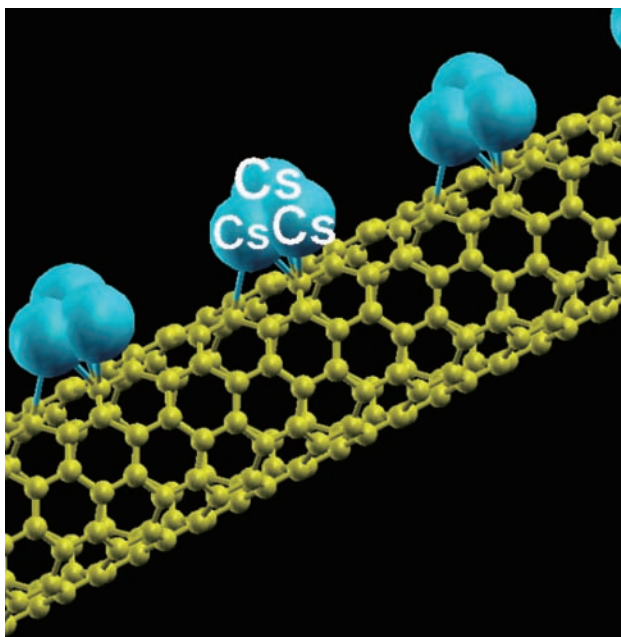


Fig. 5 Cesium clusters adsorb on the surface of CNT. CNT would be candidate for materials to remedying the radioactive Cesium atoms from environment.

adsorbed on the surface of carbon nanotube shown as in Fig. 5, the total energy additionally decreases by 1.5 eV. As for cesium, simulation on different four elements shows, as in Fig. 6, that the cesium cluster is most easily adsorbed on the surface of CNT among the four elements.

The mechanism of adsorption of cesium on the surface of CNT is considered from atomic charge movement. Figure 7 shows the number of electrons filling the atomic orbital. It shows the atomic binding changes the number of the electrons occupied, between before- and after- absorption.

We understand that the cesium atoms interact with another

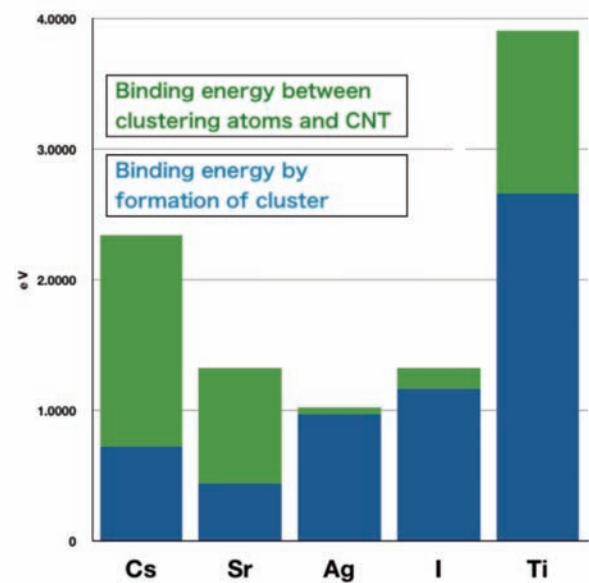


Fig. 6 Binding energy for five elements. The blue means the binding energy between three isolated atoms and their cluster and the green binding energy of cluster on the surface of CNT.

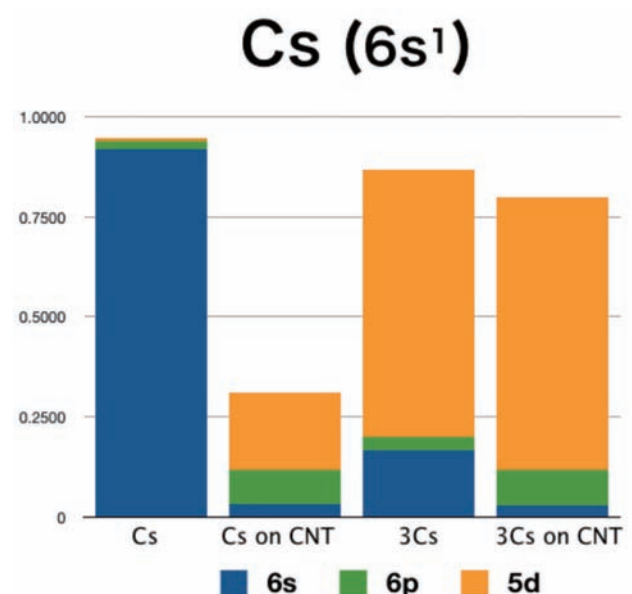


Fig. 7 Atomic orbitals are full with electrons. The isolated cesium atom consists of almost all 6s electrons of 0.9 e. On the surface of CNT, the number of electrons on cesium atom decreases. The cluster of three atoms fills with electrons of 5d-orbital.

cesium atoms and CNT by moving the electron from 6s-orbital to empty 5d-orbital. The π -orbital of CNT plays important role in the adsorption of cesium.

3.3 Electronic Transport properties of graphene for electronics device^[2]

On the basis of a tight-binding (TB) theory, we have developed a simulation program to investigate the electron transport characteristics of graphene for both basic properties and applicability for 'nano-carbon conductor.' The effect of contact between nano-carbons conductor and metallic electrodes are studied through simulations. It is our assumption that the electric transport be controlled by wave function overlap between nano-carbon structure and metal rather than by intrinsic properties of nano-carbons.

Last year we simulated an electron transport under the parameter of a hopping integral t_α coupling between electrodes and α -orbital of CNT. The results strongly depend on choice of orbitals α . The electron transport is strongly

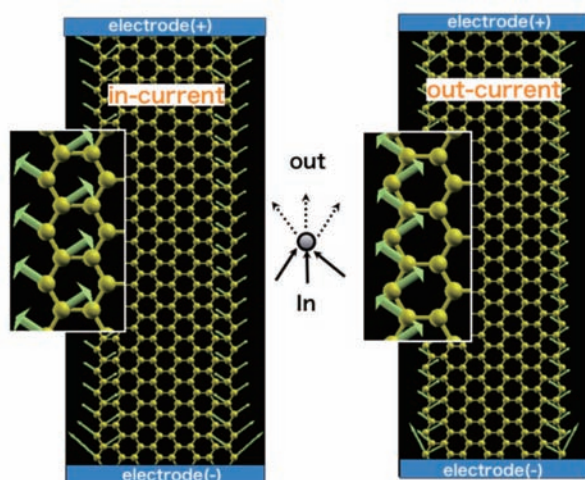


Fig. 8 The arrow shows the direction of in or out electron flow for zigzag ribbon graphene.

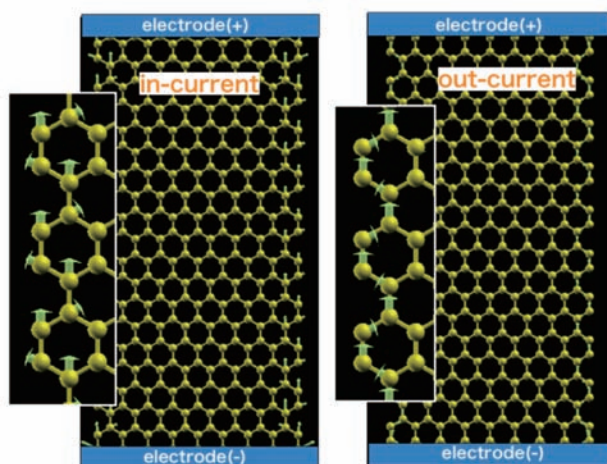


Fig. 9 The arrow shows the direction of in or out electron flow for armchair ribbon graphene.

dominated by coupling through the σ - or π -orbital. The π -orbital coupling, rather than σ -orbital coupling, of CNT allows better conductance.

This year we applied the simulation model to graphene sheets. Figure 8 shows the direction of electron flow on each atom for zigzag edge. The electrons flow almost at both edges. The graphene for armchair edge is shown in Fig. 9. It is expected that the electronic conduction becomes excellent even if graphene have a narrow width. As for electronic transport, the π -orbital coupling of graphene allows better conductance. As a result, it is considered that, as the π orbital is located vertically at the surface, the electrode can be connected with the π -orbital directly, even if graphene is sandwiched in between electrodes. Such behavior of graphene is one of promising features for highly efficient electronic conductor device.

3.4 Collective motion of molecular dimer of acetylene molecules inside CNT

Following 2010, investigation of molecular dynamics under irradiation with the femtosecond laser was continued. Last year, we proved laser-induced disintegration of HCl molecules inside (8,0) CNT, and that result was published in Phys. Rev. Lett (2010). We further tested collective motion of molecular dimer of acetylene (C_2H_2) molecules in larger diameter (14,0) CNT. Acetylene is important gas for fuel and source of higher organic molecules, and nano-space reaction inside CNT has attracted high attentions. We performed electron-ion dynamics under presence of pulse laser with alternating electric field mimicking the laser pulse by solving time-dependent Kohn-Sham equation

$$i\hbar \frac{d\Psi_n(r, t)}{dt} = \{H_{KS}(r, t) + V_{ext}(r, t)\} \Psi_n(r, t),$$

which includes scalar potential mimicking optical field.

Two acetylene molecules were investigated and the stable orientation of them was found to be perpendicular with respect to tube axis shown in Fig. 10. Laser pulse with wavelength

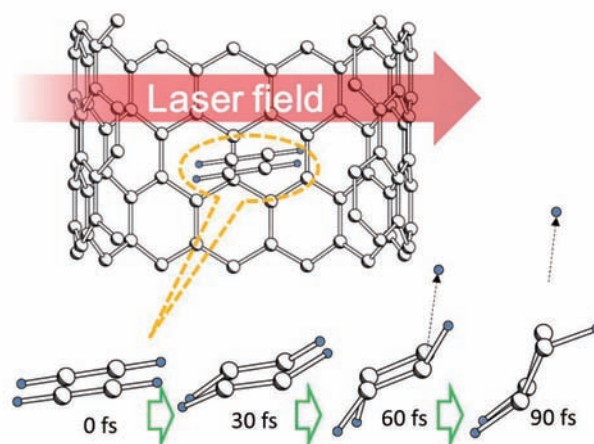


Fig. 10 Two acetylene dynamics inside (14,0) CNT upon laser irradiation. The display showing the dynamics of two acetylene molecules omits the atomic positions of (14,0) CNT for easy viewing.

800 nm with full-width of half maximum 2 fs was applied with maximum intensity of laser field $E_{\max} = 12 \text{ V/\AA}$. Interestingly, after giving ultra-short laser pulse, these two molecules start to rotate with synchronized manner, while C-H vibrations inside molecules were not synchronized.

Emission of hydrogen atom from one of the two acetylene molecules were seen but not shown in weaker intensity of pulse ($E_{\max}=10 \text{ V/\AA}$). This result was compared to isolated single acetylene molecule and artificially located two acetylene dimers under impulse of ultra-short laser. Inter-molecular interaction during the photo-excited dynamics and modulation of the laser field by CNT wall were recognized by comparing the simulation results. We believe that this kind of simulation would be useful for designing new chemical pathway forming new material with use of CNT as nano-test tube. This simulation has just accepted for the publication in Proceedings of the National Academy of Science of the United States of America (PNAS) in 2012.

4. Summary

We have developed a new computer code named MORIS from scratch. We also have performed large-scale simulations for nano materials by using large-scale simulation models, including tight-binding molecular dynamics model, *ab-initio* DFT model, and time-dependent DFT model. These models allowed us to simulate the nano material properties with excellent performance on the Earth Simulator. Our large-scale simulations can provide valuable information on physical phenomena, method of materials design, and method of development of novel functionality of nano carbon-based materials.

References

- [1] S. Tejima, Nikkei newspaper Mar.12 (2012).
- [2] S. Tejima, RIST NEWS No.52 Mar.23 (2012).

カーボンナノチューブの特性に関する大規模シミュレーション

プロジェクト責任者

手島 正吾 高度情報科学技術研究機構

著者

手島 正吾^{*1}, 中村 賢^{*1}, 宮本 良之^{*2}, 中村 壽^{*1}

*1 高度情報科学技術研究機構

*2 産業技術総合研究所 ナノシステム研究部門

1. 研究目的

優れた物性が予想されたナノテクノロジーの基本材料であるナノ炭素類（カーボンナノチューブ（CNT）、フラーレン、グラフェン）を対象として、熱伝導、機械特性、新奇な物質であるマッカーイ構造体の生成パス、次世代CPUのCNT配線における電磁作用の影響など、実験では得がたい物理現象、新物質創成法、新機能発現法を大規模な第一原理・強結合近似分子動力学シミュレーションによって明らかにし、その成果を学界、先端産業へ提供するとともに、地球シミュレータの性能を実証する。加えて、ナノ炭素類の新奇特性を人類的課題である温暖化対策としての環境技術・新エネルギー開発に役立てる大規模シミュレーション研究を実施する。

2. 成果

本研究により産業応用、学術応用、計算科学に係わる以下のような成果をあげることができた。

- (1) 有限温度における物理量を予言できる形へLCAO法を拡張した第一原理計算コードを作成した。実装にはスレーター型軌道を用いて、少ない数の基底関数で高い精度の計算を可能にした。また有限温度下にある分子のさまざまな状態において、スレーター型軌道の軌道指数を自動的に最適化することができるため、従来のLCAO法よりも物理量が基底関数の取り方に依存しないシミュレーションを可能にした。テスト計算として、27°Cでのフッ化水素のシミュレーションを実施し、軌道指数の最適化により計算結果が大幅に改善することを示した。
- (2) マッカーイ結晶の太陽電池への応用の観点から、第一原理計算法によるマッカーイ結晶の電子状態計算を実施し、その格子定数依存性を調べた。昨年度までの研究では、マッカーイ結晶はそのサイズによりバンドギャップが異なることから積層マッカーイ結晶からなる多接合型太陽電池を提案した。本年度は、安定状態の近傍で結晶を歪ませ格子定数を変化させたときのバンドギャップの変化を調べた。格子定数を小さくすれば電子軌道が重なりバンドギャップは小さくなると予想されるが、あるサイズのマッカーイ結晶では逆に大きくなる結果を得た。外力によりバンドギャップを抑制することが期待できる。そのメカニズムを今後明らかにする。
- (3) 大気中、地層、海水に拡散した放射性元素を回収する技術は社会的急務である。その材料として、安価で、豊富で、安全で、処理が容易な新素材を開発することが望まれており、本研究ではカーボンナノチューブによるセシウム元素回収の可能性を調査した。結合エネルギーの観点から、CNTへの吸着のし易さを調べた結果、孤立した3原子セシウムは結合してクラスターになり易く、さらにこのクラスターがCNTに結合し易いことが明らかになった。比較のために、4つの元素について、同様の計算をしたが、クラスター化したセシウムが最もCNTと結合し易い事が明らかになった。吸着のし易さを、電荷移動の観点から考察した結果、セシウムはCNTへ移動させ電子を減少させ、さらに6s軌道から空の5d軌道へ電子を移動させ、CNTや他のセシウムと強い結合をたもっていることが分かった。特に、CNTの π 軌道と5d軌道が強い結合をする。
- (4) 拡張した強結合近似分子動力学法により、グラフェンの高精度化した量子伝導計算を実施した。昨年度は、グラフェンの側面の影響を無視できるように電極を両端中央に小さく付け、グラフェンの電気伝導を調べた。本年度は、グラフェンの側面がジグザグ型とアームチェア型のときの影響を調べるために電極をすべてに付け、グラフェンの電気伝導を調べた。微視的に各原子位置での電子の流れを調べると、電子はグラフェンの内部ではなく端を流れやすいことが明らかになった。またジグザグ型とアームチェア型の端のバンド構造の違いによる電気伝導への影響は小さかった。CNTの場合と同様に、グラフェンの π 軌道を介した電極との接合が電気伝導を良好にすることが判った。グラフェンの電気伝導では、電子がグラフェンの端を流れることから、幅の狭いグラフェンでも良好な電気伝導が期待できる。
- (5) CNTをナノ試験管として内部にアセチレン分子ダイマーを入れてレーザーパルス照射した場合とアセチレン分子ダイマーに直接レーザーパルス照射した場合との反応を比較した。直接照射の場合、ダイナミックに分子間干渉が生じた。CNT内部での照射の場合、CNTによる光電場変調により直接照射の場合とは反対方向に水素分子は運動

し、CNTの大きな伸縮運動にともなって2個のアセチレン分子の協調的な回転運動が始まる。この運動は重合などの反応に有利に働くと期待できる。

キーワード: TB理論, 第一原理手法, 時間依存DFT, カーボンナノチューブ, フラーレン, グラフェン, マッカーイ結晶, 太陽電池, グリーンエネルギー, 量子電子伝導, 光電材料

Large-scale Simulation for a Terahertz Resonance Superconductor Device

Project Representative

Mikio Iizuka

Research Organization for Information Science and Technology

Authors

Mikio Iizuka

Research Organization for Information Science and Technology

Masashi Tachiki

Tsukuba University

Hisashi Nakamura

Research Organization for Information Science and Technology

This study is aiming at designing, by large-scale simulations, a new nano-scale devices of high temperature superconductor (HTC) that would emit the terahertz wave continuously, for the purpose of developing a new application fields of terahertz waves that have been abandoned so far as the untapped frequency range between photon and radio waves. HTC naturally forms intrinsic Josephson junction (IJJ). So we call the device IJJ device. A new light source of the continuous and frequency terahertz wave, especially in the range of 1-4 THz, would be applicable to the advanced research fields of material science, bioscience, medical and information technology.

Our challenge is set to develop the device generating the terahertz wave using IJJ device. The mechanism of generating the continuous frequency tunable terahertz waves, its optimum conditions and the frequency control have been revealed so far through the large scale simulation that run on the Earth Simulator with vast computing power.

One of challenges we are tackling is to design a wave guide method that flexibly leads the terahertz waves from inside of the device to the object being irradiated. In the wave guide the terahertz wave propagates dynamically with varying its wavelengths from nanometer to millimeters. Thus, for searching the optimum conditions of the design, it is required to perform large and multi-scale simulation on the nonlinear dynamics of terahertz wave in the three dimensional space of the device and wave guide.

Last year we made an assumption that the terahertz waves emit effectively if the ratio of the outside dielectric constant to the inside effective one of IJJ device increases. The effective dielectric constant of the inside of IJJ device can be controlled by the number of layers of IJJ. Therefore we have studied this year the effect of the ratio on the emission of terahertz waves by controlling the number of layers of IJJ.

Keywords: high-temperature-superconductor, device, generating terahertz waves, stable excitation, Josephson plasma, high performance computational resource, wave guide

1. Introduction

Terahertz wave has been untapped electromagnetic wave, in the frequency range from 0.3 to 10 THz. The range is overlapping the resonance frequencies of molecules and the low-energy collective and elementary excitations such as carrier scattering, recombination, and transporting etc in substances. Thus, terahertz wave has some potential for being applied to the advanced research field of science and technology such as spectroscopic analyses on dense or soft materials and biomolecules, medical diagnoses and information technology. Especially, the tunable, continuous and intense terahertz waves in the range of 1-4 THz are valuable for applications. But, it would be hard to generate the continuous, tunable and intense terahertz wave with 1-4 THz, by conventional methods such as quantum cascade laser and photo mixing.

Our challenges are to develop a new device of generating the

continuous and frequency-tunable terahertz waves in 1-4 THz as a first stage, and to realize a terahertz light source finally. Therefore, until 2009, we had revealed the mechanism and optimum conditions of generating terahertz wave with the new device of IJJ, by using large-scale simulation with huge power of the Earth Simulator [1, 2, 3, 4].

As a next step of our challenges, it was required to develop the wave guide that leads the terahertz waves to the objects being investigated. Thus, themes to be cleared are as follows as shown in Fig. 1: (a) Design of the optimum connection from the inside to outer space of device: configuration, size and material of device, electrode and current, etc. for realizing the efficient emission of Josephson plasma with less loss of power. (b) Design of the wave guide from space around the device to the targets: configuration, dimension and material of wave guide for realizing the efficient propagation of THz waves with less

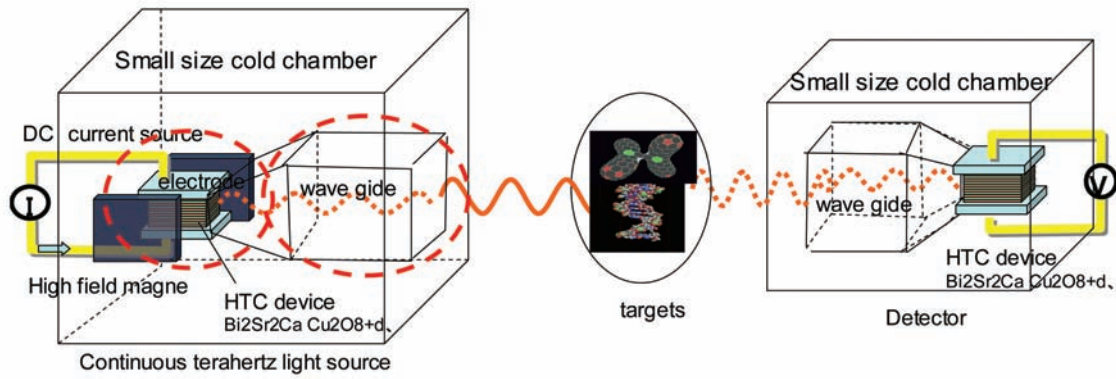


Fig. 1 Schematic diagram of measurement equipment using IJJ device.

reflection, less decay of power.

Until FY 2009, we had conducted the basic studies, focusing on the Josephson plasma excitation inside the device and using quasi two-dimensional model of Josephson plasma dynamics. Hereafter, it was made clear that it is required for us to design the optimum structure of connection or boundary among inside and outside of the IJJ device and wave guide system.

Terahertz wave emits and propagates through three-dimensional configuration of device and guide with hetero materials. Therefore, more accurate modeling efforts are required as follows; (a) to develop accurate multi-dimensional one, (b) to develop a parallel model of coupling inside and outside of the IJJ device for connecting the inside and outside of the IJJ device accurately and (c) to tune those models to high performance computer for overcoming the vast increase of computational loads during multi-dimensional analysis.

Last year we studied the effect of arrangement of electrodes and dielectrics around IJJ device on emission of terahertz waves. And we made an assumption that the terahertz waves emit effectively if the ratio of the outside dielectric constant to the inside effective one of IJJ device increases. The effective dielectric constant of the inside of IJJ device can be controlled by the number of layers of IJJ. In this year, therefore we have studied the effect of the ratio on the emission of terahertz waves by control of the number of layers of IJJ.

2. Multi-dimensional simulation models of IJJ device for generation of terahertz waves

2.1 Multi-dimensional model of IJJ device

In this year, we use the advanced two dimensional model of IJJ device for generation of terahertz waves. Its model is more accurate than the model used to 2009 and has been developed until 2010 to study the optimum conditions of emission of terahertz wave from IJJ device. The reason why more accurate multi-dimensional models are required is as follows.

Josephson plasma excites when it resonates with the array of fluxons and the most intense vibration of electric field that is induced by vibrating superconducting currents appears in parallel to layers (x-axis) and along layers (z-axis) near the surface of the device. These vibrating electric fields on the surface of the device induce the terahertz wave in the outside of the device and then, the terahertz wave propagates to the space. Until FY 2009, we had carried out the basic study on the IJJ device by using a quasi two-dimensional model neglecting the electric field parallel to the layers, because the electric field is induced by superconducting currents along to the layers (z-axis) generating intense terahertz waves. However, it was required that the vibration of superconducting currents should be correctly analyzed on the layers (x-axis) and along layers (z-axis) for simulating the emission of the terahertz waves with a high degree of accuracy.

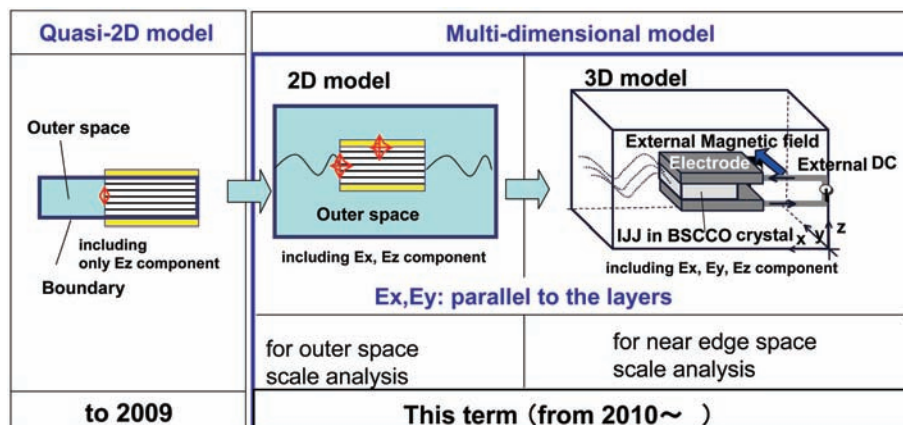


Fig. 2 Flow of development of multi dimensional models.

Thus the accurate two-dimensional model of the generation of terahertz waves was developed until 2010 by considering the electric fields that are parallel to the layers, as shown in Fig. 2.

2.2 Simulation model

Last year our simulation showed that IJJ device could emit effectively terahertz waves if it consists of the large number of layers, is enclosed by electrodes at up and down sides and the outside dielectric constant has high value. Considering the change of theoretical effective dielectrics in IJJ device, we assume that the number of IJJ layers has the most effect on the emission of terahertz waves by following mechanism. The effective dielectric constant ϵ^{eff} in IJJ device is expressed as follows:

$$\epsilon^{\text{eff}} = \left(1 + 2\lambda_{ab}^2 / (Ds)(1 - \cos(\pi q_c / (Nc + 1)))\right) \epsilon_c ,$$

here, ϵ_c is dielectric constant along c-axis, q_c is wave number along c-axis of Josephson plasma and Nc is number of layers of IJJ device. The effective dielectric constant strongly depends on Nc as shown in Fig. 3.

The effective dielectric constant ϵ^{eff} of small number of layers is very large value in inside of IJJ device as shown in Fig. 3, and dielectric constant in air is value of one. Therefore the ratio of the outside dielectric constant to the inside effective one is very small. Increase of number of layers makes effective dielectric constant extremely decrease as shown in Fig. 3. Then

the reflectivity of Josephson plasma at the edge of the device decreases by increasing the ratio of outside dielectric constant to inside effective one. Therefore IJJ device of large number of layers is expected to cause intense emission of terahertz waves.

We change the ration of outside dielectric constant to inside effective one by the control of number of IJJ layers as follows. The ratio $\epsilon/\epsilon^{\text{eff}}$ is shown in table 1.

Based on these cases, we set the model of IJJ device and its simulation model as shown in Fig. 4.

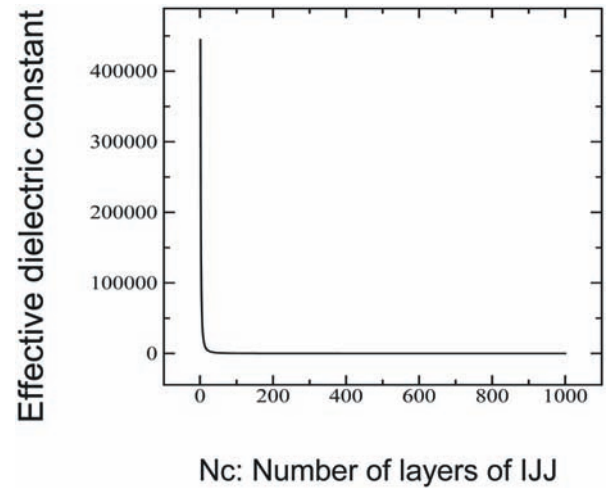


Fig. 3 Dependence of effective dielectric constant on number of layers of IJJ device for the case of $q_c=1$ that induces node-less coherent mode along c-axis.

Table 1 Simulation parameters.

CASE No.	Dielectric Constant of outside	Nc	Effective dielectric constant ϵ^{eff} of inside	Ratio: $\epsilon/\epsilon^{\text{eff}}$
1	$\epsilon=1(\text{air})$	70	2379	1/2379
2		200	245	1/245
3		400	62	1/62
4	$\epsilon=10$	70	2379	1/240
5		200	245	1/24.5
6		400	62	1/6.2

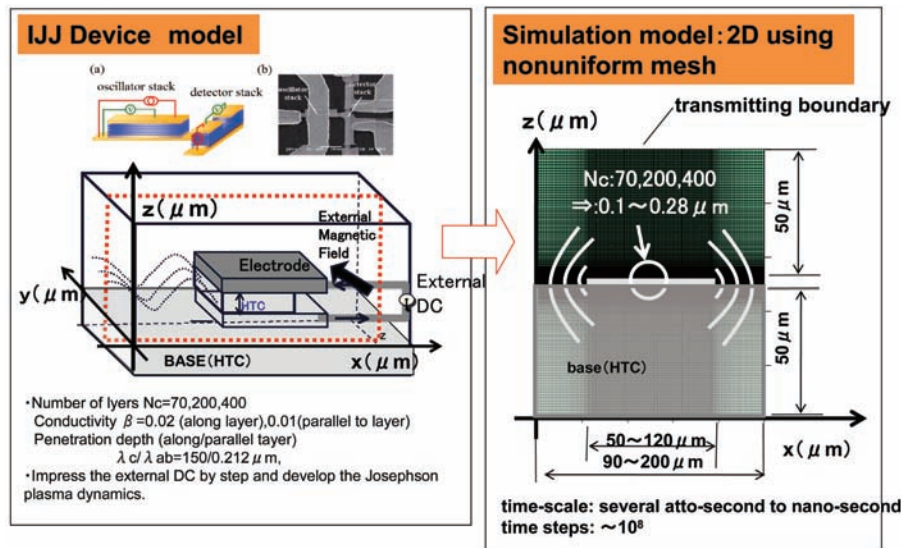


Fig. 4 IJJ device models and its simulation model.

Table 2 Summary of parameters for simulation.

Items	Value
Number of layers N_c	70, 200, 400
Device length	50 ~ 120 μm
Space area of outside	(90 ~ 200 μm) \times 100 μm ,
Magnetic field penetration depth from the bc (λ_c) and ab surface plane (λ_{ab})	$\lambda_c=150\mu\text{m}$, $\lambda_{ab}=0.212\mu\text{m}$,
Reduced quasi-particle conductivity c-axis	along c-axis: $\beta = 0.02$ paralle to layers: $\beta_{ab}= 0.01$
External magnetic field	$B_{y0}= 0.5\text{Testa}$
Reduced external DC	DC: $J'=0.4$. The reduced external DC is impressed as step wise at reduced time $t'=0$, and time development phenomena of Josphon plasma excitation was simulated up to $t'=100 \sim 200$.

Simulations were performed with parameters shown in table 2.

3. Simulation results

Figure 5 shows terahertz waves in inside and outside of IJJ device for number of layers N_c and dielectric constant of outside of IJJ device based on simulation results.

Terahertz waves are stayed locally around the edge of IJJ device for case (1), (2), (3) and (4) . Ratios $\epsilon/\epsilon^{\text{eff}}$ are 1/2379,

1/249, 1/240 and 1/62 for case(1), (2), (3) and (4). On the other, terahertz waves are traveling in the outside space of IJJ device for case (5) and (6). Ratios $\epsilon/\epsilon^{\text{eff}}$ are 1/24.5, 1/6.2 for case (5) and (6). The results show that efficient emission of terahertz waves requires increasing ratio $\epsilon/\epsilon^{\text{eff}}$ to make its ratio close to value of one. The control of number of IJJ layers is effective for increasing ratio $\epsilon/\epsilon^{\text{eff}}$.

Figure 6 shows that the power of terahertz waves were estimated from amplitude of traveling terahertz waves in the

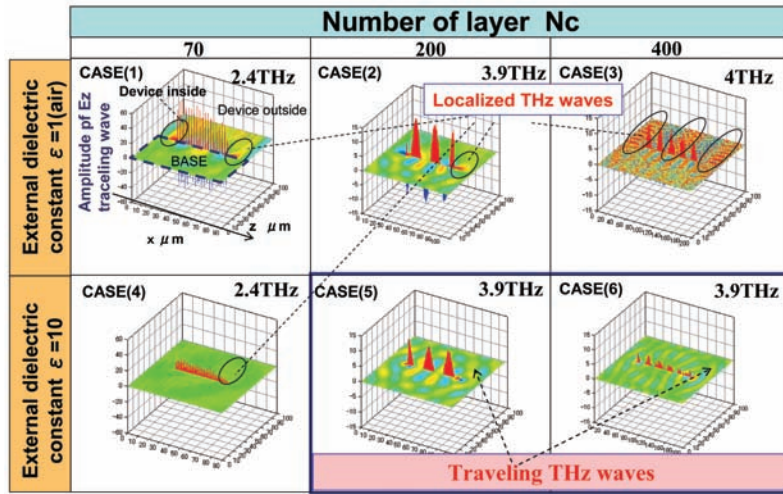


Fig. 5 Terahertz waves in inside and outside of IJJ device for number of layers N_c and dielectric constant of outside of IJJ device.

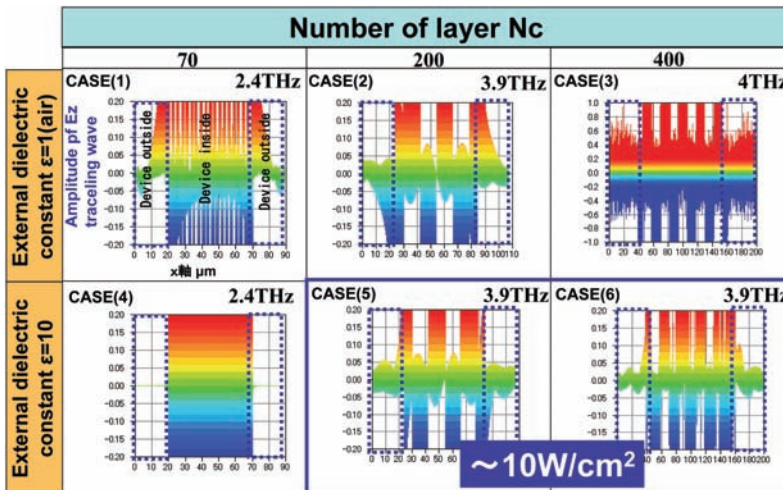


Fig. 6 Power of emitted terahertz waves.

outside space of IJJ device. The power of 10 W/cm^2 is double-digit lower than estimated power in previous study [3]. Next, therefore we would try to study the way that makes power of emission increase.

4. Conclusion and future work

This year, we have studied the effect of ratio $\epsilon/\epsilon^{\text{eff}}$ on emission of terahertz waves by controlling number of IJJ device layers. The results show that the traveling terahertz waves emit effectively from the edge of IJJ device when the value of the ratio $\epsilon/\epsilon^{\text{eff}}$ increases and is closing to one. The control of number of IJJ layers is mostly effective factor for increasing ratio $\epsilon/\epsilon^{\text{eff}}$.

Hereafter we would study how to increase the power of emission by using 2D, 3D simulation model, for investigating more design factors of a terahertz light source.

The Earth Simulator shows clearly that the large-scale simulation with high performances is an effective methodology for developing new technologies.

References

- [1] M. Tachiki, T. Koyama, and S. Takahashi, Electromagnetic phenomena related to a low frequency plasma in cuprate superconductors, *Phys. Rev. B* 10, 7065 (1994).
- [2] M. Tachiki, T. Koyama, and S. Takahashi, in: G. Deutcher, A. Revcolevshi (Eds.), *Coherent High Temperature Superconductors*, World Scientific, Singapore, 371 (1996).
- [3] Masashi Tachiki, Mikio Iizuka, Kazuro Minami, Syogo Tejima, and Hisashi Nakamura, Emission of continuous coherent terahertz waves with tunable frequency by intrinsic Josephson junctions, *Phys. Rev. B* 71, 134515 (2005).
- [4] M. Iizuka, K. Minami, S. Tejima, M. Tachiki, and H. Nakamura: Large-scale simulation on a high-temperature-superconductor device generating the continuous terahertz wave continuously, *Journal of the Earth Simulator*, Vol 8, Nov. (2007).

テラヘルツ発振超伝導素子に関する大規模シミュレーション

プロジェクト責任者

飯塚 幹夫 高度情報科学技術研究機構

著者

飯塚 幹夫 高度情報科学技術研究機構

立木 昌 筑波大学

中村 寿 高度情報科学技術研究機構

本研究は、電波と光の間の未利用周波数帯域であるテラヘルツ波応用の開拓を目指し、連続波としてテラヘルツ波を発振する高温超伝導素子及びその利用システムを大規模シミュレーションにより設計するものである。

テラヘルツ波は光と電磁波の中間域 (0.3 ~ 10THz) の未開拓領域にあり、物質、生体分子の励起振動数 (~ 6THz) を含むことから、物性、癌細胞分子の分光分析、細菌・プラスチック爆発物の検出、X線よりも低エネルギーで透過性があるため安全な医療線源、また大容量通信等へ応用が期待される。特に、1 ~ 4THzでの周波数可変で高出力の連続波光源が無いことから、テラヘルツ波の実用化においては、この帯域の連続波の光源開発が課題となっている。

この課題を解決するため、平成20年度までに、1994年に日本にて提案された高温超伝導体を使うテラヘルツ生成素子の開発を目的に、連続波テラヘルツ波を発振させる原理、その最適発振条件、さらに周波数制御法を地球シミュレータの計算力を生かした大規模シミュレーションから世界で始めて明らかにした。さらに、実用化へ向けた克服すべき課題として、素子内で励起されたジョセフソンプラズマをテラヘルツ波として対象物に自在に照射するための導波技術がある。そこでは、素子及び導波システムにおけるナノからミリスケールまでのテラヘルツ波の非線形挙動を多次元空間で扱う大規模マルチスケールシミュレーションで明らかにし、最適設計条件を求めることが必須となる。そのため、昨年度までに、素子とその外部空間を含む2次元モデルにより、高温超伝導素子の電極配置や周りの誘電体配置のテラヘルツ波生成への影響を調べ、素子上下に電極を配置し、素子外部の誘電率と素子内部の有効誘電率の比を上げることでよりテラヘルツ波を効率的に生成できるという仮説を得た。また、素子内部の有効誘電率は素子の層数により制御可能であることもつきとめた。

そこで今年度は、素子の層数を制御し、素子外部の誘電率と素子内部の有効誘電率の比を上げて1.0に近づけることにより、この仮説を検証した。この成果は、素子端面からの効率的テラヘルツ波放射のための制御変数とその制御法を示し、実験側にとって有効な情報である。しかし、得られたテラヘルツ放射の強度は、 $10\mu\text{W}/\text{cm}^2$ 程度で必要とされる強度に比べ2桁ほど低いため、今後、さらに放射強度を増す方法を地球シミュレータの大規模計算能力を利用し設計して行く。さらに、開発中の3次元コードを完成させ、3次元連続波テラヘルツ波の反射、減衰を考慮した素子・導波管系の大規模シミュレーションを行ない連続波テラヘルツ波応用の基本となるシステム概要、その設計条件を定量的に明らかにする。この3次元の計算規模はより大規模な計算資源を必要とするため、現状ではモデルの規模が制限される。そのためモデル拡張、並列性能向上、演算性能向上へ向けた階層メモリ利用法向上、そのためのアルゴリズムの高度化等を含めた大規模モデルの研究開発も進めていく予定である。本研究は新しいセンサー技術やテラヘルツデバイス技術だけでなく、大容量情報伝送やエネルギー伝送の利用研究としての側面も持つことから米、独、中、韓等でも類する研究が盛んに行われており、厳しい競争状況にある。このため、本研究から得られる設計情報は、わが国の学界・産業界に優先的に提示し、日本独自の新しい産業技術の勃興に資する。

キーワード: 高温超伝導体, デバイス, 連続波テラヘルツ波発振, 安定励起, ジョセフソンプラズマ, 高性能計算資源, 導波管

Direct Numerical Simulations of Fundamental Turbulent Flows with the World's Largest Number of Grid-points and Application to Modeling of Engineering Turbulent Flows

Project Representative

Yukio Kaneda Graduate School of Engineering, Nagoya University

Authors

Yukio Kaneda Graduate School of Engineering, Nagoya University

Takashi Ishihara Graduate School of Engineering, Nagoya University

Kaoru Iwamoto Mechanical Systems Engineering, Tokyo University of Agriculture and Technology

Tetsuro Tamura Interdisciplinary Graduate School of Science and Engineering, Tokyo Institute of Technology

Yasuo Kawaguchi Department of Mechanical Engineering, Tokyo University of Science

Takahiro Tsukahara Department of Mechanical Engineering, Tokyo University of Science

High-resolution direct numerical simulations (DNSs) of canonical turbulence were performed on the Earth Simulator 2. They include (i) high-Reynolds-number turbulent channel flows, (ii) a decaying axisymmetric turbulence, and (iii) turbulent boundary layers on sinusoidal wavy walls. They provide us with invaluable detailed information on the related various turbulence phenomena. The analyses of the DNS data show the following. (1) Intermittent nature of vorticity components is strongly related to the characteristic structures of vorticity near the wall. (2) There is no return to isotropy in a fully developed state of decaying axisymmetric turbulence. (3) The friction coefficient for the TBL with sinusoidal wavy walls differs from that with transverse square bars.

We also performed the following turbulence simulations for environmental and industrial applications. (iv) Application of LES of turbulent flows to urban environmental and strong wind disaster problems, (v) LES of the flow around circular cylinder in realistic high Reynolds number region, and (vi) DNS of turbulent heat transfer of non-Newtonian surfactant solution passing complicated geometry. The results of these simulations show the following. (4) By employing the LES technique for wind flow accompanied with heat around dense tall buildings existing in the urban area we can reproduce the complex flows among many buildings and their wakes with smaller scale. (5) The present LES model succeeded in simulating the aerodynamic characteristics at the critical Reynolds numbers. (6) In a channel flow with rectangular orifices for a viscoelastic fluid, the heat-transfer-reduction rate is lower than the drag-reduction rate, unlike the smooth channel flow.

Keywords: High-resolution DNS, turbulent channel flow, MHD turbulence, turbulent boundary layer, rough wall, LES, urban turbulent boundary layer, critical Reynolds number, non-Newtonian fluid, heat transfer, drag reduction

1. Direct Numerical Simulations of Fundamental Turbulent Flows

1.1 High resolution DNS of turbulent channel flow

To investigate the small-scale statistics in wall-bounded turbulence and to study their Reynolds number dependence, we performed a series of direct numerical simulations (DNS's) of turbulent channel flow (TCF) of an incompressible fluid obeying the Navier-Stokes (NS) equations. The flow is between two parallel flat plates in wall-normal (y) direction, and is assumed to be periodic in the streamwise (x) and span-wise (z) directions.

The computational domain is given by $(2\pi h \times 2h \times \pi h)$, the sizes of which in the x - and z -directions are twice those used in the previous year [1]. Here h denotes the channel half-width. We use the Fourier-spectral method in the x - and z -directions, and the Chebyshev-tau method in the y -direction. The alias errors are removed by the 3/2 rule. Time evolution is accomplished by a third-order Runge-Kutta method for the convection term and the first-order implicit Euler method for the viscous terms. To obtain reliable statistics we advanced each DNS at least until time t larger than $10 t_w$, where t_w is the wash-out time. The

largest-scale DNS (with $2048 \times 1536 \times 2048$ grid points) achieves the sustained performance of 6.1Tflops (11.7% of the peak performance) using 64 nodes of ES2 and generates the DNS data of TCF with the friction Reynolds number $Re_\tau = 2560$. Table 1 shows the parameters used in the series of DNS's.

In TCF, the Kolmogorov length scale $\eta = (\nu / \langle \epsilon \rangle_{xz})^{1/4}$ is a function of the distance (y) from the wall, where ν is the kinematic viscosity, ϵ the rate of energy dissipation and $\langle \cdot \rangle_{xz}$ denotes the average over a plane parallel to the wall. Figure 1 shows that the maximum mesh size in the wall-normal direction in the DNS of the TCF (Case 4) is smaller than the mesh size that was used in the DNS of homogeneous isotropic turbulence by Kaneda et al [2], i.e. $\Delta x / \eta \sim 3$ or 6. This result suggests that we can achieve $Re_\tau = 5120$ by using $2048 \times 1536 \times 2048$ grid points in a smaller computational domain $(\pi h) \times (2h) \times (\pi h/2)$. We have performed such a DNS up to $t = 4.5t_w$ in the fiscal year of 2011.

The preliminary analysis of the series of the DNS data in Table 1 showed that the flatness factor of each component of vorticity depends on the wall-normal distance and strongly relates to the characteristic vortex structures and their distributions near the wall. The DNS data suggest that the flatness factor of a certain component of vorticity at a certain wall-normal distance, which relates to the characteristic vortex structures near the wall, is an increasing function of Re_τ .

1.2 The decay of axisymmetric turbulence

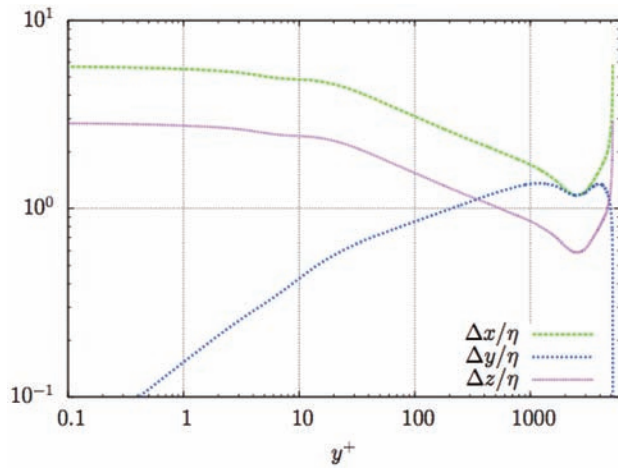


Fig. 1 y -dependence of the mesh size normalized by the Kolmogorov dissipation length scale, used in the DNS of the TCF at $Re_\tau = 2560$ on $2048 \times 1536 \times 2048$ grid points.

Table 1 Parameters used in the DNS's of TCF. Δx^+ and Δz^+ are the mesh size (normalized by u_τ and h) in the streamwise (x) and span-wise (z) directions, and Δy_c^+ is the wall-normal mesh size at the channel center.

	Re_τ	L_x/h	L_z/h	$N_x \times N_y \times N_z$	Δx^+	Δy_c^+	Δz^+
Case 1	320	2π	π	$256 \times 192 \times 256$	7.9	7.9	3.9
Case 2	640	2π	π	$512 \times 384 \times 512$	7.9	7.9	3.9
Case 3	1280	2π	π	$1024 \times 768 \times 1024$	7.9	7.9	3.9
Case 4	2560	2π	π	$2048 \times 1536 \times 2048$	7.9	7.9	3.9

In order to examine the decay of axisymmetric turbulence, we performed direct numerical simulations of freely decaying axisymmetric turbulence at different levels of initial anisotropy with the number of grid points up to 1024^3 on the ES. There are two canonical cases in the decay of freely decaying turbulence. One is $E(k \rightarrow 0) \sim k^2$ and the other is $E(k \rightarrow 0) \sim k^4$, where $E(k)$ is the energy spectrum and k the wavenumber, respectively. We examined the first of these. The DNS's were performed in a periodic domain whose size is sufficiently larger than the integral scales of the turbulence. It is found that there is no return to isotropy in a fully-developed state, irrespective of the level of initial anisotropy, and Saffman's decay laws hold true. Further details are shown in [3].

2. DNS of turbulent boundary layer on rough walls

Turbulent boundary layer on rough plates is one of the most important problems in fundamental turbulent heat transfer research, practical engineering applications and environmental processes. DNS of turbulent boundary layer on rough walls has been barely performed compared with that of other wall-bounded turbulence such as turbulent channel flows.

In this study, direct numerical simulation of turbulent boundary layer with several sinusoidal wavy walls has been performed in order to investigate the effect of the wave length of the sinusoidal wavy wall, λ , upon the turbulent statistics. The amplitude of the sinusoidal wavy wall, a , was kept constant in wall units, and the wave length was set to be $\lambda/a = 5, 7.5, 10, 12.5, 15, 22.5$ and 45 . For the spatially developing boundary layers on sinusoidal wavy walls, we provided a driver section with a flat wall and an analysis section with a sinusoidal wavy wall as shown in Fig. 2. Turbulent inflow conditions for the driver section are generated by rescaling the turbulent boundary layer at some distance downstream of the inflow and by reintroducing the recycled mean profile and fluctuation field. This technique follows those of Kong et al. [4] and Lund et al. [5]. On the other hand, we generate turbulent inflow conditions for the analysis section by exactly copying a turbulent field of the driver section. The parallel and vectorization efficiencies are 98.43% and 99.50%, respectively.

The average of the wall shear stress is at first increased and then decreased with decreasing the wavelength, whilst the pressure drag was gradually increased with decreasing the wavelength (not shown here). In consequence, the trend of the

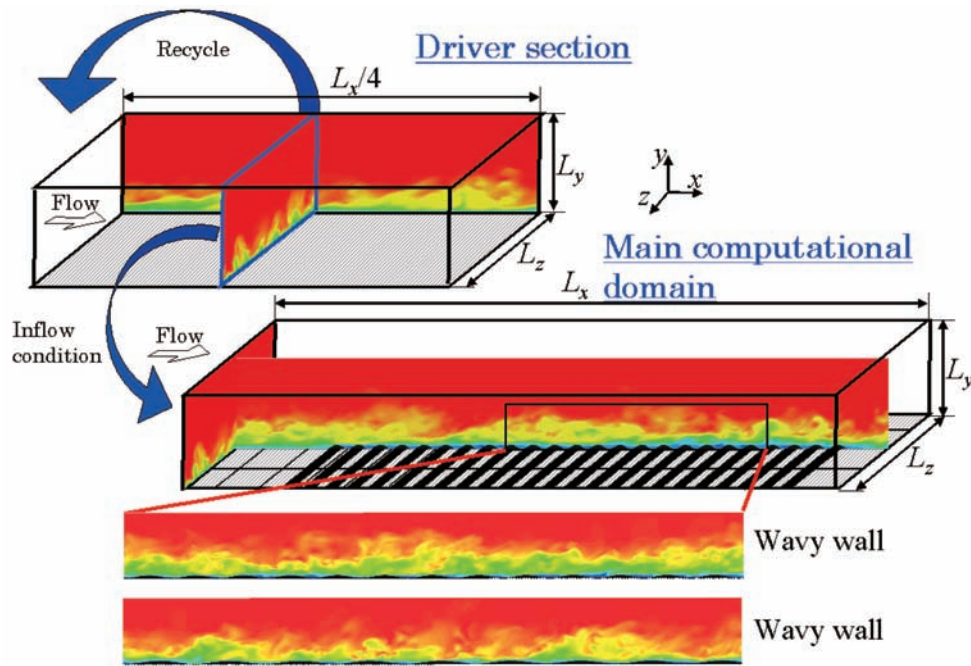


Fig. 2 Computational domains for turbulent boundary layer on several sinusoidal wavy walls.

friction coefficient, which was defined as the summation of the wall shear stress and the pressure drag, is the same as that of the wall shear stress. The friction coefficient is largest at $\lambda/a = 12.5$, which is different from that for the rough wall with transverse square bars [6].

3. Application of LES of turbulent flows to urban environmental and strong wind disaster problems

For the mitigation of heat island effects on coastal cities, it is expected that the sea breeze come into the inland area of a city, where its cold air mingles with the hotter air over and inside the urban canopies. For the numerical simulation of urban heat island, thus far the meteorological model has been

mainly employed, focusing on atmospheric winds in whole range of a city. However, in order to evaluate a local heat environment in such a part of an urban region, it is important to reproduce the complex flows among many buildings and their wakes with smaller scale. Also, for estimating the mitigation of heat island effect by the meteorological local circulation such as a sea breeze, the numerical model that can predict time sequences of unsteady flow quantities is required because the convection brought about by fluctuation behavior of turbulent flows represents directly and strictly an intense and a range of heat transport. Hence, we employ the LES technique for wind flow accompanied with heat around dense tall buildings existing in the urban area. Also, determination of the reference

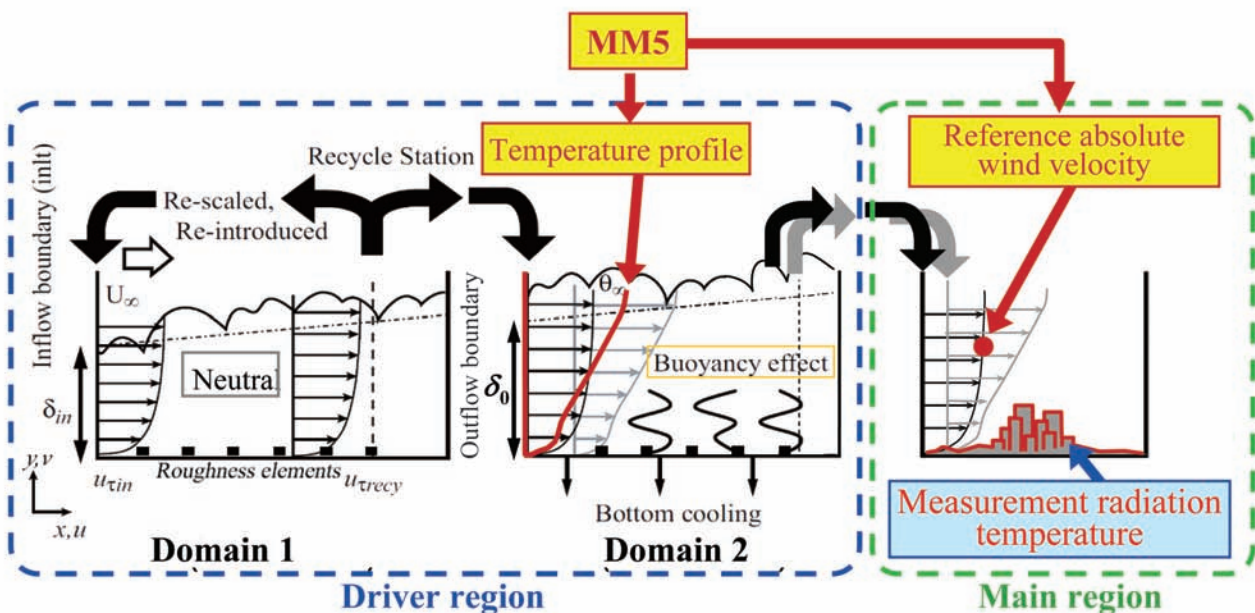


Fig. 3 Hybrid method of Meteorological and LES model.

absolute values for the simulated wind velocity and temperature is supported by the diurnal numerical results obtained by the meso-scale meteorological model (Fig. 3). By comparing with field measurement data, this computational model is validated. Also, we investigate details of a local thermal environment and provide a dominant role of the surface shape and thermal condition of a city from an environmental point of view (Fig. 4).

Recent architectural buildings have a variety of shapes based on unique designer concepts, and the curved surfaces are frequently used for building wall. Here, as a typical and a fundamental case in such buildings, a circular cylinder is focused on. The flow characteristics around a circular cylinder in realistic high Reynolds number region are investigated by use of the LES model. As a result, the present LES model succeeded in simulating the aerodynamic characteristics at the

critical Reynolds numbers. The asymmetric flow characteristics associated with a steady lift are investigated by visualization of the computed data (Figs. 5 and 6).

4. DNS of turbulent heat transfer of non-Newtonian surfactant solution passing complicated geometry

The drag-reducing effect of surfactant additives on turbulent flow has received much attention from both practical and scientific perspectives. This phenomenon can be used for reducing the transportation power in oil-pipeline circuits or district heating and cooling (DHC) recirculation systems: see, for instance, [7]. In general, the surfactant solutions used as working fluids are viscoelastic (non-Newtonian). Their properties measured even in simple shear or extensional flows are known to exhibit appreciably different from those of

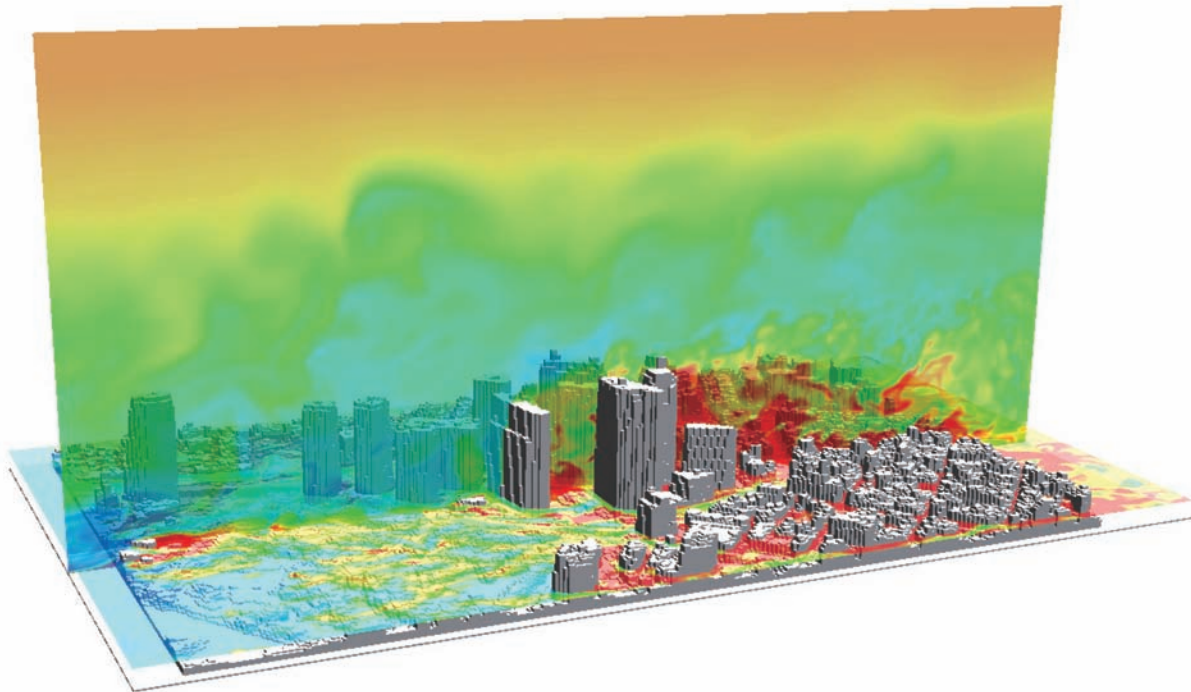


Fig. 4 Instantaneous temperature fields in vertical and horizontal sections of around dense tall buildings.

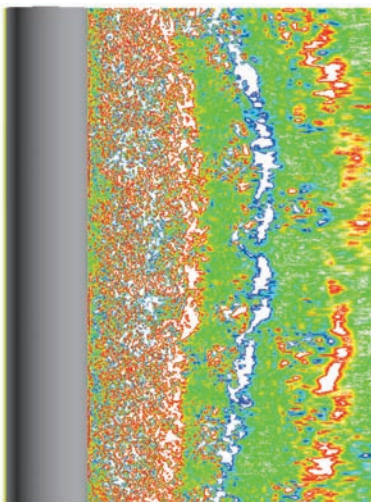


Fig. 5 Wake structures of a circular cylinder ($Re=2 \times 10^5$).

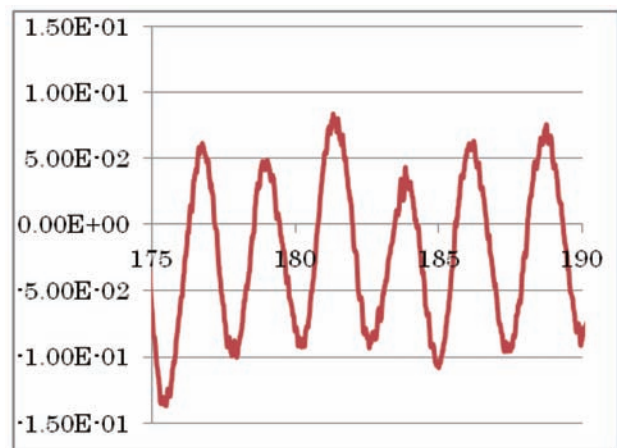


Fig. 6 Time histories of lift coefficients of a circular cylinder ($Re=2 \times 10^5$).

the pure solvent. In addition, as it is known to be a practical problem for heat transport systems, the drag-reducing effect may attenuate the heat transfer significantly due to the suppression of turbulence. In the present study, we addressed this issue and investigated regularly spaced elements (a series of orifices) that induce separation and reattachment and can be applied practically due to their excellent heat transfer performance. Based on Giesekus' viscoelastic-fluid model, DNS of a viscoelastic fluid with passive-scalar heat transfer has been carried out for the same geometry with our previous work [8]. The goal of this work is to better understand the physics and heat-transfer characteristics of the viscoelastic turbulent flow. Major differences between the present study and published works on smooth channels are related to the streamwise variation of the flow state and the main areas where turbulence is produced. Therefore, the instantaneous vortex structures and the relevant momentum and heat transport within the strong shear layer just downstream of the orifice should be explored.

Figure 7 presents a mean-flow field and Reynolds shear-stress distribution with emphasis on the orifice downstream, revealing significant differences between the Newtonian fluid and the viscoelastic fluid. The viscoelastic flow past the orifice expands remarkably due to the normal stress of the fluid elasticity. Thereby the shear layer emanating from the orifice

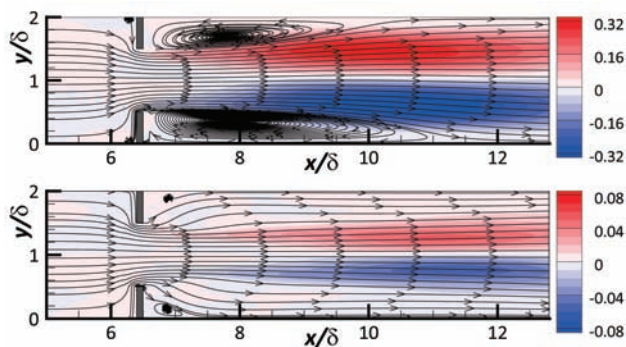


Fig. 7 Averaged streamline and contour of Reynolds shear stress, $\overline{u'v'}$, with emphasis on downstream of the orifice ribs for $Re_{\tau 0} = 30$: (top) Newtonian fluid, (bottom) viscoelastic fluid. The mean flow moves from left to right.

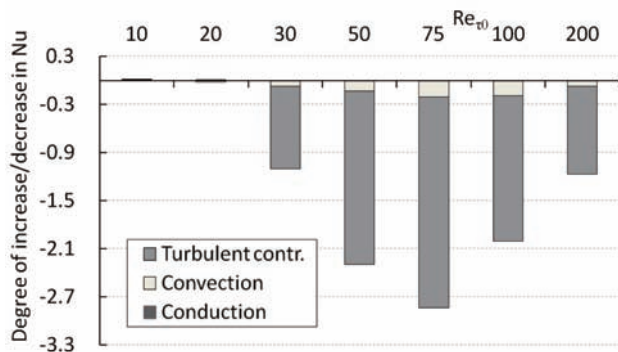


Fig. 8 Decreasing degree in heat transfer for viscoelastic flows: that is, variation of each component contributing to Nusselt number in viscoelastic flows from those of Newtonian flows.

edge and the recirculation zone behind the orifice are found to weaken in the viscoelastic flow, which is almost laminar throughout the channel while the Newtonian flow is turbulent at the same Reynolds number. As a result, the avoiding transition to turbulence gives rise to a heat-transfer reduction as shown in Fig. 8. By increasing the Reynolds number, the reduction of the Nusselt number is pronounced, but becomes less significant gradually for $Re_{\tau 0} > 75$. On the other hand, the magnitude of the drag reduction has a peak at $Re_{\tau 0} = 100$ and still large relative to that of the heat-transfer reduction (figure not shown here). This implies a presence of dissimilarity between drag-reduced flow and thermal field that may be of important practically to develop energy-saving efficient heat exchangers.

References

- [1] K. Morishita, T. Ishihara, and Y. Kaneda, "Small-scale statistics in direct numerical simulation of turbulent channel flow at high-Reynolds number," *Journal of Physics: Conference series*, 318, (2011), 022016.
- [2] Y. Kaneda, T. Ishihara, M. Yokokawa, K. Itakura, and A. Uno, "Energy dissipation rate and energy spectrum in high resolution direct numerical simulations of turbulence in a periodic box," *Physics of Fluids*, 15(2), (2003), L21-L24.
- [3] P. A. Davidson, N. Okamoto, and Y. Kaneda, "On freely-decaying, anisotropic, axisymmetric, Saffman turbulence," *J. Fluid Mech.* (in revision)
- [4] H. Kong, H. Choi, and J.S. Lee, "Direct numerical simulation of turbulent thermal boundary layers," *Phys. Fluids*, 12, (2000), 2555-2568.
- [5] T. S. Lund, X. Wu, and K. D. Squires, "Generation of turbulent inflow data for spatially-developing boundary layer simulations," *J. Comput. Phys.*, 140 (2), (1998), 233–258.
- [6] S. Leonardi, P. Orlandi, R. J. Smalley, L. Djenidi, and R. A. Antonia, "Direct numerical simulations of turbulent channel flow with transverse square bars on one wall," *J. Fluid Mech.*, 491, (2003), 229-238.
- [7] H. Takeuchi, "Demonstration test of energy conservation of central air conditioning system at the Sapporo city office building—Reduction of pump power by flow drag reduction using surfactant," *Synthesiology—English edition*, 4, (2012), 136-143.
- [8] T. Tsukahara, T. Kawase, and Y. Kawaguchi, "DNS of viscoelastic turbulent channel flow with rectangular orifice at low Reynolds number," *International Journal of Heat and Fluid Flow*, 32, (2011), 529-538.

乱流の世界最大規模直接数値計算とモデリングによる応用計算

プロジェクト責任者

金田 行雄 名古屋大学 大学院工学研究科

著者

金田 行雄 名古屋大学 大学院工学研究科

石原 卓 名古屋大学 大学院工学研究科

岩本 薫 東京農工大学 工学府

田村 哲郎 東京工業大学 大学院総合理工学研究科

川口 靖夫 東京理科大学 理工学部

塚原 隆裕 東京理科大学 理工学部

地球シミュレータ (ES2) を用いて、(i) 高レイノルズ数 (壁摩擦速度に基づくレイノルズ数 2560) の平行平板間乱流、(ii) 軸対称の減衰乱流、(iii) 正弦波状壁面上の乱流境界層を含む、カノニカルな問題の大規模直接数値シミュレーション (DNS) を実施した。これらの DNS は、関連する様々な乱流現象に対して詳細で有益な情報を与えるものである。これらの DNS で得られたデータを解析することにより (1) 高レイノルズ数壁乱流の渦度成分の間欠性を示す尖り度などの統計量は壁近傍の特徴的な渦構造と強く関係していること、(2) 軸対称減衰乱流の十分発達した状態において乱流場が等方的にならないこと、(3) 正弦波状の壁における壁乱流の摩擦係数は矩形の粗面のある壁における摩擦係数と異なることなどを見出した。また、我々は環境や工学的な応用問題に対する乱流数値計算として、(iv) 実際の都市を対象とした、環境・防災問題の低減化をめざした高解像度大規模乱流のラージ・エディ・シミュレーション (LES)、(v) 近年の多彩な高層ビルを考慮した、円柱周り的高レイノルズ数流れの LES、(vi) 複雑境界を過ぎる非ニュートン流体における乱流熱輸送の DNS を実施した。その結果、(4) 都市部での高層ビル周辺で発生する熱を伴う風の流れに対して、LES の技術を用いて建物間の小規模で複雑な流れを再現できること、(5) LES にて臨界レイノルズ数あたりの円柱周りの流れの空力特性がとらえられること、および、(6) リブ列を有する平行平板間の粘弾性流体乱流においては、滑らかな平行平板間の流れと異なり、熱伝達低減量は抵抗低減効果に比べて小さく、レイノルズ数が増加するにつれてさらに減少していくことが判明した。

キーワード: 大規模直接数値計算, 平行二平板間乱流, 減衰軸対称乱流, 乱流境界層, 粗面, LES, 都市型乱流境界層, 臨界レイノルズ数, 界面活性剤, 熱輸送, 抵抗低減

A Large-Scale Genomics and Proteomics Analyses Conducted by the Earth Simulator

Project Representative

Toshimichi Ikemura Nagahama Institute of Bio-Science and Technology

Authors

Takashi Abe Graduate school of Science and Technology, Niigata University
Nagahama Institute of Bio-Science and Technology

Kenosuke Wada Nagahama Institute of Bio-Science and Technology

Toshimichi Ikemura Nagahama Institute of Bio-Science and Technology

Self-Organizing Map (SOM) developed by Kohonen is an effective tool for clustering and visualizing high-dimensional complex data on a two-dimensional map. We previously modified the conventional Self-Organizing Map (SOM) to genome and protein informatics, making the learning process and resulting map independent of the order of data input. BLSOM thus developed on the basis of batch-learning SOM became suitable for actualizing high-performance parallel-computing, and revealed species-specific characteristics of oligonucleotides (e.g., tetranucleotides) frequencies in individual genomes, permitting clustering (self-organization) of genomic fragments (e.g., 5 kb or less) according to species without species information during the calculation. Using ES, we established the alignment-free clustering method BLSOM that could analyze far more than 10,000,000 sequences simultaneously. Sequence fragments from almost all prokaryotic, eukaryotic, and viral genomes currently available could be classified (self-organized) according to phylotypes on a single two-dimensional map. Here, we have further developed a strategy for predicting phylotypes of a massive amount of genomic fragments obtained by metagenome analyses, by mapping of each metagenomic sequence on a large-scale BLSOM that was constructed for almost all genomic sequences currently available from the International Nucleotide Sequence Databases.

Keywords: batch learning SOM, oligonucleotide frequency, phylogenetic classification, metagenomics

1. Introduction

Although remarkable progress in metagenomic sequencing of various environmental samples including the most extensively studied samples from oceans has been made, huge numbers of fragment sequences are registered without information on gene function and phylotype in International Nucleotide Sequence Databases, and thus with limited usefulness. The metagenomic sequencing is undoubtedly a powerful strategy for comprehensive study of a microbial community in an ecosystem, but for most of the sequences, it is difficult to predict from what phylotypes each sequence is derived. This situation has arisen because orthologous sequence sets, which cover a broad phylogenetic range required for constructing reliable phylogenetic trees through sequence homology searches, are unavailable for novel gene sequences. G plus C percentage (%GC) has long been used as a fundamental parameter for phylogenetic classification of microorganisms, but the %GC is apparently too simple a parameter to differentiate a wide variety of species. Oligonucleotide composition, however, can be used even to distinguish species with the same %GC, because oligonucleotide composition varies significantly among

microbial genomes and has been called the “genome signature”.

Phylogenetic clustering and classification in the present study is designed as an extension of the single parameter “%GC” to the multiple parameters “oligonucleotide frequencies”. For this purpose, we previously modified the SOM developed by Kohonen’s group [1-3] for genome informatics on the basis of batch-learning SOM (BLSOM), which makes the learning process and resulting map independent of the order of data input [4-6]. The BLSOM thus developed could recognize phylotype-specific characteristics of oligonucleotide frequencies in a wide range of genomes and permitted clustering (self-organization) of genomic fragments according to phylotypes with neither the orthologous sequence set nor the troublesome and mistakable processes of sequence alignment. Furthermore, the BLSOM was suitable for actualizing high-performance parallel-computing with the high-performance supercomputer “the Earth Simulator”, and permitted clustering (self-organization) of almost all genomic sequences available in the International Nucleotide Sequence Databases on a single map [7-9]. By focusing on the frequencies of oligonucleotides (e.g., tetranucleotides), the BLSOM has allowed highly accurate classification (self-

organization) of most genomic sequence fragments on a species basis without providing species-related information during BLSOM computation. The present unsupervised and alignment-free clustering method is thought to be the most suitable one for phylogenetic estimation for a massive amount of genomic fragments obtained by metagenome analyses. This was done by mapping of each metagenomic sequence on the large-scale BLSOM constructed with ES, which could classify almost all known prokaryotic, eukaryotic, and viral sequences according to phylotypes [10-12]. We have already employed the BLSOM method for studies of environmental genomic fragments in joint research with experimental research groups analyzing various environmental and clinical samples [10, 11].

2. Methods

Genomic fragment sequences derived from metagenome analyses were obtained from <http://www.ncbi.nlm.nih.gov/GenBank/>. Metagenome sequences shorter than 1 kb in length were not included in the present study. When the number of undetermined nucleotides (Ns) in a sequence exceeded 10% of the window size, the sequence was omitted from the BLSOM analysis. When the number of Ns was less than 10%, the oligonucleotide frequencies were normalized to the length without Ns and included in the BLSOM analysis. Sequences that were longer than a window size (1 kb) were segmented into the window size, and the residual sequences, which were shorter than the window size, were omitted from the BLSOM analysis.

Using a high-performance supercomputer "the Earth Simulator", we could analyze almost all 5-kb genomic sequences derived from 5600 prokaryotes, 411 eukaryotes, 31486 viruses, 4479 mitochondria, and 225 chloroplasts, which were obtained from the recent version released from the International Nucleotide Sequence Databanks. The 5600 prokaryotes were selected because at least 10-kb genomic sequences were registered in the Databases. One important target of the phylogenetic classification of metagenome sequences is the sequences derived from species-unknown novel microorganisms. To keep good resolution for microorganism sequences on the BLSOM, it is necessary to avoid excess representation of sequences derived from higher eukaryotes with large genomes. Therefore, in the cases of higher eukaryotes, 5-kb sequences were selected randomly from each large genome up to 200 Mb in Fig. 1A. In this way, the total quantities of prokaryotic and eukaryotic sequences were made almost equal. The separation between eukaryotes and prokaryotes was achieved with a high accuracy of 95%; the separation between organelles and viruses and between nuclear and viral genomes was also achieved with an accuracy of approximately 80%. Clear separation of the species-known prokaryote sequences into 38 major families was also observed (refer to Fig. 2A). The separation of eukaryotic sequences according to families was also observed on this 5-kb BLSOM (data not shown). During

BLSOM computation, no information was given to the computer regarding which species each sequence fragment belonged to (unsupervised learning algorithm).

BLSOM learning was conducted as described previously [4-6], and the BLSOM program was obtained from UNTROD Inc. (y_wada@nagahama-i-bio.ac.jp).

3. Results

3.1 A large-scale BLSOM constructed with all sequences available from species-known genomes

In the present study, we examined the BLSOM ability for phylogenetic separation of prokaryotic sequences and applied the BLSOM to the phylogenetic prediction of sequences obtained by metagenome analyses. Large-scale metagenomic studies of uncultivable microorganisms in environmental and clinical samples have recently been conducted to survey genes useful in industrial and medical applications and to assist in developing accurate views of the ecology of uncultivable microorganisms in each environment. Conventional methods of phylogenetic classification of gene/genomic sequences have been based on sequence homology searches and therefore, the phylogenetic studies focused inevitably on well-characterized gene sequences, for which orthologous sequences from a wide range of phylotypes are available for constructing a reliable phylogenetic tree. The well-characterized genes, however, often are not industrially attractive. It would be best if microbial diversity and ecology could be assessed during the process of screening for novel genes with industrial and scientific significance. The present unsupervised and alignment-free clustering method, BLSOM, is thought to be the most suitable one for this purpose because there was no need of orthologous sequence sets [4-6].

Metagenomic analyses can be applied to not only environmental but also medical samples such as clinical samples, and therefore, are applicable to exploring unknown pathogenic microorganisms that cause novel infectious diseases. It should be noted that the mixed genome samples in the medical and pharmaceutical fields may contain DNA from a wide range of eukaryotes, as well as from humans. Therefore, when we consider phylogenetic classification of genomic sequences derived from species-unknown environmental microorganisms obtained by metagenome studies, it is necessary to construct BLSOM in advance with all available sequences from species-known prokaryotes, eukaryotes, viruses and organelles compiled in the International DNA Databanks. According to our previous studies of metagenome sequences [7], BLSOM was constructed with oligonucleotide frequencies in 5-kb sequence fragments. In DNA databases, only one strand of a pair of complementary sequences is registered. Our previous analyses revealed that sequence fragments from a single prokaryotic genome are often split into two territories that reflect the transcriptional polarities of the genes present in the fragment [7]. For phylotype

classification of sequences from uncultured microbes, it is not required to know the transcriptional polarity of the sequence, and the split into two territories complicates assignment to species. Therefore, we previously introduced a BLSOM in which frequencies of a pair of complementary oligonucleotides (e.g., AACC and GGTT) were summed, and the BLSOM for the degenerate sets of tetranucleotides were designated as DegeTetra-BLSOM.

3.2 Phylogenetic estimation for environmental DNA sequences and microbial community comparison

More than 17 million genomic sequence fragments obtained from various environments through metagenomic analyses have been registered in the International Nucleotide Sequence Databases. A major portion of them is novel but at present moment have a limited utility because of lacks of phylogenetic and functional annotations. The phylogeny estimation of genomic sequence fragments of novel microorganisms requires the feature extraction of oligonucleotide composition of

all species-known microorganism genomes, in advance on BLSOM. Therefore, a large-scale BLSOM (Fig. 1A) covering all known sequences, including those of viruses, mitochondria, chloroplasts, and plasmids, was constructed as described in **Methods**. Next on this BLSOM, numerous sequence fragments derived from an environmental sample were mapped; i.e., the similarity of the oligonucleotide frequency in fragmental sequences from environmental samples with that of sequences from species-known genomes was examined. In Fig. 1B, 210 thousand sequences with a fragment size of 1 kb or more, which were collected from the Sargasso Sea near Bermuda [12], were mapped (Fig. 1B). This analysis of all sequence fragments obtained from one environmental sample can estimate numbers and proportions of species present in the sample. Approximately 70% of sequences from the Sargasso Sea were mapped to the prokaryotic territories, and the rest was mapped to the eukaryotic, viral or organelle territories.

To further identify more detailed phylogenies of the environmental sequences thus mapped to the prokaryotic

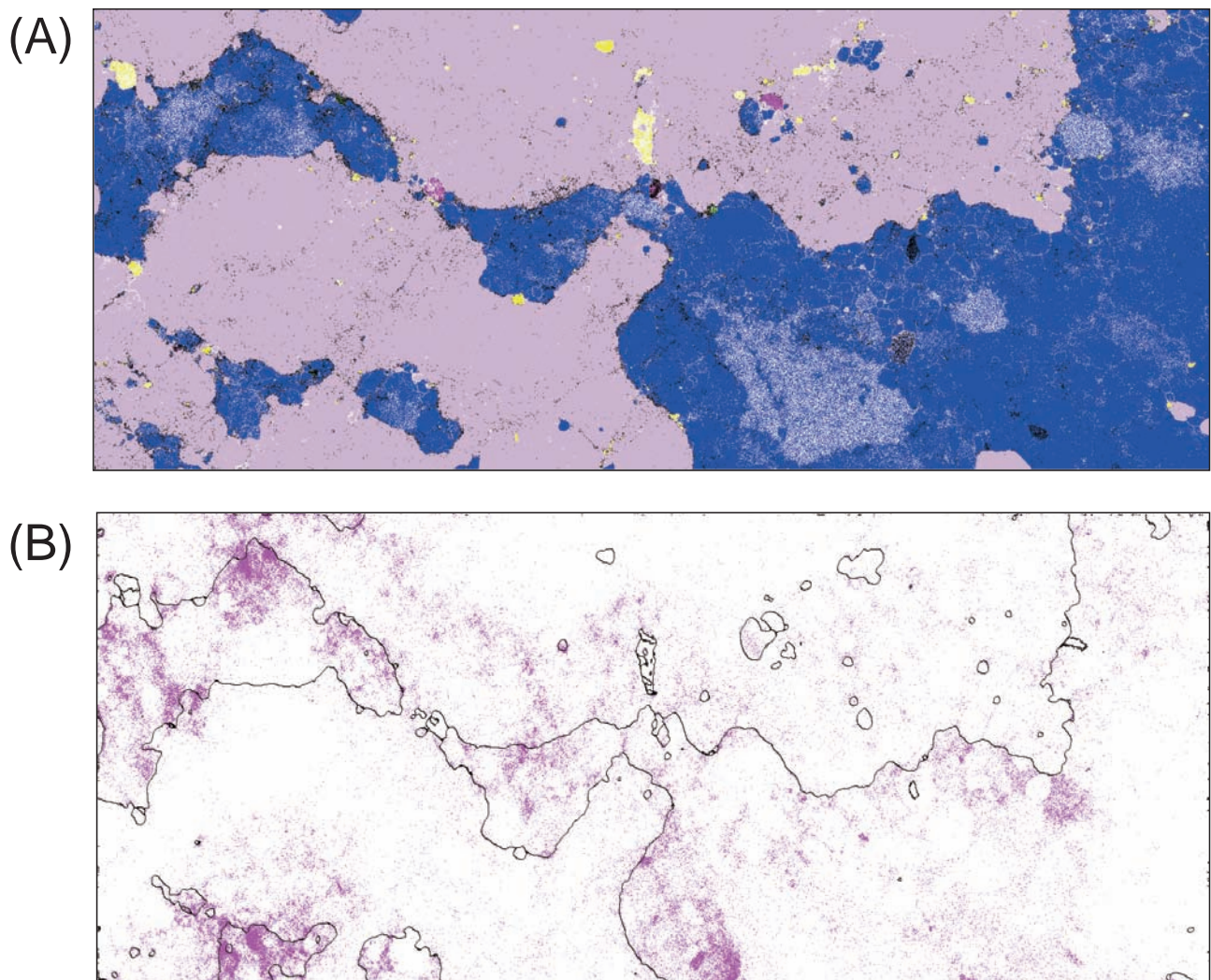


Fig. 1 BLSOM for phylogenetic classification of environmental sequence. (A) DegeTetra-BLSOM of 5-kb sequences derived from species-known 5,600 prokaryotes, 411 eukaryotes, 1,728 mitochondria, 225 chloroplasts, and 31,486 viruses. (B) Sargasso sequences longer than 1 kb were mapped on the 5-kb DegeTetra-BLSOM, after normalization of the sequence length.

territories, a BLSOM analyzing 5-kb genomic sequence fragments only from 5,600 known prokaryotes was constructed for degenerate tetranucleotide composition (Fig. 2A). On this species-known prokaryote BLSOM, the separation into 38 phylogenetic groups was examined, revealing that 85% of the sequences were properly clustered according to the phylogenetic group resulting in formation of the phylogenetic group-specific territory. The reason why 100 % separation was not achieved was mainly because of horizontal gene transfer between the genomes of different microbial species [6, 7]. The 140 thousand metagenomic sequences from the Sargasso Sea that were mapped previously to the prokaryotic territories (Fig. 1B) were remapped on the BLSOM that was constructed for sequences derived only from species known-prokaryotes, in order to get the detailed prokaryotic phylotype assignment. The mapped sequences broadly spread across the BLSOM, demonstrating that the sequences belonged to a wide range of phylotypes (Fig. 2B). Interestingly, there were areas where metagenomic sequences were densely mapped, which may

indicate dominant species/genera. In sum, the estimation of prokaryotic phylogenetic groups could provide phylogenetic information for almost half of sequence fragments from the Sargasso Sea. The present procedure can be used to estimate the phylogenetic structures of microbial communities living in a subject environment and thus to understand the diversity of microbial floras.

Through successive mapping of the subject sequences on a BLSOM created with the sequences from species-known genomes of a much restricted phylogenetic group, further detailed phylogenetic estimation, such as at the genus or species level, becomes possible. In other words, this stepwise tracking allowed us to estimate detailed structures of microbial communities present in an environmental sample, to determine the novelty of obtained environmental sequences at various phylogenetic levels and to find the novel sequences efficiently.

Recent metagenomic analyses showed an abundance of viruses in seawater [13]. Since virus genomes contain no rDNA, conventional methods of phylogenetic estimation based on

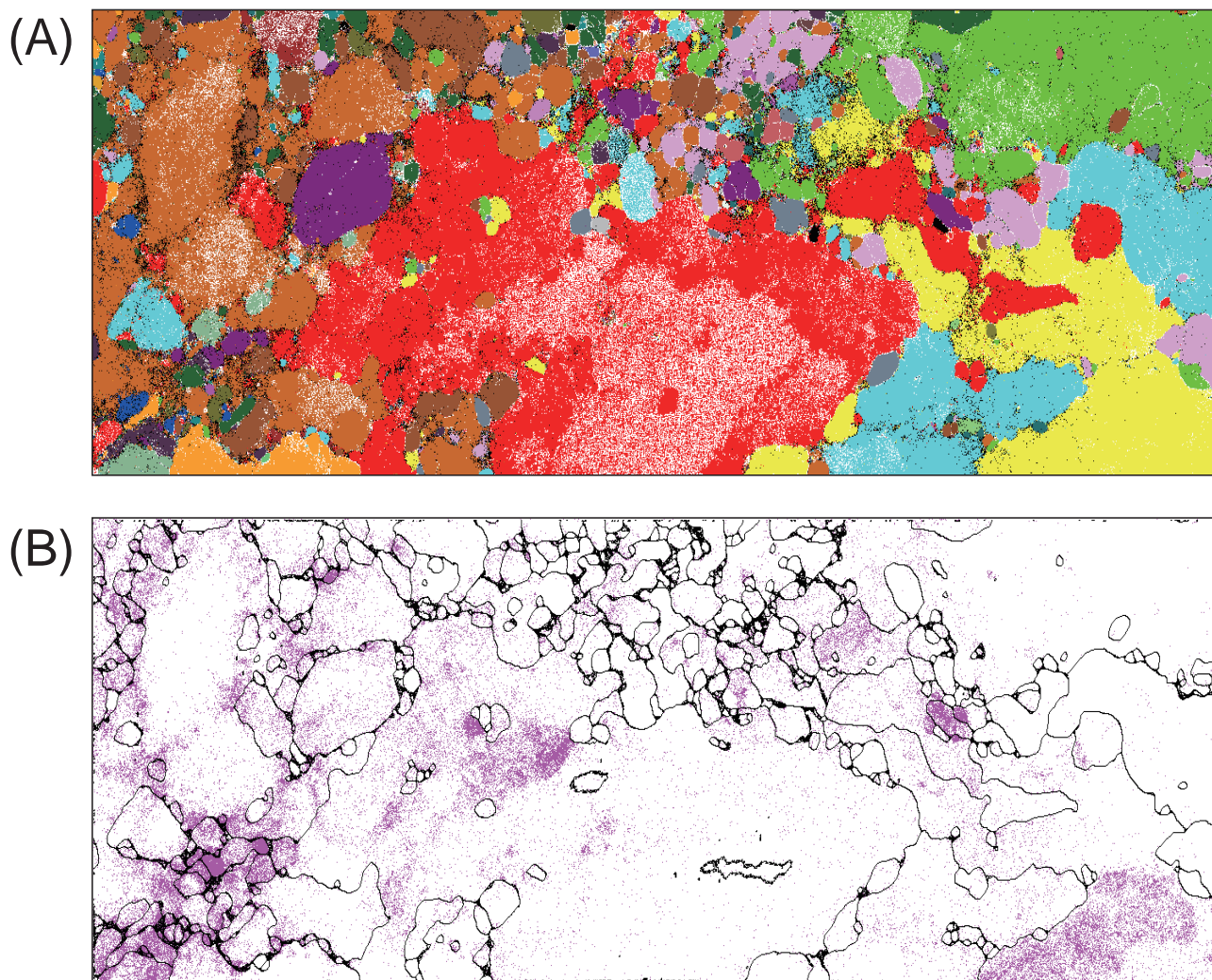


Fig. 2 Phylogenetic classification of sequences from an environmental sample. (A) DegeTetra-BLSOM of 5-kb sequences derived from species-known 5,600 prokaryotes. (B) Sargasso sequences that were classified into prokaryotic territories in Fig. 1B were mapped on the 5-kb DegeTetra-BLSOM constructed with the sequences only from the species-known 5,600 prokaryotes.

rRNA sequences cannot be used. BLSOM analysis for fully sequenced virus genomes showed a separation according to their phylogenies, allowing us to conduct phylogenetic estimation in the viral kingdom without relying on orthologous sequence sets or sequence alignments. The publication of a large-scale BLSOM, which separated all available genomic sequences including viral and organelle sequences, will provide fundamental data required in large-scale metagenomic studies. The BLSOM is applicable to a broad range of life sciences, such as medical and pharmaceutical sciences, and related industrial fields.

The mapping of novel sequences on the large-scale BLSOM that was constructed with ES can be performed using a PC-level computer; our group has made a PC software program for the BLSOM mapping. This software can be freely available at <http://bioinfo.ie.niigata-u.ac.jp>.

4. Conclusion and Perspective

Large-scale metagenomic analyses using recently released next-generation sequencers are actively underway on a global basis, and the obtained numerous environmental sequences have been registered in the public databases. Large-scale computations using various, novel bioinformatics tools are undoubtedly needed for knowledge-findings from the massive amount of sequence data. The present BLSOM is an unsupervised algorithm that can separate most sequence fragments based only on the similarity of oligonucleotide frequencies. Unlike the conventional phylogenetic estimation methods, the BLSOM requires no orthologous sequence set or sequence alignment, and therefore, is suitable for phylogenetic estimation for novel gene sequences. It can also be used to visualize an environmental microbial community on a plane and to accurately compare it between different environments.

Because BLSOM could reassociate genomic fragments according to genomes, we have recently developed a widely applicable method, which could separate metagenomic sequences according to phylotypes and hopefully to species, without coexistence of sequences from species-known prokaryotes or metagenomic sequences from other environmental samples [14]. In that study, random sequences with nearly the same mono-, di- or trinucleotide composition to each metagenomic sequence in one environmental sample of interest were generated. Then, we constructed DegeTetra-BLSOM for the metagenomic sequences plus the computer-generated random sequences. Under the presence of the random sequences, metagenomic sequences formed many well-separated territories surrounded with the random sequences. In that study, a major portion of PCB degradation enzyme genes was found within one clear territory, indicating that this territory contained the genome harboring the metabolic pathway genes for PCB degradation. This is another application of BLSOM for metagenome analyses. In the cases of conventional methods,

which were based on sequence homology searches, information concerning a gene set of one species responsible for a certain biological activity can be obtained only when a very large amount of sequences is available for constructing a nearly complete genome by sequence assembling or when a complete genome sequence is available as a reliable template for mapping of metagenomic sequences. In contrast, the BLSOM method can be achieved without a template genome for mapping and thus is applicable to the really novel, environmental genomes.

BLSOM can also be used to predict functions of proteins, for which the sequence similarity search at an amino-acid level cannot predict functions. This is because proteins with the same or similar functions can be clustered (self-organized) primarily according to functions on BLSOM for oligopeptide composition [15].

Acknowledgements

This work was supported by Grant-in-Aid for Scientific Research (C, 23500371) and for Young Scientists (B, 23710242) from the Ministry of Education, Culture, Sports, Science and Technology of Japan. The present computation was done with the Earth Simulator of Japan Agency for Marine-Earth Science and Technology.

References

- [1] T. Kohonen, "The self-organizing map", Proceedings of the IEEE, vol. 78, pp. 1464-1480, 1990.
- [2] T. Kohonen, E. Oja, O. Simula, A. Visa, and J. Kangas, "Engineering applications of the self-organizing map", Proceedings of the IEEE, vol. 84, pp. 1358-1384, 1996.
- [3] T. Kohonen, *Self-Organizing Maps*. Berlin, Springer, 1997.
- [4] S. Kanaya, M. Kinouchi, T. Abe, Y. Kudo, Y. Yamada, T. Nishi, H. Mori, and T. Ikemura, "Analysis of codon usage diversity of bacterial genes with a self-organizing map (SOM): characterization of horizontally transferred genes with emphasis on the E. coli O157 genome", *Gene*, vol. 276, pp. 89-99, 2001.
- [5] T. Abe, S. Kanaya, M. Kinouchi, Y. Ichiba, T. Kozuki, and T. Ikemura, "A novel bioinformatic strategy for unveiling hidden genome signatures of eukaryotes: self-organizing map of oligonucleotide frequency", *Genome Inform.*, vol. 13, pp. 12-20, 2002.
- [6] T. Abe, S. Kanaya, M. Kinouchi, Y. Ichiba, T. Kozuki, and T. Ikemura, "Informatics for unveiling hidden genome signatures", *Genome Res.*, vol. 13, pp. 693-702, 2003.
- [7] T. Abe, H. Sugawara, M. Kinouchi, S. Kanaya, and T. Ikemura, "Novel phylogenetic studies of genomic sequence fragments derived from uncultured microbe mixtures in environmental and clinical samples", *DNA Res.*, vol. 12, pp. 281-290, 2005.
- [8] T. Abe, H. Sugawara, S. Kanaya, M. Kinouchi, and T.

- Ikemura, "Self-Organizing Map (SOM) unveils and visualizes hidden sequence characteristics of a wide range of eukaryote genomes", *Gene*, vol. 365, pp. 27-34, 2006.
- [9] T. Abe, H. Sugawara, S. Kanaya, and T. Ikemura, "Sequences from almost all prokaryotic, eukaryotic, and viral genomes available could be classified according to genomes on a large-scale Self-Organizing Map constructed with the Earth Simulator", *Journal of the Earth Simulator*, vol. 6, pp. 17-23, 2006.
- [10] T. Uchiyama, T. Abe, T. Ikemura, and K. Watanabe, "Substrate-induced gene-expression screening of environmental metagenome libraries for isolation of catabolic genes", *Nature Biotech.*, vol. 23, pp. 88-93, 2005.
- [11] H. Hayashi, T. Abe, M. Sakamoto, H. Ohara, T. Ikemura, K. Sakka, and Y. Benno, "Direct cloning of genes encoding novel xylanases from human gut", *Can. J. Microbiol.*, vol. 51, pp. 251-259, 2005.
- [12] J. C. Venter et al., "Environmental genome shotgun sequencing of the Sargasso Sea", *Science*, vol. 304, pp. 66-74, 2004.
- [13] R. A. Edward and F. Rohwer, "Viral metagenomics". *Nat Rev Microbiol*, vol. 3, pp. 504-10, 2005.
- [14] H. Uehara, Y. Iwasaki, C. Wada, T. Ikemura, and T. Abe, "A novel bioinformatics strategy for searching industrially useful genome resources from metagenomic sequence libraries", *Genes Genet. Sys.*, vol. 86, pp. 53-66, 2011.
- [15] Takashi Abe, Shigehiko Kanaya, Hiroshi Uehara, and Toshimichi Ikemura, "A novel bioinformatics strategy for function prediction of poorly-characterized protein genes obtained from metagenome analyses", *DNA Research*, vol. 16, pp. 287-298, 2009.

全ゲノム・全タンパク質配列の自己組織化マップを用いた 大規模ポストゲノム解析

プロジェクト責任者

池村 淑道 長浜バイオ大学 バイオサイエンス学部

著者

阿部 貴志 新潟大学 大学院自然科学研究科

長浜バイオ大学 バイオサイエンス学部

和田健之介 長浜バイオ大学 バイオサイエンス学部

池村 淑道 長浜バイオ大学 バイオサイエンス学部

海洋を代表例とする、多様な地球環境で生育する微生物類は培養が困難なため膨大なゲノム資源が未開拓・未利用に残されてきた。環境中の生物群集から培養せずにゲノム混合物を回収し、断片ゲノム配列を解読し有用遺伝子を探索する「メタゲノム解析法」が開発され、注目を集めている。我々が開発した一括学習型自己組織化マップ法（BLSOM）は、断片ゲノム配列を生物種ごとに高精度に分離（自己組織化）する能力を持つ知見を元に、メタゲノム配列に対する系統推定法の開発を行ってきた。

メタゲノム解析により取得され断片ゲノム配列には、原核生物のみならず、真核生物やウイルス由来の断片ゲノム配列も豊富に含まれている。これら断片ゲノム配列からの真核生物やウイルスを探索するために、断片化サイズ 5kb での 4 連続塩基頻度にて、既知真核生物 412 種（ゲノム配列断片数：618 万件）、既知ウイルス 30,000 種（12 万件）、原核生物 1294 属（488 万件）、ミトコンドリア 4479 種（2 万件）、葉緑体 225 種（6 千件）のゲノム配列断片 1120 万件（56 ギガ塩基）の全生物種を対象にした大規模 BLSOM 解析を行なった。また、上記解析で使用した真核生物、原核生物、ウイルスについて、各生物カテゴリに推定された配列群に対し、より詳細な系統推定を行うことを目的に、断片サイズ 5kb での 4 連続頻度での BLSOM 解析を行なった。

タンパク質の機能推定にも BLSOM が有用な事を見出している。

既に 8 大学 11 グループ、6 公的研究機関 7 グループ、4 民間企業との共同研究を行っており、我が国で行われている大規模メタゲノム解析の大半で活用されている。世界の研究グループにとって必須の技術とするべく、本研究結果より得られた大規模 BLSOM 解析結果を用いたメタゲノム配列に対する系統推定を行うためのソフトウェアの公開を行っている (<http://bioinfo.ie.niigata-u.ac.jp/>)。

キーワード: 自己組織化マップ, BLSOM, 環境微生物, オリゴヌクレオチド頻度, 生物系統推定,
バイオインフォマティクス

First-principles Calculation for the Effect of Hydrogen Atoms on the Mobility of a Screw Dislocation in BCC Iron

Project Representative

Hideo Kaburaki

Japan Atomic Energy Agency

Authors

Mitsuhiro Itakura^{*1}, Hideo Kaburaki^{*1}, Masatake Yamaguchi^{*1}, Tatsuro Endo^{*1},
Kenji Higuchi^{*1}, Shigenobu Ogata^{*2} and Hajime Kimizuka^{*2}

*1 Japan Atomic Energy Agency

*2 Osaka University

Effect of hydrogen atoms on the mobility of a screw dislocation in BCC iron has been evaluated using the first-principles calculation. The stable position of a hydrogen atom is found to be near the screw dislocation core and inside the core respectively when the dislocation is at the easy-core or hard-core configuration in BCC iron. The intrinsically unstable hard-core configuration of the screw dislocation is stabilized when a hydrogen atom is trapped inside the core. On the basis of this first-principles result, an elastic string model of a dislocation is developed to predict the kink motion in the presence of a hydrogen atom. It is found that a double-kink formation is facilitated when a hydrogen atom is located near a dislocation line, however, a kink motion is retarded when a hydrogen atom is behind the kink.

Keywords: first-principles calculation, screw dislocation, BCC iron, hydrogen atom

1. INTRODUCTION

Hydrogen in metals and alloys is known to have a significant effect on the fracture properties. In particular, the presence of hydrogen in steel can lead to embrittlement typically in two forms, intergranular and/or intragranular cracking, depending on the condition [1]. In some cases, hydrogen-induced decohesion, corresponding to intergranular cracking, can occur in the low stress region. This phenomenon is caused by the segregation of impurities and solutes to grain boundaries leading to the reduction of cohesive strength, in which there is experimental and numerical evidence to support this [2][3][4]. In all these fracture experiments of steel, plasticity is interwoven in various stages of the entire fracture process and is known to be enhanced and/or retarded due to the presence of hydrogen, in particular, in iron. Therefore, the interaction of a dislocation with hydrogen atoms in iron is especially needed for a complete understanding of hydrogen embrittlement in steels. A fundamental question is whether the presence of hydrogen in the core of a screw dislocation, which mainly controls plasticity in iron, can increase or decrease the mobility of screw dislocations. Firstly, a core structure and mobility of a screw dislocation in iron must be clarified by the first-principles method since atomistic calculations with empirical potential sometimes lead to erroneous core structures. A large-scale periodic quadrupolar

array of dislocation cores in a parallelepiped cell is employed in the DFT (density functional theory) calculation to clarify the core structure and Peierls barrier map[5][6]. On the basis of these results, the interaction of a hydrogen atom with a screw dislocation core is evaluated using the first-principles method.

2. COMPUTATIONAL METHOD

Two screw dislocations with opposite helicity are placed in the cell to form a periodic quadrupolar array. Because of symmetric redundancy, the quadrupolar cell can be reduced to an equivalent dipolar cell (Fig. 1). The Cartesian coordinates X, Y, and Z are taken in the direction of $[1\ 1\ \bar{2}]$, $[1\ \bar{1}\ 0]$, and $[111]$.

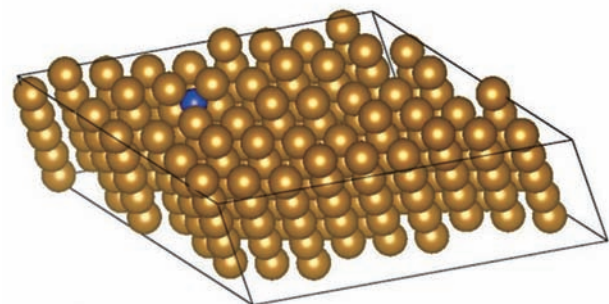


Fig. 1 Periodic quadrupolar array of screw dislocation cores in a parallelepiped cell of iron used in the DFT calculations.

The total number of atoms is 225 consisting of $45(=9 \times 5)$ in the XY plane and 5 in the Z direction. The electronic structure calculations and the structure relaxations by force minimizations in DFT steps are performed using Vienna Ab initio Simulation Package (VASP) with Projector Augmented Wave (PAW) method and ultrasoft pseudopotentials. The exchange correlation energy is calculated by generalized gradient approximation (GGA). In all cases, spin-polarized calculations are employed. The Monkhorst Pack k-point of $1 \times 1 \times 5$ mesh and the Methfessel-Paxton smearing method with 0.1-eV width are used. The cutoff energy for the plane wave basis set is 280 eV. Structural relaxation is terminated when maximum force acting on movable degree of freedom becomes less than 0.01 eV/Å.

3. RESULTS AND DISCUSSION

Figure 2 (a) and (b) show the atom configurations in the core of a BCC iron screw dislocation. In the stable easy-core configuration (Fig. 2(a)), atoms are located spirally along the Burgers vector direction of $\langle 111 \rangle$ in accordance with the BCC structure, while a large space is created in the unstable hard-core configuration. The easy and hard-core configurations are alternately located in the $\{111\}$ plane (Fig. 2(c)), the motion of a screw dislocation in BCC iron is inhibited by the large barrier of 40 meV/layer due to the presence of the hard-core configuration.

The stable position of a hydrogen atom is searched near the screw dislocation core using the first-principles calculation, and it is found that the most stable place of a hydrogen atom is near the core for the easy-core configuration (Fig. 3(a)) and inside the core for the hard-core configuration (Fig. 3(b)). The total energy of the system for the easy-core configuration is lowered to -200 meV and for the hard-core configuration to -400 meV with respect to the reference state when the hydrogen atom is in the bulk state. This indicates that the intrinsically unstable hard-core configuration is stabilized with the absorption of a hydrogen atom in the large-spaced core.

On the basis of the first-principles results on the interaction of a hydrogen atom and the screw dislocation core, an elastic string model of dislocation is constructed to predict the nucleation of a double kink and its kink motion with and without the presence of a hydrogen atom. Due to the high Peierls barrier, the motion of an entire screw dislocation line in BCC iron is prohibited. The motion of a screw dislocation is facilitated by forming a double kink, and the movement to the next easy-core configuration is accomplished by the motion of these kinks. The barrier for the double-kink nucleation is estimated to be 600 meV (Fig. 4(a)). However, when a hydrogen atom is located just near a dislocation line, it reduces the barrier by 200 meV, thus the presence of a hydrogen atom promotes a double-kink formation (Fig. 4(b)). On the other hand, the motion of a kink

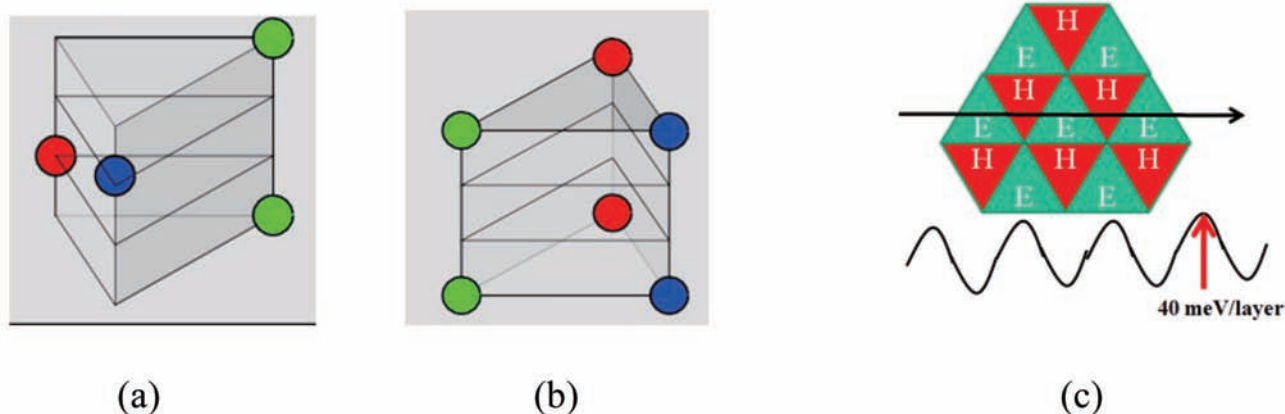


Fig. 2 Atomic positions in the core of a screw dislocation for the easy-core (a) and hard-core (b) configurations. (c) A plan view of $\{111\}$ plane in BCC iron. Easy-core and hard-core configurations are alternately located.

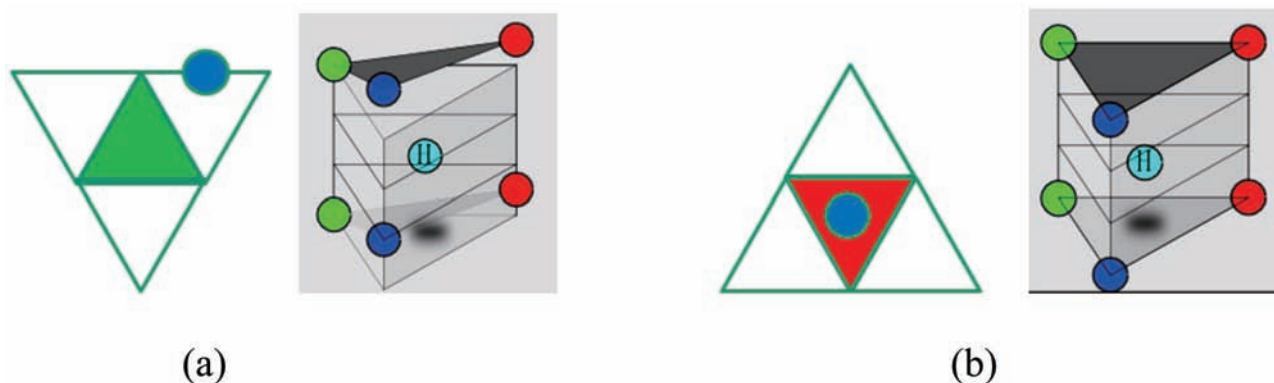


Fig. 3 The stable hydrogen atom location near the screw dislocation core for the easy (a) and hard-core (b) configurations.

is retarded when it passes near the hydrogen atom, as shown in Fig. 4(b), and the barrier for the kink to move is found to be 200 meV. And even when a kink escapes from this barrier, a hydrogen atom follows the kink to retard its motion because hydrogen atoms move easily in the bulk BCC iron. Thus, it is concluded from the above results that the motion of a screw dislocation in the environment of dispersed hydrogen atoms is difficult in BCC iron.

Lastly, it is emphasized that a transformation of a screw dislocation core occurs depending on the density of absorbed hydrogen atoms. It is found from the first-principles calculations that a hydrogen atom is trapped near the dislocation core when the screw dislocation is in the easy-core configuration. The energy reduction of one absorbed hydrogen atom in this case is 200 meV. On the other hand, in the case that a screw dislocation moves to the hard-core configuration and absorb hydrogen atoms, dislocation core energy increases by 40 meV per layer but the absorption energy increases to 400 meV. If we denote the number of absorbed hydrogen atoms per one atom layer by C , the total energy of the easy-core and hard-core configuration with absorbed hydrogen atoms is $-200C$ meV and $40-400C$ meV, respectively. When C is greater than 0.2, the hard-core configuration becomes more stable and it is predicted that the core position changes from the easy-core to the hard-core, as shown in Fig. 5(a), (b).

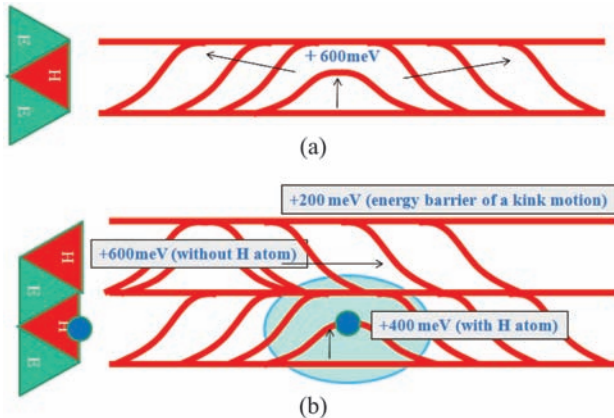


Fig. 4 (a) The process of a double-kink nucleation and its motion when a screw dislocation is in the easy-core configuration in BCC iron. (b) A double-kink nucleation and its subsequent motion when the hydrogen atom is located near a screw dislocation line.

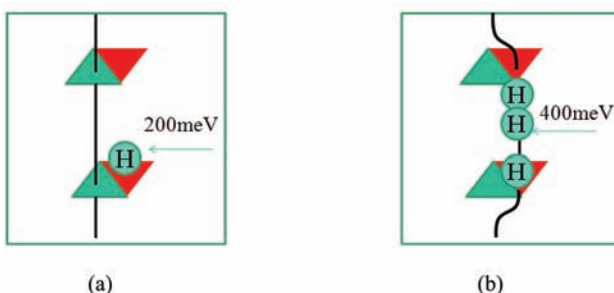


Fig. 5 Transformation of a core structure of a screw dislocation when the density of absorbed hydrogen atoms per atom layer is below (a) and above (b) 20% ($C=0.2$).

References

- [1] C. J. McMahon, *Eng. Frac. Mech.* 68, 773-788 (2001).
- [2] J. Kameda and C. J. McMahon, *Metall. Trans. A*, 14A, 903 (1983).
- [3] M. Wang, E. Akiyama, and K. Tsuzaki, *Mat. Sci. Eng. A398*, 37 (2005).
- [4] M. Yamaguchi, J. Kameda, K. Ebihara, M. Itakura, and H. Kaburaki, *Phil. Mag. A* 92, 1349 (2012).
- [5] F. Shimizu, S. Ogata, H. Kimizuka, T. Kano, J. Li, and H. Kaburaki, *Journ. Earth Simulator*, Vol.7, 17-21 (2007).
- [6] M. Itakura, H. Kaburaki, and M. Yamaguchi, *Act. Mat.* 60, 3698-3710 (2012).

第一原理計算による BCC 鉄中らせん転位の移動への水素の影響

プロジェクト責任者

燕木 英雄 日本原子力研究開発機構

著者

板倉 充洋^{*1}, 燕木 英雄^{*1}, 山口 正剛^{*1}, 圓戸 辰郎^{*1}, 樋口 健二^{*1}, 尾方 成信^{*2},
君塚 肇^{*2}

*1 日本原子力研究開発機構

*2 大阪大学

第一原理計算により BCC 鉄中の一本のらせん転位の移動度を与える水素原子の影響を調べた。BCC 鉄中の一本のらせん転位において、1 個の水素原子の安定位置は、転位が easy core の位置にいる場合は転位芯の外にあるが、不安定な hard core にいる場合は転位芯の中心の大きな空間にいる方が安定であることが分かった。この第一原理計算に基づき、転位キンクの弾性ひもモデルを構築し、水素原子との相互作用を計算した。その結果、転位運動の前方に水素原子が存在する時はキンクの形成が助長されるが、水素原子が後方に存在する時はキンク運動を阻害することが分かった。

キーワード: 第一原理計算, らせん転位, BCC 鉄, 水素原子

Development of a Fluid Simulation Approach by Massively Parallel Bit-wise Operations with a New Viscosity Control Method

Project Representative

Hiroshi Matsuoka

Research Institute of Electrical Communication, Tohoku University

Authors

Hiroshi Matsuoka^{*1}, Noriko Kikuchi^{*1,2}, Tadashi Watanabe^{*3}, Mitsuo Yokokawa^{*4}, Shin-ichi Mineo^{*4}, Ken-ichi Itakura^{*5}, Yukio Iwaya^{*1}, Yukio Fujinawa^{*6} and Yoshihiko Orita^{*7}

*1 Research Institute of Electric Communication, Tohoku University

*2 Customer System Company

*3 Japan Atomic Energy Agency

*4 Advanced Institute for Computational Science, RIKEN

*5 Earth Simulator Center, Japan Agency for Marine-Earth Science and Technology

*6 Fujinawa Earthquake Research & Development

*7 Japan Marine Science Foundation

The purpose of this project is to simulate the three-dimensional vortices from a circular cylinder in the fluid-flow by using a massively parallel Lattice Gas Method, which is expected to provide excellent computing performance on a large-scale vector computer, and to evaluate the applicability of the method to similar large-scale fluid-simulation problems by comparing the results with those of experiments or numerical calculations by solving Navier-Stokes equations. In particular, we try to realize the fluid-flow simulation at high Reynolds numbers by using a new viscosity-control method that we call “multi-stage collisions of two particles”. In case of the method, propagation of particles occurs after several times of collisions of randomly selected two particles at each node. By using the method, we can calculate fluid-flow at somewhat higher Reynolds number without increasing the number of nodes of lattice. Another feature of our method is “massively parallel bit-wise calculations”. We obtained the value of 96.8% as the calculation-efficiency by using 1024 vector CPUs of Earth Simulator. We regard that the value is a good performance.

Keywords: lattice gas automaton, fluid dynamics, massively parallel computing, vortex from a cylinder, vector computers

1. Purpose of the project

The purpose of this project is to simulate the three-dimensional vortices from a circular cylinder in the fluid-flow by using a massively parallel Lattice Gas Method, which is expected to provide excellent computing performance on a large scale vector computer, and to evaluate the applicability of the method by comparing the results with those of experiments or numerical calculations by solving Navier-Stokes equations.

In particular, we try to realize the fluid-flow simulation at high Reynolds numbers by using a new viscosity-control method without increasing the number of nodes of lattice.

2. Plan of three-year research

We are trying to complete the following three subjects in three years.

(1) Improvement of the calculation-efficiency of massively

parallel bit-wise operation method in the FY 2010

(2) Confirmation on the simulation results of vortices shedding from a circular cylinder of finite length in the FYs 2010 and 2011

(3) Simulation of the fluid-flow at high Reynolds numbers by the new viscosity-control method in the FYs 2011 and 2012.

3. Calculation method

3.1 Background of the calculation method

According to the previous study[1], it is known that wind or water tunnels can be indifferently used for testing low Mach number flows, provided the Reynolds numbers are identical. Indeed, two fluids with quite different microscopic structures can have the same macroscopic behavior because the form of the macroscopic equations is entirely governed by the microscopic conservation laws and symmetries. Such observations have

led to a new simulation strategy for fluid dynamics: fictitious micro-world models obeying discrete cellular automata rules have been found, such that two- and three-dimensional fluid dynamics are recovered in the macroscopic limit. The class of cellular automata used for the simulation of fluid dynamics is called “lattice gas models”, and many lattice gas models have been proposed.

In our study, we use one-speed models for the simulation of fluid dynamics. The relevant aspects of the models are as follows: there is a regular lattice, the nodes of which are connected to nearest neighbors through links of equal length; all velocity directions are in some sense equivalent and the velocity set is invariant under reversal; at each node there is a cell associated with each possible velocity.

Each node can be occupied by one particle at most; particles are indistinguishable; particles are marched forward in time by successively applying collision and propagation rules; collisions are purely local, having the same invariances as the velocity set; and collisions conserve only mass and momentum.

3.2 FCHC model for three-dimensional simulation

In order to simulate three-dimensional vortices shedding from a circular cylinder, we selected a face-centered-hypercubic (FCHC) model among from several one-speed models. The FCHC model is a four-dimensional model introduced by d’Humières, Lallemand, and Frisch in 1986[2]. Three dimensional regular lattices do not have enough symmetry to ensure macroscopic isotropy. The detailed FCHC model that we use in this study and the schematic diagram of simulated flow are explained in the following three figures.

As shown in Fig. 1, the coordinate X is the direction of flow, and the coordinate Z is parallel to the circular cylinder. A position of (X, Y, Z) represents the position of each cell. Every cell contains 32 nodes as depicted in Fig.1 Each node exists in the four-dimensional space. The fourth coordinate R is represented by the radius of sphere at each three-dimensional position.

As shown in Fig. 2, particles can have 24 kinds of velocities, that is, $(\Delta X, \Delta Y, \Delta Z, \Delta R) = (\pm 1, \pm 1, 0, 0), (\pm 1, 0, \pm 1, 0), (\pm 1, 0, 0, \pm 1), (0, \pm 1, \pm 1, 0), (0, \pm 1, 0, \pm 1)$ or $(0, 0, \pm 1, \pm 1)$, and the magnitude of the velocities is equal to $\sqrt{2}$, when the interval between two nearest nodes has a unit length.

Many particles propagate from node to node and make a collision at each node. The rules of propagation and collision are presented in Fig. 2 and Fig. 3, respectively.

The features of our method are “massively parallel bit-wise calculations” and “multi-stage collisions of two particles”.

Bit-wise parallel calculations are realized by vector operations on the arrangement representing the state of a cell. The arrangement is given by the form of 4-dimensional integer arrangement bit[D][Z][Y][X] that has 32 elements with the value of “1” or “0”. If the k-th bit of the arrangement bit[D][Z][Y][X] equals to “1”, this means that a particle moving toward the direction D exists at the k-th node of the cell locating at (X, Y, Z). “1” or “0” means existence or nonexistence of a particle, respectively.

Multi-stage collisions of randomly selected two particles at each node are useful for making a smaller correlation between fluid-velocities of two different cells a little apart from each other. This means that the fluid has smaller viscosity and

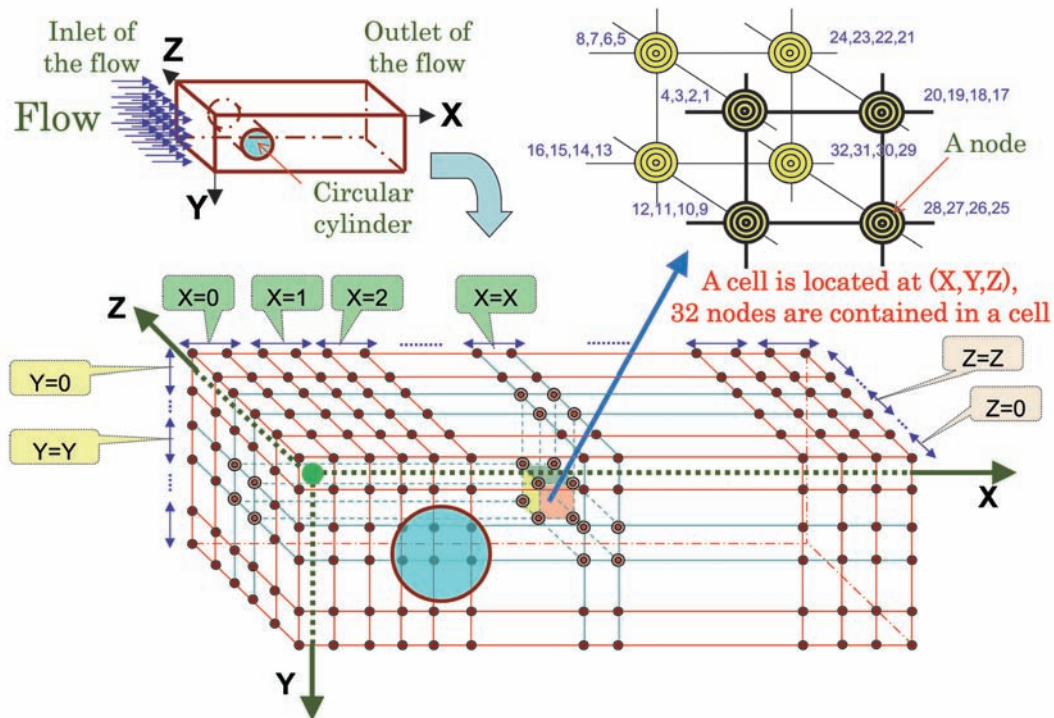


Fig. 1 Cells and nodes for simulating the three dimensional vortices shedding from a circular cylinder.

simulation at higher Reynolds numbers becomes somewhat easier.

3.3 Case study for the simulation of vortices shedding from a circular cylinder of infinite length

We numerically simulated the vortices shedding from a circular cylinder of infinite length.

Figure 4 shows the results of transient simulation of the fluid-momentum on the plane that Z equals to a certain constant value. General feature of the transient from twin vortices to Karman whirlpools is conceptually equal to those of the experiments by Taneda[3].

The number of nodes for the calculation is $3072(X) \times 768(Y) \times 768(Z) \times 4(R)$ in four dimensional space.

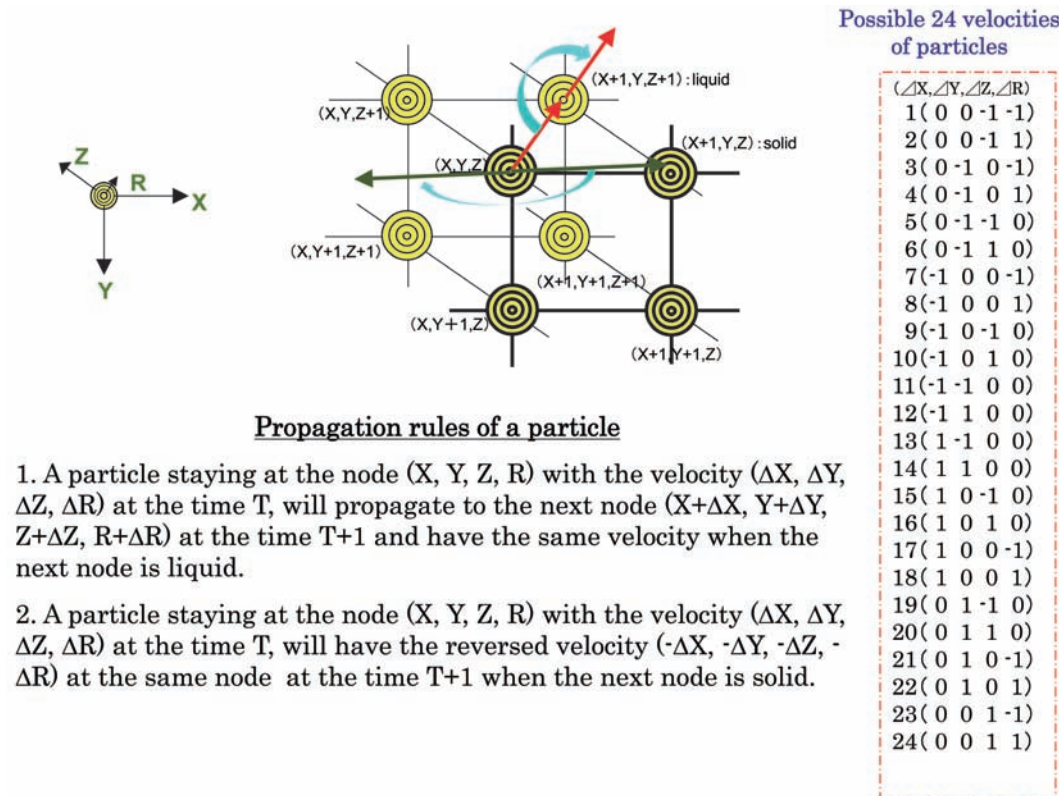


Fig. 2 Propagation rules from node to node.

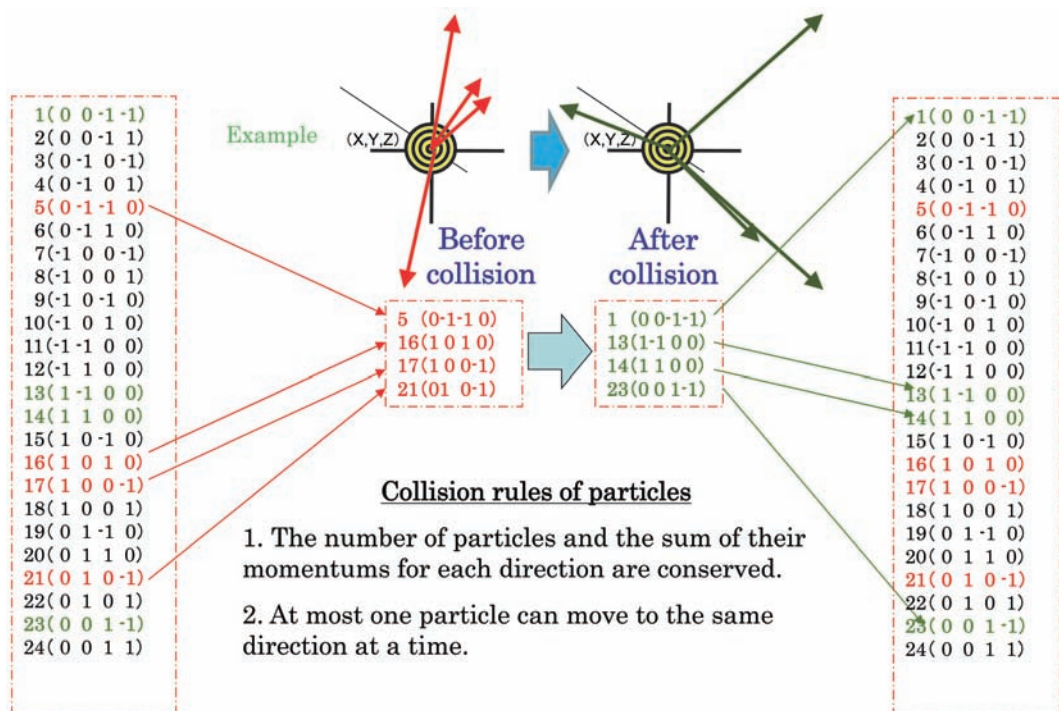


Fig. 3 Collision rules at each node.

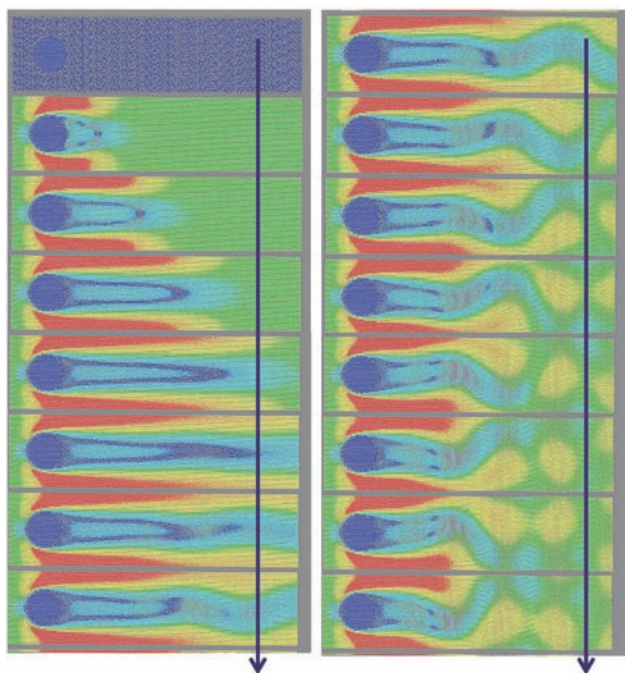
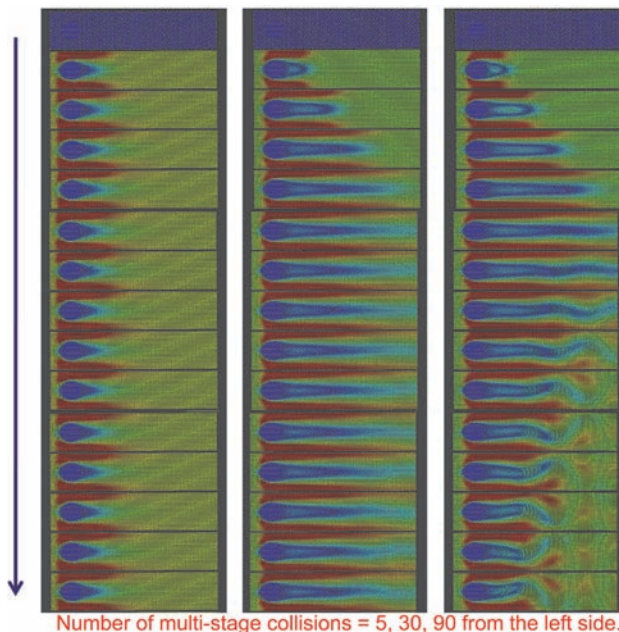


Fig. 4 A transient simulation result of the flow past a circular cylinder of infinite length.

Figure 5 shows the effects of the number of multi-stage collisions of two particles on transient simulation of the flow past a circular cylinder of infinite length[4]. Increase of the number of multi-stage collisions from 5 to 90 makes higher Reynolds numbers so that Karman whirlpools occur.

3.4 Results of the study in FY 2011

Regarding the improvement of the calculation-efficiency of “massively parallel bit-wise calculations”, we obtained the value of 96.8% by using 1024 vector CPUs of Earth Simulator. We



Number of multi-stage collisions = 5, 30, 90 from the left side.
Fig. 5 Effects of the number of multi-stage collisions on transient simulation of the flow past a circular cylinder.

regard that the value is a fairly good performance.

In FY 2011, we simulated many cases of the vortices shedding from a circular cylinder of finite length. One of the results is shown in Fig. 6. Further study is needed in FY 2012.

Acknowledgement

We greatly appreciate JAMSTEC for giving us a chance of using Earth Simulator and very kind support for our study.

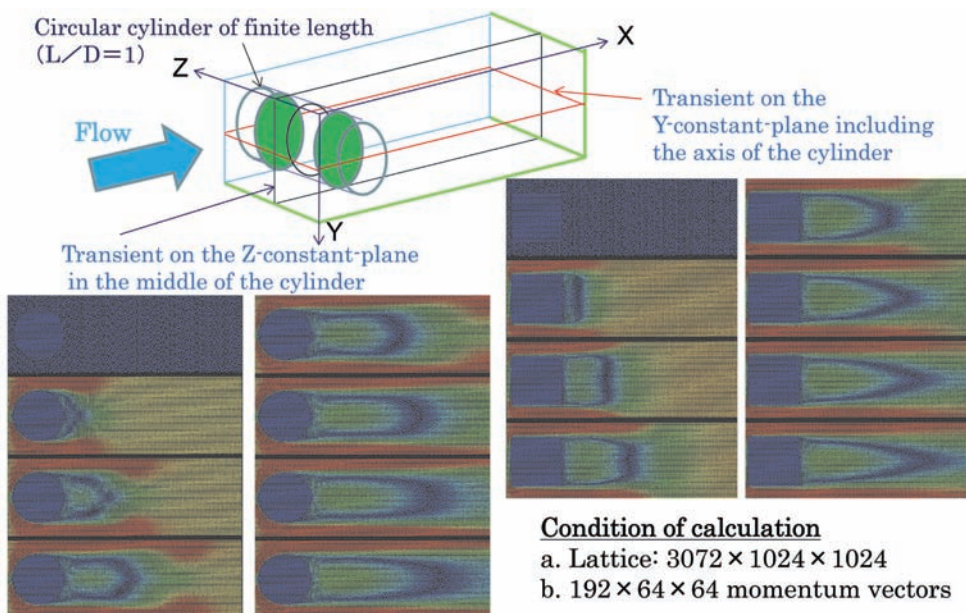


Fig. 6 Transient simulation of the flow past a circular cylinder of finite length.

References

- [1] U. Frisch, D. d'Humières, B. Hasslacher, P. Lallemand, Y. Pomeau, and J-P. Rivet, "Lattice Gas Hydrodynamics in Two and Three Dimensions", *Complex Systems*, 1(1987), pp.649-707.
- [2] D. d'Humières, P. Lallemand, and U. Frisch, *Europhys. Lett.*, 2 (1986) p.291.
- [3] Sadatoshi Taneda, "Gazou kara manabu ryuutairikigaku" (in Japanese), Asakura-shoten, p.45 and p.47.
- [4] H. Matsuoka and N. Kikuchi, "Controlling Effects on the viscosity of simulated fluid by using the method of multi-collision of two particles" (in Japanese), *SENAC Vol.44*, No.3 (2011.7), pp.21-28.

新粘性制御法による超並列ビット演算流体シミュレーション手法の開発

プロジェクト責任者

松岡 浩 東北大学 電気通信研究所

著者

松岡 浩^{*1}, 菊池 範子^{*1,2}, 渡辺 正^{*3}, 横川三津男^{*4}, 峯尾 真一^{*4}, 板倉 憲一^{*5},
岩谷 幸雄^{*1}, 藤縄 幸雄^{*6}, 折田 義彦^{*7}

*1 東北大学 電気通信研究所

*2 カストマシステム株式会社

*3 日本原子力研究開発機構

*4 理化学研究所 計算科学研究機構

*5 海洋研究開発機構 地球シミュレータセンター

*6 藤縄地震研究所

*7 日本海洋科学振興財団

本プロジェクトの目的は、大規模ベクトル計算機において優れた計算性能を発揮することが期待される格子ガス法超並列計算法を用いて、流体流れの中に置かれた円柱後流に生じる3次元渦のシミュレーションを行い、その結果を実験やナビエ・ストークス方程式を解く数値計算の結果と比較することによって、同様な大規模流体シミュレーション問題への本手法の適用可能性を評価することにある。

特に、“多段2体粒子衝突”と呼ぶ新しい粘性制御法を用いて、高いレイノルズ数領域における流体流れのシミュレーションの実現をめざす。この手法では、各ノードにおいて、ランダムに選択された2粒子が数10回衝突を起こしたあとに、粒子の並進移動を行う。本手法を用いると、格子点の数を増やすことなく、ある程度高いレイノルズ数領域の流体流れを計算することができる。本手法を用いて、有限長円柱の後流に生じる3次元渦のシミュレーションを行った。

また、我々が提案する手法のもうひとつの特徴は、“超並列ビット計算”である。地球シミュレータの1024個のベクトルCPUを用いて、並列化効率96.8%というかなり良い値を得た。

キーワード: 格子ガスオートマトン, 流体力学, 超並列計算, 円柱後流渦, ベクトル計算機

Acceleration of the Processing of Linear Equations in Characteristic 2 for RSA Decryption

Project Representative

Hidehiko Hasegawa Faculty of Library, Information and Media Science, University of Tsukuba

Authors

Yasunori Ushiro Department of Mathematics, School of Education, Waseda University

Hidehiko Hasegawa Faculty of Library, Information and Media Science, University of Tsukuba

The authors tuned the processing of linear equations, which is the second most time-consuming process in RSA decryption. As this process only tests whether the exponent part of equations are odd or even, binary numbers are used. The 64 binary numbers are stored as 64-bit integers and only the locations of non-zero elements of a sparse binary matrix are stored. The processing of linear equations in characteristic 2 requires fewer floating-point operations but an enormous amount of integer operation and list-vector processing.

The list-vector processing consumes almost of all computation time, but can be accelerated by loop unrolling. Hybrid parallelization with automatic parallelization by compiler at each node and MPI parallelization among nodes is effective for the Earth Simulator 2 (ES2). The processing of linear equations of dimension 8×10^7 in characteristic 2 required 130 hours on 4 nodes, and their parallel speedups were estimated as 3.5 for 4 nodes and 5.8 for 8 nodes. The computing time for linear equations of dimension 2×10^8 (equivalent to RSA-768) was estimated 800 hours on 4 nodes, which is a performance equivalent to that of a PC cluster with 1,700 CPUs. The computing time for linear equations of dimension 8×10^8 (equivalent to RSA-898) was estimated as 5,000 hours on 16 nodes.

Keywords: RSA cryptosystem, factorization, Characteristic 2, Block Lanczos method, GNFS

1. Introduction

The RSA cryptosystem is the most important technology for using the Internet safely; however, currently used 1,024-bit RSA code will not be safe for use in the near future [5]. The RSA cryptosystem is based on the difficulty of the factorization of long digits of a composite number, and the decryption time a of 1,024-bit RSA code is several tens of years even if the fastest supercomputer is used. For a RSA code with certain number of bits to be considered safe, its decryption time using the fastest algorithm and on the fastest supercomputer must be more than 10 years.

The present world record of RSA decryption, for RSA-768 (768 bits, 232 digits) is 1,677 CPU-year [7]. This means that if only one core in CPU (AMD64 2.2GHz) is used, then decryption takes 1,677 years. All reported world records for RSA decryption were achieved by PC clusters; no report has yet been made regarding a vector supercomputer. Therefore, a test on a vector supercomputer is necessary for a precise evaluation/discussion of the safety of 1,024-bit RSA cryptography code.

The present project intends to obtain some basic information for carrying out RSA decryption on the Earth Simulator 2 (ES2), as a representative of vector supercomputer. The decryption processing consists of three parts: the first step is “sieve

processing”, the second step is the processing of linear equations in characteristic 2, and the third step is the computation of algebraic square roots. In 2011, the second year of our project, the authors tuned the processing of linear equations in characteristic 2 for decryption software for use on the ES2.

2. RSA code

The common key cryptosystem and the public key cryptosystem are basic cryptosystems. The common key cryptosystem has only one key. It is simple and fast to process, but there is a problem to send the key in secret via the internet. The public key cryptosystem has two different keys for the encryption and decoding. The key for encryption is opened to the public, and the key for decoding is able to keep in secure, because it is not necessary to send the decoding key. A set of keys for the public key cryptosystem is based on the RSA code, which is innovated by R. L. Rivest, A. Shamir and L. M. Adlman in 1978. The RSA code uses two long digits prime numbers P and Q , and a prime number e , then computes $n = P \times Q$, $F = (P-1) \times (Q-1)$, and $D = e^{-1} \pmod{F}$. Numbers n and e are used for the key for encryption, and the number D is used for the key for decoding. The safeness of this is based on a result that, for a given long digits number n , the factorization

Table 1 Computational complexity of RSA-768 (768 bits, 232 digits).

	PC-year	Ratio (%)
Exploration of polynomial	20	1
Sieve processing	1500	90
Processing of linear equations	155	9
Algebraic square root	1	0
Others	1	0
Total	1677	100

algorithm of n to P and Q has high computational complexity and consumes enormous computation time.

3. Decryption of RSA code

The sieve method is a factorization method for a composite number N which obtains a relationship $a^2-b^2=0 \pmod{N}$ for some a, b . Because natural numbers a and b are constructed as the products of prime numbers provided by the sieve, the exponent of each prime number must be an even number.

For a composite number N , we assume X is the nearest integer to $N^{1/2}$ and calculate $(X+k)^2-N = A_k, k=0,1,2,\dots$. Then, we collect A_k that can be factorized using only prime numbers in factor base P . We can factorize N into a product of prime numbers using a combination of A_k whose exponent part is even. This provides the squared numbers for $a^2-b^2=0 \pmod{N}$.

The processing of linear equations in characteristic 2 involves choosing a and b that satisfy $a^2-b^2=0 \pmod{N}$. Since only the exponent part is tested for whether it is even or odd, we can use 0-1 binary computation. First, we create a matrix A whose elements are 0 or 1 by modulo operation from the sieved result, and then apply Gaussian Elimination to $A+I$, setting U equal to the result. If one row in the left part of U has all zero then non-zero columns in the right part of U indicate dependent rows. For these rows we test whether $a^2-b^2=0 \pmod{N}$ can be satisfied. As the probability of being factored correctly is 50%, enormous rows having dependent columns must be listed.

Table 1 shows the computational complexity of RSA-768 in PC-year of AMD64 (2.2GHz).

4. Processing of linear equations in characteristic 2

Because the dimension of the matrix for the decryption of RSA code is more than 10^8 and each row has nearly a hundred non-zero elements, on average, for solving this system of linear equations, iterative methods are preferred over Gaussian elimination. Using an iterative method, the least squares solution of the $A^T x=0$ is computed by the following steps:

- (1) Set y_0 equal to a random 0-1 vectors,
- (2) Compute the 0-1 vector $b = AA^T y_0$,
- (3) Solve the system of linear equations $AA^T y = b$ by iterative method,
- (4) $x = y - y_0$ is a least squares solution of $A^T x=0$.

The 64-bit integer can store 64 binary (0-1) numbers. The arrays for $x, b, x_0,$ and y can each store 64 binary vectors, and can be computed at the same time by 64 parallel computation.

In this study, the block Lanczos method is used as the iterative method. Binary vectors give an inner product equal to zero with probability 1/2, which is significant since division by zero in a simple Lanczos algorithm interrupts the iteration step in which it occurs. However, in the block Lanczos method with a block size of 64, a scalar in the simple Lanczos method becomes a 64×64 binary matrix in the processing of linear equations in characteristic 2, and the computation will not terminate if the matrix is regular. The 64 systems of linear equations with the same coefficient matrix are solved by the block Lanczos method; in this computation 64 solutions are computed simultaneously, and the iteration count is less than the dimension, $N/64$. The computation time of $q = AA^T p, \alpha = p^T q,$ and $q = p\alpha$ exceeds 99% in the block Lanczos method calculation, where A and A^T are binary (0-1) sparse matrices whose dimension are more than 10^8 , p and q each consist of 64 binary (0-1) vectors, and α is a 64×64 binary matrix. The vectors $p, q,$ and w and their arrays represent 64 binary vectors because a 64-bit integer can store 64 binary numbers.

The matrices and vectors are distributed among the nodes. To compute $w = A^T p$ and $q = Aw$ in multiple nodes, an enormous amount of communication is needed. Since the vector p and w are computed in parallel and stored in distributed manner, the full values of p and w are copied to each node before the sparse matrix computation. There are eight CPUs in each node of the ES2 and they have a common memory space. Each node must store all portion of p and w for the hybrid parallelization, but each CPU must hold all of p and w for the pure MPI parallelization. Thus, pure MPI parallelization requires much more memory than the hybrid parallelization, and the difference between the memory requirements for the pure MPI parallelization and the hybrid parallelization is particularly significant when using many nodes.

The following considerations and facts are used:

4.1. Sparse matrix computation: $q = AA^T p$

The full vector p must be stored in each node, whereas matrices and other vectors are distributed among nodes.

(1) Hybrid parallelization

Hybrid parallelization is applied to reduce the required memory. Automatic parallelization by the compiler is applied to each node, and MPI is used for parallelization among nodes.

(2) Both A and A^T are stored

To use long vector computation, matrices A and A^T are stored in different arrays on the ES2. Since the elements of binary matrices are 0 or 1, the locations of non-zero elements are stored rather than the values themselves. At each node, the number of non-zero elements in A and A^T set to be the same, and they are sorted at the beginning of the computation to construct long vectors on the ES2.

(3) AA^T is not computed

The matrix multiplication AA^T is not computed for the large

sparse matrices A and A^T . To obtain $q=AA^T p$, the computations $w=A^T p$ and $q=Aw$ are performed. Because nodes require the full value of p and w for this computation, the communications among nodes is necessary.

(4) Loop unrolling for the list-vector processing

Because the speed of list-vector processing on the ES2 strongly depends on the number of loop unrollings, the 2, 4, 8, and 16 unrolling by hand coding are tested.

4.2. Inner-product computation: $\alpha=p^T q$

The following method A with loop unrolling is chosen because, although method B has less computational complexity, it is not vectorized.

Method A:

The 64 times 64 (64^2) inner-products are computed simultaneously. Since a 64-bit integer can hold 64 binary numbers, the result of 64^2 inner-products is stored in 64 arrays: TH[0] to TH[63]. The outmost loop k is unrolled by 8, which means eight parallel executions take place per node. The parallelization among nodes is done by dividing the dimension N by the number of nodes.

```
for (k=0; k<64; k++)
{ S = 0;
  for (i=0; i<N; i++)
  { Wk = (P[i] >> k) & 1;
    S ^= Wk*Q[i]; }
  TH[k] = S;
}
```

Method B:

The amount of computation is one eighth of that of method A, but this method is not vectorized because of the dependency of $W[ir]$. This method is appropriate for a PC, but not for the ES2.

```
for (k=0; k<8; k++)
{ for (i=0; i<256; i++) W[i] = 0;
  for (i=0; i<N; i++) { Bit = 8*k; <-- Main part
    ir = (P[i] >> Bit) & 255; W[ir] ^= Q[i]; }
  for (i=0; i<8; i++) { S = 0;
    for (j=0; j<256; j++)
    { is = (j >> i) & 1; S ^= is*W[j]; }
    TH[k*8+i] = S;
  }
}
```

4.3. Multiply-and-add computation: $q=p\alpha$

Method A:

TH[k] stores 64 times 64 (64^2) binary numbers for scalar α , and Q[i] stores the result of 64 times 64 vectors. This has approximately the same performance as method A for the inner-product computation on the ES2.

```
for (k=0; k<64; k++)
{ for (i=0; i<N; i++)
  { Wk = (P[i] >> k) & 1;
    Q[i] ^= Wk*TH[k]; }
```

```
}
```

Method B:

The amount of computation is one eighth of that of method A, and this computation can be vectorized. The outmost loop j is unrolled by 8, and then 8 times 256 $W[i]$ are computed simultaneously. This means eight parallel executions take place per node. The parallelization among nodes is done by dividing the dimension N .

```
for (j=0; j<8; j++)
{ j8 = j*8;
  for (i=0; i<256; i++)
  { k = 0; id = i; S = 0;
    while (id) { S ^= (id & 1)*TH[k+j8];
      id = id >> 1; k++; }
    W[i] = S; }
  for (i=0; i<N; i++) <-- Main part
  { Q[i] ^= W[(P[i] >> j8) & 255]; }
}
```

5 Performance of the processing of linear equations in characteristic 2

Figure 1 shows the performance of a transposed binary sparse matrix vector multiplication $w=A^T p$ on one node of the ES2. The length of vector is sufficiently long but low performance is observed compared to having continuous memory access

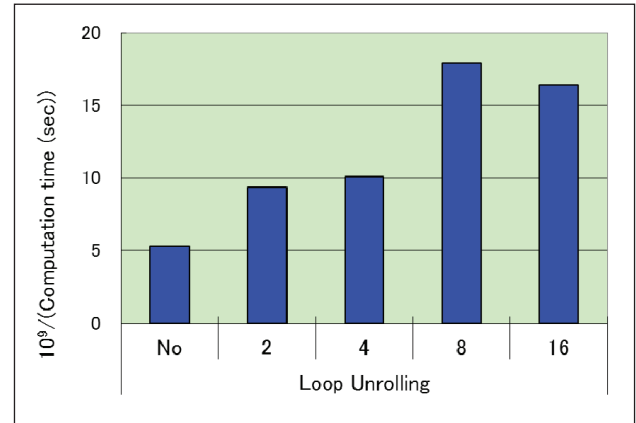


Fig. 1 Performance of binary sparse matrix multiplication $w=A^T p$ on one node.

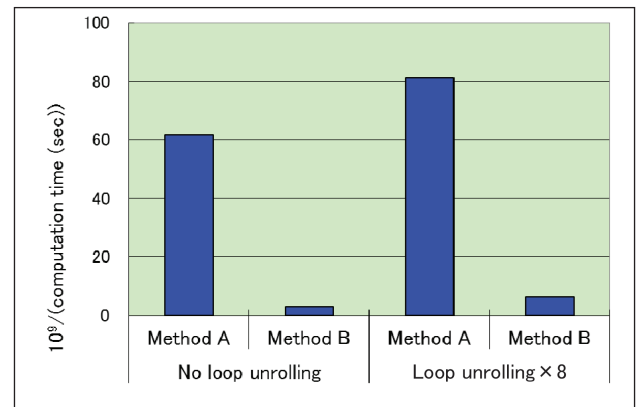


Fig. 2 Performance of inner-product $\alpha=p^T q$ on one node.

because the use of a list-vector. The vector operation ratio exceeds 99%. The performance of a matrix vector multiplication $q=Aw$ is nearly equal to that of $w=A^T p$.

Figure 2 shows the performance of an inner-product $\alpha=p^T q$ on one node of the ES2. A computational complexity of method B is assumed to be the same as that of method A. The real operation cost of method B is 1/8 times that of method A; however, method B has very poor performance because of the lack of vector computation. The vector operation ratio of the method A exceeds 99%.

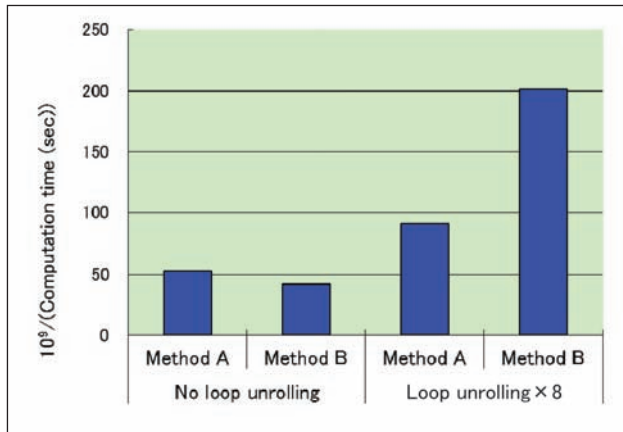


Fig. 3 Performance of multiply-and-add $q=pa$ on one node.

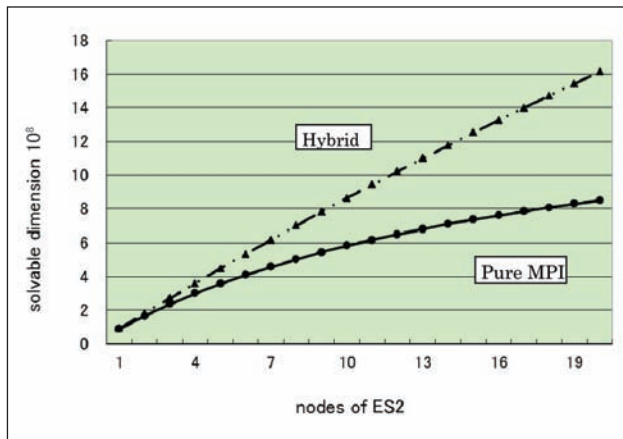


Fig. 4 Potential size problem when processing of linear equations in characteristic 2.

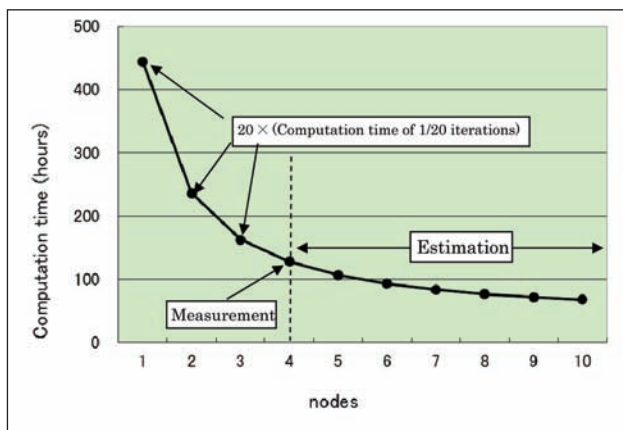


Fig. 5 Computation time of processing linear equations of dimension 8×10^7 .

Figure 3 shows the performance of a multiply-and-add $q=pa$ on one node of the ES2. The computational complexity of method B is assumed to be the same as that of method A. In this case, method B can be vectorized, after which it has a high performance value. The vector operation ratios of both methods exceed 99%.

Figure 4 shows a potential size problem when processing of the linear equations in characteristic 2. In the case of 20 nodes (160 CPUs) of the ES2, the dimension size of the hybrid parallelization is twice that of the pure MPI parallelization.

Figure 5 shows the computation time of processing of linear equations in characteristic 2 whose dimension is 8×10^7 . The computation required 130 hours on 4 nodes of the ES2. The iteration count does not depend on the number of nodes. The computation time shown for 4 nodes is real measurement, whereas the values for 1, 2, 3 nodes are calculated by multiplying 20 the computation time for 1/20 of the total required iterations. The case of 5 to 10 nodes are estimated based on the other results and the communication cost among nodes. The dimension 8×10^7 was selected because it is the largest problem size that can be stored in the memory on one node of the ES2.

Figure 6 shows the speedups of the processing of linear equations in characteristic 2 whose dimension is 8×10^7 based on the result shown in Figure 5. The speedup is estimated to be 3.5 on 4 nodes and 5.8 on 8 nodes of the ES2. Herein, speedup of

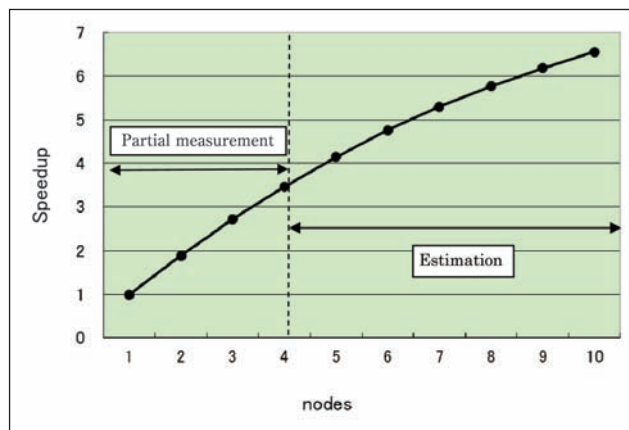


Fig. 6 Speedup of processing of linear equations of dimension 8×10^7 .

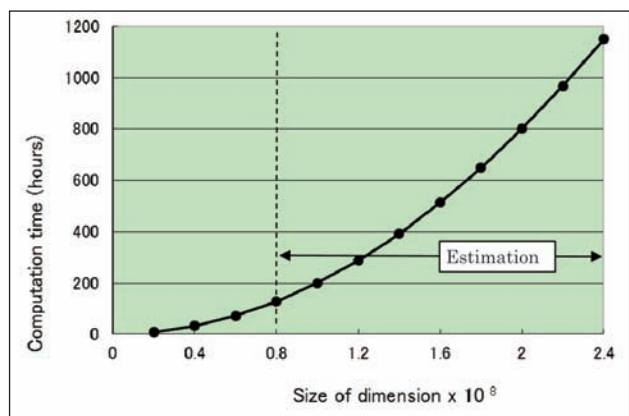


Fig. 7 Processing time of linear equations in characteristic 2 on 4 nodes.

an ES2 computation is defined as the time measured for a single node divided by the time measured for multiple nodes.

Figure 7 shows the estimation of computation time for the processing of linear equations in characteristic 2 on 4 nodes of the ES2. As the iteration count is proportional to the square of the dimension, an estimation of the iteration counts is calculated for measurement for dimensions of 2×10^7 to 8×10^7 . An estimation of the computation time is calculated from the measurement of 1,000 iterations.

The computation time of the processing of linear equations in characteristic 2 whose dimension is 2×10^8 is estimated to be 800 hours on 4 nodes of the ES2. Four nodes of the ES2 are equivalent to 1,700 (AMD64 2.2GHz) CPUs, based on that the present world record RSA-768 is 150 CPU-year (AMD64 2.2GHz).

6. Summary

The authors tuned the processing of the linear equations in characteristic 2 in the RSA decryption processing. The following basic information on the ES2 were obtained:

- 1) This portion of the decryption processing is more than 99% vectorized, and has less floating-point operations. The list-vector processing consumes almost of all computation time and has accelerated by loop unrolling. The maximum improvement obtained by loop unrolling is 4.8-fold in the case of the multiply-and-add operation ($q=p\alpha$).
- 2) Binary sparse matrices computation and multiply-and-add computation ($q=p\alpha$) have sufficient performance; however, the inner-product computation ($\alpha=p^Tq$) does not realized a good speedup relative to scalar performance because the faster method (method B) was not applicable.
- 3) Hybrid parallelization with automatic parallelization by compiler on one node and MPI parallelization among nodes is effective for the ES2.
- 4) The processing of the linear equations in characteristic 2 whose dimension is 8×10^7 requires 130 hours on 4 nodes of the ES2. The speedup of the processing of linear equations in characteristic 2 whose dimension is 8×10^7 is estimated to be 3.5 on 4 nodes and 5.8 on 8 nodes of the ES2.
- 5) The computation time of the processing of linear equations in characteristic 2 whose dimension is 2×10^8 (equivalent to RSA-768) is estimated 800 hours on 4 nodes of the ES2. This is equivalent to 1,700 (AMD64 2.2GHz) CPUs. The computation time of the processing of linear equations in characteristic 2 whose dimension is 8×10^8 (equivalent to RSA-898) is estimated 5,000 hours (7 months) on 16 nodes of the ES2.

Acknowledgement

The authors thank to Dr. Yoshinari Fukui and Mr. Tadashi Kai of JAMSTEC, who gave us precious advice on speeding up the ES2.

References

- [1] Yasunori Ushiro, "RSA Decryption using Earth Simulator", Annual Report of Earth Simulator Center, 167-171, 2011.
- [2] Yasunori Ushiro, "A high speed sieve method for RSA cipher using the vector computer", RIMS Kokyuroku 1733, 101-117, March 2011. (in Japanese)
- [3] Richard A. Mollin, "RSA and PUBLIC-KEY CRYPTOGRAPHY", CRC Press, 2002.
- [4] Yuji Kida, "Prime factoring by General Number Field Sieve", 2003. http://www.rkmath.rikkyo.ac.jp/~kida/nfs_intro.pdf (in Japanese)
- [5] Junichi Yamazaki and Souta Kamaike, "The 2010 problem of the Cryptography", ASCII technologies, 75-93, Sept. 2010. (in Japanese)
- [6] Neal Koblitz, translate by Kouichi Sakurai, "A Course in Number Theory and Cryptography", Springer, 1997. (in Japanese)
- [7] Kazumaro Aoki, "Advances in Integer Factoring Technique: The Way to Factor RSA-768", IPSJ Magazine, 51(8), 1030-1038, Aug. 2010. (in Japanese)

RSA 暗号の解読処理向け標数 2 の線形計算の高速化

プロジェクト責任者

長谷川 秀彦 筑波大学 図書館情報メディア系

著者

後 保範 早稲田大学 教育学部 数学科

長谷川秀彦 筑波大学 図書館情報メディア系

RSA 暗号の解読処理で「ふるい処理」の次に時間を占める「標数 2 の線形計算」を ES2 向けに高速化した。0-1 の 2 値データを扱うため、64 ビット整数ではサイズ 64 のブロックが自然に扱え、ブロックランチョス法が利用できる。0-1 の疎行列では値を格納する必要はなく、非ゼロ要素の位置だけを記憶すればよい。課題は 64 ビット整数の演算とリストベクトル処理の高速化であり、2 億次元 (RSA-768 相当) の標数 2 の線形計算は ES2 の 4 ノードで約 800 時間と推定され、約 1,700 台の PC クラスタと同程度の性能が達成できた。

RSA 暗号はインターネットを安全に使ううえで欠かせない技術である。RSA 暗号には桁数の多い合成数の因数分解の困難性が利用されており、現在使用されている 1,024 ビット RSA 暗号の安全性はスーパーコンピュータを数年使用しても解読されないという仮定のもとで成り立っている。これまでの RSA 暗号解読の世界記録はすべて PC クラスタで達成されており、ベクトル方式のスーパーコンピュータによる RSA 暗号の解読実験は全く報告されていない。そこで、本研究では代表的なベクトル方式のスーパーコンピュータである地球シミュレータ (ES2) において RSA 暗号の解読実験を行う。

一般的な RSA 暗号解読は、ふるい処理、標数 2 (0-1 データ) の線形計算、代数的平方根の計算の 3 段階からなり、RSA 暗号解読プログラムはすべて PC 向きに開発されている。プロジェクト 2 年目となる本年度は「ふるい処理」の次に時間を占める「標数 2 の線形計算」と ES2 の相性を評価した。

標数 2 の線形計算にはブロックランチョス法を使用するため、疎行列とベクトルの乗算、内積計算および積和計算が必要となった。これらは PC とは異なる最適化が必要であるが、ES2 との相性は良いことが明らかになった。実際、64 ビット整数を用いると 0-1 データ 64 個分が一括計算できる。リストベクトル処理に対するループアンローリングの効果が大きいこと、疎行列 A および A^T とベクトルの乗算ではベクトル長を長くするため A と A^T を別に保持する必要があることなどが明らかになった。標数 2 の内積計算と積和計算は演算量を約 1/8 に削減する方法が知られているが、内積計算では演算を削減する方法のデータ依存性を取り除くことができなかった。ES2 では、内積計算は演算を削減しない方法、積和計算は演算を削減する方法を採用した。

この結果、8,000 万次元の標数 2 の線形計算が ES2 の 4 ノードを使用して約 130 時間で計算できる。8,000 万次元での並列性能は、4 ノードで 1 ノードの 3.5 倍、8 ノードで 5.8 倍と推定できた。浮動小数点数の演算はないが、ベクトル化率は 99% 以上で、ふるいと異なり並列化率は通信性能に依存する。これから、2 億次元 (RSA-768 相当) の標数 2 の線形計算は ES2 の 4 ノードで約 800 時間と推定され、これは 2.2GHz の PC 1,700 台のクラスタと同程度の性能になる。

キーワード: RSA 暗号, 因数分解, 標数 2, ブロックランチョス法, GNFS

謝辞

地球シミュレータ (ES2) における高速化について貴重なご意見を頂いた海洋研究開発機構地球シミュレータセンターの福井義成氏及び甲斐恭氏に謹んで感謝の意を表す。

参考文献

- [1] Y. Ushiro, "RSA Decryption using Earth Simulator", Annual Report of Earth Simulator Center, 167-171, 2011
- [2] 後 保範, "ベクトル計算機による RSA 暗号ふるいの高速化", 京大数理解析研講究録 1733, 101-117, 2011 年 3 月
- [3] Richard A. Mollin, "RSA and PUBLIC-KEY CRYPTOGRAPHY", CRC Press, 2002
- [4] 木田 祐司, "数体ふるい法による素因数分解", 2003; http://www.rkmath.rikkyo.ac.jp/~kida/nfs_intro.pdf
- [5] 山崎 潤一, 釜池 聡太, "暗号の 2010 年問題", ASCII Technologies, 75-93, 2010 年 9 月
- [6] N. コブリッツ, 桜井 幸一訳, "数論アルゴリズムと楕円暗号理論入門", シュプリンガー・フェアラーク東京, 1997 年
- [7] 青木和磨呂, "素因数分解技術の進展: RSA-768 の分解達成への道のり", 情報処理, 51(8), 1030-1038, 2010 年 8 月

Development of Sophisticated Simulation Analysis Method of Actual Reinforced Concrete Building by Shaking Table Test-II

Project Representative

Yoshiyuki Kasai

Department of Urban Environment and Information Sciences, Graduate School, Maebashi Institute of Technology

Authors

Yoshiyuki Kasai

Department of Urban Environment and Information Sciences, Graduate School, Maebashi Institute of Technology

Haruji Tsubota

Department of Architecture, Graduate School, Maebashi Institute of Technology

Yoshikazu Kanai

Department of Urban Environment and Information Sciences, Graduate School, Maebashi Institute of Technology

Yoshinori Konno

Department of Architecture, Graduate School, Maebashi Institute of Technology

Shigefumi Takeda

ARTES Corporation

Kazukuni Niwa

Terrabyte Co. Ltd.

Yoshio Manabe

Terrabyte Co. Ltd.

The impact analysis code of the explicit method that demonstrates effectiveness in the collision analyses of automobiles etc. was applied to the seismic response analyses of buildings to study the methods enabling computer analyses of reinforced concrete building collapse phenomena that were frequently observed in the Hanshin Awaji Earthquake but not yet clarified. In this study, the authors performed simulation analyses of shaking table tests at the E-Defense in which the phenomenon close to collapse of a full-scale six-story RC building was found and the evaluation of effectiveness of seismic reinforcement, which is an issue of seismic design in recent years. In addition, the seismic response analyses considering collision with the retaining walls of a RC building subjected to long-period pulse earthquakes.

This study enabled elasto-plastic seismic response analyses by constructing huge number of approximately 4 million finite element model consisting of concrete and reinforcing bars as they are, and thus the prospect of the possibility of a reduction in the vast expense required by full-scale shaking table tests for various structures and the improvement in the effectiveness of such tests was obtained by using the sophisticated simulation analysis method (the numerical shaking table).

Keywords: Seismic response, Shaking table test, RC frame, Earth simulator, FEM, Base isolation, Seismic reinforcement

1. Introduction

The impact analysis code of the explicit method that demonstrates effectiveness in the collision analyses of automobiles etc. was applied to the seismic response analyses of buildings to study the methods enabling computer analyses of reinforced concrete (abbreviated as RC hereafter) building collapse phenomena that were frequently observed in the Hanshin Awaji Earthquake but not yet clarified. In this study, the authors performed simulation analyses of shaking table tests at the E-Defense in which the phenomenon close to collapse of a full-scale six-story RC building subjected to a seismic intensity of 6 upper. Specifically, precise and detailed simulation analyses were performed by applying the impact analysis program (LS-DYNA) for comparisons with test results to verify the analysis

method. Moreover, based on the afore-mentioned analysis system, the procedures for numerical shaking tests were developed.

The items of the study to be implemented in this fiscal year are shown below from the viewpoint of simulation and application:

- (1) Improvement of the simulation analysis for the shaking table test of full-scale six-story RC building and the additional pushover analysis
- (2) Applied seismic response analyses of various buildings by the verified sophisticated simulation analysis method (Numerical shaking table)
 - ① Seismic response analysis of the full-scale six-story RC building built on ground considering building-soil

interaction effect (Applied analysis)

- ② Seismic response analysis of the full-scale three-story RC buildings with and without seismic reinforcement on the shaking table (Simulation Analysis)
- ③ Seismic response analysis of base-isolated RC building considering collision with retaining wall placed around the building (Applied analysis)

2. Simulation analysis of full-scale six-story RC building by shaking table

The analytical results of this test were shown in references [1] through [3]. The analyses were performed using the Finite Element model shown in Fig. 1. As for the mesh sizes, the analytical model was divided into approximately 2.08 million elements in total consisting of approximately 1.48 million elements of concrete and approximately 0.57 million elements

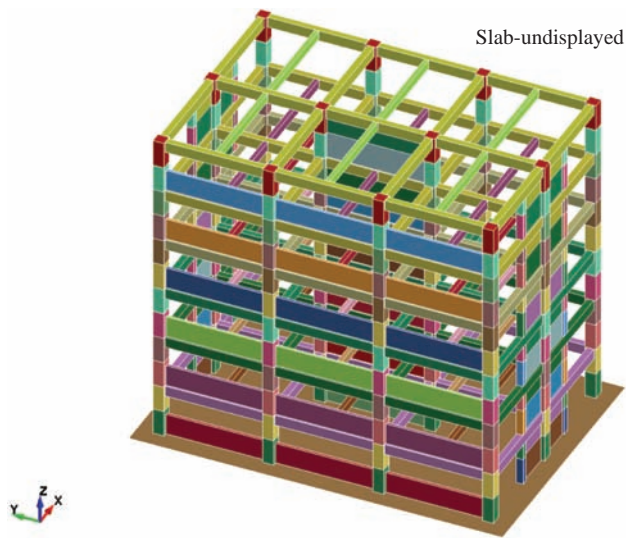


Fig. 1 FEM analytical model.

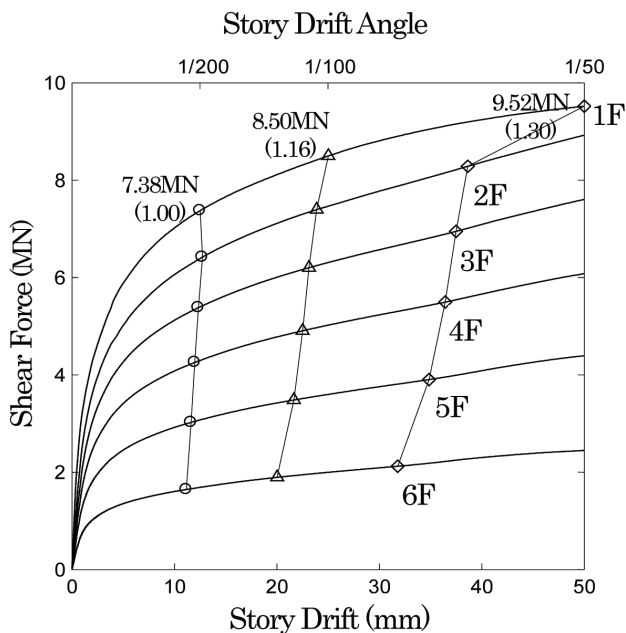


Fig. 2 Result of pushover analysis (y-direction).

of reinforcing bars. According to the advice of the researcher who was in charge of the tests, the pushover analyses in which horizontal force distributing vertically similar to seismic force was stepwise increased were performed to calculate the relationship between the shear force and the story drift that is the basic structural characteristic of a building as shown in Fig. 2. This characteristic was not experimentally verified because a large size loading apparatus is required. However, these results are very important to identify the structural characteristics of a building, and it was found that determination by analysis is possible.

In the simulation analyses of shaking table tests, the consideration of shaking history provided the analysis results that can simulate the test results better as shown in Fig. 3. Furthermore, earthquakes with a input acceleration factor of 1.2, 1.5 and 2.0 that are impossible to load in the shaking tests were applied to the analytical model. Therefore, the authors found it is possible to verify that the building has seismic margin that shows no collapse by 1.5 times earthquake but possibly shows collapse by 2.0 times earthquake.

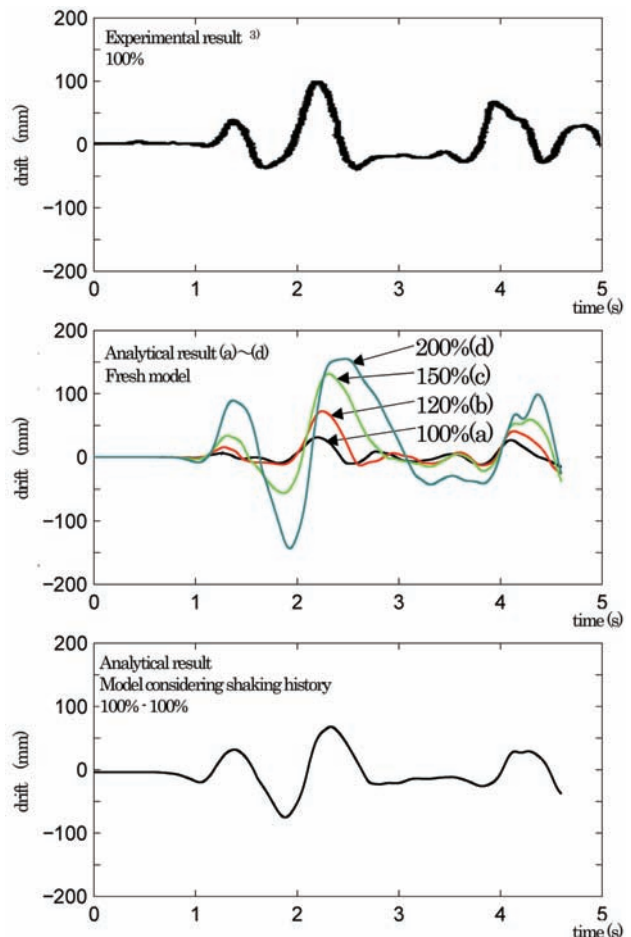


Fig. 3 Story drift time history (y-direction,1F).

3. Seismic response analysis of full-scale six-story RC building placed on ground considering building–soil interaction effect (Applied analysis)

The aforementioned tests were performed under the condition of a divided foundation for the purpose of investigating properties of upper building nevertheless the foundation should primarily be integrated. In this study, a foundation was newly designed as shown in Fig. 5, modeling was performed to realize the condition that well simulates an actual building as shown

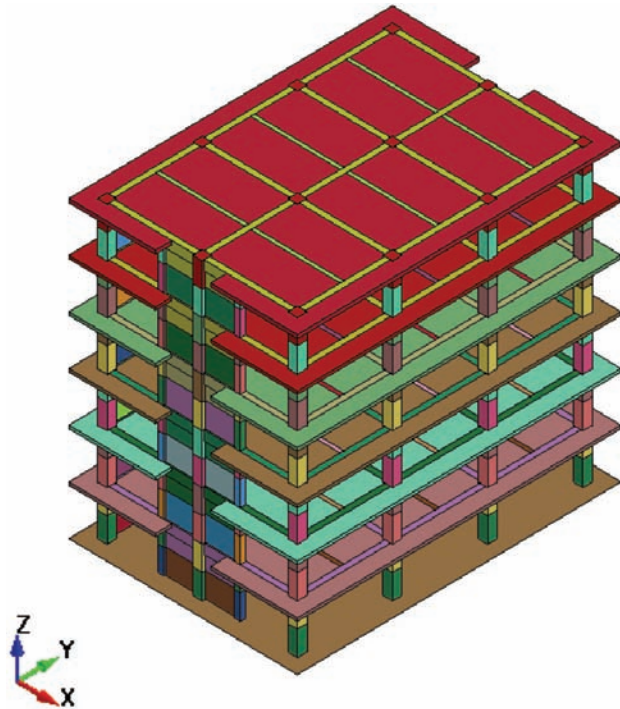


Fig. 4 Fixed column base model.

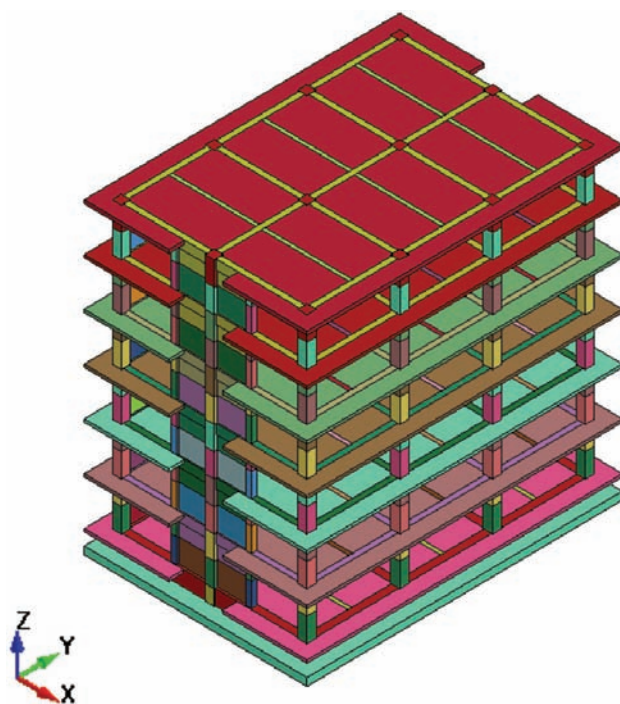


Fig. 5 Building model including foundation.

in Fig. 6 by considering the ground for bearing the building, detailed analyses [4] were performed in the three-dimensional elasto-plastic Finite Element Method, and the analytical results were compared with the model of only the upper structure with column bases fixed (Fig. 4) to examine the effects of the interaction of the building and the ground (soil) on the seismic response of the building. [4] As for the ground used for the analyses, the subsurface ground on the engineering basement was modeled by dividing into solid elements to make it elastic ground with a layer thickness of 10 m, a density ρ of 1.6 t/m^3 , shear wave velocity of 200 m/s, and shear modulus G of 64 N/mm^2 . In addition, the non-reflection boundary against shear wave was provided in the periphery of the ground model. The contact surface was defined without allowing share of nodal points between the building and the ground, assuming friction coefficient to be 0.3. This definition enables realization of slip, floating, etc. between the building and the ground, making it possible to perform analyses similar to the actual phenomena. As for the mesh sizes, the coupled model was divided into approximately 3.0 million elements in total after dividing the ground model into approximately 0.4 million elements. Damping was assumed to be 3% of mass proportion type. As shown in Fig. 7, the response of the building placed on the ground was about 30% smaller in comparison with the seismic response in the model of only the upper structure, that is, fixed column base model.

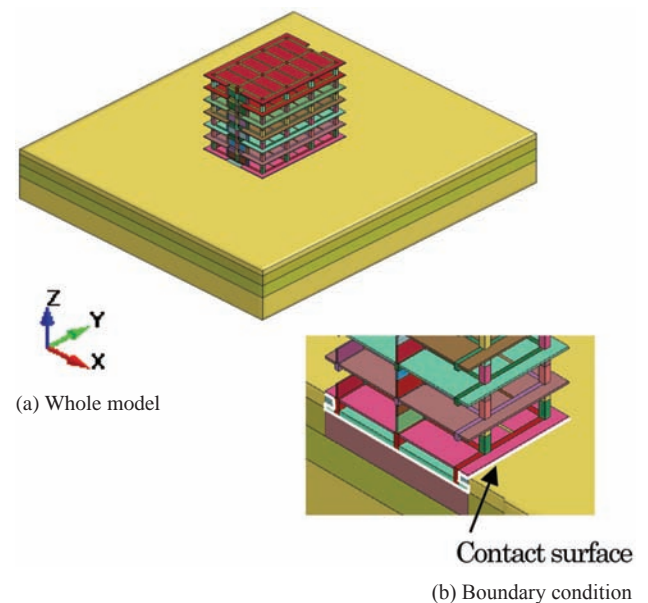


Fig. 6 Interaction model on ground.

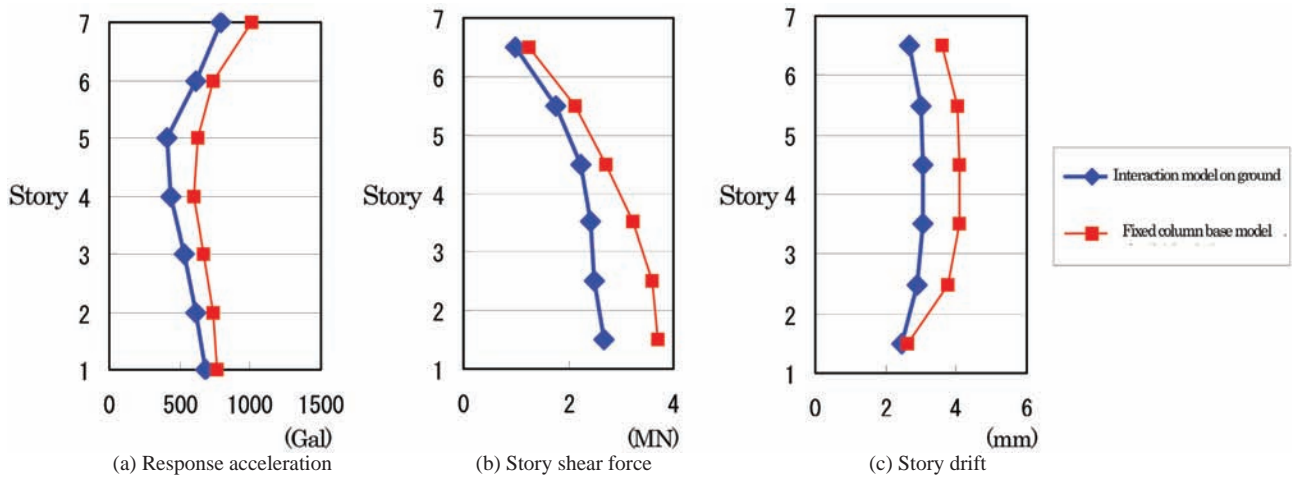


Fig. 7 Comparison of maximum response distribution.

4. Seismic response analysis of three-story RC buildings with and without seismic reinforcement on the shaking table (Simulation Analysis)

The objects to be analyzed [5] were assumed to be two specimens without and with seismic reinforcement as shown in Figs. 8 and 9 of a three-story RC building of which shaking table tests at the E-Defense were conducted. An analytical model was created by dividing concrete into solid elements and reinforcing bars into beam elements and assuming nodal points between

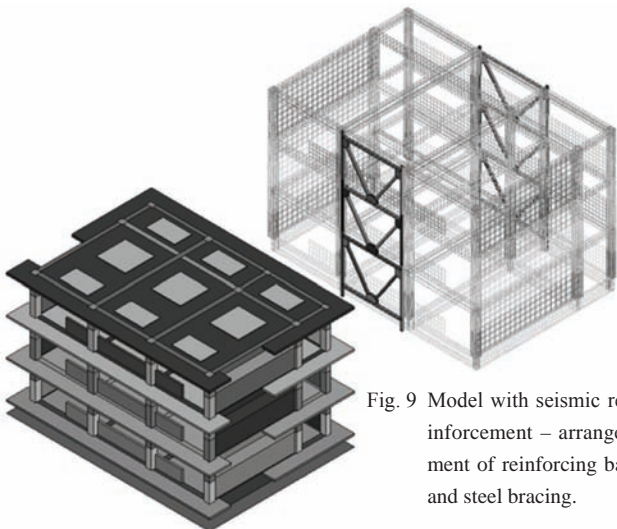


Fig. 9 Model with seismic reinforcement - arrangement of reinforcing bar and steel bracing.

Fig. 8 Model without seismic reinforcement.

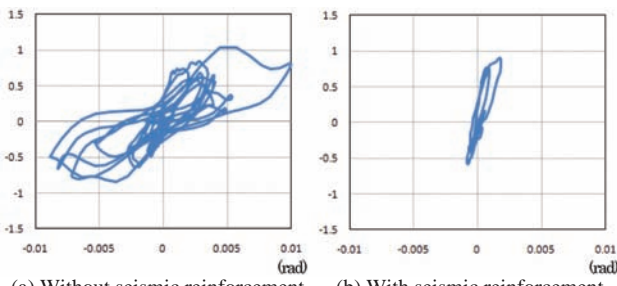


Fig. 10 Story shear coefficient - story drift angle. (Analytical results, 1F)

them to be completely bonded. Foundation section was divided into completely fixed rigid shell elements. As for the mesh size, the model of the specimen without seismic reinforcement was divided into approximately 0.84 million elements in total consisting of approximately 0.54 million elements of concrete, approximately 0.27 million elements of reinforcing bars and approximately 0.17 million elements of rigid shell. The model of the specimen with seismic reinforcement was divided into approximately 0.97 million elements in total consisting of approximately 0.67 million elements of concrete, approximately 0.28 million elements of reinforcing bars and approximately 0.02 million elements of rigid shell. Fig. 10 shows the relationship between the story shear coefficient of the first-story and the story drift angle obtained by the analysis. Although the maximum story shear coefficient showed almost no difference between the specimens without and with seismic reinforcement, the maximum story drift angle in the specimen with seismic reinforcement was found to be smaller, namely approximately 1/5 of that without seismic reinforcement. This result enables to say seismic performance of the building was improved by seismic reinforcement from the viewpoint of dynamic response during an earthquake.

5. Seismic response analysis of base-isolated RC building considering collision with retaining wall (Applied analysis)

Seismic response analyses [6, 7, 8] of a three-dimensional RC building model considering a collision with the retaining wall placed around the building by three-dimensional inputs in two horizontal directions and one vertical direction were performed concerning long-period pulse earthquakes that are observed in strong local earthquakes in recent years.

This analytical model was created by dividing the concrete of the upper structure, retaining walls and the backfill soil into solid elements and dividing the reinforcing bars into beam elements as they are shown in Fig. 11. The concrete and the reinforcing bars were made to share nodal points completely

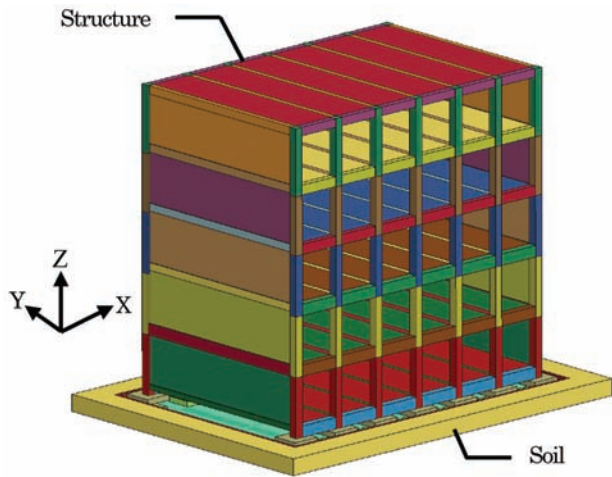
bonded. Backfill soil was modeled by dividing into rigid elements, and seismic wave at K-NET Kashiwazaki observation points of Niigataken Chuetsu-oki Earthquake in 2007 (NIG008) where a long-period pulse was observed was used. A model of base isolation system was created by replacing with horizontal and vertical spring elements. The analytical model was divided into approximately 3.9 million elements in total, and the primary natural period of the base isolation building was 2.79 s.

Among the analysis results, the orbit of horizontal displacement in a base isolation story is shown in Fig. 12. The

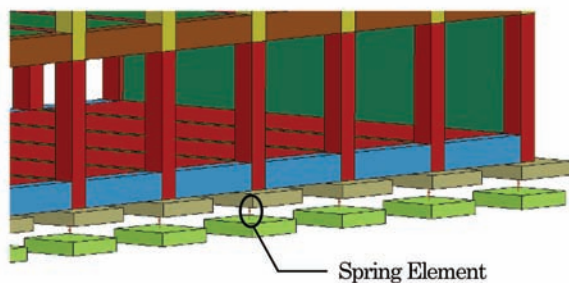
dotted line in the figure shows clearance between the building and the retaining wall (375 mm), and crossing over this line results in a collision. Fig. 13 shows the time history impact force waveform which shows the generation of collisions 5 times in total in 6.0 s. In addition, since there is a possibility that the collision of the building and the retaining walls results in behavior like sending and sweeping legs in judo, generating tensile force that reduce base isolation performance, and therefore some effective measures should be taken.

6. Conclusion

This study enabled elasto-plastic seismic response analyses by constructing huge number of approximately 4 million finite element model consisting of concrete and reinforcing bars as they are, and thus the prospect of the possibility of a reduction in the vast expense required by full-scale shaking table tests for various structures and the improvement in the effectiveness of such tests was obtained by using the sophisticated simulation analysis method (the numerical shaking table).



(a) Overall Building



(b) Part of base isolation layer

Fig. 11 Perspective View of Detailed FEM Model.

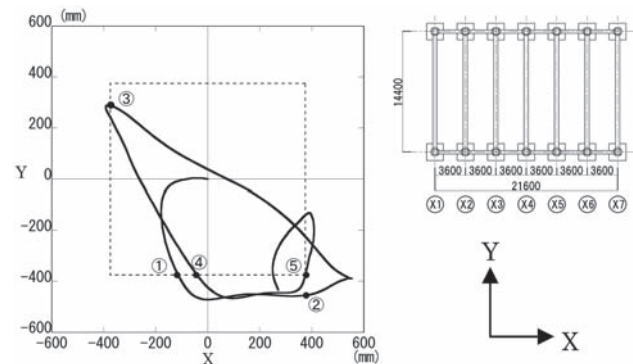
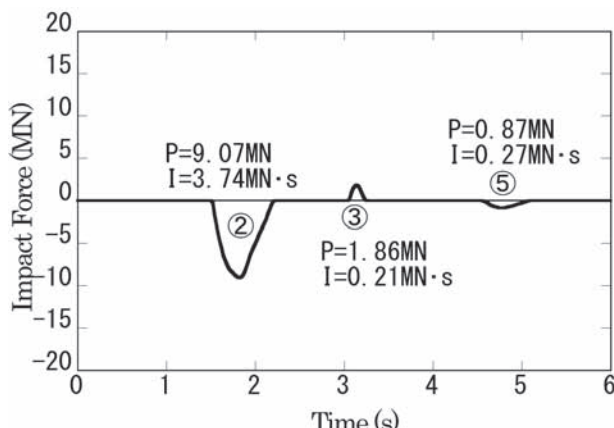
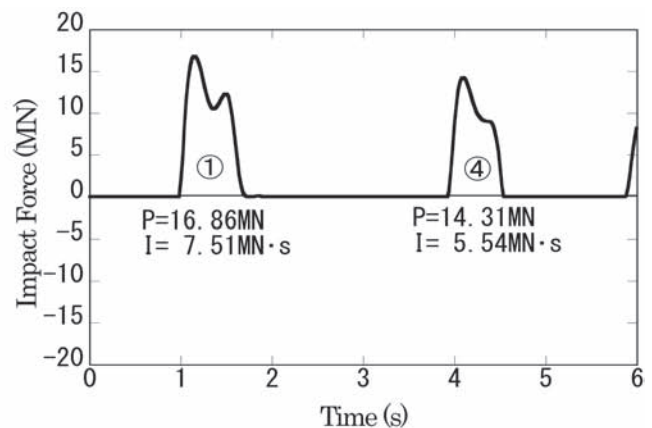


Fig. 12 Orbit of horizontal displacement.



(a) X-direction



(b) Y-direction

Fig. 13 Impact force time history waveform (X, Y-direction).

References

- [1] Yoshiyuki Kasai, et al. "Development of Sophisticated Simulation Analysis Method of Actual Reinforced Concrete Building by Shaking Table Test-I", Annual Report of the Earth Simulator Center, April 2010-March 2011, pp. 173-179.
- [2] Shigefumi Takeda, et al. "Application of Impact Analysis Code based on the Explicit Time Integration to the Shaking Table Tests of Full-Scale Six Story RC Building, Part2", Bulletin of Maebashi Institute of Technology, No.14, pp.17-24, March 2011. (in Japanese)
- [3] Shigefumi Takeda, et al. "Simulation Analysis of Shaking Table Tests of Full-Scale Six-Story RC Building using the Earth Simulator", International Symposium on Disaster Simulation & Structural Safety in the Next Generation (DS'11), pp.153-160, September 2011.
- [4] Yoshikazu Kanai, et al. "Analytical Study of Six-Story RC Building Considering Surrounding Soil Using the Earth Simulator", Summaries of Technical Papers of Annual Meeting, Architectural Institute of Japan, Structural Division, 20115, pp.229-230, 2011. (in Japanese)
- [5] Yoshikazu Kanai, et al. "Analytical Study of RC 3-Story Buildings with and without Seismic Strengthening for Shaking Table Test using the Earth Simulator", Summaries of Technical Papers of Annual Meeting, Architectural Institute of Japan, Structural Division, 20116, pp.231-232, 2011. (in Japanese)
- [6] Yoshinori Konno et al. "Seismic Response Analysis of Base-isolated Building Considering Collision with Retaining Wall", International Symposium on Disaster Simulation & Structural Safety in the Next Generation (DS'11), pp.161-168, September 2011.
- [7] Yoshinori Konno et al. "Earthquake Response Analysis of Base-isolated Building Considering Collision with Retaining Wall Using Earth Simulator Part1 Fundamental Characteristics of Collision Vibration", Research Conference of Kanto Branch, Architectural Institute of Japan, pp.253-256, 2012. (in Japanese)
- [8] Yoshinori Konno et al. "Earthquake Response Analysis of Base-isolated Building Considering Collision with Retaining Wall Using Earth Simulator Part2 Effect of Vertical Motion of Earthquake on Collision Vibration", Research Conference of Kanto Branch, Architectural Institute of Japan, pp.257-260, 2012. (in Japanese)

実大鉄筋コンクリート造建物の振動台実験の精密・詳細シミュレーション解析システムの開発 その2

プロジェクト責任者

河西 良幸 前橋工科大学 大学院工学研究科 環境・情報工学専攻

著者

河西 良幸 前橋工科大学 大学院工学研究科 環境・情報工学専攻

坪田 張二 前橋工科大学 大学院工学研究科 建築学専攻

金井 喜一 前橋工科大学 大学院工学研究科 環境・情報工学専攻

金野 剛典 前橋工科大学 大学院工学研究科 建築学専攻

武田 慈史 株式会社 アルテス

丹羽 一邦 株式会社 テラバイト

眞鍋 慶生 株式会社 テラバイト

自動車等の衝突解析に有効性を発揮している陽解法の衝撃解析コードを建物の地震応答解析に応用し、阪神淡路大震災で多発し未解明の鉄筋コンクリート建物の崩壊現象のコンピュータ解析を可能にする研究を行った。本年度は昨年度に引き続き、下記(1)に示すE-ディフェンスで行われた実大6階建て鉄筋コンクリート建物の崩壊に近い現象に至った振動台実験のシミュレーション解析の精度向上とその現象解釈に重要なプッシュオーバー解析(静的漸増解析)を行った。

更に振動台実験により検証を行なった「精密・詳細シミュレーション解析システム」の適用範囲の拡大と精度の検証増加の観点から下記(2)に示す解析を行なった。

- (1) 実大鉄筋コンクリート造6階建建物の振動台実験のシミュレーション解析の精度向上とその現象解釈に重要なプッシュオーバー解析(静的漸増解析)
- (2) 「精密・詳細シミュレーション解析システム」(数値振動台)による各種建物の地震応答解析
 - ① 地盤上の実大鉄筋コンクリート造6階建物の地震応答解析(応用解析)
 - ② 耐震補強有・無の鉄筋コンクリート造3階建物振動台実験のシミュレーション解析
 - ③ 長周期パルス地震に対する免震建物の周辺擁壁との衝突振動解析(応用解析)

上記のような2年間の研究により、鉄筋やコンクリートがあるがままにモデル化した400万要素程度の有限要素による弾塑性地震応答解析が可能となり、数値振動台として各種構造物の実大振動台実験にかかる膨大な費用の軽減と効率化が可能となる目途を得ることができた。

キーワード: 地震応答, 振動台実験, 鉄筋コンクリート骨組, 地球シミュレータ, FEM, 免震, 耐震補強

Evaluations of Fluid Dynamic Forces and Blood Vessel Stresses of an Artery with a Cerebral Aneurysm

Project Representative

Tadashi Tanuma Applied Fluid Dynamics & Energy Machinery Systems, Joint Program Center, Teikyo University

Authors

Tadashi Tanuma Applied Fluid Dynamics & Energy Machinery Systems, Joint Program Center, Teikyo University

Tadayoshi Nakagomi Department of Neurosurgery, Faculty of Medicine, Teikyo University

Hiroshi Okuda Graduate School of Frontier Sciences, The University of Tokyo

Gaku Hashimoto Graduate School of Frontier Sciences, The University of Tokyo

Yoshiko Nagumo Graduate School of Engineering, Tohoku University

Takao Kobayashi Toshiba Information Systems Corporation

Satoru Watanabe Toshiba Information Systems Corporation

Yoshinari Fukui Earth Simulator Center, Japan Agency for Marine-Earth Science and Technology

The enhancement in diagnosis of cerebrovascular disorders and the reduction of mortality caused by these diseases should be contended with much further because the receive rate of medical treatment for cerebrovascular disorders with hospital stays was the highest among all disorders according to the 2008 statistical data by Japan Health, Labor and Welfare Ministry and the woman's mortality of these diseases was the third highest while the man's mortality of these diseases was the fourth highest among all diseases according to the 2009 statistical data by Japan Health, Labor and Welfare Ministry. In our project, we introduced the rupture strength diagram to explain the mechanical root causes of originations, enlargements and the rhexis risks of cerebral aneurysms. Because the blood vessels are composite materials with some viscoelastic living materials, the time axis should be considered. Then we introduced several kind of rupture strength diagrams with the frequency of the heart pulsing motion and some dominant frequencies in the power spectrum of an artery system with a cerebral aneurysm. In this first year report, the result of CFD analysis and structural analysis of an artery with a typical large cerebral aneurysm that was chosen from our 312 cases collected for the current research program.

Keywords: Cerebral Aneurysm, Blood Vessel, Fluid dynamics, Stress Analysis

1. Introduction

The improvement in diagnosis of cerebrovascular disorders and the reduction of mortality caused by these diseases should be contended with much further because the receive rate of medical treatment for cerebrovascular disorders with hospital stays was the highest among all disorders according to the 2008 statistical data by Japan Health, Labor and Welfare Ministry and the woman's mortality of these diseases was the third highest while the man's mortality of these diseases was the fourth highest among all diseases according to the 2009 statistical data by Japan Health, Labor and Welfare Ministry.

There are three effective analytical approaches to investigate the mechanical phenomena of cerebrovascular disorders. The first approach is the fluid dynamical approach to analyze the blood flows through the brain blood vessels with cerebrovascular disorders. The second approach is the structural

dynamical approach to analyze the stresses and strains of the brain blood vessels result from blood pressures, blood flow shear forces and other forces from the surrounding area. And the third approach is the integrated approach that couples the fluid and structural dynamical approaches to study the both dynamics and the reciprocal interferences between the fluid and structural phenomena.

To investigate the originations, enlargements and the rhexis risks of cerebral aneurysms, there were many studies with the fluid dynamic approach and some studies using the structural dynamic and the coupled approaches from 1990's. Yamaguchi et al [1][2] presented the strong correlation between the wall shear stress gradient and the origination site of cerebral aneurysms measuring the wall shear stresses and their gradient with a laser Doppler anemometer in a scale model of anterior communicating artery (ACA). They also reported that there

were periodic vibrations in blood flows through branch artery form an aneurysm. Ujiie et al. [3][5] introduced the aspect ratio (aneurysm depth/neck width, AR) as a parameter of blood flow stagnation in an artery using the similar experiment of blood flow visualizations and their clinical study information. They presented that there was a threshold AR around 1.6 between un-ruptured and ruptured aneurysm and blood flow stagnations in arteries were deeply related with the processes of aneurysm ruptures. They indicated the possibility that the high frequency vibrations occurred around aneurysms stimulate enlargements of aneurysms. Ohshima et al. [4][6][7][8] conducted coupled computer simulations of fluid and structural dynamic analyses to simulate the reciprocal interferences between the blood flows and artery wall motions and deformations using three-dimensional geometry data around artery in the brain observed with a X-ray computed tomography. They presented that the wall shear stresses were affected by the geometry of the branches of the artery and the deformations of the wall. They also conducted simulations of computational fluid dynamics (CFD) on twenty cases of un-ruptured and ruptured aneurysms in the middle cerebral artery (MCA) and evaluated the correlation between the wall shear stresses and the AR. The Department of Neurosurgery of Teikyo University had joined these CFD studies. Funazaki et al. [9][10] conducted coupled computer simulations of fluid and structural dynamic analyses to simulate the Mises stress distributions of the artery walls around un-ruptured aneurysms at two artery branches. Recently, Harada et al. [11] and Murayama et al. [12] presented that the pressure or energy losses of blood flows through aneurysms can be used as a parameter to explain the differences of the blood flows between un-ruptured and ruptured aneurysms statistically.

As explained above, existent studies have demonstrated the relationship between the blood flow phenomena around aneurysms and the originations, enlargements and the rhexises of cerebral aneurysms successfully. However, the approaches that can be used by medical doctors in clinical practices should be developed for the next step.

In general, the rupture strengths of elastic materials are able to be depicted as two dimensional envelope diagrams with steady stress and unsteady stress as the abscissa and vertical axis respectively. In our current study, we introduced this rupture strength diagram to explain the mechanical root causes of originations, enlargements and the rhexis risks of cerebral aneurysms. However the blood vessels are composite materials with some viscoelastic living materials, the time axis should be considered. Then we introduced several kind of rupture strength diagrams with the frequency of the heart pulsing motion and some dominant frequencies in the power spectrum of an artery system with a cerebral aneurysm.

In this first year report, the result of CFD analysis and structural analysis of an artery with a typical large cerebral aneurysm that was chosen from our 312 cases collected for the

current research program.

2. Three dimensional geometrical modeling from medical image data

For the current program, we have collected 312 cases with Magnetic Resonance Imaging (MRI) and X-ray computed tomography (CT) data that were diagnosed and treated in recent a couple of years. One case of typical large cerebral aneurysm was chosen for the first CFD and finite element analysis (FEA) to evaluate actual fluid dynamic forces and blood vessel stresses of an artery with a cerebral aneurysm. While both MRI and X-ray CT data can be used for the geometrical modeling, MRI data was used for the current study because we needed to estimate the wall thickness of an aneurysm and blood vessels.

Figure 1 shows a MRI slice close-up image near the top of a cerebral arterial aneurysm that was chosen for the first CFD and finite element analysis (FEA). Figure 2 shows MRI slice image near at the center height of the same cerebral arterial aneurysm. The top sides of Figs. 1, 2 are the face sides. The cut sections of the aneurysm can be seen around the center of the both figures. The actual maximum diameter of this aneurysm is around 20 mm. This size is larger than the average size of cerebral aneurysms. Some cut sections of artery can be seen around the aneurysm near the bottom sides of these figures. The aneurysm wall actual thickness was measured as 0.6 mm at the back left side of Fig. 2. However, there was very thin wall region that was

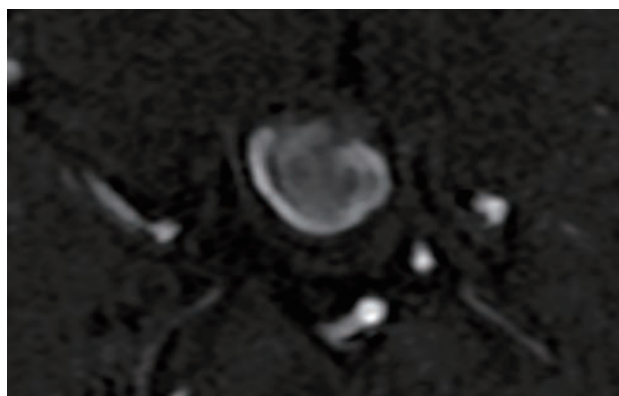


Fig. 1 MRI slice image near the top of a cerebral arterial aneurysm.

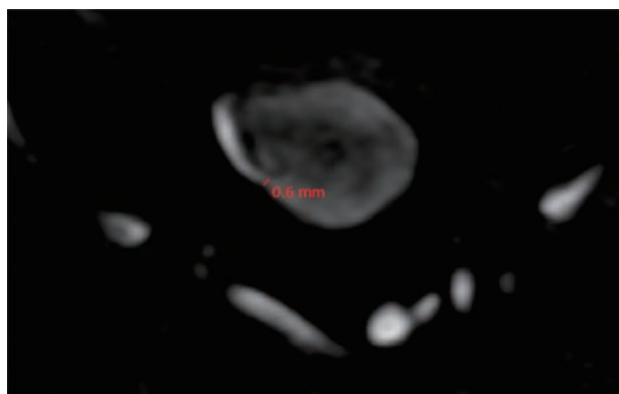


Fig. 2 MRI slice image near the center height of a cerebral arterial aneurysm.

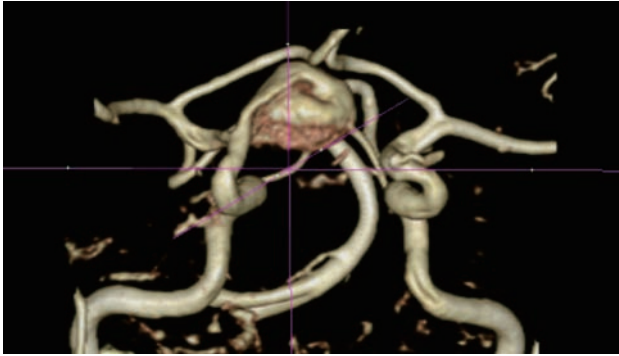


Fig. 3 Volume data around a cerebral arterial aneurysm.

difficult to be measured near the face side, we assumed the wall thickness as 0.3 mm for the FEA.

After removing the image of cranial bones and surrounding tissues, the range of MRI values for blood flows and walls of aneurysm and artery was searched using a three dimensional boxel data visualization and edit software (INTAGE Volume Editor, CYBERNET SYSTEMS Corp.). Figure 3 shows volume data around a cerebral arterial aneurysm extracted using this information of the range of MRI values for blood flows and walls of aneurysm and artery from the original boxel data as the format of Digital Imaging and Communications in Medicine (DICOM).

3. Fluid dynamic analysis

The stereo lithography (STL) geometry data was generated from the volume data of this artery with a cerebral aneurysm.



Fig. 4 Streamlines & velocity contours of blood flow.

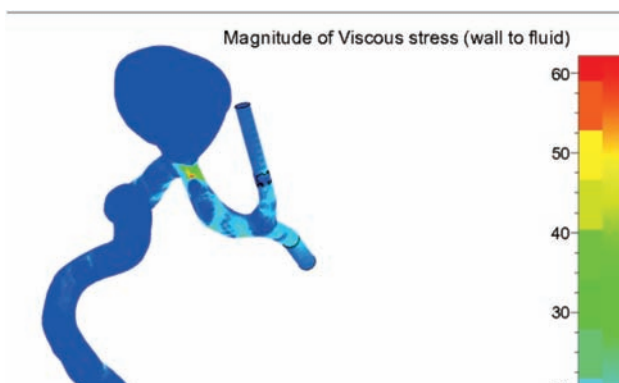


Fig. 5 Viscous stress contours on the wall.

The computational mesh for the fluid dynamic analysis was generated from this STL data using the mesh generation software (FINE/Open, NUMECA Corporation).

The results of fluid dynamic analysis are shown in Figs. 4 and 5. Figure 4 shows streamlines and velocity contours of blood flow in the aneurysm and the artery. A low speed vortex flow was generated inside the aneurysm and the maximum velocity (around 1m/s) is generated in the artery near the outlet of the aneurysm. Figure 5 shows viscous stress contours on the wall. The maximum viscous stress occurs on the inner wall of the artery at the maximum velocity section stated above.

4. Structural analysis

Structural analysis was conducted using the FEA software, FrontISTR [13]. The computational mesh for FEA was generated from the same STL geometry data that was used for the CFD mesh considering the blood vessel thickness. Figure 6 shows the volume data around a cerebral aneurysm including blood vessel wall for FEA. Because the deep concave geometry on the surface of the aneurysm was due to the incompleteness of the automatic data translation process from voxel data to STL data, the concave geometry was modified manually. The yellow color surface was modified manually in Fig. 6. Figure 7 shows the FEA computational mesh of the artery with a cerebral aneurysm.

As the boundary conditions, inlet and outlet ends of artery were supported simply, inside of the artery and the aneurysm was pressurized with 100 mmHg steady blood pressure while outside was pressurized with 100 mmAq steady brain pressure.

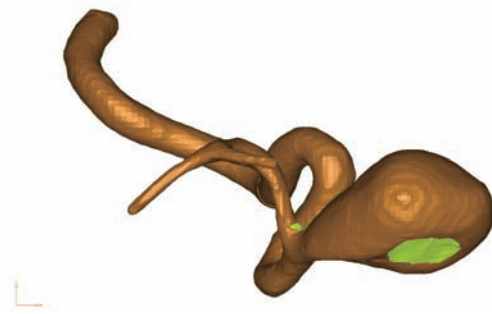


Fig. 6 Volume data around a cerebral arterial aneurysm including blood vessel wall for FEA.



Fig. 7 FEA computational mesh of the artery with a cerebral aneurysm.

The calculation results are shown in Figs. 8 and 9. Figure 8 shows the calculated stress contours on the wall of artery and the aneurysm. Maximum stress was found on the aneurysm wall and this maximum stress was roughly five times of the average stress in the normal artery. Figure 9 shows the calculated stress contours on the inside and outside of the cerebral arterial aneurysm (cut view). Since the large stress occurs at the bottom

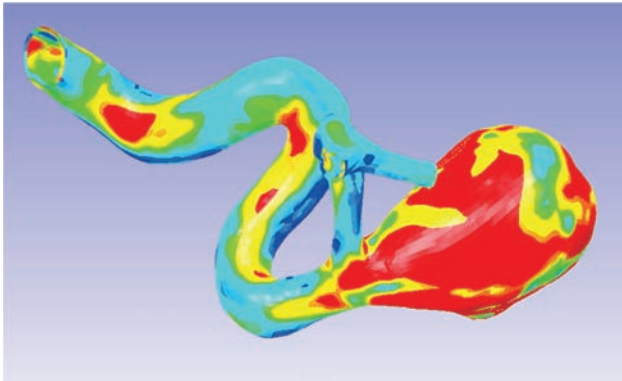


Fig. 8 Stress contours on the wall.

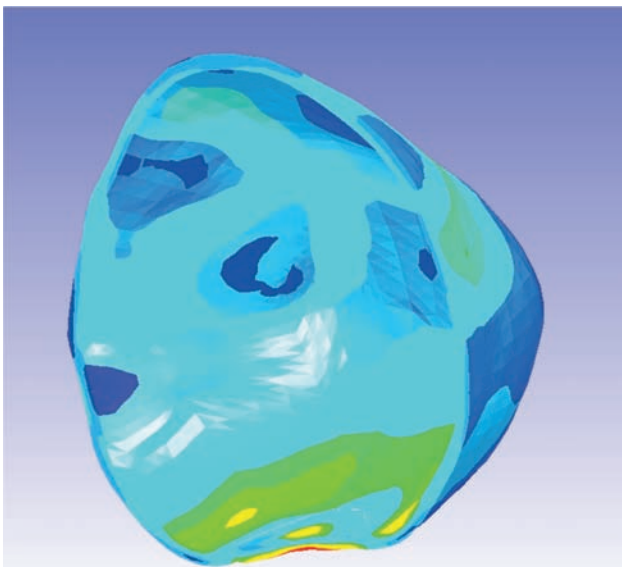


Fig. 9 Stress contours on the inside and outside of the cerebral arterial aneurysm (cut view).

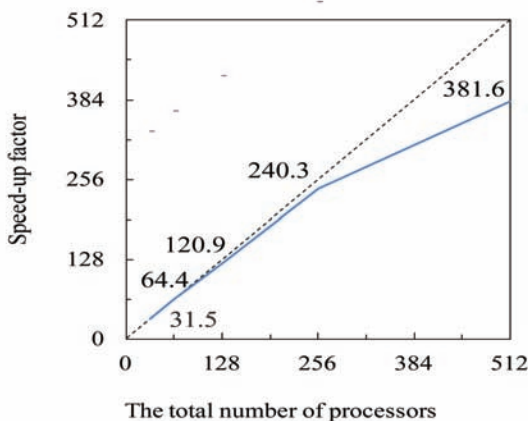


Fig. 10 The relationship between the total number of processors and the speed-up factor of the Earth Simulator.

of the concave geometry, the measurement accuracy of the aneurysm geometry is important.

The FEA software FrontISTR was optimized on the Earth Simulator to be used faster and efficiently. Figure 10 shows the relationship between the total number of processors and the speed-up factor measured on the Earth Simulator using a 100 million mesh for our benchmarking.

5. Conclusions

The calculated maximum stress on the aneurysm was roughly five times of the average stress in the normal artery while the maximum viscous stress is very small (less than 100 Pa). The maximum stress on the aneurysm was less than a published aneurysm strength data. However, if we would consider more high blood pressure case or actual pulsing blood pressure, the maximum stress would be increased near the similar level that might cause some damage on the aneurysm wall.

The result of first year study of our Earth Simulator Project shows that the steady structural analysis brings important information concerning the risk of aneurysm ruptures in case of large size cerebral aneurysms.

For the second year research program, we are planning to start the integrated approach that couples the fluid and structural dynamical analysis to study the both dynamics and the reciprocal interferences between the fluid and structural phenomena. This coupled analysis study will bring more accurate information on the risk of cerebral aneurysm ruptures even in cases of small size aneurysms.

Acknowledgment

We appreciate JAMSTEC for giving us a opportunity to use the Earth Simulator for our study of cerebral aneurysms and we also wish to acknowledge their kind support for our optimization study of FrontISTR on the Earth Simulator.

References

- [1] T. Yamaguchi et al., Bulletin of JSME series B, Vol.63, pp.2335-2340, 1997.
- [2] T. Yamaguchi, Performance report of Grant-in-Aid for Scientific Research Japan, 1999.
- [3] H. Ujiie, Journal of Japanese Society of Biorheology, Vol 15, 1, 2001.
- [4] M. Oshima, Nagare, Vol.21, pp.122-128, 2002.
- [5] H. Ujiie, Surgery for Cerebral Stroke, Vol.32, pp.351-355, 2004.
- [6] R. Torii et al., Bulletin of JSME series A, Vol.70, 697, pp.1224-1231, 2004-9.
- [7] M. Oshima et al., Bulletin of JSME series A, Vol.70, 697, pp.1240-1246, 2004-9.
- [8] M. Shojima et al., Stroke, pp.2500-2505, November 2004.
- [9] K. Funazaki et al., Bulletin of JSME series B, Vol.72, 713, pp.1-8, 2006-12.

- [10] K. Funazaki et al., Bulletin of JSME series B, Vol.73, 731, pp.1472-1479, 2007-03.
- [11] T. Harada et al., Proceedings of JSME Bioengineering Conference, pp.88-89, 2007.
- [12] Y. Murayama et al., 2010 International Stroke Conference Poster Presentations, e265, pp.42, 2010.
- [13] H. Okuda, Parallel Computing Finite Element Analysis using FrontSTR, Baifu-kan, 2008. (in Japanese)

脳動脈瘤を含む血管系の流体力と応力の評価

プロジェクト責任者

田沼 唯士 帝京大学 ジョイントプログラムセンター

著者

田沼 唯士 帝京大学 ジョイントプログラムセンター

中込 忠好 帝京大学 医学部脳神経外科学講座

奥田 洋司 東京大学 大学院新領域創成科学研究科人間環境学専攻
マルチシナリオシミュレーション環境学分野

橋本 学 東京大学 大学院新領域創成科学研究科人間環境学専攻
マルチシナリオシミュレーション環境学分野

南雲 佳子 東北大学 大学院工学研究科ナノメカニクス専攻

小林 孝雄 東芝インフォメーションシステムズ株式会社

渡邊 論 東芝インフォメーションシステムズ株式会社

福井 義成 海洋研究開発機構 地球シミュレータセンター

本プロジェクトの目標は、精度の高い流体解析と構造解析、及び流体構造連成解析を行って、脳動脈瘤の発生、増大、破裂のプロセスを力学的に明らかにして、医師が臨床の場で活用できる解析法及び解析法の結果を用いて脳動脈瘤の破裂または出血のリスクを予測する方法を確立することである。

脳血管疾患を含む血管系疾患に関しては、血管内を流れる血流に対する流体力学的なアプローチと血管に作用する血流の圧力とせん断力及び血管を取り囲む周辺部位からの力学的影響を評価する構造力学的アプローチ、そして流体解析と構造解析を連成して、双方の作用が相互に及ぼす影響を含めて評価する統合的なアプローチが有効と考えられ、これまで国内及び国外において数多くの研究がなされてきた。これまでの研究によって脳動脈瘤周辺の流動と脳動脈瘤の発生、増大、破裂との関連が明らかにされつつあり、次のステップとして医師が臨床の場で実際に利用できるアプローチが必要とされている。

一般に弾性材料の変形と破壊は部材にかかる定常応力を横軸、非定常応力を縦軸とした2次元グラフ中の領域で示すことができる。血管は一般的には粘弾性体としてモデル化することが適切と考えられているが、私達のグループでは、単純に時間軸を追加する方法に加えて、非定常応力の power spectrum 中の卓越する複数の周波数帯において前述した定常、非定常応力の2次元グラフ上で変形及び破断のリスクが高い領域を可視化する方法を目指している。

初年度の定常解析で計算された大型動脈瘤の最大主応力は推定される血管壁の引張強度より小さいが、渦流などの非定常成分を含む流体力と相乗することで血管壁に損傷を与えるオーダーであると考えられる。引き続き、小型動脈瘤も含めて、相乗効果を考慮した流体構造連成解析を行い、臨床的なリスク予測が可能な解析法の検討を行う。

キーワード:脳動脈瘤, 血管, 流体解析, 構造解析

Large-Scale Electronic-State Calculations of Protein-Ligand Systems for Drug Design with Fragment Molecular Orbital Method

Project Representative

Shigenori Tanaka

Graduate School of System Informatics, Kobe University

Authors

Shigenori Tanaka

Graduate School of System Informatics, Kobe University

Yuji Mochizuki

Faculty of Science, Rikkyo University

Katsumi Yamashita

NEC Soft Ltd.

Chiduru Watanabe

Institute of Industrial Science, The University of Tokyo

Yoshio Okiyama

Institute of Industrial Science, The University of Tokyo

Kaori Fukuzawa

Mizuho Information and Research Institute Inc.

Tatsuya Nakano

National Institute of Health Sciences

Large-scale fragment molecular orbital (FMO) calculations for protein systems were performed on the Earth Simulator. The four-body corrected fragment molecular orbital (FMO4) method was recently developed and implemented at the second-order Møller-Plesset perturbation (MP2) level. A series of accuracy tests relative to the previous two-body (FMO2) and three-body (FMO3) treatments were carried out. As expected, FMO4 provided better results of total energies in comparison with the reference values by conventional molecular orbital calculations. A nonconventional fragmentation by discriminating the main and side chains in amino acid residues was then examined for a large complex of HIV-1 protease (total 198 residues) with lopinavir, where the four-body corrections were shown to be substantial.

Keywords: FMO (fragment molecular orbital) method, MP (Møller-Plesset) perturbation theory, Four-body correction, HIV-1 protease

1. Introduction

The fragment molecular orbital (FMO) scheme [1-3] enables one to perform fully quantum-mechanical calculations for large-scale molecular systems like proteins at affordable cost of computations with parallelism. It is recognized that the FMO2 scheme [1-3] in which the fragments up to the dimers are taken into account provides reasonable accuracy in energy calculations such as that for interaction energy analyses to describe the details of protein-ligand docking in the pharmacophore [2, 3]. However, the inclusion of three-body terms (FMO3) is desirable to ensure the total reliability in some cases, e.g., hydrogen-bonded water clusters [2-4]. Fedorov and Kitaura thus developed the three-body corrected FMO scheme at the levels of Hartree-Fock (HF) approximation (FMO3-HF) [5, 6] and second-order Møller-Plesset perturbation (MP2) theory (FMO3-MP2) [7] on the GAMESS-US package. Recently, Katouda [8] provided an alternative FMO3-MP2 scheme with the technique of resolution-of-identity approximation of integrals in the GAMESS-US. On the other hand, with the ABINIT-MPX package, Fujita et al. [9] examined the importance of three-body contributions and

also the matching with several approximations in the FMO3-HF energy for the hydration of a sodium ion. Both FMO3-MP2 energy and gradient were then implemented with an efficient integral-direct parallelism [10].

Here, we report the development of four-body FMO (FMO4) calculations of HF and MP2, that is, FMO4-HF and FMO4-MP2, on the ABINIT-MPX package [11]. The four-body corrections were already proposed and tested in the literature [12-15]. These references showed certain improvements by the four-body treatment over the three-body one, in particular for the calculations of solids [12, 14]. The present motivation to develop the FMO4 method arises from the interest in more detailed modeling for the fragment-based drug discovery or design (FBDD) [16, 17]. In FBDD, it is highly desirable that various functional groups of ligands are divided as the respective fragments and also that the main and side chains of amino acid residues in proteins are segmented correspondingly. Such a way of fragmentation is of nonconventional type in earlier FMO calculations [1-3], while its importance has been recognized [18]. A large complex of HIV-1 protease and lopinavir (previously

employed in Ref. [19]) is calculated with 1024 processors of the Earth Simulator (ES2) as a currently available platform of massively parallelized computation.

2. Methods

In the original scheme of FMO method [1], the FMO2-HF energy ("HF" is omitted here for simplicity) is given by the energies of fragment monomers and dimers:

$$E^{\text{FMO2}} = \sum_{I>J} E_{IJ} - (N-2) \sum_I E_I = \sum_{I>J} \Delta E_{IJ} + \sum_I E_I \quad (1)$$

$$\Delta E_{IJ} \equiv E_{IJ} - E_I - E_J \quad (2)$$

where N is the number of fragments in a given system and IJ are the fragment dimer indices. The HF calculation for each monomer is carried out under the presence of environmental electrostatic potential (ESP) which is a key point of the FMO scheme [2-4]. The fragment indices are distributed over the groups of processors (upper level), and the Fock matrix constructions are then parallelized with respect to the indices of atomic orbital (AO) within an assigned group (lower level). This dual parallelization accelerates the computations significantly [2-4]. For further acceleration, Nakano et al. [20] devised a couple of approximations to evaluate the ESP matrix elements based on the Mulliken AO charge (ESP-AOC) and the Mulliken point charge (ESP-PTC).

The FMO3-HF energy formula [5, 6, 9] as

$$\begin{aligned} E^{\text{FMO3}} &= \sum_{I>J>K} E_{IJK} - (N-3) \sum_{I>J} E_{IJ} + \frac{(N-2)(N-3)}{2} \sum_I E_I \\ &= \sum_{I>J>K} [\Delta E_{IJK} - \Delta E_{IJ} - \Delta E_{IK} - \Delta E_{JK}] \\ &\quad + \sum_{I>J} \Delta E_{IJ} + \sum_I E_I \end{aligned} \quad (3)$$

$$\Delta E_{IJK} \equiv E_{IJK} - E_I - E_J - E_K \quad (4)$$

may be regarded as a next-order form of many-body expansion [21] and has been used widely to improve the numerical accuracy of total energies [4]. In FMO3, a trimer is specified by IJK , and the parallelized HF calculations are carried out when three composite monomers are adjacent within a threshold of van der Waals contact [9]. Care should be taken for the application of ESP approximations [20] to the FMO3-HF calculations, as addressed in Refs. [6, 9]. The FMO3-MP2 correction [7, 8, 10] may then be considered for the HF-calculated trimers. Fedorov et al. [5, 6] found that the accuracy of FMO3-HF with single-residue fragmentation is better than that of FMO2-HF with double-residue fragmentation for model Ala-polymers, illuminating the importance of explicit three-body corrections. The following literature [7] reported the corresponding MP2 results.

The formulas for the four-body corrections were presented in Ref. [14] for the modeling of solid systems and also in Ref. [15] for proteins. The form of FMO4-HF energy is essentially the same as that of many-body expansion series:

$$\begin{aligned} E^{\text{FMO4}} &= \sum_{I>J>K>L} E_{IJKL} - (N-4) \sum_{I>J>K} E_{IJK} + \frac{(N-3)(N-4)}{2} \sum_{I>J} E_{IJ} \\ &\quad - \frac{(N-2)(N-3)(N-4)}{6} \sum_I E_I \\ &= \sum_{I>J>K>L} \{ \Delta E_{IJKL} - \Delta E_{IJ} - \Delta E_{IK} - \Delta E_{IL} - \Delta E_{JK} - \Delta E_{JL} - \Delta E_{KL} \\ &\quad - [\Delta E_{IJK} - \Delta E_{IJ} - \Delta E_{IK} - \Delta E_{JK}] - [\Delta E_{IJL} - \Delta E_{IJ} - \Delta E_{JL} - \Delta E_{IL}] \\ &\quad - [\Delta E_{IKL} - \Delta E_{IK} - \Delta E_{IL} - \Delta E_{KL}] - [\Delta E_{JKL} - \Delta E_{JK} - \Delta E_{JL} - \Delta E_{KL}] \} \\ &\quad + \sum_{I>J>K} [\Delta E_{IJK} - \Delta E_{IJ} - \Delta E_{IK} - \Delta E_{JK}] \\ &\quad + \sum_{I>J} \Delta E_{IJ} + \sum_I E_I \end{aligned} \quad (5)$$

$$\Delta E_{IJKL} \equiv E_{IJKL} - E_I - E_J - E_K - E_L \quad (6)$$

where the actual tetramer HF calculation is performed similarly to the trimer case. Ref. [15] showed that the tetramer corrections improve the total energy of Leu1-zervamicin at the HF/STO-3G level. The minimal set of STO-3G basis should, however, be too small to conclusively assess the accuracy, and further testing with at least double-zeta (DZ) quality basis (e.g., 6-31G) would be necessary at the correlated level. The four-body MP2 corrections are then taken into account straightforwardly.

Employing the DZ or DZ-plus-polarization (DZP) basis sets, the size of fragment tetramer would be demanding for the FMO calculations of real proteins potentially containing twenty variations of amino acid residues from the smallest Gly to the largest Trp, unless an alternative protocol to the conventional single-residue fragmentation is taken. As addressed above, the segmentation of main and side chains in amino acid residues (or the bond cutting at both C_α and C_β atoms) is rather essential for FBDD [16, 17], and it may be beneficial to make the FMO4 calculations tractable. Nonetheless, the increased number of fragments with this new fragmentation is an alternative factor to enlarge the gross computational cost covering up to tetramers. The use of massively parallel computers is thus encouraged to reduce the computation time in large-scale applications of FMO4-MP2.

3. Results

The FMO4 method was implemented in a recent version of ABINIT-MPX with the vectorizable HF and MP2 modules (under MPI control) of Ref. [22]. The frozen-core restriction was imposed at the MP2 stage throughout. As a test case, the HIV-1 protease-lopinavir complex was calculated at the FMO4-MP2/6-31G level, by using 1024 processors of ES2. This model was the same one as that employed in Ref. [19]. The number of amino acid residues of HIV-1 protease was 198 (99 of each subunit). The number of fragments by the main/side chain fragmentation was 358, where no Cys-Cys bridge was contained. The lopinavir ligand was divided into 4 fragments,

and a water molecule crucial in the hydrogen-bond network was also included in the pharmacophore. The numbers of atoms, fragments and 6-31G basis AOs were thus 3225, 363 (203 in the conventional fragmentation) and 17423, respectively. The number of used nodes of ES2 was 128, and each node consisted of 8 vector processors (102.4 GFLOPS per processor) with 128 GB shared memory. The fragments from monomers to tetramers were processed in a single node throughout. The ESP-AOC approximation [20] (in which the two-electron integrals were computed, unlike the classical approximation of ESP-PTC with Mulliken charges) was adopted for this protease complex.

The HF and MP2-corrected energies of the HIV-1 protease complex are given in Table 1 (upper part). The FMO4 results are used as a tentative reference since the regular MO calculations of this sized molecule were impossible with the ABINIT-MPX program; we regard the energy with conventional main-chain fragmentation as the best effort value. An unacceptable difference is found for the FMO2 results with the main/side chain fragmentation, which implies that at least FMO3 expansion is required for reliable analyses (even for the inter-fragment interaction energy (IFIE) [23, 24]).

The breakdown timings are tabulated in the lower part of Table 1. Let us recall here that the monomer-stage calculation requires the achievement of SCC (self-consistent charge) condition [2-4]. This is the reason why its computational time is longer than that of the dimer stage for both fragmentations. It is notable that the incremental cost of MP2 over HF is maintained quite small for the calculations of monomers and dimers [22]. The MP2 calculations for trimers and tetramers show sizable increases in the computational time over the HF

calculations, leading to the incremental cost factor relative to FMO2 (about ten times for FMO4). Comparison in timings between two fragmentations indicates that the tetramer part governs the slightly increased cost of FMO4 calculation with the nonconventional fragmentation of main/side chains. The FMO4-MP2/6-31G job was actually completed in 1.4 hours (to be compared with 1.2 hours of the conventional case). If massively parallel computing resources such as the current ES2 or the K-computer are available, the FMO4 calculations (with much long task list of up to fragment tetramers) can be carried out for real proteins, in short time without the ESP-PTC approximation which has a vulnerability of the Mulliken partitioning of charges [20]. In addition, the computational time can be reduced with the use of the Cholesky decomposition technique [25], as seen in Fig. 1.

Although we here refrain from the presentation of IFIE results of this complex [24], the enhanced resolution of analyses matches with the FBDD scheme including the lead search and optimization [16, 17]. We hope that the FMO4 method will become a useful tool to accelerate drug discovery and design. Manifestly, several efforts are necessary to improve the speed and reliability of FMO calculations. The introduction of the fast multipole method to evaluate the ESP elements is a plausible option in this regard.

In this report, we have addressed the development of the four-body FMO (FMO4) scheme [11]. Test calculations were systematically carried out at the HF and MP2 levels in comparison with the reference energies of regular MO calculations. It was confirmed that the FMO4 method is better in the accuracy of energy than the FMO3 method by one-order

Table 1 Total energies and timings of FMO calculations for HIV-1 protease - lopinavir complex.

Total energy	Main/side frg.	(total 363)	Main frg.	(total 203)
(au)	HF	MP2	HF	MP2
FMO2	-77554.2779	-77709.0268	-77589.3751	-77744.7417
Diff.(4) ^a	35.4754	36.1544	0.3059	0.3737
FMO3	-77590.0557	-77745.5971	-77589.6024	-77745.0359
Diff.(4) ^a	-0.3024	-0.4159	0.0786	0.0796
FMO4	-77589.7533	-77745.1812	-77589.6810	-77745.1155
Diff.(M) ^b	-0.0723	-0.0657		
Timing ^c				
(sec)				
Monomer	356.0	359.2	252.0	253.1
Dimer	120.8	141.2	131.7	175.3
Trimer	765.3	1040.1	648.2	1110.0
Tetramer	2352.3	3374.4	1358.2	2663.2
Total	3594.4	4914.9	2390.1	4201.6

^a Relative to the corresponding FMO4 energy.

^b Relative to the FMO4 energy with conventional fragmentation in main chains (as the best effort value).

^c Breakdown timing analysis of the FMO4 jobs with 1024 processors of ES2.

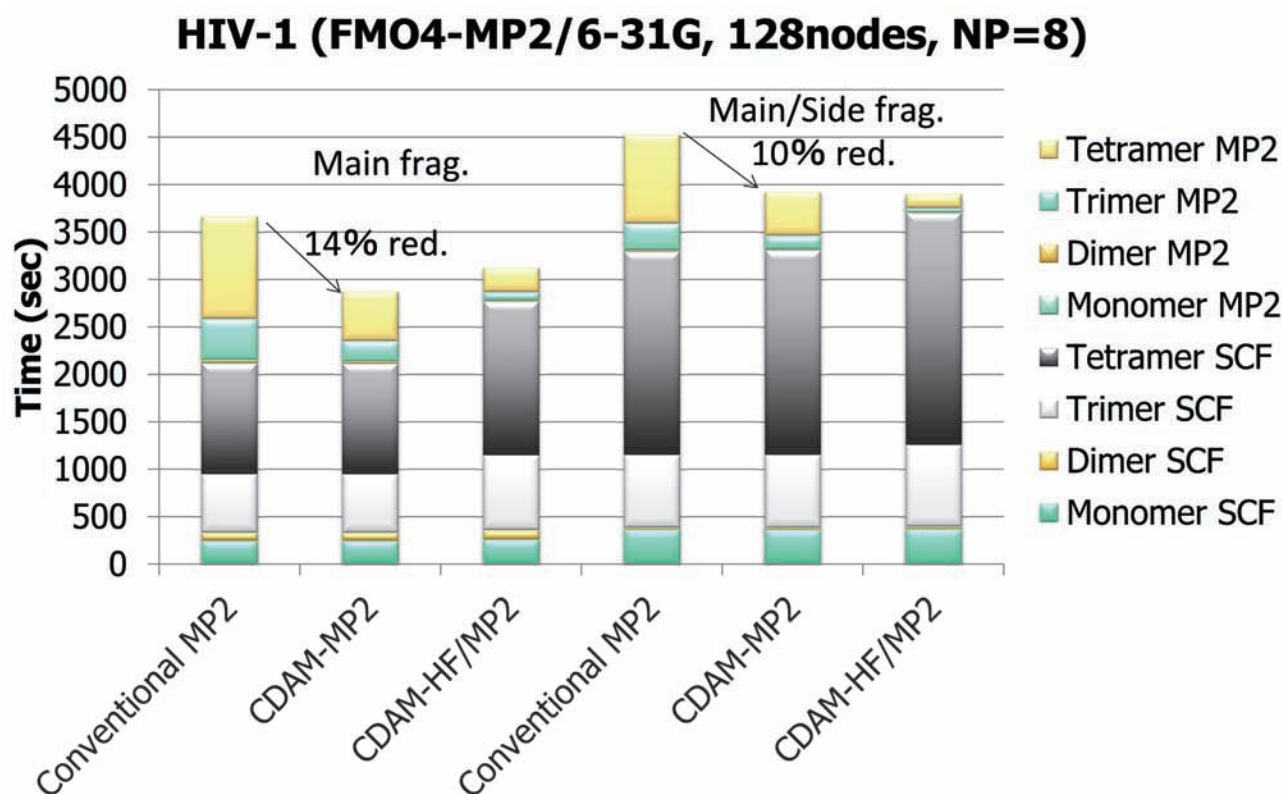


Fig. 1 Breakdown timing data for FMO4-MP2/6-31G calculations of HIV-1 protease complex. The computational times on ES2 with and without the CDAM (Cholesky decomposition with adaptive metric) [25] are compared in both the cases of main chain and main/side chain fragmentations.

or more. Particularly, FMO4 worked well for a nonconventional fragmentation procedure of peptides in which the main and side chains of amino acid residues were segmented. The HIV-1 protease - lopinavir complex as a practical example was calculated at the FMO4-MP2/6-31G level, by using ES2. The incremental cost of FMO4 relative to FMO2 was observed to be about ten times for this archetypical example of protein-ligand complex, while it would be justified by considering the utility of FMO4 in fragment-based drug discovery and design (FBDD) [16, 17]. The use of massively parallel computers is recommended for FMO4 calculations. Work to perform extensive IFIE analyses [2-4, 23] is underway for the HIV-1 protease complex as well as the estrogen receptor complex in the FBDD context [24]. Considering the recent developments of linear-scaling methods, the FMO scheme should be improved to provide better total energies for future benchmark comparisons. The FMO4 method is a promising approach in this direction.

Acknowledgements

This work was supported by the RISS project at the Institute of Industrial Science (IIS) of the University of Tokyo. YM and KF acknowledge the SFR-aid by Rikkyo University.

References

- [1] K. Kitaura, E. Ikeo, T. Asada, T. Nakano, and M. Uebayasi, *Chem. Phys. Lett.* 313 (1999) 701.
- [2] D. G. Fedorov and K. Kitaura, *J. Phys. Chem. A* 111 (2007) 6904.
- [3] D. G. Fedorov and K. Kitaura, ed., *The Fragment Molecular Orbital Method: Practical Applications to Large Molecular Systems*, CRC Press, Boca Raton, 2009.
- [4] M. S. Gordon, D. G. Fedorov, S. R. Pruitt, and L. V. Slipchenko, *Chem. Rev.* 112 (2012) 632.
- [5] D. G. Fedorov and K. Kitaura, *J. Chem. Phys.* 120 (2004) 6832.
- [6] D. G. Fedorov and K. Kitaura, *Chem. Phys. Lett.* 433 (2006) 182.
- [7] D. G. Fedorov, K. Ishimura, K. Ishida, K. Kitaura, P. Pulay, and S. Nagase, *J. Comp. Chem.* 28 (2007) 1476.
- [8] M. Katouda, *Theor. Chem. Acc.* 130 (2011) 449.
- [9] T. Fujita, K. Fukuzawa, Y. Mochizuki, T. Nakano, and S. Tanaka, *Chem. Phys. Lett.* 478 (2009) 295.
- [10] Y. Mochizuki, T. Nakano, Y. Komeiji, K. Yamashita, Y. Okiyama, H. Yoshikawa, and H. Yamataka, *Chem. Phys. Lett.* 504 (2011) 95.
- [11] T. Nakano, Y. Mochizuki, K. Yamashita, C. Watanabe, K. Fukuzawa, K. Segawa, Y. Okiyama, T. Tsukamoto, and S. Tanaka, *Chem. Phys. Lett.* 523 (2012) 128.
- [12] B. Paulus, P. Fulde, and H. Stoll, *Phys. Rev. B* 51 (1995) 10572.
- [13] J. Friedrich, M. Hanrath, and M. Dolg, *J. Chem. Phys.* 126 (2007) 154110.
- [14] H. M. Netzloff and M. A. Collins, *J. Chem. Phys.* 127 (2007) 134113.

- [15] L. Huang, L. Massa, and J. Karle, *Proc. Nat. Acad. Sc.* 105 (2008) 1849.
- [16] R. Law, O. Barker, J. J. Barker, T. Hestekamp, R. Godemann, O. Andersen, T. Fryatt, S. Courtney, D. Hallett, and M. Whittaker, *J Comp. Aided Mol. Des.* 23 (2009) 459.
- [17] M. Whittaker, R. J. Law, O. Ichihara, T. Hestekamp, and D. Hallett, *Drug Discov. Today* 7 (2010) e163.
- [18] A. Yoshioka, K. Takematsu, I. Kurisaki, K. Fukuzawa, Y. Mochizuki, T. Nakano, E. Nobusawa, K. Nakajima, and S. Tanaka, *Theor. Chem. Acc.* 130 (2011) 1197.
- [19] Y. Mochizuki, S. Koikegami, T. Nakano, S. Amari, and K. Kitaura, *Chem. Phys. Lett.* 396 (2004) 473.
- [20] T. Nakano, T. Kaminuma, T. Sato, K. Fukuzawa, Y. Akiyama, M. Uebayasi, and K. Kitaura, *Chem. Phys. Lett.* 351 (2002) 475.
- [21] H. Stoll, *Chem. Phys. Lett.* 191 (1992) 548.
- [22] Y. Mochizuki, K. Yamashita, T. Murase, T. Nakano, K. Fukuzawa, K. Takematsu, H. Watanabe, and S. Tanaka, *Chem. Phys. Lett.* 457 (2008) 396.
- [23] S. Amari, M. Aizawa, J. Zhang, K. Fukuzawa, Y. Mochizuki, I. Iwasawa, K. Nakata, H. Chuman, and T. Nakano, *J. Chem. Inf. Model.* 46 (2006) 221.
- [24] C. Watanabe, K. Fukuzawa, K. Yamashita, Y. Okiyama, T. Tsukamoto, T. Murase, Y. Mochizuki, S. Tanaka, and T. Nakano, in preparation.
- [25] Y. Okiyama, T. Nakano, K. Yamashita, Y. Mochizuki, N. Taguchi, and S. Tanaka, *Chem. Phys. Lett.* 490 (2010) 84.

フラグメント分子軌道法による薬剤設計のためのタンパク質 - リガンド系に対する大規模電子状態計算

プロジェクト責任者

田中 成典 神戸大学 大学院システム情報学研究科

著者

田中 成典 神戸大学 大学院システム情報学研究科

望月 祐志 立教大学 理学部化学科

山下 勝美 NEC ソフト ニューソリューション事業部

渡邊 千鶴 東京大学 生産技術研究所

沖山 佳生 東京大学 生産技術研究所

福澤 薫 みずほ情報総研 サイエンスソリューション部

中野 達也 国立医薬品食品衛生研究所 医薬安全科学部

フラグメント分子軌道 (Fragment Molecular Orbital; FMO) 法に基づき、タンパク質とリガンド分子結合系の大規模電子状態計算を地球シミュレータ (ES2) を用いて行った。フラグメントの4体項までを考慮する FMO4 法が最近開発され、Møller-Plesset の2次摂動 (MP2) レベルでの計算が ABINIT-MPX プログラムに実装されている。従来までの FMO2 および FMO3 法による計算と比較したところ、エネルギー精度の顕著な改善が見られた。例として、198 残基の HIV-1 プロテアーゼとロピナビルの複合体を用い、従来のアミノ酸主鎖分割に加えて、主鎖・側鎖分割、さらにはリガンド分子の分割を試みたところ、FMO4 法を用いることで、計算精度を落とすことなく以前より細かいフラグメント分割が可能となることが判明した。今後、FMO4 法を用いた超並列計算が Fragment Based Drug Design などによる合理的薬剤設計の重要なツールとなることが期待される。

キーワード: フラグメント分子軌道法, メラー・プレセット摂動法, 4体フラグメント補正, HIVプロテアーゼ

Development of the Next-generation Computational Fracture Mechanics Simulator for Constructing Safe and Sustainable Society

Project Representative

Ryuji Shioya Faculty of Information Sciences and Arts, Toyo University

Authors

Kaworu Yodo Technology & development group, Insight, Inc.

Hiroshi Okada Faculty of Engineering, Tokyo University of Science

Hiroshi Kawai Faculty of System Engineering, Tokyo University of Science, Suwa

Masao Ogino Information Technology Center, Nagoya University

Ryuji Shioya Faculty of Information Sciences and Arts, Toyo University

The authors have been developing a crack propagation analysis system that can deal with arbitrary shaped cracks in three-dimensional solids. The system is consisting of mesh generation software, a large-scale finite element analysis program and a fracture mechanics module. To evaluate the stress intensity factors, Virtual Crack Closure-Integral Method (VCCM) for the quadratic tetrahedral finite element is adopted and is included in the fracture mechanics module. The rate and direction of crack propagation are predicted by using appropriate formulae based on the stress intensity factors. Combined with ADVENTURE system, a large-scale fully automatic fracture analysis can be performed on Earth Simulator 2.

Keywords: fracture mechanics, crack propagation analysis, finite element method, domain decomposition method, aging structure

1. Introduction

For the realization of sustainable society in the 21 century, structural integrity assessments for gradually aging social infrastructures are increasingly gaining their importance. Fracture mechanics simulation will be one of the key numerical methodologies for the structural integrity assessments. However, three-dimensional crack analyses for realistic highly complex structures have not widely been used so far, because of many obstacles such as the lack of computational power. The authors have been developing an open-source CAE system, ADVENTURE [1]. It is based on the hierarchical domain decomposition method (HDDM) with the balancing domain decomposition (BDD) pre-conditioner [2] [3]. A general-purpose structural analysis solver, ADVENTURE Solid, is one of the solver modules of the ADVENTURE system. On the other hand, the authors have been developing a fracture mechanics analysis system that can deal with arbitrary shaped cracks in three-dimensional structures. The system consists of mesh generation software, a finite element analysis program and a fracture mechanics module. In our system, a Virtual Crack Closure-Integral Method (VCCM) for the quadratic tetrahedral finite elements [4] is adopted to evaluate the stress intensity factors. This system can perform the three-dimensional fracture analyses. Fatigue and SCC (stress corrosion cracking) crack

propagation analyses with more than one cracks of arbitrary complicated shapes and orientations. The rate and direction of crack propagation are predicted by using appropriate formulae based on the stress intensity factors.

In this year, we developed a fracture mechanics analysis system with ADVENTURE and VCCM for large scale and complex-shape crack models with over 100 million DOFs tetrahedral mesh on Earth Simulator2.

2. Overview of VCCM

VCCM for the quadratic tetrahedral elements that is proposed by Okada et al. [4] is adopted for the computations of the stress intensity factors. In this section, a very brief summary of the VCCM is presented. The readers are referred to Okada et al. [4] for the full details of the VCCM. In the VCCM, the energy release rate is expressed by energy which is required to virtually close a finite element face which is adjacent to the crack front. the is able to evaluate the energy release rate G_I from nodal displacement and reaction force nearby crack front calculated by structural analysis.

$$G_I(S_1) = \frac{2\delta\bar{W}_I(S_1)}{3S_1} \quad (1)$$

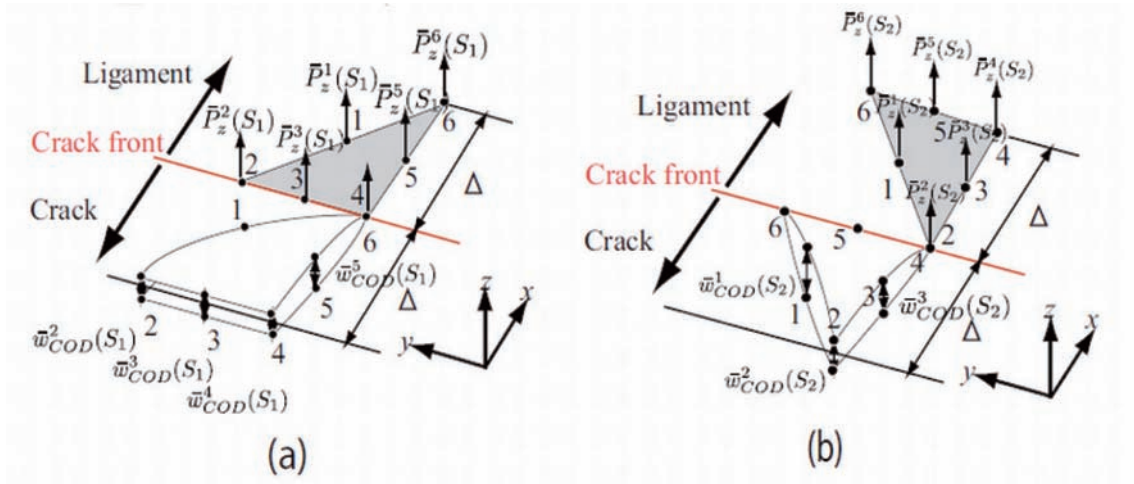


Fig. 1 VCCM calculation [(a) for area S1, (b) for area S2].

$$G_I(S_2) = \frac{2\delta\bar{W}_I(S_2)}{S_2} \quad (2)$$

where G_I is the mode I energy release rate, S_1 and S_2 are the areas of element faces whose vertex node and edge are on the crack front, respectively. S_1 and S_2 are illustrated in Fig. 1 (a) and (b). $\delta\bar{W}_I(S_1)$ and $\delta\bar{W}_I(S_2)$ are the energies that are required to virtually close the faces S_1 and S_2 . $\delta\bar{W}_I(S_1)$ and $\delta\bar{W}_I(S_2)$ can be computed by using the nodal crack opening displacements \bar{w}_{COD} and the nodal forces \bar{P}_z^I arising from the cohesive stress on the element faces at the ligament side. \bar{w}_{COD} and \bar{P}_z^I are schematically presented in Fig. 1. The energies $\delta\bar{W}_I(S_1)$ and $\delta\bar{W}_I(S_2)$ are expressed by:

$$\delta\bar{W}_I(S_1) = \frac{1}{2} \sum_{I=1}^6 \bar{P}_z^I(S_1) \bar{w}_{COD}^I(S_1) \quad (3)$$

$$\delta\bar{W}_I(S_2) = \frac{1}{2} \sum_{I=1}^6 \bar{P}_z^I(S_2) \bar{w}_{COD}^I(S_2) \quad (4)$$

The stress intensity factor is computed from the energy release rate. The stress intensity factor K_I is expressed, by:

$$K_I = \sqrt{E'G_I} \quad (5)$$

where $E' = E$ or $E' = E/(1-\nu^2)$ for the plane stress or the plane strain conditions. E and ν are the Young's modulus and the Poisson's ratio, respectively.

3. Numerical Analysis

In this section, a case study is demonstrated. The analysis model is a notched round bar with 3 inclined cracks (Fig. 2). Mesh of this model consists of 128,875,945 nodes and 95,663,296 elements. In FE analysis, calculation time and memory usage of solver depend on domain decomposition parameter and preconditioner. Based on our experience of analysis using Earth Simulator2 [5], we adopt about 12,000 DOF per domain for domain decomposition parameter and apply incomplete BDD-diag preconditioner on the Earth Simulator2.

Calculation result is as follows (Fig. 3). In calculation on ES2, we used 64 PEs and mesh decomposed to 512 parts/32,768

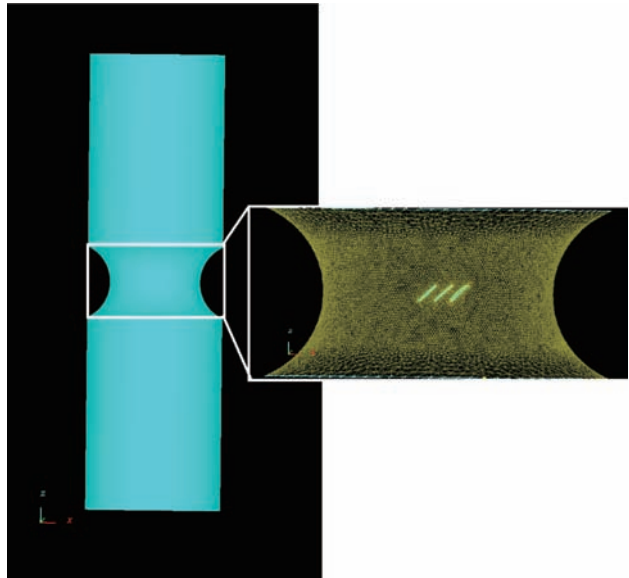


Fig. 2 CAD view of analysis model.

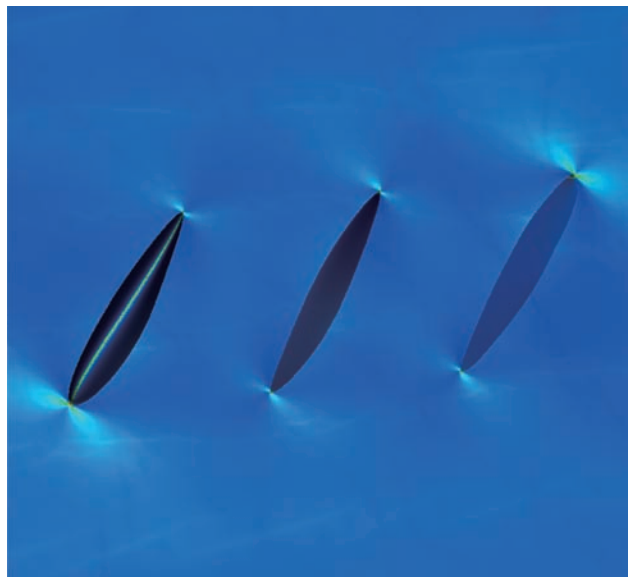


Fig. 3 Contour plot of Mises stress near by cracks.

subdomains and achieved 1717.3 sec. as calculation time and 2204.8 GFLOPS.

Finally, we evaluate the stress intensity factors. The results are presented in Figs. 4, 5 and 6 for the left side, center and right side cracks, respectively.

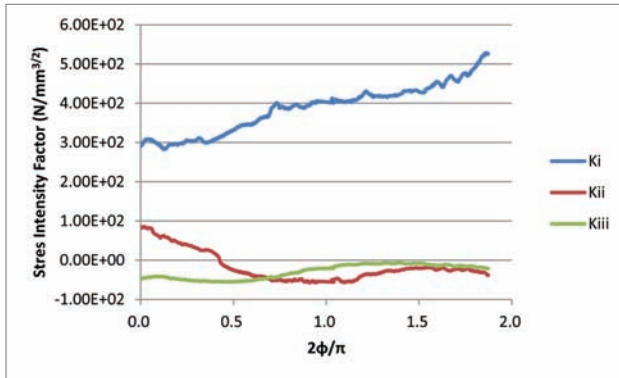


Fig. 4 Stress intensity factors of left crack.

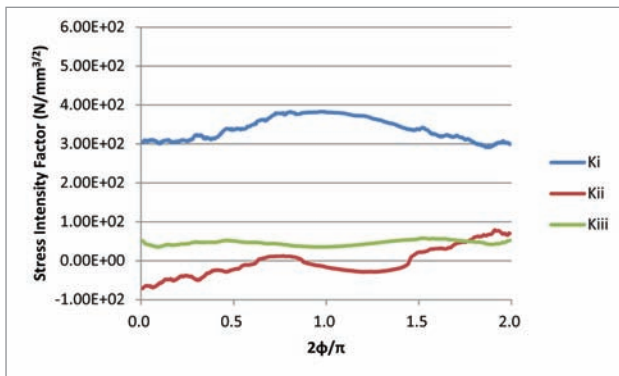


Fig. 5 Stress intensity factors of center crack.

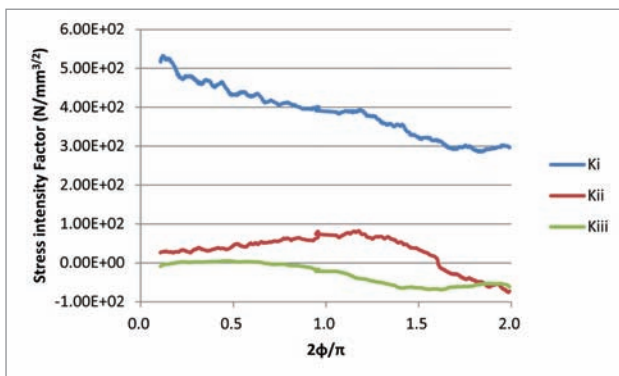


Fig. 6 Stress intensity factors of right crack.

4. Conclusions

We have developed an analysis system which can perform large scale fracture analyses on ES2. The quadratic tetrahedral finite element is adopted so that we can make use of automatic mesh generation methodologies. Therefore, our system is very advantageous over the conventional fracture analysis procedures that commonly adopt the hexahedral finite elements. It is noted that the mesh generation processes cannot be fully automated when we use the hexahedral elements.

We will continue present development and ultra-realistic large scale fracture mechanics analysis for the structural integrity assessments for aging structures will be possible in near future.

Acknowledgements

Part of research performed by H. Okada has been performed under the support of Grant-in-Aid-for-Scientific-Research (C) No. 22560149 (JSPS, Japan Society of Promotion of Science). The support is gratefully acknowledged.

References

- [1] ADVENTURE project, <<http://adventure.sys.t.u-tokyo.ac.jp/>>
- [2] M. Ogino, R. Shioya, and H. Kanayama, "An inexact balancing preconditioner for large-scale structural analysis", *Journal of Computational Science and Technology*, Vol. 2(1), pp.150-161, May 2008.
- [3] H. Kawai, M. Ogino, R. Shioya, and S. Yoshimura, "Large Scale Elasto-Plastic Analysis Using Domain Decomposition Method Optimized for Multi-core CPU Architecture", *Key Eng. Materials*, Vol. 462-463, pp. 605-610, Jan. 2011.
- [4] H. Okada, H. Kawai, and K. Araki, "A virtual crack closure-integral method (VCCM) to compute the energy release rates and stress intensity factors based on quadratic tetrahedral finite elements", *Engineering Fracture Mechanics*, Vol. 75(15), pp.4466–4485, Oct. 2008.
- [5] R. Shioya, M. Ogino, H. Kawai, and H. Okada, "Development of the Next-generation Computational Fracture Mechanics Simulator for Constructing Safe and Sustainable Society", *Annual Report of the Earth Simulator*, April 2011 – March 2012, pp. 131-134, Sept. 2011.

安全・安心な持続可能社会のための 次世代計算破壊力学シミュレータの開発

プロジェクト責任者

塩谷 隆二 東洋大学 総合情報学部

著者

淀 薫 株式会社インサイト 技術開発部

岡田 裕 東京理科大学 理工学部

河合 浩志 諏訪東京理科大学 システム工学部

荻野 正雄 名古屋大学 情報基盤センター

塩谷 隆二 東洋大学 総合情報学部

既に多くの超並列計算機や PC クラスタ上において実績を示している、1 億自由度級の大規模メッシュを用いた人工物や自然物の丸ごと詳細解析を可能とする汎用計算力学システム ADVENTURE をもちいて、実用大規模構造材料・機器の直接破壊シミュレータを ES2 上で開発し、低炭素社会構築のカギを握る小型高圧水素貯蔵タンクの超精密破壊解析や、安全・安心社会の基盤である経年化した社会的インフラストラクチャーの超精密破壊解析を通して本技術の確立を目指すことにより、21 世紀の持続可能社会の構築に寄与することを目的としている。

破壊力学パラメータの評価手法として、岡田らが開発を進めている四面体要素を用いた VCCM を用いることで、任意複雑形状モデルに複数のき裂が存在するような問題においても十分な精度を保証している。

今年度は、昨年度までの成果を基に、複数のき裂を持つ試験片の約 4 億自由度メッシュの有限要素解析を行い、その結果からき裂ごとに応力拡大係数を求めることに成功した。メッシュ生成には岡田・河合らが開発してきた CAD モデルから生成したメッシュの任意位置にき裂を挿入する手法を用い、さらに昨年度開発した要素細分割による大規模メッシュ生成プログラムを併用することで、4 億自由度のメッシュの生成に成功した。地球シミュレータ上での有限要素解析を行う際には、昨年度のパラメータチューニングの成果から最適な領域分割パラメータ及び前処理手法の選択を行い、2.2 Tflops（ピーク性能比約 4.2%）、1 回の静解析を 28.6 分での解析に成功した。また、計算結果からき裂周辺の変位を抽出し、そこから VCCM を用いてき裂ごとの応力拡大件数を計算した。

キーワード : fracture mechanics, crack propagation analysis, finite element method, domain decomposition method, aging structure

Chapter 3

■ Visualization ■

Studies of Large-Scale Data Visualization: EXTRAWING and Visual Data Mining

Project Representative

Fumiaki Araki

Earth Simulator Center, Japan Agency for Marine-Earth Science and Technology

Authors

Fumiaki Araki^{*1}, Shintaro Kawahara^{*1} and Daisuke Matsuoka^{*1}

^{*1} Earth Simulator Center, Japan Agency for Marine-Earth Science and Technology

Progress of EXTRAWING, the research and development project for attractive representations and transmissions of results of geophysical and environmental fluid simulations is reported. The software tool to make KML contents of simulation results has been improved as following three points. First, the GUI of the software is modified for improving usability. Second, color-contour plots become available on horizontally- and/or vertically-sliced planes. Third, the functions to output animation data is implemented for analysis of time-developing simulations. An effective method to render for a set of laminated layer surfaces is newly designed.

Progress in terms of visual data mining techniques for semi-automatic feature extraction of oceanic currents has been also reported. It contains two themes which techniques of cluster analysis are applied. One is about a density-based method and another is a hybrid method combined between non-hierarchical and hierarchical methods. The density-based method has successfully extracted both of Kuroshio and Oyashio currents from OFES simulation data, but its computational cost is too high. The hybrid method has been also tested to solve such the difficulty from the density-based method.

Keywords: EXTRAWING, tool development, feature extraction, cluster analysis, oceanic currents

1. EXTRAWING

EXTRAWING [1] is a project for novel and attractive representations of results of geophysical and environmental fluid simulations and effective transmission of those results to the general public. In the FY2011, we describe about following two progresses.

1.1 Volume visualization software tool

We have developed a program, called “Volume Data Visualizer for Google Earth (VDVGE)”, to make EXTRAWING contents since FY2010. Fig. 1 shows the GUI of this program. VDVGE can read a volumetric dataset, visualize it using our original volume visualization method [1], and output a content file written in KML format for Google Earth. Such the specification means that VDVGE can be utilized for not only contents-making but also three-dimensional visual analysis of earth-scientific data. To strengthen it further, we implemented additional visual analysis functions, especially two-dimensional contour-plot in the extracted surface from the volume dataset, that is the cross-section, and file-saving function of time-sequential rendering results.

Fig. 2 shows an example of the visualization result by the contour-plot function. This function extracts cross-sections from the target volume data via interpolation process and plots two-dimensional color-contour on the cross-section. The normal

direction of the cross-section is selected from the axes of polar coordinates. In terms of file-saving, the function not only exports a KML file but also saves rendering results on the main window in Fig. 1 as sequential images or a movie file of MPEG format.

With implementation of these additional functions, the GUI of VDVGE had been complicated. So we also reconstructed the program design of VDVGE and improved the GUI for better usability.

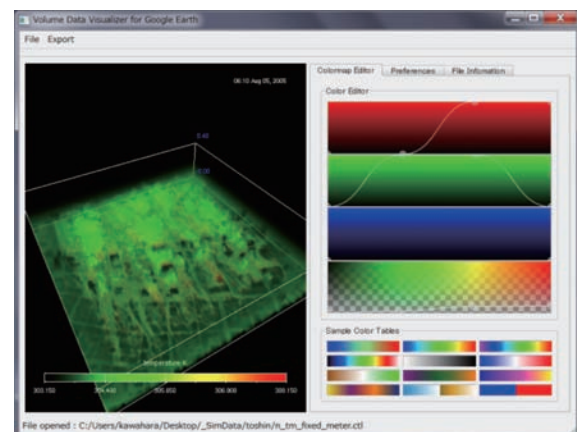


Fig. 1 Main window of VDVGE.

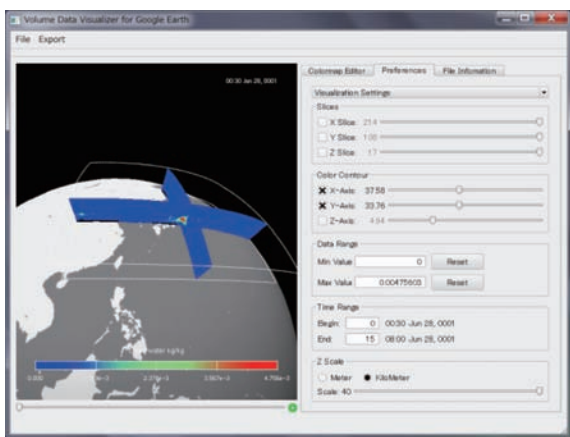


Fig. 2 Color slices on VDVGE.

1.2 Novel method for laminated surfaces

We devised a novel surface-ordering method to render effectively a set of laminated surfaces with color-contour images mapped on each ones. Usually, when sliced planes with transparencies are rendered, an accurate rendering result can be got by using a combination of a couple of techniques, z-sorting and alpha blending. The z-sorting process must perform at every change of viewing position. On the other hand, our algorithm enables us to get a fixed rendering result by devising the rendering order of each sliced plane without re-sorting the order, even when viewing position changed. Fig. 3 shows examples of the rendering order in this method. The number of 1 to 5 in Fig. 3 means those orders. The signs A and B mean viewing directions of users. In these examples, a slice of #1 is set as the reference plane and the number of other slices become larger with increasing of the distance from the reference plane. Fig. 4 shows a rendering diagram based on proposed method,

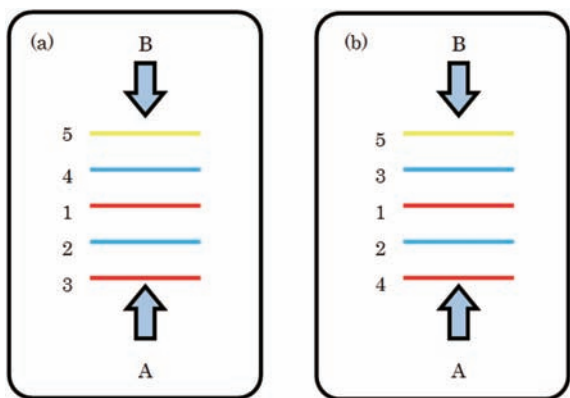


Fig. 3 Rendering order of slice planes.

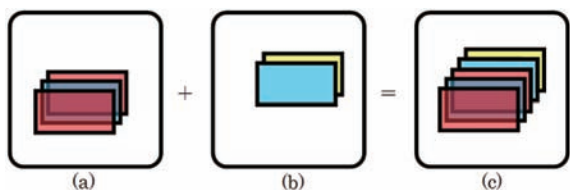


Fig. 4 Diagram of rendering based on proposed method; (a) Planes which are nearer than the reference plane, (b) Planes which are farther than the reference plane and (c) visualization result.

when rendering orders are set up as in Fig. 3. Alpha-blending is carried out nearer than the reference plane (Fig. 4 (a)) and z-buffering is carried out farther than the reference plane (Fig. 4 (b)). Fig. 5 shows differences of rendering results in the case with (right) / without (left) this method. These figures mean that we can get an accurate result about planes close to the viewing position from the reference plane.

We applied for a patent about this algorithm (Application Number (2012) 005541). Use in the visual representation on low-resource devices such as mobile phones can be expected.

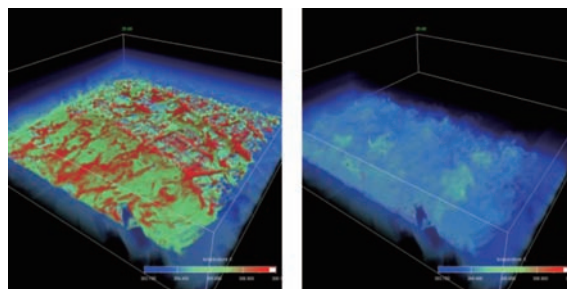


Fig. 5 Differences of rendering result with/without use of the proposed method. Right hand side of the images was the case which our method applied and left hand side was not.

2. Visual data mining for oceanic simulation

Visualization of numerical simulation results is effective way to understand complex phenomena and/or configuration intuitively. Nevertheless, there is still a challenge to extract information from huge amount of data obtained from large-scale and high-resolution simulation on the massively parallel super computer. In the fiscal year 2010, we developed a novel 2-dimensional transfer function (color map) which can simultaneously represent two physical values by using H-V space of HSV color [5]. We visualized ocean currents effectively by applying this method to OFES data. While this approach extracts the oceanic currents successively in the case of two variables, it is still difficult to expand to higher dimensions. In order to establish feature extraction of oceanic currents in the further multi-variable cases, in the fiscal year 2011, we have developed two different approaches applying techniques of cluster analysis.

2.1 Extraction of ocean currents via density-based cluster analysis

In our method, it is necessary to set the following parameters, density in the variable space, range for calculating density, range for exploration and range for clustering. For instance, regarding to set parameters of density and range, we visualize “similarity density” which represents density of elements in arbitrary range within the multi-dimensional variable space as shown in Fig. 6. In this figure, the red (or blue) region indicates that many elements of the surrounding area have similar (or different) characteristics. In addition to these parameters, initial seeds for extraction of the Kuroshio and Oyashio are shown in

Fig. 7. Clustering results are also visualized in Fig. 7. The red and blue area indicates the Kuroshio and Oyashio, respectively. Both results can be seen that the clustering is roughly correct.

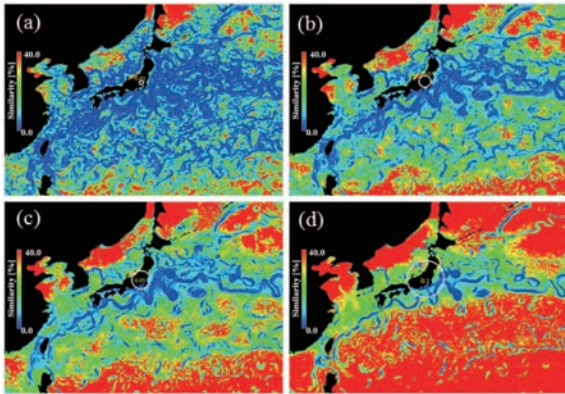


Fig. 6 Similarity density map. Eps = (a) 0.1, (b) 0.3, (c) 0.5 and (d) 1.0.

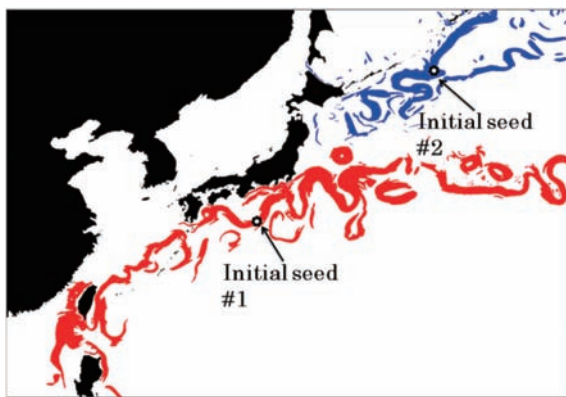


Fig. 7 Extraction result of Kuroshio and Oyashio by density-based method.

2.2 Extraction of ocean currents via non-hierarchical and hierarchical cluster analysis

The density-based method, which is one of the cluster analysis techniques, can extract ocean currents but enlarges its computational cost too high. We study also the case adopting the non-hierarchical cluster method, which is another cluster analysis technique.

One of the important steps of cluster analysis is to select a distance measure, which can determine how to calculate the similarity between two elements. The distance between two elements (i and j) in 4-dimensional Euclidean space is defined as:

$$D_{ij}^2 = C_T (T_i - T_j)^2 + C_V (V_i - V_j)^2 + C_X (X_i - X_j)^2 + C_Y (Y_i - Y_j)^2$$

where, T , V , X and Y is temperature, flow speed and x- and y-positions, respectively. The coefficients, C_T , C_V , C_X and C_Y , are constant values to make the similarity dimensionless.

The resulting image of non-hierarchical cluster analysis and 16 centroids, initial points of non-hierarchical clustering, are shown in Fig. 8. In this figure, each cluster is indicated in different colors. Not only the Kuroshio (cluster #1 and #2), the Kuroshio Extension region (cluster #3 and #4) and the Oyashio (cluster #14 and #15) but also the mixed layer in the Kuroshio/Oyashio Extension region and the vortices in the Sea of Japan

seem to be clustered almost correctly.

Furthermore, let us also adopt hierarchical method to extract the hierarchical structure of these small clusters obtained by the non-hierarchical method. We can recognize from the resulting diagram by the hierarchical method as shown in Fig. 9 that Kuroshio is composed from cluster #1 - #4 and Oyashio is done from cluster #14 and #15, respectively.

How the validity of clustering results and optimization of the parameters should be evaluated is a key issue in the future works.

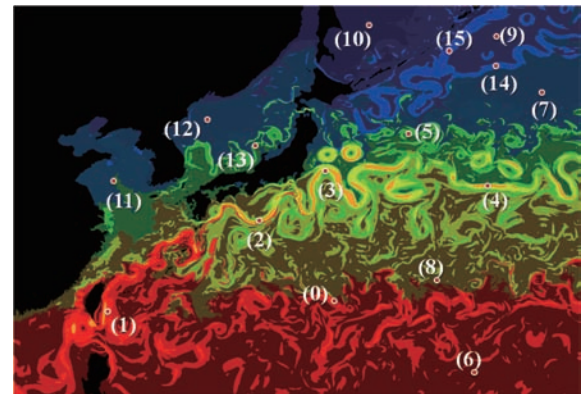


Fig. 8 Extraction result of Kuroshio and Oyashio by the non-hierarchical method.

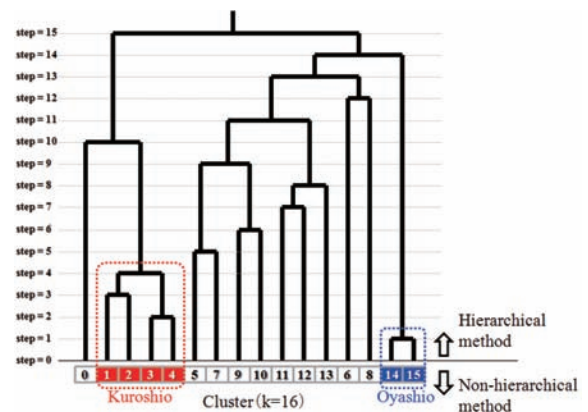


Fig. 9 A diagram in case of non-hierarchical and hierarchical hybrid method.

References

- [1] Fumiaki Araki, Shintaro Kawahara, Daisuke Matsuoka, Takeshi Sugimura, Yuya Baba and Keiko Takahashi, "Studies of Large-Scale Data Visualization: EXTRA WING and Visual Data Mining", Annual Report of the Earth Simulator Center, April 2010-March 2011, pp.195-199, 2011.
- [2] GrADS, <http://www.iges.org/grads/>
- [3] Fumiaki Araki, Hitoshi Uehara, Nobuaki Ohno, Shintaro Kawahara, Mikito Furuichi and Akira Kageyama, "Visualizations of Large-scale Data Generated by the Earth Simulator", Journal of the Earth Simulator, vol.6, pp.25-34, 2006.
- [4] Conduit, <http://www.mechdyne.com/conduit.aspx>

- [5] N. Ohno and D. Matsuoka, Visualization of Global Geophysical Fluid Simulation, NAGARE, Vol.30, No.5, pp. 409-414, 2011.

大規模データ可視化研究： EXTRAWING とビジュアルデータマイニング

プロジェクト責任者

荒木 文明 海洋研究開発機構 地球シミュレータセンター

著者

荒木 文明^{*1}, 川原慎太郎^{*1}, 松岡 大輔^{*1}

*1 海洋研究開発機構 地球シミュレータセンター

地球環境流体シミュレーションの結果を魅力的に表現し一般社会へ発信する研究開発プロジェクト、EXTRAWING の進捗を報告する。2011 年度は、シミュレーション結果の KML コンテンツを作成するソフトウェアの改良を以下の 3 点：(1) 利便性の向上のための GUI の変更、(2) 水平 / 垂直断面上でのカラーコンタ表示、(3) 時間発展シミュレーションを解析するための連番画像および動画ファイルの出力機能の実装、を中心に実施した。また積層面の全体をレンダリングする上で効果的な新しい方法を考案した。

海流の特徴抽出を半自動的に実行するためのビジュアルデータマイニング技術についての進捗も報告する。本年度はクラスタ分析法を応用した二つのテーマに取り組んだ。一つは要素間の類似度密度に基づいた方法、もうひとつは非階層的クラスタ分析法と階層的クラスタ分析法を組み合わせたハイブリッドな方法である。一つ目の類似度密度に基づいた方法では、黒潮と親潮の両方の海流を正しく抽出できることが確かめられた。しかしながら計算コストは極めて高い。そこでこの困難を解決するために二つ目のハイブリッド手法も試みられた。

キーワード: EXTRAWING, ツール開発, 特徴抽出, クラスタ分析, 海流

Published by

The Earth Simulator Center, Japan Agency for Marine-Earth Science and Technology

3173-25 Showa-machi, Kanazawa-ku, Yokohama, 236-0001 JAPAN

Tel: +81-45-778-5861 Fax: +81-45-778-5491

<http://www.jamstec.go.jp/esc/>

First edition: October 15, 2012

© The Earth Simulator Center

Reproduction or distribution of the contents of this publication without permission is strictly prohibited.